Università degli Studi di Pavia
Dottorato di Ricerca in Fisica - xxxiii Ciclo

Raman Spectroscopy and Nanostructured Complex Systems:
A satisfactory win to win game?

Benedetta Albini

2020

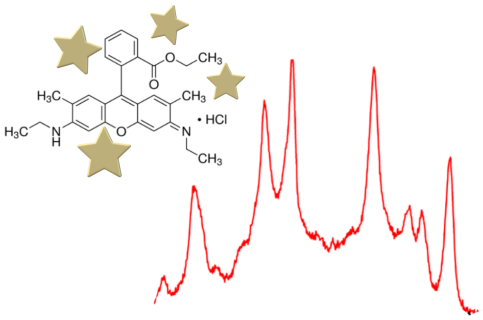

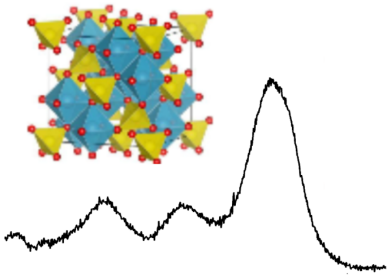

When you have excluded the impossible,
whatever remains, however improbable,
must be the truth.
Sherlock Holmes - Sir Arthur Conan Doyle

Contents

Abstract

This PhD work is mainly based on two pillars centred on the coupling between Raman spectroscopy and nanostructured complex systems.
The first pillar is a quite popular scientific topic, i.e. the study of Surface Enhanced Raman Scattering (SERS) effect by targeting molecules - for different applicative perspectives - using nanostructured metallic substrates, mainly gold nanostars (GNS).
On the other hand, the thread of the second pillar can be understood adapting the incipit of a popular review of Dresselhaus [1] to the present matter. Complex oxides, even nanostructured, have proven to be very suitable systems in order to investigate different aspects of Raman spectroscopy, and at the same time Raman spectroscopy has provided an extremely powerful tool for the characterization of nanostructured complex oxides. Indeed cationic disorder, oxygen deficiency, grain size effects, structural distortions and phase transformations have a direct impact on their vibrational degree of freedom.

The first area of research regards the study of SERS spectroscopy applied to nanostructured metallic solid planar substrates, properly functionalized in order to obtain robust, recyclable and reusable SERS-active devices, characterized by moderate enhancement factors (EFs), for industrial as well as biomedical applications.
At this regards we have investigated the feasibility of microscopy cover glass slides functionalized with gold nanostars (GNS), acting as enhancer medium. The SERS substrates have been synthesized by the research group of Prof. Taglietti, with which this activity has been carried out. Starting from a self assembled monolayer approach (SAM), the GNS have been firstly grafted on glass sides through electrostatic interactions. Then the surfaces have been terminated with a thin layer of silica in order to achieve mechanical and chemical stability as well as chemical inertness to possible contaminants that again could mine the stability of the active layer.
The Raman probe has allowed us to verify that the silica layer imparts mechanical and chemical stability to the substrates as well as chemical inertness an important feature that makes the SERS substrates also reusable. Moreover,

the Raman inspection has pointed out the homogeneity of the SERS response not only within the same samples but also from samples coming from different preparation batches, ensuring the validity of the synthesis procedure.
An other important aspect is that through the variations of the silica thickness we have been able to evaluate the dependence of the enhancement factor as a function of the distance between the analyte and the SERS active layer with evidence of a negligible chemical enhancement and an electromagnetic enhancement which drops to zero beyond 10 nm.
An other approach that has been exploited to stabilize the SERS active layer, has consisting in its functionalization with different thiols coating. This strategy has been put in place to exploit also the hydrophobicity as well as hydrophilicity imparted by the thiols layers to the substrate surface. Indeed, the aim of chemical group of Prof. Taglietti is to design robust and stable GNS functionalized chips, in the same simple and low cost way, to be employed as smart antibacterial surfaces in the pan-drug resistance bacteria emergency, by exploiting the photo-thermal activity of GNS to properly kill bacteria and the anti-adhesive properties given by thiols coating to prevent their adhesion and in turn the contamination of the devices, themselves. In this frame, SERS technique has been used as an analytical tool that has allowed to verify the homogeneity of the SERS response and thus the homogeneity of the GNS layer. Moreover, exploiting the SERS effect we have been able to identify the best concentration of thiols coating in order to obtain a monolayer of covering. Finally, we have verified the stability of the SERS active layer before and after photo-thermal cycles that the substrates have undergone.

The second aspect of my research activity has consisted in the study of the Raman response of an intriguing class of nanostructured oxide spinels, i.e. $ZnFe_2O_4$ (ZFO) ones. ZFO, as the general class of iron oxides compound with the chemical formula AB_2O_4, displays interesting magnetic, mechanical, chemical, thermal and electrical properties that make it suitable to be used in different applicative fields, as for instance the biomedical one.
Zinc ferrite spinel has a bulk normal spinel structure in which all the Zn^{2+} cations occupy only the tetrahedral site (A) while the Fe^{3+} cations the octahedral one (B). However, at the nanometer regime, a partial cation inversion occurs and thus some of the Fe^{3+} cations occupy also the A site. This reflects in a change of the magnetic properties of this compound: indeed, the paramagnetic behaviour characterizing the spinel in the bulk regime is replaced by a superparamagnetic (SPM) behaviour at room temperature. This room temperature SPM behaviour is of extreme utility in biomedical applications such as drug delivery or MRI, since the nanoparticles exhibit no magnetic properties upon removal of the external field and thus they do not attract each other, eliminating the major driving force of aggregation. Since the magnetic behaviour is strictly correlated to the cationic arrangement between the two sublattices of the spinel structure, it is thus clear that a careful control of the

functional parameters of this compound is of extremely importance for its application, in particular in the biomedical fields. This control can be achieved by tuning the material properties in terms of size, shape, composition, namely substitutions, doping, cation distribution, and shell-core design. Thus, it is obvious that also synthesis methods play an important role.
Raman spectroscopy has been widely used to characterize zinc ferrite nanoparticles as well as the general class of iron oxides spinels. Indeed, we have satisfactory used the Raman probe to investigate pure and Ga and/or Mg doped zinc ferrite nanoparticles synthesized by a co-precipitation route. This research activity has been carried out in collaboration with the group of Prof. Bini, where the samples have been synthesized and partially characterized. These data have been discussed taking into account our previous results on zinc ferrites. Indeed, we have already investigated zinc ferrite nanoparticles synthesised by a different method, i.e. microwave combustion one, and with different doping cations, namely Ca and Sr on A site and Gd and Al on B site. Through the Raman probe we have been able to verify the phase homogeneity of the investigated samples. Moreover, we have extract semi-quantitative information on the inversion degree of our spinels. The stability of the samples structure has been proved by performing laser-induced thermal cycles. This test has allowed us to evaluate possible presence of phase and structural transitions; in particular to evaluate the insurgence of maghemite and/or haematite, whose presence can alter the functional properties, favouring aggregation, highly dangerous for biomedical applications. The results seems to indicate that at least in the outer part of the nanoparticles a Zn-deficient region is present and it represents the trigger for haematite formation. This information, derived from laser- induced cycles, has been confirmed comparing Raman spectra obtained at different excitation energies. Indeed, we have performed measures at 633, 532 and 266 nm in order to change the investigated volumes at variance of the energy probe. These results indicate that higher the energy probe greater the contribution of FeO_4 stretching modes with respect to those related to ZnO_4 tetrahedral units. This seems to validate the presence of an highly defective external shell in ZFO nanoparticles. The results obtained with the Raman probe have been also discussed and validate by means of complementary techniques, namely X-ray powder diffraction, electron paramagnetic resonance and SQUID measures to evaluate the magnetic response of our samples. The intention was to find further and direct confirmation by Mössbauer spectroscopy but due to COVID emergency this task will be pursued in the next year.

The interesting results obtained both in the SERS study on metallic substrates and Raman investigation on zinc ferrite nanoparticles, have been used to deal with the study on hybrid devices made up of Ag and ZFO nanoparticles in order to design possible sensing substrates exploiting the SERS enhancement of the metallic part and the superparamagnetic property of the oxide one for

biomedical applications.
This project is only at its preliminary stage. Indeed, we are still evaluating the best recipe of these coupled devices in order to achieve stability and, of course, high enhancement properties.

The versatility of the Raman probe and the possibility of different collaborations that the PhD project offers have allowed me to give relevant contributions on hot-burning topics in materials science even if different (or at least collateral) from the core of my activity.
In particular, we have satisfactory used the Raman probe to characterize two intriguing compounds which are arising great interest as anode materials in solid state batteries, namely black phosphorus and $FeNb_{11}O_{29}$.
As regards the study on black phosphorous, Raman investigation has allowed to evaluate the crystallinity of the black phosphorous compounds obtained as a result of the ball milling processing starting from a commercially red phosphorous. In particular, we have been able to correlate the structural properties of the resulting samples to the ball milling parameters. The obtained results are consistent with ones obtained by means of NMR and XRD measures performed by the chemical group of Prof. Quartarone that has also synthesised the investigated samples.
On the other hand the research work on $FeNb_{11}O_{29}$ has been carried out in collaboration of the research group of Prof. Bini. Through Raman inspection we have been able to evaluate the structural order/disorder of the compounds by varying their composition in terms of the different doping as well as different reaction atmospheres in the synthesis process.
We have also investigated the formation of a crystalline superficial TiO_2 layer on dental screw-type implants by varying the starting bulk medium as well as the surface treatments. Indeed, the creation of a superficial titanium dioxide layer imparts suitable physical, chemical and bio-compatible features to these endo-osseous implants. In particular, we have analysed the Raman response of two different series of samples made up of two different titanium alloys at each step of surface treatment. The obtained results have allowed to identify the best starting material and surface process that ensure the formation of crystalline TiO_2 layer.
An other study on nanostructured oxide systems regards the research on CeO_2 and ZnO nanoparticles bonded with HeLa epithelium cancer cells. This is an open research still at its early stages. The aim is to use Raman spectroscopy in order to reveal the vibrational fingerprint of these oxides in a biological environment, evaluating possible changes in their structure due to the binding with cancer cells.

All the activities outlined in this thesis probably give a small contribution in the overall science progress, however they surely represent a very important step for my scientific growth and some of the illustrated arguments will be the

starting point of my future research activity.

Introduction

This PhD thesis reports on my research works, developed in these three years, on which Raman spectroscopy undoubtedly played a central role. This is the reason why the introduction, moving from a short historical consideration, tries to sketch a review on the different applications of this technique in basic and applied research fields as well as analytical or industrial cases.

Raman spectroscopy is a highly sensitive vibrational technique which allows to identify molecules through their unique vibrational "fingerprint" within a fast time scale investigation. Raman effect consists in the inelastic scattering of photons from matters induced by molecular vibrations. It is a two-photon process that occurs upon changes in the polarizability of the molecular bonds of the analyte in response to the vibrations. The inelastic scattering of light was first observed by Sir C.V. Raman and his co-workers and reported in his famous publication on Nature in 1928. After a period in which his research work was focused on the study of light scattering by water, he convinced himself that what he was looking at was the optical analog to the Compton effect for electrons

> *If we assume that the X-ray scattering of the 'unmodified' type observed by Prof. Compton corresponds to the normal or average state of the atoms and molecules, while the 'modified' scattering of altered wave-length corresponds to their fluctuations from that state, it would follow that we should expect also in the case of ordinary light two types of scattering, one determined by the normal optical properties of the atoms or molecules, and another representing the effect of their fluctuations from their normal state [2].*

Following this inference, he and his student, Krishnan, performed different experiments on gaseous, liquids and also some crystals and amorphous solids, coming to the conclusion that

> *The experiments we have made have confirmed this anticipation, and shown that in every case in which light is scattered by the molecules in dust-free liquids or gases, the diffuse radiation of the*

> *ordinary kind, having the same wave-length as the incident beam, is accompanied by a modified scattered radiation of degraded frequency [2].*

To perform these experiments, Raman used a simple set-up with the sunlight as excitation source, a telescope as the collector and his eyes as detector. Using proper filters, he was able to observe weak lines of a different colour with respect to the excitation source, scattered by the investigated molecules. It was not trivial to detect the inelastic scattered light because this effect is a very weak phenomenon; indeed, the differential Raman cross section is about $10^{-27} - 10^{-30}$ cm^2 sr^{-1}, namely approximately 12 order of magnitude weaker than the one of fluorescence. This is the reason why the widespread of Raman spectroscopy (RS) as analytical tool is linked to the development of ever more high-performance instrumentation. In particular, the turning point in the progress of Raman instrumentations is strictly related to great technological discoveries as for instance, the advent of laser that gives a coherent monochromatic excitation source, the use of holographic gratings and the birth of low noise charge-coupled-device (CCD) detectors. Moreover, between 80s and 90s, Micro Raman spectroscopy has been developed thanks to the joint used of a microscope and a Raman spectrometer, allowing inspection in sample areas as small as few micrometers. The subsequent improvements in the technological development, like the advent of compact, high power solid state lasers, holographic filters to cut the Rayleigh component of scattered light, as well as optical fibers, have paved the way to the development not only of highly sensitive bench-top Raman systems but also of new portable and handle ones enabling also in situ Raman measurements.
The non-invasiveness and non-destructiveness of the RS probe coupled to the ability of easily providing information about the investigated analyte in "real time" without the need of sampling, have risen the use of Raman spectroscopy not only in the academic research field but also in the industrial one.
As regard the industrial applications, RS is employed in different fields as for instance pharmaceutical, petrochemical and quality control ones.
Turnkey bench-top systems have been developed by different companies for drug detection [3]; in particular, thanks to the joint-use of multivariate analyses software, these instruments are able to perform quantitative analyses on the prepared drugs from the single pill to the entire blister; by collecting the Raman signal through the scan of the compound surface, it is possible to control the uniform distribution of the active pharmaceutical ingredients (API), to discern them from the excipient and also to differentiate the different API polymorphs [4].
The petrochemical applications of RS concern not only the analysis of fuels, but also the possibility to control the good condition of the pipelines. In particular, Raman inspection allows to discriminate between different fuels by characterizing their composition and to control their purity degree identifying the absence or presence of additives [5]. Moreover, the Raman probe allows

to control the degree of pipelines corrosion; indeed, the steps of a corrosion process is marked by the presence of different iron oxide and hydroxide phases that Raman measures enable to discriminate because each phase is marked by well defined Raman features [6]. The portable probe-Raman instruments also allow to perform all these controls in situ and underwater too, facilitating the procedure and preventing high cost operations.
Raman probe is efficiently used in the quality control chain. For example, new handle devices based on the Spatially Offset Raman Spectroscopy (SORS) are employed to verify the correct identity of raw materials stored in opaque containers in order to avoid manufacturing errors [7]. The basic principle of SORS relies on the ability to detect the Raman signal of the inner compound through a thin layer of non transparent medium by introducing a spatial offset between the excitation source and the detector, exploiting higher photon migration in highly diffusive materials [8]. These are only same examples of the use of RS in the industrial field.
I think that Raman spectroscopy represents a brilliant example of the overlapping between academic and industrial research fields sometimes considered as neatly distinct; indeed, there is a mutual exchange of notions and knowledge between these two research fields which is the key factor to achieve further progress in the Raman technology and to promote its widespread in different applicative fields.
As regards the academic field RS is fruitfully employed in a wide variety of research areas as for instance solid state physic, material science, chemistry, biomedicine, food safety, geology and cultural heritage. It is to ambitious to pretend to exhaust in few lines the numerous applications of RS, however in the following I will describe a couple of outstanding research works as an example.
Through Raman inspection it is possible to study a variety of materials like semiconductors, magnetic systems, superconductors, complex oxides based systems, ferroelectric and ferrielectric compounds and carbon based materials; these studies concern not only 3D structured compounds but also 2D ones. In general, RS allows to study different properties of the aforementioned compounds, for example structural transitions, defect-induced properties, plasmon modes, charge-density-waves, soft-modes, magnon and electromagnon modes and superconducting gap excitations. All these physical features could be inspected also in critical conditions of temperature, pressure and high magnetic fields.
Just to give an example about the versatility of Raman spectroscopy in the field of solid state physics, I will briefly report some recent Raman studies on a current topic regarding the magnetic van der Waals layered materials. These materials have attracted a lot of interest for their peculiar physical and chemical properties and the possibility to access the fundamental, low dimensional physical principles. Indeed, these systems are characterize by strong intralayer interaction and weak interlayer coupling that allow them to be exfo-

liated, obtaining thin layers of only few atoms. As all the other 2D materials, these systems display mechanical flexibility, the possibility, by combining these atomic layers from different materials, to realize heterostructures whose properties could be tune by quantum confinement and proximity effect and the capability to tune their transport properties with an external electric fields, just to mention few of their properties. These functional parameters make these systems suitable to be employed in magneto-optical and magnetoelectric devices as wall as spintronics. Among these Van der Waals magnetic compounds, there are the transition metal phosphorus trisulfides $TMPS_3$ (TM = Fe, Mn, Ni, V, Co or Zn), antiferromagnets that have been investigated in 2D limit. Even if they are isostructural, they are characterized by different spin structures below the Néel temperature (T_N) and, in particular, the different transitional metal chosen leads to different magnetic phenomena because of the different way in which the spins align antiferromagnetically within the layers. In the recent years, Raman spectroscopy has been demonstrated to be a powerful technique in studying the properties of these materials, not only for the possibility to perform non-destructive measures and to achieve information within few minutes but also for the ability to probe thin atomic layers without requiring large scale sampling and to achieve a spatial resolution till the diffraction limit. Moreover, RS represents a simpler alternative to common direct magnetic measurements in deepening the magnetic properties of atomically thin magnetic compounds through changes in the Raman spectrum on approaching a magnetic transition. In this regard, I would like to briefly describe the research activity that has been performed on one of the transition metal phosphorus trisulfides, $FePS_3$, a Mott insulator, which is of particular interest as a 2D Ising antiferromagnet on a honeycomb lattice (Figure (1)). $FePS_3$ is an intriguing candidate to be investigated by Raman spectroscopy

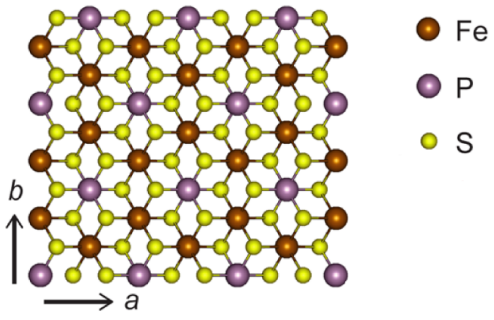

Figure 1: $FePS_3$ crystal structure [9].

because the Brillouin zone folding leads to the growth of new modes below T_N, caused by the antiferromagnetic alignment of the spins and the consequent increase in the unit cell, as reported in Figure (2a). The RS inspection has allowed to monitoring the antiferromagnetic ordering, also as a function of the number of layers, by the growth of new peaks from zone folding below T_N (Figure (2b)). In particular, it has been proved an intrinsic Ising-type

antiferromagnetic order which survives till the monolayer limit suggesting that the the magnetic intralayer interaction dominates against the weak interlayer one [9] [10]. Moreover, magneto-Raman measurements have demonstrated that one of the modes appearing below T_N could be ascribed to a quantized spin wave, a magnon [11].

Another field in which RS is widely employed as a label-free analytical tool is

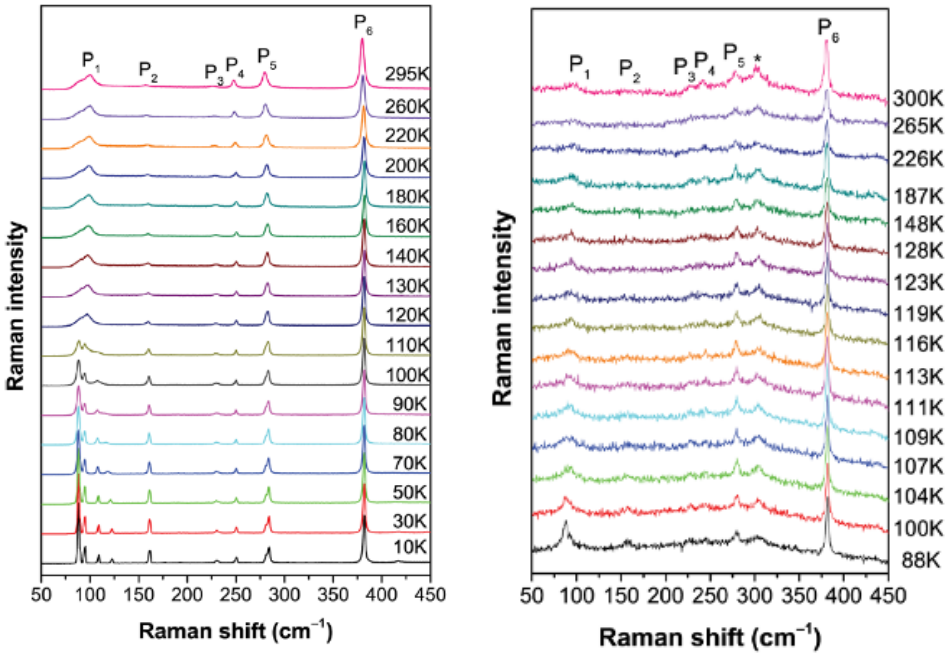

Figure 2: Temperature dependence of the Raman spectrum for bulk (a) and, in a parallel polarization configuration, for one monolayer (b) $FePS_3$. The graphs are taken from [9].

the biomedical one. From the beginning of the 90s, Raman spectroscopy has been progressively used in studying the biochemical properties of cells and tissues, from the investigation of bacteria, enabling the identification of the spices and also their antibiotic resistance [12], to whole human cells and tissues. Indeed, RS turns out to be an appropriate tool to investigate the biological systems because, at first, the Raman spectrum is less affected by the interference of water, with respect to other techniques like infrared spectroscopy, thus enabling measures on aqueous samples, and furthermore, by proper choosing wavelength, incident laser power density and exposure time, RS does not perturb live cells, being a non-destructive probe. RS inspection has allowed to get detailed information about the human cell properties and the biochemical processes that they undergo, also by collecting images of the interested areas with Raman imaging measures. In particular, it is possible to monitor the apoptotic cell process thanks to the possibility to discriminate between live and death cells, to differentiate between healthy and pathological tissues and of course to discriminate between each single component of the cell itself, i.e.

nucleus and cell membranes [13]. By extension, RS is widely employed in the study of blood and body fluids for disease diagnosis, biomarker discovery and drug monitoring [14]. An interesting case of application is presented in [15], in which an endoscopic Raman probe has been developed in order to diagnose in vivo dysplasia in Barrett's esophagus disease. The authors have designed an experimental apparatus consisting of a fiberoptic confocal Raman probe with a near-infrared diode laser as excitation source that has the dual role of delivering laser light and collecting Raman signals. The fiber tip is coupled with a sapphire ball lens to enable a tightly focusing of the light onto the epithelium tissue; this allows to minimize the inspected volume such that it is lower than 0.02 mm^3, and thus, this prevents to collect spurious contributions from deeper tissue layers. The entire fiberoptic confocal probe could be easily inserted into a conventional endoscope ensuring the contact with the epithelial surface and, in addition, it has been integrated with a multivariate analysis system allowing, in the end, in vivo tissues characterization and the possibility to extract and analyse information in real-time. The described case study represents one of the research works aimed to push the frontier of Raman spectroscopy into routine clinical diagnostic.

Besides the great potential of RS, in particular in studying the basic physical principles, it has been pointed out in different applicative fields like biology or cultural heritage, namely when organic compounds are investigated, at least two main drawbacks of this technique that limits its application: i) the Raman effect is a weak phenomenon and this results in very weak signals with a low signal to noise ratio, requiring measures characterised by high exposure times; ii) the Raman response could be, in many cases, overlapped or even quenched by fluorescence. To overcome these limitations different technological strategies have been devised leading to the birth of new techniques based on an enhanced Raman effect, as described in different review papers [16–18]. However, at the same time, these "new" spectroscopies have brought out interesting and still not fully clarified physical processes at the basis of the enhancement that, in turn, need the basic physics to be understood.

Resonant Raman Scattering (RRS). In RRS, the energy of the incoming laser light is tuned in order to be in resonance with an electronic transition; thus, the intensity of the vibrational modes, responsible for this particular transition, results to be greatly increased by a factor of about 10^6 with the possibility to work on solution diluted till 10^{-8}.

Coherent Anti-Stokes Raman Scattering (CARS). CARS is a third order non linear optical process which requires high intensity laser pulses; in particular, multiphotons excitation is used in order to produce a signal characterized by coherent emitted waves. With respect to RS, CARS is more sensitive, which means higher intensity signals (10^5 - 10^{10}) and, in addiction, it is slightly affected by fluorescence interference because CARS signal is at high frequency.

Tip Enhanced Raman Spectroscopy (TERS). TERS exploits the com-

bination of a scanning probe device, like an atomic force microscope, with a Raman spectrograph. The scanning probe consists of a metallic, generally Au, Ag or Cu, tip acting as a lightning rod which leads to highly confined local electric fields and strong optical resonances. TERS allows to obtain extremely enhanced Raman signal with the sensitivity at the single molecule level and, at the same time, to perform imaging at the nanometer scale.
The last technique that I would like to introduce is the Surface Enhanced Raman Spectroscopy (SERS).

The SERS effect could be defined a nanoscale phenomenon, indeed it could be observed only thanks to the use of nanostructured substrates, the SERS active substrates. Its discovery dates back to 1974 when Fleischman and co-workers observed a surprisingly enhanced Raman signal of pyridine adsorbed on electro-chemical roughened silver electrode [19]. As it is well known, the first observation was not followed by a correct explanation of the observed event; indeed, Fleischman thought that the origin of the huge enhancement had to be trace back to the increased number of adsorbed molecules due to the roughness of the electrodes. Only three years later, Jeanmaire and Van Duyne [20] and, independently, Albrecht and Creighton [21] proved that an increased surface area could not be the origin of the effect but instead other mechanisms, directly acting on the Raman intensities, must be invoked.
Since its discovery, SERS technique has been fruitfully used, further enlarging the fields where RS could be applied, gaining in signal intensity, suppression of fluorescence and enabling even single molecule detection; just to have an idea of the impact of SERS on the scientific community, in Figure (3) the number of publications regarding SERS is reported since 1985. The increased use of SERS as analytical technique is strictly linked to the huge technological progress in the nanostructures field during the 1990s, allowing the development of ever more effective nanostructured substrates to performed enhanced Raman measures.

Besides its rapidly widespread, a consolidated theory explaining the origin of the enhanced effect is still missing, even if there is agreement on which are the two main mechanisms at the basis of the enhancement: the electromagnetic contribution, driven by the localized surface plasmon resonances, and the chemical one, given by the charge-transfer resonances.
The first theoretical explanation of the huge increase in the Raman cross-section has been proposed by M. Moskovits in 1978 [22]; he linked this enhanced effect to the excitation of the localized surface plasmons (LSPs) sustained by the subwavelength roughness features of the silver substrate. When the incident wavelength matches the plasmon resonances, the incident and Raman scattered field are magnified with a consequent enhancement of the Raman signal of the irradiated molecules adsorbed on the nanostructured surface. This is all enclosed in the expression of the *effective* polarizability given in [23] for a molecule in the proximity of a metallic surface

$$\alpha_{eff} = \frac{\alpha}{1 - (\alpha/4r^3)(\epsilon - \epsilon_0)/(\epsilon + \epsilon_0)} \tag{1}$$

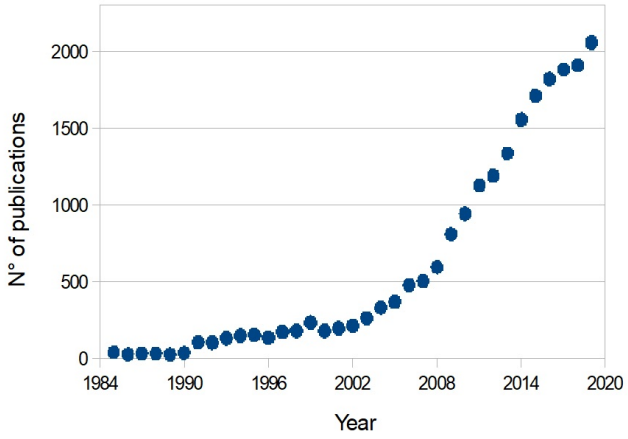

Figure 3: Bibliographic data for SERS publications since 1985. The data has been collected from the Web of Science database, by typing SERS as topic research field.

This expression has a pole when the real part of the metallic dielectric function is equal to $-\epsilon_0$, namely when the surface plasmon is excited.
This leads Moskovits also to suggest that the presence of metallic nanostructures with dimensions much lower than the incident wavelength is essential to observe the SERS effect; that the possibility to observe enhanced signal is also given by using proper colloidal suspensions of metallic nanostructures and, finally, that this effect would be primarily achieved with nanostructures made of coinage or alkali metals. This paved the way to the study of the suitable configuration of SERS substrates, concerning in particular the type of the employed metal, i.e. the most used ones are Ag and Au, and the shape and dimension of the nanostructures; in addiction, it was supposed that at least two other parameters have great importance in achieving high enhancement, in particular the wavelength of the incident radiation as well as the polarization of incident and scattered light with respect to the orientation of the nano-objects.
Nowadays the electromagnetic (EM) theory is still the most accredited one; indeed, all its predictions have been experimentally proved during the years. However, different experimental evidences have raised the question if the EM mechanism is the only phenomenon at the basis of the SERS effect. Indeed, if the excitation of LSP resonances is the only mechanism at stake, high enhancement would be recorded for every type of molecule, but some experimental researches have pointed out a close correlation between the SERS substrate and the chemical nature of the molecule; as for instance, a negatively charged analyte will not be adsorbed on a negatively charged metallic substrate and, in turn, its SERS signal is absent. Thus, in 1980 Otto et al [24] suggested the existence of a short-range effect due to the formation of ligand complex between the adsorbate molecules and the metal surfaces; this is known has the chemical enhancement (CE) driven primarily by charge-transfer mechanisms. The CE mechanism is considered a multiplicative effect that contributes much

more less to the enhancement than the principal EM one.
The existence and the relevance of the chemical enhancement is really controversial, although experimental evidence of a "first layer" enhancement has been recorded [25]; in particular, different experiments on electrochemical cells for which it is possible to tune the energy difference between the adsorbate analyte and the metal through the application of an external potential [26] [27], provided evidences to support that also charge-transfer resonances of the molecule-metal complex are of importance in the enhancement process.
Soon after, SERS experiment employing metal-free systems as active substrates, came out; in particular, in 1982 Yamada at al. published the first paper showing the enhancement on the pyridine spectrum from NiO compound and later they expanded the research on TiO_2 systems [28]. Moreover, in 1988 an enhanced Raman signal of copper phthalocyanine molecules deposited on GaP small nanoparticles have been recorded with a maximum enhancement factor of about 700 [29]. These findings have increased the interest in the search of new SERS substrates besides the well-known metal ones. In particular, following studies on TiO_2 [30] and CuTe [31] substrates have pointed out SERS enhancement factor (EF) of even 10^6. The possibility to achieve average EF of the order of the ones obtained with metallic systems has opened the research to semiconductors substrates [32]. Semiconductors display interesting properties as for instance better control on nanoparticles shape and size through different synthetic routes like Chemical Vapor Deposition, nanolitography and Molecular Beam Epitaxy, higher stability and the possibility to tune their functional properties by performing different doping; moreover, they are less affected by degradation and, in particular, oxide-based systems display higher biocompatibility in order to be used for biomedical sensing.
If the EM theory is said to satisfactory explain the experimental evidences on metal substrates in most cases, this is not always true for semiconductor ones. Apart from some dielectric systems as for instance TiO_2 ones for which by properly engineer the nanostructured geometry of the substrate, the bulk vacuum-ultraviolet plasmon, due to valence electrons, could be red-shifted so that it falls in the visible range [30], the majority of semiconducting compounds display surface plasmon resonances far from the visible light range and in turn far from the laser excitation source because of the low density of electrons in the conduction band. Consequently, other mechanisms had to be invoked to explain the observed enhancement. In 2008, J. R. Lombardi and R. L. Birke proposed a unified theory in order to explain the SERS effect in metals [33] and later they extended this theory to semiconductors [34]. They identified three sources of enhancement: the electromagnetic contribution, the chemical one and the molecular resonances. The first mechanism is driven by localized surface plasmons resonances, the second one by the charge-transfer mechanisms that occurs upon the formation of a metal/semiconductor-molecule complex and, finally, the resonances proper of the investigated molecule; generally, when this last mechanism is involved one speaks about Surface Enhanced Resonant

Raman Spectroscopy.
The idea of Lombardi and Birke is that the SERS effect has not to be considered a combination of independent phenomena, but a single effect which is due to three resonances that are tightly related to each other and cannot take into account separately. The authors present a single expression of the enhancement that includes in the denominator the product of all the three resonances, related to each others by the therms in the numerator which give the SERS selection rules:

$$R_{IFK} = \frac{\mu_{KI}\mu_{FK}h_{IF}\langle i|Q_k|f\rangle}{\left((\epsilon_1(\omega)+2\epsilon_0)^2+\epsilon_2^2\right)\left((\omega_{FK}^2-\omega^2)+\gamma_{FK}^2\right)\left((\omega_{IK}^2-\omega^2)+\gamma_{IK}^2\right)} \quad (2)$$

As regard the denominator the first therm $\left((\epsilon_1(\omega)+2\epsilon_0)^2+\epsilon_2^2\right)$ takes account of the plasmon resonances, the second one of the charge-transfer ones and the last one of the molecular resonances. μ_{KI} and μ_{FK} are the dipole moments of the molecular transitions and charge-transfer ones, respectively; h_{IF} is the Herzberg-Teller coupling constant.
The extension of this unified approach to semiconductor, leads to a therm similar to the one of Eq. (2). However, for semiconductor the possibility to exploit plasmon resonances is restricted to a few case, so one has to deal with the Mie theory in order to increase the near field scattering efficiency thanks to the optimization of the geometry of the nano-objects. Moreover, semiconductors offer the possibility of new resonances, i.e. the exciton transitions [35].
Besides the heterogeneity in the theoretical approach to the SERS effect, another important issue is the correct estimation of the enhancement factor (EF). As it is well know from the theoretical point of view, the magnitude of EF is generally approximated to the fourth power of the local field enhancement. However, as regards its experimental evaluation, it is not a trivial task because of the difficulty in properly determining the different variables that play a key role in the effect.

The sketched landscape about Raman and SERS world represents the bases on which my PhD program has been developed. In particular, my research activity has followed two distinct but overlapped arguments connected to Raman and SERS phenomena.
The first one concerns the study of SERS effect on metallic substrates: the activity is focused on the study and characterisation of Au nano-objects grafted on glass substrates decorated with different stabilizing agents in order to achieve mechanical and chemical stability, reproducibility and re-usability. The aim is to study the SERS response at variance of these different coverings in particular silica one; moreover, from the applicative point of view, the task is to produce this kind of substrates through a fast and economic synthesis route.
The second one deals with a deep study on the Raman response of nanostructured pure and doped zinc ferrite spinels ($ZnFe_2O_4$). This mixed oxide,

belonging to the AB_2O_4 spinel class, exhibits intriguing chemical and physical properties for which a microscopic key parameter is the so-called inversion degree, related to the amount of Zn^{2+} cations on the octahedral (B) site and the corresponding amount of Fe^{3+} cations on the tetrahedral (A) site.
Through the Raman probe we have been able to study the vibrational and structural properties of these compounds by testing their structural stability under irradiation, their phase homogeneity, the presence of extrinsic iron oxide phases that could affect their magnetic properties and, of course, their cationic distribution. The Raman results have been discussed and validated within a multi-techniques approach, in particular taking into account the information achieved from complementary techniques, like X-ray powder diffraction reaction, Electron Paramagnetic Resonance spectroscopy and, of course, SQUID magnetometry through which the magnetic response has been recorded.
The performed studies on both SERS effect on metallic enhancers and Raman response of nanostructured $ZnFe_2O_4$ are also aimed to investigate the possibility of realize oxide-metallic systems not only as SERS substrates but also as sensing devices for biomedical applications. The basic idea of these devices is to exploit the magnetic properties of the nanostructured $ZnFe_2O_4$ in order to be use for biomedical applications, like hyperthermia, coupled with the ability of metallic nano-objects to enhance the electric field in order to perform SERS sensing measures. In this regard, we are in the early stage of an open project focused on the preparation of hybrid systems, made up of $ZnFe_2O_4$ nanoparticles covered with a stabilizing MPTS layer and decorated with Ag nanoparticles.
Moreover, the versatility of the Raman expertise achieved during the PhD activity has also allowed me to give some fruitful contributions to other research topics different from the core of my thesis work, but in any case related to the material science frame.
The unceasing search for ever higher performant solid state batteries, leads to the need of advanced researches on promising materials.
In this regard, we have used the Raman probe to assess the quality of black phosphorus (BP) samples, synthesized starting from commercially available red phosphorus through ball milling route and we have also been able to correlated the crystalline BP formation as a function of the ball milling parameters.
We have also characterized pure and doped $FeNb_{11}O_{29}$ samples, investigating the role of vibrational degrees of freedom in its functional properties.
Finally, as regard the study of nanostructured oxide-based systems, an experimental investigation moved its first steps looking at the vibrational fingerprint of CeO_2 and ZnO nanoparticles bound with HeLa epithelium cancer cells, trying to evaluate their structural order/disorder upon binding to cancer cells.
The compatibility of oxides in biological environments is the frame in which an additional task has been performed: the Raman investigation of the dioxide titanium formation on dental screw-type implants made up of titanium-based alloy at variance of the purity of the starting medium and manufacturing pro-

cesses.

The Phd thesis is structured as follows.
Chapters 1 and 2 illustrate the basic theoretical principles of Raman and SERS spectroscopies, respectively. In particular, an as much as possible exhaustive description of the effect itself and the most important correlated aspects is presented.
Chapter 3 presents the results of the research activity performed on SERS metallic substrates, properly functionalized with a silica layer of variable thickness as well as different thiols coating, in order to obtain robust, recyclable and reusable SERS-active substrates for biomedical and industrial applications.
In Chapter 4, the results of the characterization performed through Raman spectroscopy on pure and doped $ZnFe_2O_4$ nanoparticles are presented; together with the information obtained by means of the complementary techniques.
Chapter 5 is aimed to describe all the open projects and research activities which I have carried out during my PhD research on some specific topics in the material science field as previously briefly described.
In Appendix A the detailed synthesis procedures used to prepare all the investigated samples are reported. In Appendix B, the physical/chemical properties as well as the Raman spectrum of molecules used in SERS measures are shown. Appendix C encloses some of the collected data discussed in Chapter 3 and 4 that are presented here in order to lighten the structure of the concerned Chapters, as supporting information. In Appendix D the experimental details of all the techniques used to characterised the investigated samples are reported.

Chapter 1

Theoretical principles of Raman spectroscopy

When a monochromatic light of frequency ω_1 is incident on a molecule, the scattered radiation presents not only the component at the same frequency ω_1 but also other components at shifted frequencies ($\omega_1 \pm \omega_S$) that are associated to transitions between rotational, vibrational and electronic levels. The component of scattered light with the same frequency of the incident one corresponds to the Rayleigh scattering while the other ones with shifted frequencies to the inelastic Raman scattering.
The source of the scattered light is the presence of an induced oscillating dipole in the molecule, generated by the displacement in the distribution of the electron cloud with respect to the positive charges, in response to an applied external electric field.
The induced dipole moment could be written as sum of time-dependent contributions:

$$\boldsymbol{p} = \boldsymbol{\alpha} \cdot \boldsymbol{E} + \frac{1}{2}\boldsymbol{\beta} : \boldsymbol{EE} + \frac{1}{6}\boldsymbol{\gamma} \vdots \boldsymbol{EEE} \tag{1.1}$$

where $\boldsymbol{\alpha}$ is the polarizability, a second-rank tensor, $\boldsymbol{\beta}$ is the hyperpolarizability, a third-rank tensor, and $\boldsymbol{\gamma}$ is the second hyperpolarizability, a fourth-rank tensor. The first term is linear in $\mathbf{E}$ and it takes account of the ordinary Raman scattering, while the second and third ones are quadratic and cubic in $\mathbf{E}$, respectively, and they are responsible for Hyper-Raman scattering effects.
The experimental activity of this research work deals with the ordinary Raman effect, thus, in the following, the classical approach to RS theory is proposed, in order to highlight the elastic and inelastic scattered light components, taking into account only the term of the dipole moment linear in the electric field. Therefore, let us consider a plane, monochromatic wave of frequency ω_1 with an electric field vector $\mathbf{E}$, incident on a molecule:

$$\boldsymbol{p} = \boldsymbol{\alpha} \cdot \boldsymbol{E} \tag{1.2}$$

Restricting the treatments only to vibrational transitions in the molecule, each term $\alpha_{\rho\sigma}$ of the $\boldsymbol{\alpha}$ tensor could be expanded in a Taylor series as a function of the normal vibrating coordinates Q_k:

$$\alpha_{\rho\sigma} = (\alpha_{\rho\sigma})_0 + \sum_k \left(\frac{\partial \alpha_{\rho\sigma}}{\partial Q_k}\right)_0 Q_k + \frac{1}{2}\sum_{k,l}\left(\frac{\partial^2 \alpha_{\rho\sigma}}{\partial Q_k\, \partial Q_l}\right)_0 Q_k Q_l + \dots \tag{1.3}$$

Assuming electrical harmonicity, we restrict the Taylor expansion to the second term:

$$\alpha_{\rho\sigma} = (\alpha_{\rho\sigma})_0 + \sum_k \left(\frac{\partial \alpha_{\rho\sigma}}{\partial Q_k}\right)_0 Q_k \tag{1.4}$$

if the third (or higher) term would be considered it will lead to the presence of additional induced dipoles characterised by frequencies like $(\omega_1 \pm 2\omega_k)$ or $(\omega_1 \pm (\omega_k \pm \omega_l))$ which correspond to second order Raman phenomena, namely overtones and combinations. Moreover, another assumption has to be done in order to exclude again second order contributions: that is, the mechanical harmonicity which means assuming simple harmonic motion. In turn, the time dependence of normal modes is given by

$$Q_k = Q_{k_0} \cos(\omega_k t + \delta_k) \tag{1.5}$$

Thus, by introducing Eq. (1.4) and Eq. (1.5) into Eq. (1.2) and taking into account the field frequency dependence $\boldsymbol{E} = E_0 \cos\omega_1 t$, the linear induced electric dipole turns out to be:

$$\boldsymbol{p} = (\alpha_{\rho\sigma})_0 \boldsymbol{E}_0 \cos\omega_1 t + (\alpha'_{\rho\sigma})_k \boldsymbol{E}_0 Q_{k_0} \cos(\omega_k t + \delta_k)\cos\omega_1 t \tag{1.6}$$

where $\alpha_{\rho\sigma}$ are the components at the equilibrium configuration of the polarizability tensor $\boldsymbol{\alpha}_0$, while $(\alpha'_{\rho\sigma})_k = \left(\frac{\partial \alpha_{\rho\sigma}}{\partial Q_k}\right)_0$ are components of a new tensor $\boldsymbol{\alpha'_k}$, namely the derivative polarizability tensor. By using the proper trigonometry formula, we can rewrite Eq. (1.6) in this form

$$\boldsymbol{p} = \boldsymbol{p}(\omega_1) + \boldsymbol{p}(\omega_1 - \omega_k) + \boldsymbol{p}(\omega_1 + \omega_k) \tag{1.7}$$

which highlights the three components of the scattered light: the first term, $\boldsymbol{p}(\omega_1) = \boldsymbol{\alpha}_0 \boldsymbol{E}_0 \cos\omega_1 t$, represents the Rayleigh scattering, while the second and third terms, $\boldsymbol{p}(\omega_1 \pm \omega_k) = \frac{1}{2}\boldsymbol{\alpha'_k} \boldsymbol{E}_0 Q_k \cos(\omega_1 \pm \omega_k \pm \delta_k)t$, take account of the inelastic scattered light components, in particular, the second term gives rise to the Stokes radiation, while the third one to the Anti-Stokes radiation.
If we consider the Stokes component at the shifted frequency $\omega_s = \omega_1 - \omega_k$, the total average power radiated by a single induced dipole moment is given by

$$P = \frac{\omega_s^4 |p|^2}{12\pi\epsilon_0 c^3} \tag{1.8}$$

Thus, by using Eq. (1.6), the intensity of the Raman shifted light in terms of the incident intensity $I_0 = \epsilon_0 E_0^2 c/2$ turns out to be

$$I = \frac{\omega_s^4 I_0 Q_k^2}{6\pi\epsilon_0^2 c^4} \left(\frac{\partial \alpha_{\rho\sigma}}{\partial Q_k} \right)_0^2 \tag{1.9}$$

Eq. (1.9) highlights the dependence of the Raman scattered light on the 4^{th} power of the vibration frequency and on the derived polarizability tensor components. This second dependence leads to the requirement that a non-zero polarizability change, with respect to the normal coordinate of vibration, has to be matched in order to observe the Raman effect. However, the classical approach to the Raman scattering is not exhaustive. Indeed, at first, the requirement of a change in the polarizability is a necessary condition but not sufficient to observe the phenomena under consideration; in addition, it gives a partially correct formulation of the vibrational Raman scattering tensor, being related only qualitatively to the molecular properties. Moreover, from the classical point of view, the intensity ratio of the Stokes and anti-Stokes contributions does not reflect the experimental evidence.
Accordingly, in the following section, the quantum mechanical treatment of the Raman scattering effect is introduced.

1.1 Quantum mechanical treatment

The quantum mechanical treatment developed in this section follows the reasoning and notation proposed by Derek A. Long in his book [37].
However, it is possible to give an effective pictorial view of the effect through the Feynman diagram, reported in Figure (1.3): in the first step a photon of wave vector **k** and polarization η is annihilated and in turn the molecule goes to an intermediated virtual state r, then a second photon characterized by **k'** and η' is created. Each interaction event is described by an interacting Hamiltonian H_{int}, involving different component of the electric field operator. The change in the radiation field energy corresponds to the change in the molecular states energy, namely $E_a - E_0$, where a is related to a vibrational excitation.

The starting point of the theoretical treatment is considering the molecular system quantum mechanically while the electromagnetic field is still treated classically. The interaction Hamiltonian when considering an electromagnetic radiation incident on a molecular system, could be generally given by a sum of the three more sizeable terms:

$$\hat{H} = \hat{H}_p + \hat{H}_m + \hat{H}_\theta \tag{1.10}$$

where $\hat{H}_p$ is the electric dipole term, $\hat{H}_m$ the magnetic one and $\hat{H}_\theta$ electric quadrupole one. For our purpose, we consider only the electric dipole interaction; this approximation is justified by the fact that the operators $\hat{H}_m$ and

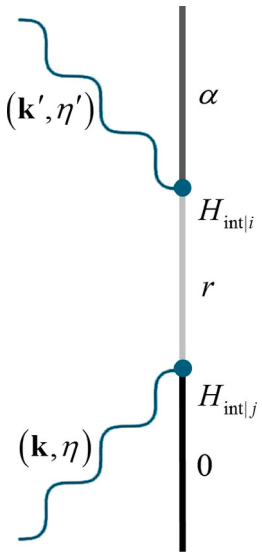

Figure 1.1: Feynman diagram of Raman process. The Figure is taken from [38].

$\hat{H}_\theta$ are non-zero only if the electric gradient field is non-zero, but in the visible range, the wavelength of the incident radiation is much grater than the molecular dimensions, so that $\boldsymbol{E}$ is basically constant over the molecular system.
If we consider an incident time-dependent electric field associated to a monochromatic electromagnetic wave of frequency ω_1 which induces a transition between an initial (i), and final (f) molecular state, the total associated transition electric dipole is given by

$$(\boldsymbol{p})_{fi} = \left\langle \Psi'_f \middle| \hat{\boldsymbol{p}} \middle| \Psi'_i \right\rangle \tag{1.11}$$

$\hat{\boldsymbol{p}}$ is the electric dipole moment operator and Ψ'_i and Ψ'_f are the time-dependent perturbed wave functions which could be represented by a series expansion valid for both the initial and final state of the molecular system:

$$\Psi' = \Psi^{(0)} + \Psi^{(1)} + \Psi^{(2)} + \Psi^{(3)} + \dots \tag{1.12}$$

This means expanding the wave functions of the transitional states in terms of $\Psi^{(0)}$, the unperturbed state, $\Psi^{(1)}$, the first-order perturbed state, namely the first-order modification of the unperturbed one by the electric dipole perturbation, $\Psi^{(2)}$, the second-order perturbed state and so on. The transition electric dipole $(\boldsymbol{p})_{fi}$ is given by a sum of terms which are linear, quadratic, cubic and so forth in the electric field $\mathbf{E}$, as it has been already stated within the classical approach; thus if we consider only the linear term in $\mathbf{E}$, its expression turns out to be

$$(\boldsymbol{p})_{fi} = \left\langle \Psi_f^{(1)} \middle| \hat{\boldsymbol{p}} \middle| \Psi_i^{(0)} \right\rangle + \left\langle \Psi_f^{(0)} \middle| \hat{\boldsymbol{p}} \middle| \Psi_i^{(1)} \right\rangle \tag{1.13}$$

Each of the two terms in Eq. (1.13) involves only a first-order perturbed wave function that could be expressed as linear combination of the unperturbed wave functions for both the initial and final state, namely $\Psi_{i/f}^{(1)} = \sum_n a_{p_{(i/f)r}}^{(1)} \Psi_n^{(0)}$,

where $a^{(1)}_{p_{(i/f)n}}$ are the coefficients which are linear in $\mathbf{E}$.
In the following, we will consider the electric field amplitude to be complex while the time-dependent wave functions to be real; however, the substitution of the perturbed time-dependent wave functions in Eq. (1.13), leads to terms which are inherently complex because of their exponential time-dependent parts, thus the real induced transition electric dipole $(\boldsymbol{p})_{fi}$ is given by

$$(\boldsymbol{p})_{fi} = (\tilde{\boldsymbol{p}})_{fi} + (\tilde{\boldsymbol{p}})^*_{fi} \tag{1.14}$$

where the second term in the sum is the complex conjugate of $(\tilde{\boldsymbol{p}})_{fi}$. The ρ component of the real induced transition electric dipole for real wave functions is given by:

$$\begin{aligned}
(p_\rho)_{fi} = \frac{1}{2\hbar}\sum_{r\neq i}\Bigg(&\frac{\langle\psi_f|\hat{p}_\rho|\psi_r\rangle\ \langle\psi_r|\hat{p}_\sigma|\psi_i\rangle}{\omega_{ri}-\omega_1-i\Gamma_r}\tilde{E}_{\sigma_0}e^{-i(\omega_1-\omega_{fi})t}\\
&+\frac{\langle\psi_f|\hat{p}_\rho|\psi_r\rangle\ \langle\psi_r|\hat{p}_\sigma|\psi_i\rangle}{\omega_{ri}+\omega_1+i\Gamma_r}\tilde{E}^*_{\sigma_0}e^{i(\omega_1+\omega_{fi})t}\Bigg)\\
+\frac{1}{2\hbar}\sum_{r\neq f}\Bigg(&\frac{\langle\psi_f|\hat{p}_\sigma|\psi_r\rangle\ \langle\psi_r|\hat{p}_\rho|\psi_i\rangle}{\omega_{rf}-\omega_1-i\Gamma_r}\tilde{E}^*_{\sigma_0}e^{i(\omega_1+\omega_{fi})t}\\
&+\frac{\langle\psi_f|\hat{p}_\sigma|\psi_r\rangle\ \langle\psi_r|\hat{p}_\rho|\psi_i\rangle}{\omega_{rf}+\omega_1+i\Gamma_r}\tilde{E}_{\sigma_0}e^{-i(\omega_1-\omega_{fi})t}\Bigg)\\
&+\text{complex conjugate}
\end{aligned} \tag{1.15}$$

The wave functions $\psi_{i,f,r}$ are the time-independent unperturbed ones; in particular, ψ_r is related to the time-dependent wave function Ψ_r in the following way

$$\Psi_r = \psi_r e^{-i(\omega_r - i\Gamma_r)t} \tag{1.16}$$

where $\omega_r = E_r/\hbar$. In the same way, the relation between $\Psi_{i,f}$ and $\psi_{i,f}$ for the initial and final state, respectively, is given by

$$\Psi_{i,f} = \psi_{i,f} e^{-i\omega_{i,f}t} \tag{1.17}$$

but, instead, their lifetimes are assumed to be infinite, so that $\Gamma_i = \Gamma_f = 0$. According to Placzek theory, only the terms in Eq. (1.15) depending on $(\omega_1 - \omega_{fi})$ are the one describing the Rayleigh and Raman scattering effects if the condition $(\omega_1 - \omega_{fi}) > 0$ is satisfied. Indeed, this is true for elastic scattering since ω_{fi} is zero and also for anti-Stokes scattering, because ω_{fi} is negative; for Stokes scattering, since ω_{fi} is positive, the requirement $(\omega_1 - \omega_{fi}) > 0$ leads to the condition that the incident photon must have more than sufficient energy to reach the final state, namely $\hbar\omega_1 > \hbar\omega_{fi}$. Thus, we can rewrite Eq. (1.15) for the Stokes and anti-Stokes Raman scattering in the following way, by

simplifying the notion using f instead of ψ_f and the same for the unperturbed wave functions of i and r states:

$$(p_\rho)_{fi} = \frac{1}{2\hbar} \sum_{r \neq i,f} \left(\frac{\langle f|\hat{p}_\rho|r\rangle \ \langle r|\hat{p}_\sigma|i\rangle}{\omega_{ri} - \omega_1 - i\Gamma_r} + \frac{\langle f|\hat{p}_\sigma|r\rangle \ \langle r|\hat{p}_\rho|i\rangle}{\omega_{rf} + \omega_1 + i\Gamma_r} \right) \tilde{E}_{\sigma_0} e^{-i\omega_s t} + \text{complex conjugate} \tag{1.18}$$

where $\omega_s = \omega_1 - \omega_{fi}$ is the frequency of the scattered radiation. In view of Eq. (1.18), it is possible to outline the expression of the $(\alpha_{\rho\sigma})_{fi}$ components of the general polarizability tensor $(\boldsymbol{\alpha})_{fi}$

$$(\alpha_{\rho\sigma})_{fi} = \frac{1}{\hbar} \sum_{r \neq i,f} \left(\frac{\langle f|\hat{p}_\rho|r\rangle \ \langle r|\hat{p}_\sigma|i\rangle}{\omega_{ri} - \omega_1 - i\Gamma_r} + \frac{\langle f|\hat{p}_\sigma|r\rangle \ \langle r|\hat{p}_\rho|i\rangle}{\omega_{rf} + \omega_1 + i\Gamma_r} \right) \tag{1.19}$$

This equation is a generalised formulation of the components of the polarizability tensor that encloses all the possible Raman scattering processes. Indeed, if $\omega_1 << \omega_{ri}$ the molecule undergoes a first transition from an initial stationary state $|i\rangle$ to a virtual state (indicated by dash line in Figure (1.2)) and a subsequent transition from the virtual state to the finale stationary one. This virtual state does not correspond to a well-defined value of the energy, thus this process is said to be a virtual absorption. Such condition corresponds to normal Raman scattering, while for values of ω_1 approaching, matching or even exceeding ω_{ri}, Eq. (1.19) describes pre-resonance, resonance or continuum resonance Raman scattering.
This consideration regards the denominator of the first term of Eq. (1.19). Concerning the second term denominator which involves a sum between ω_1 and ω_{ri}, it would never give dominant contribution to the polarizability components; in particular, it is almost negligible when there are dominant contributions in the first term of $(\alpha_{\rho\sigma})_{fi}$.
As regard the numerators of the terms in Eq. (1.19), the first one, namely $\langle f|\hat{p}_\rho|r\rangle \ \langle r|\hat{p}_\sigma|i\rangle$ is the product of two transition electric dipoles, one for a transition from a state $|i\rangle$ to a state $|r\rangle$ which is an absorption and the other one for a transition from a state $|r\rangle$ to a state $|f\rangle$ which is an emission, providing that ω_r is grater than ω_i and ω_f. The second term could be consider as a virtual process: the absorption of an incident photon follows the emission of a scattered one.

The general formulation of $(\alpha_{\rho\sigma})_{fi}$ given by Eq. (1.19) is the starting point of the following treatment in which different valid approximations will be done in order to achieve a more treatable expression for the polarizablity tensor components.
The first approximation to be done is the Born-Oppenheimer one, namely, the adiabatic approximation, which allows to treat separately the electronic and nuclear motions.
Thus, if we consider a generic electronic-nuclear state j, it is possible to write it

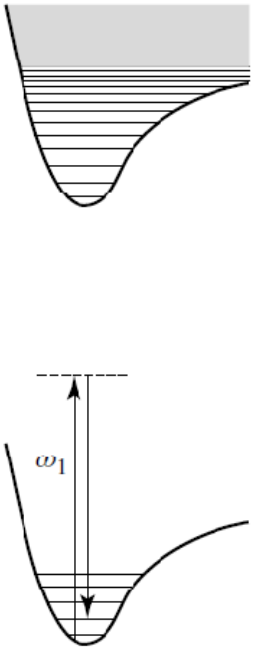

Figure 1.2: Normal Raman process. [37, Figure 4.2(a)])

as $|j\rangle = |e^j v^j R^j\rangle$, namely in terms of its electronic, vibrational and rotational parts which are identified by the quantum number e^j, v^j and R^j, respectively, and its energy as $\omega_{e^j v^j R^j}$. However, by introducing the adiabatic approximation, it is allowed to rewrite the general state j, as the product of the separate electronic, vibrational and rotational parts:

$$|j\rangle = \left|e^j\right\rangle \left|v^j\right\rangle \left|R^j\right\rangle \tag{1.20}$$

and, in turn, its energy as $\omega_{e^j v^j R^j} = \omega_{e^j} + \omega_{v^j} + \omega_{R^j}$.
In view of the Born-Oppenheimer approximation, the $\rho\sigma$ component of the polarizability tensor (Eq. (1.19)) associated to a transition between $e^i v^i R^i$ and $e^f v^f R^f$ states could be written in the following way

$$(\alpha_{\rho\sigma})_{fi} = \left\langle R^f\right| \left\langle v^f\right| \left\langle e^f\right|\hat{\alpha}_{\rho\sigma}(e^r, v^r, R^r)\left|e^i\right\rangle \left|v^i\right\rangle \left|R^i\right\rangle \tag{1.21}$$

where $\hat{\alpha}_{\rho\sigma}(e^r, v^r, R^r)$ is the $\rho\sigma$ component of the polarizibility tensor operator defined as

$$\begin{aligned}\hat{\alpha}_{\rho\sigma}(e^r, v^r, R^r) = \frac{1}{\hbar}\sum_{r\neq i,f}\Bigg(&\frac{\hat{p}_\rho \left|e^r\right\rangle \left|v^r\right\rangle \left|R^r\right\rangle \left\langle R^r\right| \left\langle v^r\right| \left\langle e^r\right| \hat{p}_\sigma}{\omega_{e^r e^i} + \omega_{v^r v^i} + \omega_{R^r R^i} - \omega_1 - i\Gamma_{e^r v^r R^r}} \\ &= \frac{\hat{p}_\sigma \left|e^r\right\rangle \left|v^r\right\rangle \left|R^r\right\rangle \left\langle R^r\right| \left\langle v^r\right| \left\langle e^r\right| \hat{p}_\rho}{\omega_{e^r e^f} + \omega_{v^r v^f} + \omega_{R^r R^f} + \omega_1 + i\Gamma_{e^r v^r R^r}}\Bigg)\end{aligned} \tag{1.22}$$

A further simplification could be done in view of the fact that in most Raman scattering experiments the rotational structure is not resolved and also because

our aim is to obtain a more tractable formulation for the polarizability in case of pure vibrational Raman scattering. Thus, considering the initial electronic state as a non-degenerate ground state, namely $e^i = e^g$ and providing that the incident frequency ω_1 is much smaller than any electronic absorption frequency and, at the same time, grater than any vibrational or rotational one of the investigated system, it is possible to display a closure over the complete set of rotational states and, in turn, to neglect the denominator terms $\omega_{R^r R^i}$ and $\omega_{R^r R^f}$ and to replace Γ_{e^r,v^r,R^r} with Γ_{e^r,v^r} in Eq. (1.22). Thus, $\hat{\alpha}_{\rho\sigma}(e^r, v^r, R^r)$ will be write as $\hat{\alpha}_{\rho\sigma}(e^r, v^r)$.
The following step consists in a change of reference axes for $\hat{\alpha}_{\rho\sigma}(e^r, v^r)$: this means that $\hat{\alpha}_{\rho\sigma}(e^r, v^r)$, defined with respect to space-fixed axes, ρ, σ, ..., is transformed into $\hat{\alpha}_{\rho'\sigma'}(e^r, v^r)$ which instead is defined in relation to molecular-fixed axes, ρ', σ', ... This transformation is carried out by using direction cosines $l_{\rho\rho'} l_{\rho\rho'}$ which act only on rotational transitions, namely

$$(\alpha_{\rho\sigma})_{fi} = \left\langle R^f \middle| l_{\rho\rho'} l_{\sigma\sigma'} \middle| R^i \right\rangle \left\langle v^f \right| \left\langle e^f \middle| \hat{\alpha}_{\rho\sigma}(e^r, v^r) \middle| e^g \right\rangle \left| v^i \right\rangle \tag{1.23}$$

At this stage, it is possible to write the $\rho\sigma$ component of the polarizibility tensor for vibrational transition with unresolved rotational structures as follows

$$(\alpha_{\rho\sigma})_{fi} = \left\langle v^f \right| \left\langle e^f \middle| \hat{\alpha}_{\rho\sigma}(e^r, v^r) \middle| e^g \right\rangle \left| v^i \right\rangle \tag{1.24}$$

with the condition that, when it is required, isotropic averaging has to be performed. The isotropic averaging, a classical process consisting on assuming that all molecular orientations are equally possible, is performed by using Eq. (1.23) and summing the expressions of the intensities over the complete set of rotational state.
Thus, taking into account the closure over the rotational states, the $\rho\sigma$ component of the transition polarizability, $(\alpha_{\rho\sigma})_{fi}$, turns out to be:

$$\begin{aligned}(\alpha_{\rho\sigma})_{fi} = \frac{1}{\hbar} \sum_{r \neq i,f} \Bigg(& \frac{\left\langle v^f \right| \left\langle e^f \middle| \hat{p}_\rho \middle| e^r \right\rangle |v^r\rangle \langle v^r| \langle e^r | \hat{p}_\sigma | e^g \rangle |v^i\rangle}{\omega_{e^r e^g} + \omega_{v^r v^i} - \omega_1 - i\Gamma_{e^r v^r}} \\ & + \frac{\left\langle v^f \right| \left\langle e^f \middle| \hat{p}_\sigma \middle| e^r \right\rangle |v^r\rangle \langle v^r| \langle e^r | \hat{p}_\rho | e^g \rangle |v^i\rangle}{\omega_{e^r e^f} + \omega_{v^r v^f} + \omega_1 + i\Gamma_{e^r v^r}} \Bigg)\end{aligned} \tag{1.25}$$

At this point, D. A. Long prospects two possible ways to further simplify the polarizibaility tensor expression for normal pure vibrational Raman scattering: on one side, the Placzek approach, introducing radical approximations, and on the other side, the alternative approach consisting in introducing the approximations by subsequent steps.
For the purpose of this thesis, a proper elaboration of the second approach, starting from Eq. (1.25), will be presented because it will introduce and declare terms that will come into play in the unified approach of SERS theory proposed by J. R. Lombardi and R. L. Birke [33–35].

In particular, all the following considerations will ne made in the Born-Oppenheimer approximation frame.
In order to lighten this chapter, each simplification step to Eq. (1.25) will be introduce and the complete formulation of the $\rho\sigma$ component of the transition polarizibility for normal pure vibrational Raman scattering, will be give in the end of the treatment.

The first assumption is to consider that the electronic transition dipole moment is slightly dependent on the normal vibrational coordinates Q. This means assuming the Herzberg-Teller effect as a perturbation of the electronic state within the Born-Oppenheimer regime.
In particular, the electronic hamiltonian $\hat{H}_e$ has an inherent dependence on Q coordinates which could be express by the following expansion:

$$\hat{H}_e(Q) = (\hat{H}_e)_0 + \sum_k \left(\frac{\partial \hat{H}_e}{\partial Q_k}\right)_0 Q_k + \frac{1}{2}\sum_{k,l}\left(\frac{\partial^2 \hat{H}_e}{\partial Q_k \partial Q_l}\right) Q_k Q_l + \dots \tag{1.26}$$

If the displacement is small, the perturbation is represented by just the second term of the expansion; in turn, the perturbed state $\left|e^{r'}(Q_0)\right\rangle$, resulting from the electronic hamiltonian which mixes each other the unperturbed states $|e^r(Q_0)\rangle$ and $|e^s(Q_0)\rangle$, could be written as

$$\left|e^{r'}(Q_0)\right\rangle = |e^r(Q_0)\rangle + \frac{1}{\hbar}\sum_{e^s \neq e^r}\sum_k \frac{h^k_{e^s e^r}}{\omega_{e^r} - \omega_{e^s}} Q_k \, |e^s(Q_0)\rangle \tag{1.27}$$

where

$$h^k_{e^s e^r} = \langle \psi_{e^s}(Q_0)| \left(\frac{\partial \hat{H}_e}{\partial Q_k}\right)_0 |\psi_{e^r}(Q_0)\rangle \tag{1.28}$$

is the coupling integral, known as the *Herzberg-Teller coupling constant.*
It is possible to obtain a similar expression also for the "bra" state, $\left\langle e^{r'}(Q_0)\right|$; in particular, since $\langle e^r| = |e^r\rangle^*$ and $(h^k_{e^s e^r})^* = h^k_{e^r e^s}$, one obtains

$$\left\langle e^{r'}(Q_0)\right| = \langle e^r(Q_0)| + \frac{1}{\hbar}\sum_{e^s \neq e^r}\sum_k \langle e^s(Q_0)| \frac{h^k_{e^r e^s}}{\omega_{e^r} - \omega_{e^s}} Q_k \tag{1.29}$$

It is therefore possible to evaluate the perturbative effect of the electronic hamiltonian on the components of the electric transition dipoles occurring in Eq. (1.25). Considering the first product $\left\langle e^f\right|\hat{p}_\rho\left|e^r\right\rangle \langle e^r|\hat{p}_\sigma|e^g\rangle$ and, in particular, starting from σ component of the electronic transition dipole, we will substitute the perturbed states $\left|e^{r'}\right\rangle$ (Eq. (1.27)) and $\left\langle e^{g'}\right|$ (Eq. (1.29)) and by properly multiplying the terms, it results:

$$\begin{aligned}(p_\sigma)_{e^{r'}e^{g'}} = {} & \langle e^r|\hat{p}_\sigma|e^g\rangle + \frac{1}{\hbar}\sum_{e^s \neq e^r}\sum_k \frac{h^k_{e^r e^s}}{\omega_{e^r} - \omega_{e^s}} Q_k \langle e^s|\hat{p}_\sigma|e^g\rangle \\ & + \frac{1}{\hbar}\sum_{e^t \neq e^g}\sum_k \left\langle e^r\right|\hat{p}_\sigma\left|e^t\right\rangle \frac{h^k_{e^t e^g}}{\omega_{e^g} - \omega_{e^t}} Q_k\end{aligned} \tag{1.30}$$

The expression of the transition electric dipole, when the perturbation electronic hamiltonian is taking into account, leads to the occurrence of additional contributions, namely $\langle e^s|\hat{p}_\sigma|e^g\rangle$ and $\langle e^r|\hat{p}_\sigma|e^t\rangle$. In particular, as it is possible to observe in Figure (1.3), the first term involves states $|s\rangle$ which have to be accessible by the dipole transition from the state $|g\rangle$,while this requirement has not to be met for the second term. A similar expression to Eq. (1.30) could be achieved for the ρ component of the electric transition dipole.

Thus, these acquired additional contributions to the transition dipole arising

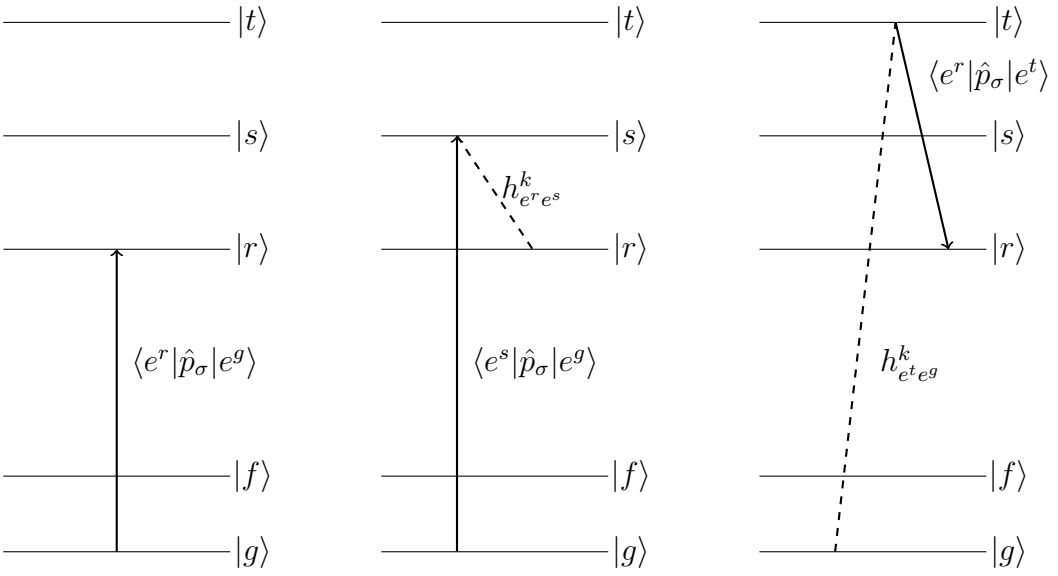

Figure 1.3: The contributions to $(p_\sigma)_{e^{r'}e^{g'}}$ that arise from the Herzberg-Teller coupling of the involved states.

from the vibronic coupling, besides being proportional to the coupling integral and to the normal coordinate of vibration, are inversely proportional to the energy gap between the two involved states, meaning that terms like $\omega_{e^r} - \omega_{e^s}$ will be dominant with respect to the others. Moreover, symmetry conditions have to be satisfied in such a way that the the product between the coupling integral and the displacement Q_k has to be non-zero.

At this point, if we introduce the effect of the perturbing electric hamiltonian in Eq. (1.25), the transition polarizability would be written in the following way:

$$(\alpha_{\rho\sigma})_{fi} = A + B + C + D \tag{1.31}$$

In particular, A is given by the sum of two terms each involving unperturbed transition electric dipoles, while B, C and D arise from the vibronic coupling. Indeed, B is the sum of four terms, each involving the product between an unperturbed electronic transition dipole and electronic transition dipoles arising from the Herzberg-Teller coupling of two electronic excited states; each of the two terms in C is given by the product of an unperturbed electric transition dipole with electronic transition dipoles due to the vibronic coupling between

an excited electronic state and the initial and final electronic ones; finally, D is the sum of two terms, each of them being the product of two electronic dipoles which arise from the Herzberg-Teller coupling (see pp. 72-73 in [37]).

The second simplification is aimed to strictly maintain the Born-Oppenheimer approximation for the vibration wave functions which are not affected by the electronic transition moments as well as the coupling integral.

In order to consider only normal Raman scattering, i.e. non-resonant one, the third simplification consists on considering an incident frequency ω_1 which is far from any electronic transition, namely $\omega_{e^r e^g} + \omega_{v^r v^i} \gg \omega_1$. This condition that affects the denominators of the terms in Eq. (1.31) allows the closure over the set of vibrational states in each electronic state e^r.
Moreover, in case of non-resonance Raman scattering, a number of excited state s will contribute to the B, C and D terms of the polarizability and the magnitude of these contributions is difficult to proper be assessed, thus in turn the components of the electronic transition dipole (Eq. (1.30)) should be write in a less explicit form by using Taylor series expansions:

$$(p_\rho)_{e^{f'} e^{r'}} = (p_\rho)^0_{e^f e^r} + \sum_k (p_\rho)^k_{e^f e^r} Q_k \tag{1.32}$$

with

$$(p_\rho)^k_{e^f e^r} = \left(\frac{\partial (p_\rho)_{e^f e^r}}{\partial Q_k} \right)_0 \tag{1.33}$$

where the derivative with respect to Q_k encloses the vibronic coupling without explicitly define it.

The last requirement to obtain the proper expression for the transition polarizability in case of pure vibrational Raman scattering is that either the initial and final electronic state are the ground electronic state, thus $e^f = e^g$. Finally, we could explicate the four terms in Eq. (1.31) in their final formulation:

$$A = \frac{1}{\hbar} \sum_{e^r \neq e^g} \left(\frac{(p_\rho)^0_{e^g e^r} (p_\sigma)^0_{e^r e^g}}{\omega_{e^r e^g} - \omega_1} + \frac{(p_\sigma)^0_{e^g e^r} (p_\rho)^0_{e^r e^g}}{\omega_{e^r e^g} + \omega_1} \right) \left\langle v^f \middle| v^i \right\rangle \tag{1.34}$$

$$\begin{aligned} B + C = \frac{1}{\hbar} \sum_{e^r \neq e^g} \sum_k \Bigg(& \frac{(p_\rho)^k_{e^g e^r} (p_\sigma)^0_{e^r e^g} + (p_\rho)^0_{e^g e^r} (p_\sigma)^k_{e^r e^g}}{\omega_{e^r e^g} - \omega_1} \\ & + \frac{(p_\sigma)^0_{e^g e^r} (p_\rho)^k_{e^r e^g} + (p_\sigma)^k_{e^g e^r} (p_\rho)^0_{e^r e^g}}{\omega_{e^r e^g} + \omega_1} \Bigg) \left\langle v^f \middle| Q_k \middle| v^i \right\rangle \end{aligned} \tag{1.35}$$

$$D = \frac{1}{\hbar} \sum_{e^r \neq e^g} \sum_{kk'} \left(\frac{(p_\rho)^k_{e^g e^r} (p_\sigma)^{k'}_{e^r e^g}}{\omega_{e^r e^g} - \omega_1} + \frac{(p_\sigma)^{k'}_{e^g e^r} (p_\rho)^k_{e^r e^g}}{\omega_{e^r e^g} + \omega_1} \right) \left\langle v^f \middle| Q_k Q_{k'} \middle| v^i \right\rangle \tag{1.36}$$

It is possibile to relate Eqs. (1.34) - (1.36) to the Placzek or adiabatic polarizability

$$(\alpha_{\rho\sigma})_{fi} = \left\langle v^f \middle| \hat{\alpha}_{\rho\sigma}(Q) \middle| v^i \right\rangle \tag{1.37}$$

by introducing the Taylor expansion, to the second order, of $\alpha_{\rho\sigma}(Q)$; thus, we obtain:

$$\begin{aligned}(\alpha_{\rho\sigma})_{fi} = (\alpha_{\rho\sigma})_0 \left\langle v^f \middle| v^i \right\rangle + \sum_k \left(\frac{\partial \alpha_{\rho\sigma}}{\partial Q_k}\right)_0 \left\langle v^f \middle| Q_k \middle| v^i \right\rangle \\ + \frac{1}{2} \sum_k \sum_l \left(\frac{\partial^2 \alpha_{\rho\sigma}}{\partial Q_k \partial Q_l}\right)_0 \left\langle v^f \middle| Q_k Q_l \middle| v^i \right\rangle\end{aligned} \tag{1.38}$$

By comparing Eqs. (1.34) - (1.36) to Eq. (1.38), it results that:

$$(\alpha_{\rho\sigma})_0 = \frac{1}{\hbar} \sum_{e^r \neq e^g} \left(\frac{(p_\rho)^0_{e^g e^r} (p_\sigma)^0_{e^r e^g}}{\omega_{e^r e^g} - \omega_1} + \frac{(p_\sigma)^0_{e^g e^r} (p_\rho)^0_{e^r e^g}}{\omega_{e^r e^g} + \omega_1} \right) \tag{1.39}$$

$$\begin{aligned}\left(\frac{\partial \alpha_{\rho\sigma}}{\partial Q_k}\right)_0 = \frac{1}{\hbar} \sum_{e^r \neq e^g} \left(\frac{(p_\rho)^k_{e^g e^r} (p_\sigma)^0_{e^r e^g} + (p_\rho)^0_{e^g e^r} (p_\sigma)^k_{e^r e^g}}{\omega_{e^r e^g} - \omega_1} \right. \\ \left. + \frac{(p_\sigma)^0_{e^g e^r} (p_\rho)^k_{e^r e^g} + (p_\sigma)^k_{e^g e^r} (p_\rho)^0_{e^r e^g}}{\omega_{e^r e^g} + \omega_1} \right)\end{aligned} \tag{1.40}$$

$$\left(\frac{\partial^2 \alpha_{\rho\sigma}}{\partial Q_k \partial Q_l}\right)_0 = \frac{1}{\hbar} \sum_{e^r \neq e^g} \left(\frac{(p_\rho)^k_{e^g e^r} (p_\sigma)^{k'}_{e^g e^r}}{\omega_{e^r e^g} - \omega_1} + \frac{(p_\sigma)^{k'}_{e^g e^r} (p_\rho)^k_{e^g e^r}}{\omega_{e^r e^g} + \omega_1} \right) \tag{1.41}$$

The derivatives of Eqs. (1.40) and (1.41) relate the transition polarizability components for one specific vibration where only one quantum number v^k changes. It has to be noted that Eq. (1.41) holds only if the Taylor expansion of the electric transition dipole moment is cut at the first order.

1.1.1 Raman selection rules

If we assume the harmonic oscillator approximation, the total vibration wave function ϕ could be written as the product of harmonic oscillator wave functions for each normal mode of vibration; moreover, by assuming electrical harmonicity, namely considering only Eq. (1.38) to the first order, it is possible to write Eq. (1.38) itself, in the following way:

$$\begin{aligned}(\alpha_{\rho\sigma})_{fi} = (\alpha_{\rho\sigma})_0 \left\langle \prod_k \phi_{v_k^f}(Q_k) \prod_k \phi_{v_k^i}(Q_k) \right\rangle \\ + \sum_k \left(\frac{\partial \alpha_{\rho\sigma}}{\partial Q_k}\right)_0 \left\langle \prod_k \phi_{v_k^f}(Q_k) |Q_k| \prod_k \phi_{v_k^i}(Q_k) \right\rangle\end{aligned} \tag{1.42}$$

The first term of Eq. (1.42) corresponds to the Rayleigh scattering, while the second to the Raman scattering. In particular, it is possible to determine the

condition under which these two terms are non-zero, by recalling the properties of harmonic oscillating wave functions:

$$\left\langle \phi_{v_k^f}(Q_k) \middle| \phi_{v_k^i}(Q_k) \right\rangle = \begin{cases} 0 & \text{for } v_k^f \neq v_k^i \\ 1 & \text{for } v_k^f = v_k^i \end{cases} \tag{1.43}$$

$$\left\langle \phi_{v_k^f}(Q_k) \middle| Q_k \middle| \phi_{v_k^i}(Q_k) \right\rangle = \begin{cases} 0 & \text{for } v_k^f \neq v_k^i \\ (v_k^i+1)^{1/2} b_{v_k} & \text{for } v_k^f = v_k^i + 1 \\ (v_k^i)^{1/2} b_{v_k} & \text{for } v_k^f = v_k^i - 1 \end{cases} \tag{1.44}$$

where $b_{v_k} = \left(\frac{\hbar}{2\omega_k}\right)^{1/2} = \left(\frac{h}{8\pi^2 c_0 \bar{\nu}_k}\right)^{1/2}$.
The appearance of the elastic scattering follows from the orthogonality of the harmonic oscillator functions (Eq. (1.43)); indeed, the first term of Eq. (1.42) will not vanish only if there's no change in any vibrational quantum numbers, namely $v_k^f = v_k^i$. As regard the occurrence of the Raman scattering for the k^{th} vibrational mode, it follows from Eq. (1.44) that the requirement of a non-vanishing product in the second term of Eq. (1.42), is that the vibrational quantum numbers of every mode except the k^{th}, have to be equal to each other for the initial and final state, while for the k^{th} mode the vibrational quantum number has to change by unity, i.e. $v_k^f = v_k^i \pm 1$.
In turn, the electrical and mechanical harmonicity approximation leads to transition polarizability component which could be express in the following form for Stokes and anti-Stokes scattering:

$$\begin{aligned} (\alpha_{\rho\sigma})_{v_k^i+1, v_k^i} &= (v_k^i+1)^{1/2} b_{v_k} \left(\frac{\partial \alpha_{\rho\sigma}}{\partial Q_k}\right)_0 \\ (\alpha_{\rho\sigma})_{v_k^i-1, v_k^i} &= (v_k^i)^{1/2} b_{v_k} \left(\frac{\partial \alpha_{\rho\sigma}}{\partial Q_k}\right)_0 \end{aligned} \tag{1.45}$$

The Stokes Raman scattering is associated to transition in which the change in the vibrational quantum number for the k^{th} mode is equal to $+1$, i.e. $\Delta v_k = +1$, while for anti-Stokes Raman scattering is $\Delta v_k = -1$.
Therefore, the quantum mechanical treatment gives the other necessary condition so that the transition from v^i to v^f is Raman active. In the end, in order to observe the Raman effect at least one of the elements of the derived polarizability tensor must be non-zero, as it has been pointed out also by the classical treatment, and, at the same time, the condition $\Delta v_k = \pm 1$ has to be satisfied.
This leads to a general vibrational selection rule for the occurrence of the Raman effect; in particular, recalling Eq. (1.37), it follows that at least one of the products $v^f \alpha_{\rho\sigma} v^i$ has to belong to the totally symmetric representation Γ_1, namely $\Gamma_1 \subset \Gamma(v^f) \times \Gamma(\alpha_{\rho\sigma}) \times \Gamma(v^i)$.

1.1.2 Raman scattered intensity

If we consider an ensemble of N molecules, the scattered intensity will not be merely the product of the scattered intensity of a single molecule times N, but instead one has to take account of the occupancy of each vibrational state involved in the transition through the Boltzmann distribution law. Consequently, if one consider a Stokes vibrational transition from v_k^i to $v_k^i + 1$, the scattered intensity will be proportional to

$$N \sum_i (v_k^i + 1) f_{v_k^i} = \frac{N}{1 - e^{-hc_0\bar{\nu}_k/kT}} \tag{1.46}$$

while, for an anti-Stokes vibrational transition from v_k^i to $v_k^i - 1$, it will be proportional to

$$N \sum_i (v_k^i) f_{v_k^i} = \frac{N}{e^{hc_0\bar{\nu}_k/kT} - 1} \tag{1.47}$$

Finally, the scattered intensity for a Stokes vibration transition for the k^{th} mode from v_k^i to $v_k^i + 1$ in a back-scattered geometry, where the incident radiation is polarized along the z axis of a fixed laboratory axis system, is given by the following formula:

$$I = \frac{k_{\bar{\nu}} h N \bar{\nu}_S^4}{8\pi^2 c_0 \bar{\nu}_k (1 - e^{-hc_0\bar{\nu}_k/kT})} \frac{45(\alpha_k')^2 + 7(\gamma_k')^2}{45} \mathscr{I} \tag{1.48}$$

where $\bar{\nu}_S = \bar{\nu}_L - \bar{\nu}_k$ is the absolute wave number of the Stokes shifted Raman signal, α_k' and γ_k' are the the derived polarizability tensor invariants for the considered k^{th} mode and $\mathscr{I}$ is the irradiance of the incident radiation which is given by $\mathscr{I} = \frac{1}{2} c_0 \epsilon_0 E_{y0}^2$.
The expression for the scattered intensity of an anti-Stokes transition from v_k^i to $v_k^i - 1$ will be obtained by replacing Eq. (1.47) into Eq. (1.48), noting that $\bar{\nu}_{aS} = \bar{\nu}_L + \bar{\nu}_k$.
A general formulation for the Raman scattering intensity is given by

$$I = \frac{d\sigma}{d\Omega} \mathscr{I} \tag{1.49}$$

where $\frac{d\sigma}{d\Omega}$ is the differential Raman cross section. As it is possible to observe by comparing Eq. (1.48) and Eq. (1.49), the differential cross section is essentially a property of the investigated molecule, giving an indication of its scattering efficiency.
The introduction of the scattering intensity for Stokes and anti-Stokes transitions, allows to define the Stokes to anti-Stokes ratio as follows

$$\frac{I_S}{I_{aS}} = \frac{\bar{\nu}_S^4}{\bar{\nu}_{aS}^4} \exp\{hc_0\bar{\nu}_k/kT\} \tag{1.50}$$

This ratio rigorously points out that the intensity of the anti-Stokes features in a Raman spectrum is weaker with respect to the Stokes counterparts. Moreover, it follows that through a Raman experiment it is possible to determine

the temperature of the investigated sample by exploiting Eq. (1.50).

1.2 Raman effect in crystals

Till now, the theory of the Raman effect has been treated from the molecular point of view. However, some considerations on the Raman effect on crystals have to be done.
In a crystal with full translational symmetry, the interaction with the incident light is subject to

- Energy conservation: $\hbar\omega_i = \hbar\omega_s \pm \hbar\Omega$
  where ω_i and ω_s are the frequencies of the incident and scattered radiation, while Ω the frequency of the excitation.
- Momentum conservation: $\mathbf{k}_i = \mathbf{k}_s \pm \mathbf{q}$
  where $\mathbf{k}_i$ and $\mathbf{k}_f$ are the wave vectors of the incident and scattered photons, respectively, and $\mathbf{q}$ is the wave vector of the excitation.

In particular, in Raman experiments Ω is much smaller than the incident and scattered frequencies, since in the visible range $\omega_{i,s} \sim 10^{14-15}$ Hz, while $\Omega \sim 10^{10-13}$ Hz; this implies that $|\mathbf{k}_i| \sim |\mathbf{k}_f|$ and therefore the condition of the wave vector conservation can be well approximated to $|\mathbf{q}| = 2|\mathbf{k}_i|sen(\theta/2)$, where θ is the angle between the incident and scattered photons direction.
The maximum value of the excitation wave vector, achievable in the backscattering geometry, is equal to $2\mathbf{k}_i$, namely about 5×10^4 cm^{-1}. Thus, the probed wave vector is much smaller than the wave vector of the full phonon dispersion curve, extending till the boundary of the Brillouin zone, namely $\pi/a \sim 10^8$ cm^{-1}. This means that in Raman experiments only phonons very closed to the centre of the Brillouin zone can be probed and therefore the Raman selection rule for crystal can be written as $\mathbf{q} \sim 0$.
As an example in Figure (1.4) the Raman mode of crystalline Si is reported together with the silicon phonon dispersion curve.

Other important selection rules for Raman modes in crystals are given by the crystal symmetries. Let us consider a general formulation for the differential scattering cross-section

$$\frac{d^2\sigma}{d\Omega d\omega_s} = \frac{\omega_i \omega_s^3 V}{(4\pi)^2 c^4} \frac{n_s}{n_i} \left| \epsilon_s \cdot \frac{d\chi(\omega)}{dX} \cdot \epsilon_i \right|^2 \langle X(q,\omega) X^*(q,\omega) \rangle \tag{1.51}$$

where n_i and n_s are the refractive indexes of the incident and scattered light inside the sample, while ϵ_i and ϵ_s are the incident and scattered polarizations, respectively [39].
The symmetry selection rules for the Raman process are enclosed in the factor $\left| \epsilon_s \cdot \frac{d\chi(\omega)}{dX} \cdot \epsilon_i \right|$ and they are ruled by the Neumann's principle, namely by

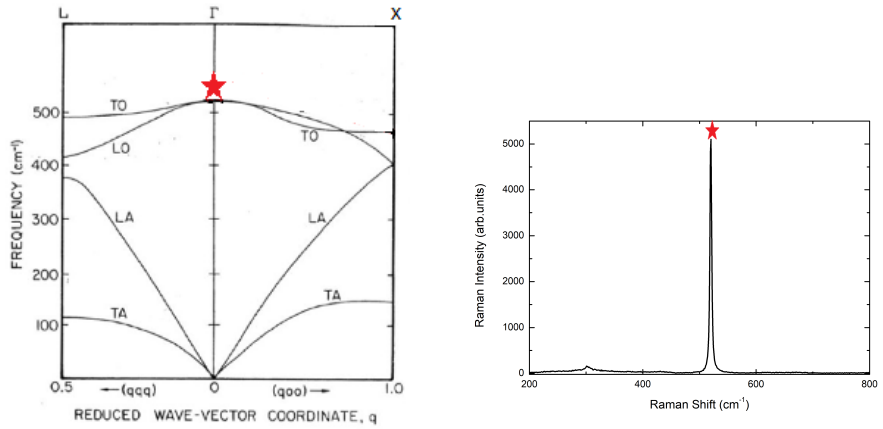

(a) (b)

Figure 1.4: (a) Silicon phonon dispersion curve and (b) 522 cm^{-1} first-order Raman mode corresponding to the optical phonon at the centre of the Brillouin zone.

the requirement that the physical properties of the crystals (in particular, incident field, induced polarization and Raman susceptibility tensor) must be invariant under all the symmetry operations of the crystal point group. This leads to two important symmetry constrains: i) since both ϵ_i and ϵ_s transform like polar vector, the only non-zero susceptibility derivatives $d\chi/dX$ are those with symmetries Γ_x belonging to the decomposition $\Gamma^* \bigotimes \Gamma$, where Γ is the irreducible representation; ii) according to the particular crystal point group, only some elements are zero and equal or related. As an example in Figure (1.5), the allowed Raman tensors, with the corresponding non-zero elements, are reported for the O_h cubic point group.

Through polarized Raman measures it is possible to excite different com-

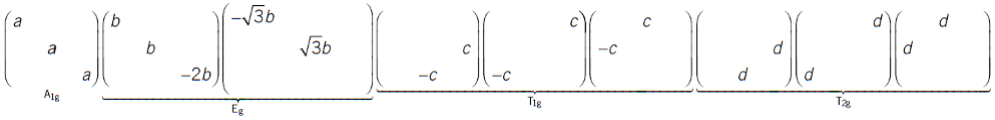

Figure 1.5: Allowed Raman tensors for the O_h cubic point group [39].

ponents of the susceptibility tensor and so determine the symmetry of the observed mode, by varying the polarizations of the incident and scattered light with respect to the crystalline axes of the investigated sample. In general, to indicate the geometry of a particular Raman experiment, the Porto notation is used: $\mathbf{k}_i(\epsilon_i, \epsilon_s)\mathbf{k}_s$.

1.2.1 Linewidth of Raman modes as a function of the crystal dimension

As introduced in the previous section, Raman spectroscopy is able to probe only phonon modes in the centre of the Brillouin zone and the selection rule

$\mathbf{q} \sim 0$ is the consequence of the infinite periodicity of the crystal lattice.
In an ideal structure, neglecting all possible perturbations, the Raman effect can be seen as a resonance process involving different vibrational state. Thus, the line shape of a Raman mode is well reproduced by a single Lorentzian curve.
However, different phenomena can affect the linewidth of the Lorentzian curve or even alter the mode shape: electron-phonon interaction, defects, grain boundaries, stresses, etc. As for instance, in nanocrystals the confinement of photons leads to a relaxation of the $\mathbf{q} \sim 0$ rule. This occurs because the propagation of phonons is interrupted by the grain boundaries and in the case of a single isolated grain, the phonon mode is reflected from the boundaries and it is confined within the grain.
In particular, since the phonon wave function has to decay to a very small value in the proximity of the crystal boundary and considering the uncertainty principle, it follows that the uncertainty of the wave vector associated to a specific vibration is given by $\Delta\mathbf{q} = \pi/d$, where d is the nanocrystal size, or the interspace between two defects or anything that interrupts the phonon propagation [40]. This means that phonon modes with different $\mathbf{q}$ over the complete Brillouin zone contribute to the first order Raman spectrum and this reflects in an asymmetric broadening of the Raman lines as well as in a shift of the peak position.
One has to notice that the effects of the phonon confinement can be clearly noticed when the grain size is smaller than in general 20 lattice parameters [41].
In order to correlated the observed spectral changes to the crystal dimension, different semiempirical models have been proposed; among them the most used is the Phonon Confinement Model (PCM) with a Gaussian weighting function, also known as the RWL model, since it has been proposed by Richter, Wang and Ley.
In particular, it consists on considering, in case of a nanosphere of diameter d, a plane wave for the phonon of wave vector $\mathbf{q}$ which has to be multiplied by a confinement function of Gaussian shape, *W(r)*, written as: $W(r) = e^{\alpha r^2/d^2}$; α is a parameter that determines how fast the wavefunction decays approaching the boundary. In particular, in this model $\alpha = 2$, since the considered boundary condition is that the phonon amplitude, which is proportional to $|W(r)|^2$ reduces to 1/e at the particle boundary $r = d/2$. Within this model the C(q) weight factor used to estimate the contributions of phonons away form the centre of the Brillouin zone, is equal to the Fourier transform of the Gaussian confinement function:

$$|C(q)|^2 = e^{-\frac{q^2 d^2}{4}} \tag{1.52}$$

Finally, the integration of these contributions over the whole Brillouin zone allows to obtain the first-order Raman spectrum which is given by the following formula:

$$I(\omega) = \int_{BZ} \frac{|C(q)|^2 d^3 q}{[\omega - \omega(q)]^2 + (\Gamma_0/2)^2} \tag{1.53}$$

where $\omega(q)$ is the phonon dispersion curve, while Γ_0 is the natural linewidth of the zone-centre Raman line in bulk.

Chapter 2

Theoretical principles of Surface-Enhanced Raman Scattering

SERS spectroscopy is one of the analytical tools that exploits enhancement mechanisms of electromagnetic field in order to increase the Raman cross section of the analyte with a consequent gain in the intensity of the recorded Raman spectrum (Figure (2.1)).

The key-factor to observe the SERS effect and, in turn, the enhanced Raman

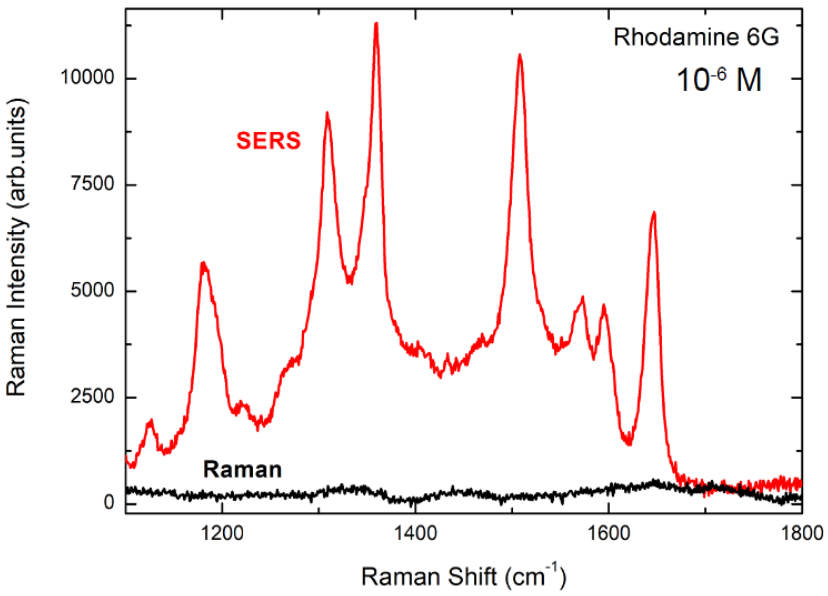

Figure 2.1: SERS effect. Comparison between the Raman signal of a drop of 10^{-6} M solution of Rhodamine 6G deposited on a microscope glass (black line) and the enhanced signal of a drop with the same R6G molar concentration deposited on a SERS substrate of Ag nanoislands (red line).

signal, is the presence of a nanostructured system that acts as SERS-active substrate. Indeed, the enhancement effect is achieved through surface effects that occur between the nanostructured substrates and the analyte, leading to enhancement factors of about 8 order of magnitude or more (10^{12}), in case of single molecule detection.
Since the discovery of SERS effect, metallic nano-objects have been used as SERS-active substrates, thus the established theoretical explanations of the enhancement mechanisms at the basis of the effect have been developed starting from the modelling of a metal nanostructured system.
In particular, instead of Eq. (1.2), if we consider that the molecular system is in the proximity of a nano-metallic substrate, the previous equation has to be rewritten in the following form

$$\boldsymbol{p}^* = \boldsymbol{\alpha_R} \cdot \boldsymbol{E}_{local} \tag{2.1}$$

This simple equation encloses the two main mechanisms at the basis of the enhancement. Indeed, $\boldsymbol{E}_{local}$ takes account of the so-called *electromagnetic enhancement* (EE) that occurs when the frequency of the incident field matches the localized surface plasmon resonances. The other term, $\boldsymbol{\alpha_R}$, is the polarizability of the scatterer as modified by the interaction of the molecule with the metal nano-object. In particular, the adsorption of the molecule on the metal surface of the nano-object leads to an increased Raman scattering cross section of the complex due to charge transfer contributions that are at the basis of the second enhancement mechanism, namely the *chemical enhancement* (CE).

In the following, the electromagnetic theory and the mechanisms of the chemical enhancement are described in the contest of a metallic SERS-active substrate. However, in the end of this chapter, the unified theory proposed by J. R. Lombardi and R. L. Birke [33–35] is illustrated in case of both metal and semiconductor substrates. Indeed, as it has been already pointed out, it is possible to observe the SERS effect with considerable high enhancement also with non-metallic substrates.

2.1 Electromagnetic theory

As suggested by M. Moskovits in 1978, the SERS effect occurs when the incident field matches the localized surface plasmon resonances; if this condition is satisfied both the incident and Raman scattered fields are magnified.

Localized surface plasmons are generally defined as collective oscillations of the conduction electrons with respect to the background of the ionic metal cores and they occur in a nanoparticle when its dimensions are much smaller than the incident light wavelength. The general theoretical approach to treat the optical properties of small metallic particles has been developed by G.

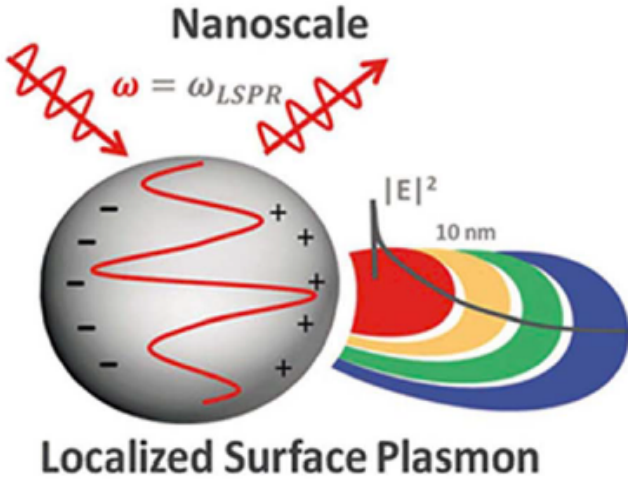

Figure 2.2: Schematization of the electromagnetic enhancement induced by localized surface plasmons [42].

Mie in 1908. However, if we consider a metallic sphere immersed in a dielectric medium with radius R much smaller than the incident wavelength (λ_i), the necessary condition to excite localized surface plasmons (LSPs) in this nanoparticle could be achieved by applying the quasi-electrostatic approximation, instead of approaching the complete Mie theory and, thus, solving the full set of Maxwell's equations. The quasi-electrostatic approximation approach consists in solving the Laplace equation $\nabla^2\phi = 0$, imposing the appropriate boundary conditions at the sphere surface, and neglecting the retardation effect of light propagation. This leads to a relative simple equation:

$$l\epsilon(\omega) = -(l+1)\epsilon_m \tag{2.2}$$

where $\epsilon(\omega)$ is the dielectric function of the metal and ϵ_m is the dielectric constant of the surrounding medium. In particular, by using the metal dielectric function of the Drude model, i.e. $\epsilon(\omega) = 1 - \frac{\omega_P^2}{\omega_l^2}$, it is possible to obtain the localized surface plasmon frequencies

$$\omega_l = \frac{\omega_P}{\sqrt{1 + \frac{l+1}{l}\epsilon_m}} \tag{2.3}$$

as a function of the plasma frequency $\omega_P = \sqrt{\frac{ne^2}{m\epsilon_0}}$, where n is the charge density of the electrons, m is the effective electron mass and ϵ_0 is the permittivity of free space.
Thus, in case of a metallic sphere with $\epsilon(\omega) < 0$ in the visible range, the modes given by Eq. (2.2) are LSPs; in particular, in the considered limit, R$\ll \lambda_i$, all the surface plasmon multipoles other than the dipolar one (l = 1) could be ignored (Figure(2.3)).

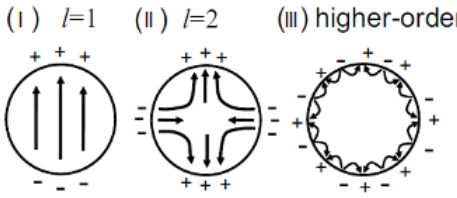

Figure 2.3: Surface modes in a small metallic nanoparticle [43].

Having introduced which are the conditions for LSPs resonances to be excited, it is now possible to evaluate the enhancement effect when the consider metal sphere of radius R is irradiated by an external electric field of frequency ω_0. In particular, such metal sphere is polarized with the consequent formation of surface charges that induces a depolarization field, opposed to the external one. In turn, the sphere polarization, as a function of the external field $\boldsymbol{E}_{ext}$, results to be

$$\boldsymbol{P} = \frac{3}{4\pi}\left(\frac{\epsilon(\omega)-\epsilon_m}{\epsilon(\omega)+2\epsilon_m}\right)\boldsymbol{E}_{ext} \tag{2.4}$$

Thus, it is clear from Eq. (2.4) that the polarization became very large as the denominator tends to zero, namely when the resonance condition is matched:

$$\epsilon(\omega) = -2\epsilon_m \tag{2.5}$$

which is exactly Eq. (2.2) with $l = 1$ for the dipolar mode. A huge increase in the polarization implies an increase of the external field magnitude, in particular near the sphere surface.
Moreover, if we consider a z polarized incident light, in the quasi-static approximation, the expression of the external field magnitude is given by the following formula, in terms of the Cartesian coordinates [44]:

$$E_{ext}(x,y,z) = E_0\hat{\boldsymbol{z}} - \alpha E_0\left[\frac{\hat{\boldsymbol{z}}}{r^3} - \frac{3z}{r^5}(x\hat{\boldsymbol{x}} + y\hat{\boldsymbol{y}} + z\hat{\boldsymbol{z}})\right] \tag{2.6}$$

where r is the radial distance and α is the polarizability of the metal sphere that is generally defined as

$$\alpha = gR^3 \tag{2.7}$$

with g is

$$g = \frac{\epsilon(\omega)-\epsilon_m}{\epsilon(\omega)+2\epsilon_m} \tag{2.8}$$

Thus, from Eq. (2.6), leaving aside for the moment the scaling dependence of the enhanced field with the distance from the sphere surface (it will be discussed later in Subsection 2.1.1), it turns out that g is exactly the field enhancement over the whole surface of the metal sphere:

$$g = \frac{\boldsymbol{E}_{ext}(\omega_0, r)}{\boldsymbol{E}_0(\omega_0, r)} \tag{2.9}$$

However, this is not the only contribution to the enhanced Raman signal; indeed, the electromagnetic enhancement is generally defined as a two-step process, namely not only the incident field is enhanced by the metallic nanostructured, but also the Raman scattered field is enhanced. This means that the metal nanosphere can scatter light at the shifted Raman frequency ω_R, giving another contribution to the enhancement, i.e. g':

$$g' = \frac{\boldsymbol{E}_{ext}(\omega_R, r)}{\boldsymbol{E}_0(\omega_R, r)} \tag{2.10}$$

It results that the overall magnitude of the SERS-scattered field will be given by

$$E_{SERS} \propto \alpha_R g g' E_0 \tag{2.11}$$

where α_R, as already stated, is the scatterer polarizability that encloses both molecule and metal contributions in view of adsorption of the molecule on the nanosphere surface. Accordingly, the SERS intensity will be proportional to the squared modulus of E_{SERS} given in Eq. (2.11):

$$I_{SERS} \propto |\alpha_R|^2 |g g'|^2 I_0 \tag{2.12}$$

In the end, it is now possible to introduce the SERS enhancement factor (EF) which is defined as the ratio between the Raman scattered intensity in the presence of a metallic nanostructure and its value in the absence of the nanostructure; in particular, by considering Eq. (2.12) and outlining the expression for g and g', it results that:

$$EF(\omega_0, \omega_R, r) = \frac{I_{SERS}}{I_0} = \left|\frac{\alpha_R}{\alpha_0}\right|^2 \left|\frac{\boldsymbol{E}_{ext}(\omega_0, r)}{\boldsymbol{E}_0(\omega_0, r)}\right|^2 \left|\frac{\boldsymbol{E}_{ext}(\omega_R, r)}{\boldsymbol{E}_0(\omega_R, r)}\right|^2 \tag{2.13}$$

where α_0 is the polarizability of the molecule in the absence of the metallic nanostructure.
When the Raman-scattered frequency is closed to the incident one and this holds, in particular, for low wavenumbers modes, it results that $g \sim g'$ and, in turn, the well-known dependence of EF on the 4^{th} power of the local incident field enhancement is recovered.
Eq. (2.13) points out that the enhancement is dependent also on the modification that could occur on the polarizability of the molecule as a consequence of the adsorption on the metal surface; as already introduced, these mechanisms are enclosed in the so-called chemical enhancement (Section 2.2).

2.1.1 Dependence of the enhanced signal on the distance

The electromagnetic field outside a metallic nanoparticle is given by Eq. (2.6). It is evident that there is a tight dependence of the EE on the parameter r, namely the distance between the analyte and the metallic surface, and, in turn, the distance plays a key-role in achieving high enhancement. Moreover,

this scaling dependence is essential in order to decouple the electromagnetic and chemical contribution to the enhancement, indeed the last one occurs only upon adsorption of the analyte on the metal surface.
Since the electric field outside the metallic nanosphere scales with r^{-3}, the overall distance dependence of the SERS intensity, in view of its proportionality to the 4^{th} of the field enhancement, in the dipole approximation, is given by:

$$I_{SERS} \approx \left(\frac{R+r}{R}\right)^{-12} \tag{2.14}$$

where we recall that R is the radius of the considered metallic nanosphere.
However, if one consider a shell of molecules around the sphere surface, the increased surface area scales with r^2, thus the distance dependence that one could observe experimentally turns out to be:

$$I_{SERS} \approx \left(\frac{R+r}{R}\right)^{-10} \tag{2.15}$$

Different research works have dealt with the experimental determination of the distance dependence of the enhancement, recovering the scaling dependence on r^{-10}; in particular, among these works, in [46] [47] ad hoc SERS substrates have been used, namely self-assembled monolayers, in which the organic molecules adsorbed on the roughened silver surface, create ordered monolayers that act as spacer allowing to follow, with high precision, the SERS intensity at variance of its thickness. The result of these researches shows that the enhancement tends to fall down when the analyte is at 3 -5 nm away from the metal surface. Even in my research work, we deal with the distance dependence of the SERS intensity on silica-coated gold nanostars grafted on properly functionalized glass chip. The aim of this research work will be discussed in detail in the following Chapter, here I want to highlight that also our experimental measurements of the SERS intensity at variance of the silica coating show the r^{-10} dependence. However, the dependence illustrates by Eq. (2.15) could be deviated at variance of particle shape and size and also due to coupled fields as a consequence of interparticle interactions. As for instance, in [48], the authors show a surprising long-range dependence with a drop of the enhancement after $\sim$ 30 nm in Ag/SiO nanostructures; in particular, they claim that the observed behaviour is related to collective surface plasmon polariton waves.

2.1.2 Dependence of the electromagnetic enhancement on SERS substrate properties

The plasmon resonances and, in turn, the electromagnetic enhancement of the field, are strictly related to the nature and geometry of the SERS substrates. Therefore the research of the proper SERS substrate is of extremely importance because it is mandatory to optimize the substrate parameters, namely type of the metal, size and shape of the nano-objects, that are the key-factors in order to tune the LSP resonances and thus to achieve high EFs.

Type of metal. The importance of the nature of the metal is enclosed in Eqs. (2.2) and (2.8). Indeed, the maximum EE is achieved when the denominator of g is closed to zero, namely when the resonance condition $\epsilon(\omega) = -2\epsilon_m$ is matched.
The metal dielectric function is generally a complex quantity; thus the resonance condition implies that the real part of $\epsilon(\omega)$ is equal to $-2\epsilon_m$, meaning that it must be negative in the visible range, and that the imaginary part must be closed to zero, i.e. $Im[\epsilon(\omega)] \approx 0$.
The metals that satisfy both the two conditions are the ones that are most suitable to be use for SERS substrates. In particular, by looking at Figure (2.4) where the real and imaginary part of the dielectric functions of different transition metals are reported, it is clear why the coinage metals (Ag, Au and Cu) are the most used metals since the discovery of SERS. Indeed, the imaginary part of their dielectric functions are very small and in the case of silver basically close to zero in the visible range between 500 and 800 nm where the most used laser wavelengths fall.
However, the nature of the metal is essential to achieve the proper resonance condition, but shape and size play an important role in order to tune the LSPs.

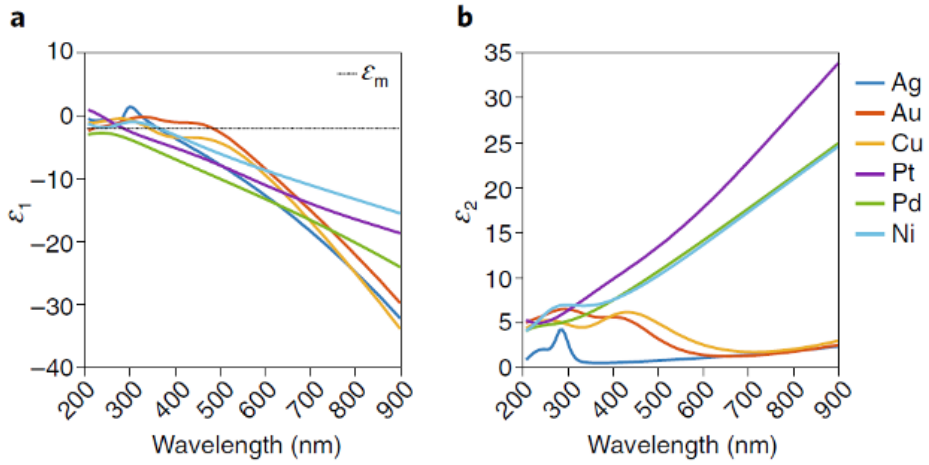

Figure 2.4: Real (**a**) and imaginary (**b**) part of the dielectric function of different transition metals [49].

Size. The upper limit for the size of nano-objects is set by the necessary condition that has to be satisfied in order to excite the dipolar LSPs, namely the dimension of the metallic object must be small with respect to the wavelength of the incident excitation source. On the contrary, if this condition is not met, higher order dipoles are excited and the SERS efficiency drops because, unlike the dipoles, these modes are non-radiative.
However, there is also a lower limit that must not be overcome; indeed, if the particle is too small the radiated field is reduced because the effective con-

ductivity of the metal particle itself decreases as a consequence of electronic scattering process occurring at the surface. Moreover, if the particle dimensions are even smaller, the metal object has to be treated as a quantum object, displaying quantum size effects.
A simple model allows to understand how the reduction of the particle dimensions affects the SERS enhancement. Thus, let's consider a small nanoparticle in the vacuum, whose polarizability is expressed by Eq. (2.7) with $\epsilon_m = 1$ in the expression of g (Eq. (2.8)). If we consider as the metal dielectric function, the expression given by the Drude model, properly modified for interband transitions, namely

$$\epsilon(\omega) = \epsilon_b(\omega) + 1 - \frac{\omega_P^2}{\omega^2 + i\omega\gamma} \tag{2.16}$$

where $\epsilon_b(\omega)$ takes account of the interband transitions contribution to the metal dielectric function and γ is the electronic scattering rate, inversely proportional to the electronic mean free path; it results that the complete expression for the metal polarizability is given by:

$$\alpha = \frac{R^3\left(\epsilon_b(\omega)\omega^2 - \omega_P^2\right) + i\omega\gamma\epsilon_b(\omega)}{\left((\epsilon_b(\omega) + 3)\omega^2 - \omega_P^2\right) + i\omega\gamma(\epsilon_b(\omega) + 3)} \tag{2.17}$$

where $\gamma(\epsilon_b(\omega)+3)$ is the width of the resonance, occurring when $\omega = \frac{\omega_P}{\sqrt{\epsilon_b(\omega)+3}}$.
From this Equation, it is clear that when γ is large the quality of the resonance is reduced and in turn the SERS enhancement. The enlarging of γ could be due to intrinsic low conductivity of the metal or, as already said, to the electronic scattering at the surface that becomes dominant when the particle sizes are reduced. In the end it is possible to assert that the proper dimension of the metallic nano-objects must be smaller than the incident wavelength and grater than the electronic mean free path; this means nanoparticle size in the range of 10-100 nm for coinage metals [50].

Shape. Besides the classical spheroidal or cylindrical nanoparticle shapes that are generally introduced since they are the only simple cases which could be analytically solved, other geometries could lead to higher near field enhancement. Indeed, nano-objects characterised by tips and edge display the so-called *lightning rod effect* [51], namely a high electromagnetic near field concentration at sharp ends, generating hot areas in the proximity of which the particle Raman signal is further enhanced. As an example, in Figure (2.5), the numerical solution of the spatial distribution of the local field intensity enhancement factor (LFIEF) for a bidimensional nano-triangle is reported. It is possible to observe a high concentration of the e.m. field at the tips.
Moreover, this example allows to introduce other important aspects: i) as it is evident from Figure (2.5c), in case of a shape different from the simple sphere or cylinder, more than one resonance condition could be achieved; ii) the maximum near field enhancement could occur in different points for different excitation wavelengths.

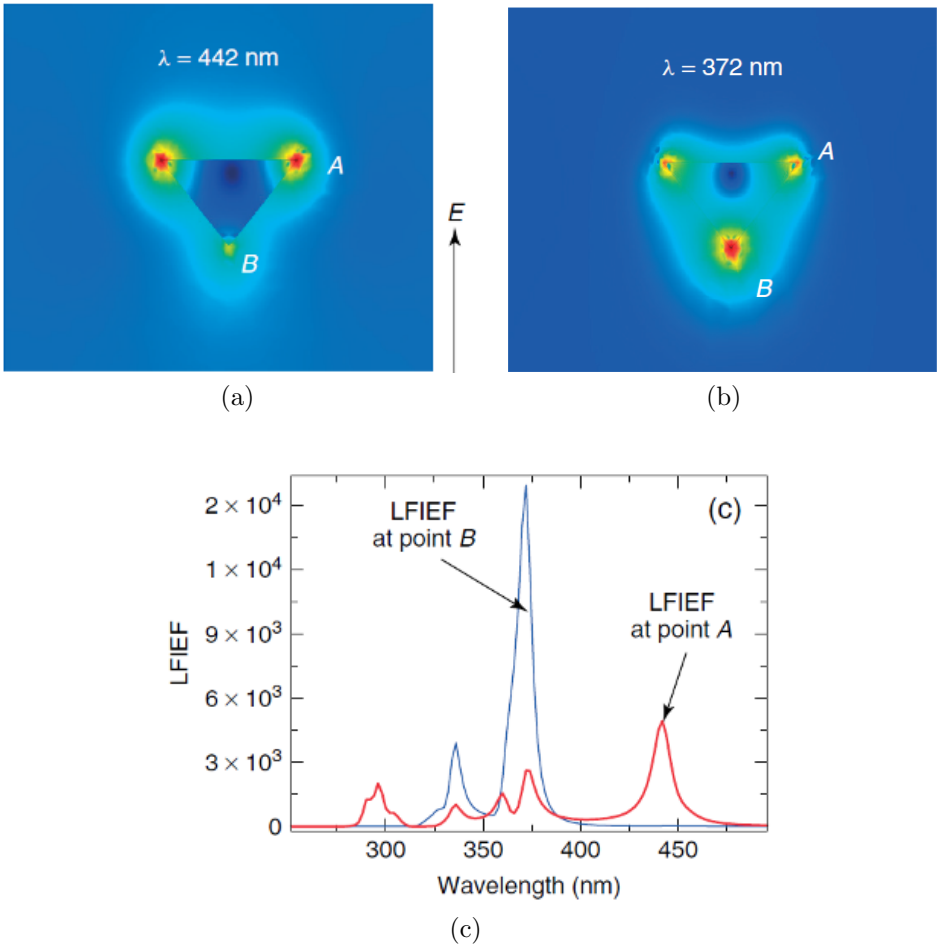

Figure 2.5: LFIEF at different wavelengths (a) 442 nm and (b) 372 nm for an Ag nanotriangle. In Figure (c) the LFIEF at point A and B is reported at variance of the wavelength [52].

The electromagnetic theory and its related arguments have been introduced by considering the simple case of a single nanosphere; however, the experimental evidence in the history of SERS has pointed out that this effect is not truly been observed in case of an isolated nano-object. On the contrary, high enhanced Raman signals have been recorded on SERS-active substrates made up of aggregates of single nanoparticles, as well as rough metal surfaces and island films.
In this regard, the comparison between the calculation of the LFIEF through Mie theory in case of a single Ag sphere and two closely-spaced Ag spheres, forming a 2 nm gap, proposed in Figure (2.6), well illustrates this argument. In particular, the LFIEF is calculated for a molecule located at 1 nm from the surface of the single sphere and from the dimer (position A in Figure (2.6)); as it is possible to observe, the enhanced local field intensity reaches higher values ($\sim 10^5$) when the molecule is located in the gap of the dimer with respect to the value obtain for the single sphere (~ 470). The gap-region with

this increased enhancement is the so-called *hot spot*.
Moreover, in the dimer case, the interaction between the two nanoparticles generates *new* LSP resonances as a result of the coupling between the LSP resonances of the two isolated nanoparticles and the local field enhancement is kept large throughout most of the visible range, as it is possible to observe in Figure (2.6b). As in the case of a single nanoparticle, among these coupled-LSP resonances, the most important is the more red-shifted one which is due to the dipolar interaction between the dipolar LSP resonances of the two single nanoparticles. The other resonances at lower wavelengths generally arise from high-order interactions between the dipolar LSP resonance of the isolated nano-objects or from the dipolar interaction between high-order individual LSP resonances.
The simple model of a dimer well introduces the experimental evidence of a

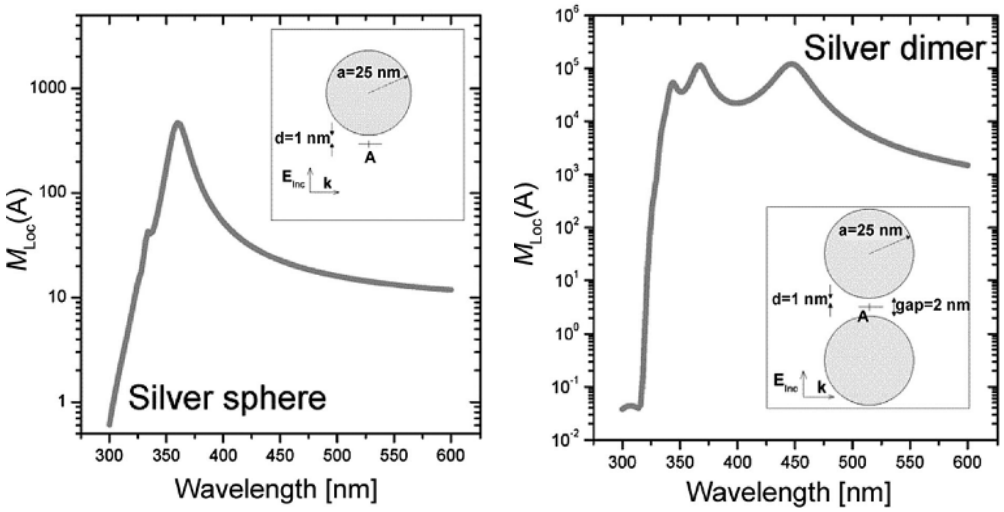

(a) (b)

Figure 2.6: LFIEF trend for a molecule located at 1 nm (position A) from the surface of a single silver sphere (a) and of a dimer (b). In [53], from which these calculations are taken, $M_{loc}(A)$ is defined as $|g|^2$.

high SERS enhancement, as well as the broadening and the red-shifting of its spectral maximum that the case of a single isolated particle does not explain. However, this model is still too simplified to well reproduce the experimental evidences; thus, in order to fully explain these aspects, one has to face with the fractal theory [54].

2.2 Chemical Enhancement

The chemical contribution to the enhancement is one of the more debated argument in SERS theory till its discovery. Nowadays, even if it is not completely resolved, the chemical enhancement is recognized by most researchers of the field as the second major mechanism at the basis of the SERS effect.

The CE could be defined as *any modification of the Raman polarizability tensor upon adsorption of the molecule onto the metal surface* [53]. These modifications could both quench or enhance the Raman spectrum of the analyte; the enhancement occurs when the modified polarizability is more resonant with the incident wavelength. The most accredited mechanisms at the basis of these modifications are the *charge-transfer* ones which are schematically illustrate in Figure (2.7). In particular, three types of charge-transfer processes have been identified.
Within the first type, the simplest one, the molecule and the metal do not create a covalent bond; however, the presence of the metal acts as a perturbation to the analyte electronic structure, determining a slight modification of its electronic cloud distribution and a consequently change in its Raman polarizability. This might result in an increased Raman cross section.
The second process which is illustrated by transition (a) in Figure (2.7), requires the creation of a metal-molecule complex through a direct covalent bond or an indirect one mediated by an electrolyte ion. The complex creation could lead to a significant change of the intrinsic molecular polarizabilty. This happens because the presence of the metal modifies the gap between the HOMO and LUMO orbitals of the molecule enabling new possible transitions that in the absence of the metal would never be accessible by the incident excitation source.
The final type of charge-transfer process involves photon-driven charge trans-

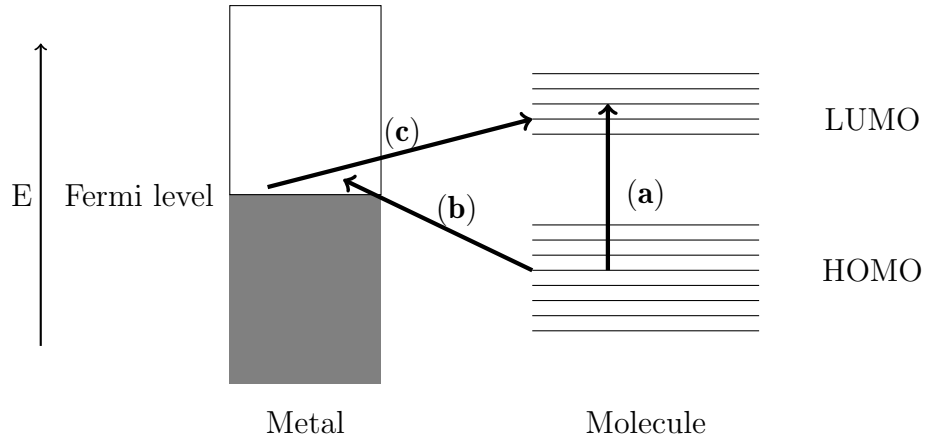

Figure 2.7: Schematization of the charge-transfer mechanisms at the basis of the chemical enhancement.

fer mechanisms, namely it occurs when the incident laser wavelength matches the energy difference between the Fermi level of the metal and HOMO or LUMO orbital of the molecule; as for instance, as depicted by the transition (b) and (c) in Figure (2.7), the incident radiation absorbed by the molecule, excites an electron which is promoted to the Fermi level of the metal from the HOMO molecular orbital, subsequently another photon excites the electron that is promoted to the LUMO orbital of the molecule.

2.3 Unified SERS theory

The general approach to SERS theory is the one that we have followed in this Chapter, namely, to treat separately the EE and CE mechanisms. However, an intriguing contribution that allows to treat together the main contributions to the SERS effect, previously described, has been given by J.R. Lombardi and R.L. Birke. In particular, they consider the phenomenon as "*a single effect drawing on up to three resonances which are intimately tied to each other and cannot easily considered separately*" [33]. The three cited resonances are: the LSP ones which are a property of the metal, the molecular resonances owned by the molecular system and, finally, the charge-transfer ones which are properties of the combined metal-molecule complex.
This approach is only one of the possible strategies to face the SERS effect in metal as well as dielectric systems. Indeed, in particular for semiconducting substrates, different mechanisms could be evoked to explain the enhanced effect like light-trapping, subwavelength-focusing and morphology-dependent resonances, as described in [32].

In order to achieve an analytical expression for the Raman signal intensities of a molecule in proximity of metal nanostructures, the reasoning proposed by the two authors starts by considering the expression of the polarizability that we have described in detail in Chapter 1, namely the Albrecth approach to the Raman effect by the introduction of the Herzberg-Teller coupling that leads to the polarizability expression in terms of A, B and C. In particular, Lombardi and Birke extended the Raman theoretical treatment to the case in which a molecule is bound to the metal surface through a weak covalent bond and, in turn, the molecule-metal complex is considered together in the calculation. This assumption leads to the inclusion of the metal conduction band (M) in the sum over all the possible excited states of the system in the polarizability terms. Thus, the charge-transfer transitions "borrow" intensity from the allowed molecular ones through the Herzberg-Teller coupling, as depicted in Figure (2.8). In addition, the authors demonstrate that the maximization of the charge-transfer intensity occurs when the Fermi level is the one involved among the metal states; this means removing the sum over the M states and replacing this generic state M with the appropriate Fermi state, $|F\rangle$.
The following step is to consider that the incident frequency is not only resonant with the surface plasmons but also to charge-transfer resonances of the metal-molecule complex. This means considering only the terms in the expression of the polarizability, that include a charge-transfer state F.
Lombardi and Birke show that for the A component, only two terms have to be considered, namely A_f and A_k whose expression is given in the Eq. (2.18) together with the ones for B and C terms. The following expressions are taken from [33] with a minimum change in the notation in order to keep the nomen-

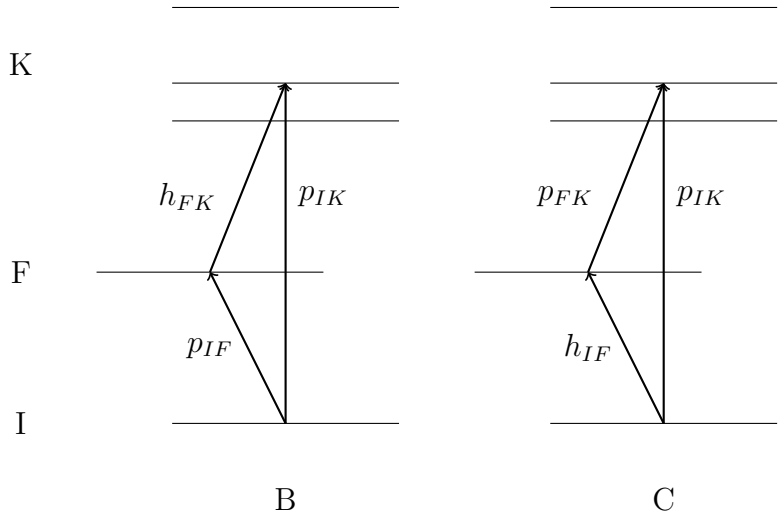

Figure 2.8: Diagram of the allowed transitions for the B and C terms of the metal-molecule system polarizability. This diagram is reproduced on the basis of Figure 1 in [33].

clature consistent with the one chosen in this thesis work.

$$
\begin{aligned}
A_f &= \frac{2}{\hbar} p^{\sigma}_{FI} p^{\rho}_{FI} \langle i|k\rangle \langle k|f\rangle \frac{\omega_{FI}+\omega_f}{(\omega_{FI}+\omega_f)^2-\omega^2} \\
B &= -\frac{2}{\hbar^2} \sum_{K\neq I} \frac{[p^{\sigma}_{KI} p^{\rho}_{FI} + p^{\rho}_{KI} p^{\sigma}_{FI}]\,(\omega_{KI}\omega_{FI}+\omega^2) h_{KF} \langle i|Q|f\rangle}{(\omega^2_{KI}-\omega^2)(\omega^2_{FI}-\omega^2)} \\
A_k &= \frac{2}{\hbar} p^{\sigma}_{FK} p^{\rho}_{FK} \langle i|k\rangle \langle k|f\rangle \frac{\omega_{FK}+\omega_f}{(\omega_{FK}+\omega_f)^2-\omega^2} \\
C &= -\frac{2}{\hbar^2} \sum_{K\neq I} \frac{[p^{\sigma}_{KI} p^{\rho}_{FK} + p^{\rho}_{KI} p^{\sigma}_{FK}]\,(\omega_{KI}\omega_{FK}+\omega^2) h_{IF} \langle i|Q|f\rangle}{(\omega^2_{KI}-\omega^2)(\omega^2_{FK}-\omega^2)}
\end{aligned}
\tag{2.18}
$$

A_f and B terms correspond to molecule to metal transitions, while the A_k and C terms to metal to molecule ones. The A terms, shown in Eq. (2.18), account for totally symmetric modes through the restriction imposed by the numerator which is not vanishing only in case of resonance Raman spectroscopy; indeed, only on resonance, appreciable intensity are forecasted. The B and C terms predict which are the active totally and nontotally symmetric vibrational modes; thus they have to be included since the SERS spectra are also markedly characterized by nontotally symmetric modes.
If we consider, as for instance, the case of metal to molecule charge-transfer, namely the C term, by combining Eq. (2.18) with the g expression for the metallic nano-object (Eq. (2.8)) and the expression of the Raman intensity, Lombardi and Birke find out that the overall SERS enhancement is proportional to the squared modulus of terms like the one given in the following

expression:

$$R_{IFK}(\omega) = \frac{p^{\sigma}_{KI} p^{\rho}_{FK} h_{IF} \langle i|Q_k|f\rangle}{((\epsilon_1(\omega) + 2\epsilon_m)^2 + \epsilon_2^2)\left((\omega^2_{FK} - \omega^2) + \gamma^2_{FK}\right)\left((\omega^2_{IK} - \omega^2) + \gamma^2_{IK}\right)} \tag{2.19}$$

As it is possible to observe, the denominator in this equation encloses the product of three contributions, each of which corresponds to a resonance that contribute to the SERS enhancement. The first term, $((\epsilon_1(\omega) + 2\epsilon_m)^2 + \epsilon_2^2)$ is due to the LSP resonance that occurs, in the simplest case of a single nanoparticle, when the real part of the metal dielectric function, $\epsilon_1(\omega)$, satisfies the following condition: $\epsilon_1(\omega) = -2\epsilon_m$ and its imaginary part is closed to zero, $\epsilon_2 \approx 0$. The second one, namely $(\omega^2_{FK} - \omega^2) + \gamma^2_{FK}$ corresponds to charge-transfer resonance that will occur when $\omega = \omega_{FK}$; finally, the last term, $(\omega^2_{IK} - \omega^2) + \gamma^2_{IK}$, represents the molecular resonance and when this resonance is matched, i.e. $\omega = \omega_{IK}$, we are in the case of surface-enhanced resonance Raman spectroscopy. One has to notice that the SERS enhancement is also dependent on the magnitude of damping parameters, ϵ_2, γ_{FK} and γ_{IK} with the general dependence of γ^{-4}.
Thus, in order to have a complete idea of the contribution of the three resonances to the enhancement, experiments have to be performed by varying the laser incident frequency or the applied voltage in electrochemical measures or the LSP resonance through the proper optimization of the substrate geometry. In Figure (2.9) is reported as an example the resonances involved in a pyridine-Ag nanoparticles system. The pyridine absorption falls in the UV re-

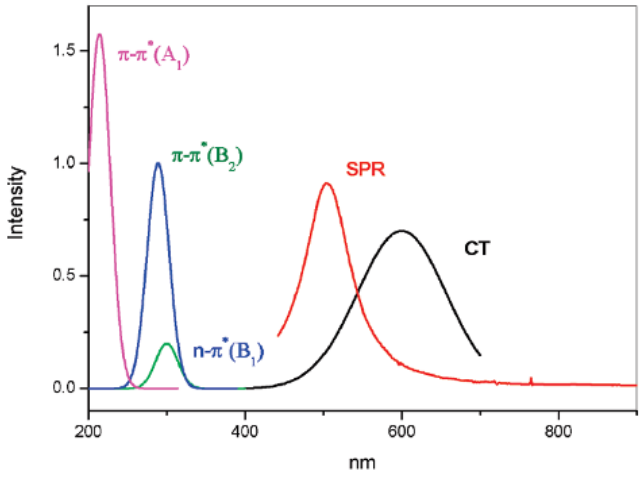

Figure 2.9: Involved resonances in a pyridine-Ag nanoparticles system. This Figure is taken from [55].

gion with three molecular transitions, while in the near-UV and in the visible range there are the LSP and charge-transfer resonances. By tuning the incident laser wavelength at 480 nm, it is possible to excite only the plasmon resonance

while at higher wavelength a mixed contribution of LSP and charge-transfer is achieved; in this region, there are no molecular transitions, but as stated by Eq. (2.19), the intensity could be borrowed by these resonances through the Herzberg-Teller coupling.
The three resonances in the denominator are linked to each other through the terms in the numerator. Indeed, when the incident frequency matches the localized surface plasmons, the electric field at the surface of the nano-object is enhanced and it is coupled with both the charge-transfer resonance (p_{FK}) and the molecular one (p_{IK}); moreover, these two resonances are coupled to each other through the Herzberg-Teller coupling constant, h_{IF}.
The requirement that the numerator is not vanishing provides the SERS selection rules. The factor $\langle i|Q_k|f\rangle$ gives the normal oscillator selection rules, namely $f = i \pm 1$, while other restrictions to the observable modes are given by the combination of the transition moments, the Herzberg-Teller coupling and the direction of the enhanced electric field induced by LSPs; this means that to achieve an appreciable SERS intensity the three terms in the following product have to be simultaneously non zero:

$$p^{\sigma}_{KI} p^{\rho}_{FK} h_{IF} = \langle I_e|p^{\sigma}|K_e\rangle \, \langle K_e|p^{\rho}|F_e\rangle \, \langle F_e|\frac{\partial V_{eN}}{\partial Q_k}|I_e\rangle \tag{2.20}$$

Moreover, the surface selection rule that follows from the condition that the electric plasmon-induced field is in large part produced in the direction perpendicular to the metal surface, leads to the requirement that one of the two transition moments p^{σ}_{KI} and p^{σ}_{KI} is polarized in the same perpendicular direction; this could be simply expressed as $\langle F_e|p^{\perp}_{CT}|K_e\rangle$.
With these considerations in mind, it is possible to translate the selection rules given by Eq. (2.20) in a simpler way by noticing that the electronic states appear twice in the considered Equation. This means that these states together belong to the totally symmetric irreducible representation, therefore one has only to take into account the symmetry species of the involved operator. In the end, the Herzberg-Teller-surface selection rules are expressed by

$$\Gamma(Q_k) = \sum_K \Gamma(p^{\perp}_{CT}) \times \Gamma_K \tag{2.21}$$

where $\Gamma(Q_k) = \Gamma(\partial/\partial Q_k)$ is the irreducible representation pertaining to the allowed SERS vibration, $\Gamma(p_{CT})$ is the one to whom the charge-transfer dipole, perpendicular to the metal surface, belongs and, finally, Γ_K is the irreducible representation of the molecular excited state associated to an allowed transition between $|I\rangle$ and $|K\rangle$ states.

2.3.1 Enhancement from semiconducting substrates

Lombardi and Birke also extend the unified treatment of the SERS phenomenon to the case in which semiconducting nanostructures are used as

SERS-active substrates.
The theoretical procedure that they follow in case of a molecule-semiconductor complex, is the same that the one used for a molecule-metal system. Indeed, what they have done is to replace the sum over the metal states with the one over the semiconductor states; in particular, by proper calculations, it was found that the maximum SERS enhancement occurs when the involved semiconductor states match the band edges, namely E_C and E_V for conduction and valence bands, respectively.
Thus, the charge-transfer transitions involved are the ones from the HOMO molecular orbitals to the conducting band edge, with the relative dipole moment p_{IC} and the ones from the valance band edge to the LUMO molecular orbitals with the corresponding transition moment p_{VK}. These transitions, as stated in the molecule-metal description, could borrow the intensity from the molecular transition (p_{IK}), but also from another transition that occurs in many semiconductors, namely the exciton transition, p_{VC}, as illustrated in Figure (2.11). The described treatment leads to polarizability terms like

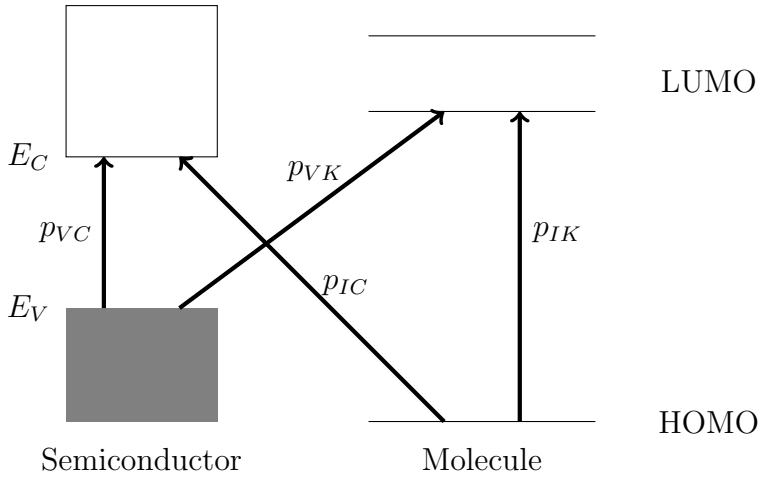

Figure 2.10: The resonances in the molecule-semiconductor system: p_{VC} is the dipole moment associated to the exciton transition, p_{IC} and p_{VK} are charge-transfer dipole moments and p_{IK} corresponds to the molecular dipole moment. This scheme has been designed according to the one proposed in [34].

the ones obtained for the metal substrates (Eq. (2.19)); in particular, in the

following equations, the expressions that appears in the C-term [34] are shown

$$R_{IVK}(\omega) = \frac{p_{VK}p_{KI}h_{IV}\langle i|Q_k|f\rangle}{((\epsilon_1(\omega)+2\epsilon_m)^2+\epsilon_2^2(\omega))\left((\omega_{VK}^2-\omega^2)+\gamma_{VK}^2\right)\left((\omega_{KI}^2-\omega^2)+\gamma_{KI}^2\right)} \tag{2.22}$$

$$R_{KVC}(\omega) = \frac{p_{CV}p_{VK}h_{KC}\langle i|Q_k|f\rangle}{((\epsilon_1(\omega)+2\epsilon_m)^2+\epsilon_2^2(\omega))\left((\omega_{VK}^2-\omega^2)+\gamma_{VK}^2\right)\left((\omega_{CV}^2-\omega^2)+\gamma_{CV}^2\right)} \tag{2.23}$$

As it is possible to observe from these expressions, the three resonant contributions are found again in the denominator, as in the metal case. Indeed, there is the contribution from LSP resonance and the charge-transfer transition from the valence band to LUMO orbitals at $\omega = \omega_{VK}$ (while for the B term from the conduction band to the HOMO orbitals) which are coupled through the Herzberg-Teller constant to the molecular transition when $\omega = \omega_{IK}$ or to the exciton one when $\omega = \omega_{CV}$.
One has to notice that in semiconductors, the contribution from the localized surface plasmons is in general low for an excitation wavelength in the visible range because, as we have previously described, the LSP frequency is a function of the plasma frequency, $\omega_P = \sqrt{\frac{ne^2}{m\epsilon_0}}$, that, in turn, is dependent on the charge density of the electrons, n; thus, in semiconductor, the density of the conducting electrons is small and it leads LSPs frequencies in the infrared region, while n for the valence electrons is very high, namely, about $10^{22} - 10^{24}$ cm^{-3} and, in turn, the plasmons originating from the valence electrons tend to lye in the vacuum UV. However, by properly tuning size and shape of the nano-objects in order to provide a cavity resonance, it is possible to increase the near-field efficiency by maximizing the Mie resonances in the spectral region where the laser wavelengths fall; this has been shown to occur for particle size in the range 100-300 nm [35].
Therefore, higher enhancement factors could be achieved when the three resonances are coincident. In particular, the way to follow is to choose the proper semiconductor substrate in order to control the involved resonances; this could be achieved by properly selecting the band gap, as well as the conduction and valence band, also through efficient doping strategies, the refractive index and nanoparticle shape and size.

As it has been described for metals, also in the case of semiconductor system, the requirement that the numerators of the B and C terms is not vanishing, leads to the definition of surface selection rules, namely the irreducible representation, $\Gamma(Q_k)$, to whom the allowed vibrational modes belong is given

by

$$\begin{aligned}\Gamma(Q_k) &= \sum_K \Gamma(p_{CT}) \times \Gamma_{mol} \\ \Gamma(Q_k) &= \sum_K \Gamma(p_{CT}) \times \Gamma_{ex}\end{aligned} \tag{2.24}$$

where the second expression takes account of the new resonances displayed by the semiconductor systems, i.e. the excitons, while the first one is the same as in the case of metal, expect that, as it has been already stated, the charge-transfer transitions involve the band edge and not the Fermi level.

2.4 Working definitions of Enhancement Factor

The enhancement factor (EF) is theoretically defined as the ratio between the SERS intensity and the Raman one of the same analyte under investigation. Despite the clarity and simplicity of this definition, from the experimental point of view, its real calculation is not a trivial task, at least for two main reasons: on one side, it is not simple to correctly estimated the parameters on which it depends, as for instance, the scattering cross-section as well as the number of molecules effectively involved in the effect and their distribution, on the other side a rigorous definition of EF and the way in which it has to be calculated is still missing.
This leads to find in literature values of enhancement factor ranging from 10^4 to even 10^{14}, in case of single-molecule detection, even for almost apparently similar experimental conditions.
The impossibility to achieve just one "working" expression of the EF is intrinsic in the SERS phenomenon: the SERS effect and, in turn the EF, is strictly dependent on the type of substrate, the analyte itself, the molecular distribution on the substrate surface, the excitation wavelength and also all the instrumental parameters. Thus, different substrates need different calculation strategies for the EF calculation. However, as suggested by Le Ru *et al.* in a reference work [56] on the issue of the SERS EF, it is, at least, necessary to standardise the possible expressions of the EF related to the type of the performed experiment in order to avoid persistent discrepancies and inconsistencies due to an improper calculation route.
The working definitions of enhancement factor widely used in literature and also reported in [56] are: the *single molecule enhancement factor* (SMEF), the *SERS substrate enhancement factor* (SSEF) and the *analytical enhancement factor* (AEF). In the following these three definitions are reported and described.

Single molecule enhancement factor. It is the enhancement experienced by a molecule in a specific point, generally dependent on the Raman polarizability tensor of the analyte and on its orientation with respect to the local field.

This definition also relies on the orientation of the substrate with respect to the incident laser polarization and direction, thus it is mandatory to know the geometry of the substrate as well the position and orientation of the analyte. The general definition is

$$SMEF = \frac{I_{SERS}}{\langle I_{RS} \rangle} \tag{2.25}$$

where I_{SERS} is the SERS intensity of the single detected molecule, while $\langle I_{RS} \rangle$ is the mean Raman intensity and it takes account of the fact that in a Raman experiment, it is generally impossible to detect a single molecule, but instead an ensemble of molecules without knowing their orientation. At this regard, it is also possible to define the orientation-averaged SMEF in which the average SERS intensity has to be taken over all the allowed orientations of the single molecule, thus, in Eq. (2.25) I_{SERS} is replaced by $[I_{SERS}]$.
In general, what is important is to calculate the maximum SMEF on a given SERS substrate.

SERS substrate enhancement factor. In most experimental cases, one is more interested in knowing the average enhancement factor that could be achieve with a given substrate, thus it is possible to use the definition of the SERS substrate enhancement factor. This formulation also allows to compare the enhancement efficiency among different substrates.
The general expression of the SSEF is

$$SSEF = \frac{I_{SERS}/N_{Surf}}{I_{RS}/N_{Vol}} \tag{2.26}$$

where N_{Surf} represents the average number of molecules adsorbed onto the substrate in the scattering volume, while $N_{RS} = c_{RS}V$ is the average number of molecules in the scattering volume in case of non-SERS measure.
However, this formulation is not rigorous enough, indeed it presents some criticisms: i) it is not specify how the number of molecules adsorbed on the substrate, N_{Surf}, has to be counted; ii) the definition of the scattering volume is not well defined and also the precise metallic surface area is difficult to measure. These issues could lead to an error in the estimation of about 2 orders of magnitude [56].
In [56], Le Ru *et al.* present a more rigorous definition of Eq. (2.26) by starting from the SMEF definition and relating the formulation to the experimental measured signals

$$SSEF = \frac{I_{SERS}/\left(\mu_M \mu_S A_M\right)}{I_{RS}/\left(c_{RS} H_{eff}\right)} \tag{2.27}$$

where μ_M is the surface density of the nanostructures which produce the enhancement and μ_S the one of the molecules on the metal surface, A_M is the surface area of the metallic substrate, while c_{RS} is the molecular concentration of the solution used in Raman measures and H_{eff} the effective height of the scattering volume. Eq.(2.26) could be restored by replacing $N_{Surf} = \mu_M \mu_S A_M A_{eff}$

and $N_{Vol} = c_{RS} H_{eff} A_{eff}$, where A_{eff} represents the effective area of the scattering volume.

Analytical enhancement factor. The formulation of the AEF is different from the previous proposed definitions because it not deals with the intrinsic characteristics of the substrate, but instead it gives an indication on how much it is possible to gain in intensity through the SERS effect with respect to normal Raman. The AEF expression is

$$AEF = \frac{I_{SERS}/c_{SERS}}{I_{RS}/c_{RS}} \tag{2.28}$$

This definition is particularly useful for specific practical applications like the analytical chemistry ones. However, AEF is strongly dependent on different factors such as the adsorption properties and surface covering of the nanoparticles, namely if there is a formation of a multilayer or a monolayer; moreover, it neglects that SERS effect is a surface phenomenon. Thus, this definition is not exactly correct to calculate the SERS EF for substrates as planar 2D ones; nevertheless, provided that the experimental conditions are described in detail and that the monolayer coverage is guarantee, also the AEF could be used. Concerning what it has been described, it is clear that AEF could be fruitfully used to determine the magnitude of the EF for liquid substrates, like colloidal ones.

2.5 Possible strategies for SERS-active substrates

As already pointed out the engineering of the SERS substrates is of extremely importance in order to reach high, stable and reproducible enhancement factors, and in turn high performances.
Different strategies of SERS-based sensors can be implemented in view of the specific foreseen application. In particular, according to [57], SERS substrates can be classified in three main categories on the basis of the origin of the collected signal: i) surface-affinity strategies (SASs), ii) SERS-tags strategies (STSs) and iii) probe-mediated strategies (PMSs). In Figure (2.11), a pictorial summary of the all possible strategies is reported.

Surface-affinity strategies. This category encloses all the possible strategies in which the recorded signal is collected directly from the analyte. Within this approach, the analyte can be directly adsorbed on the metal surface or, instead, the binding with the metallic nano-object can be conveyed by the presence of a functionalized surface.
The case of unfunctionalized substrate is the most simplest strategy in practise; however, the main drawback is the possibility of a lack of affinity between the

metallic surface and the analyte, as for instance electrostatic repulsion. This limitation can be overcome by functionalizing the surface with the presence of a particular ligand or receptor that assists the binding displaying affinity to the specific analyte. In this case, attention must be paid on the chosen receptor molecule in order to avoid that the its signal overcomes the one of the analyte, in particular in case of bulky ligand for which the captured analyte can be too far from the metallic surface. Following this considerations it is thus clear that the Raman scattering cross-section of the investigate molecule must be much grater than the one of the receptor.

SERS-tags strategies. In case of STSs, the signal arises from a specific Raman reporter, avoiding the difficulties in bringing the analyte closer to the substrate surface. As depicted in Figure (2.11), different mechanisms can be put in place. In particular, through the use of an analyte-selective targeting ligand, specificity can be achieved. In particular, the presence of the analyte can induce several changes that can be monitored, like immobilization or accumulation of the SERS-tags in specific areas, aggregation or disaggregation of the SERS-tags, corresponding to generation or breakdown of hotspots and finally, variations in the distance between the Raman reporter and the SERS-active substrate.

Probe-mediated strategies. Within this approach, the recorded signal arises from probe molecules instead of the analytes. In particular, what is monitored is a change in the SERS spectrum of the probe as a consequence of a specific interaction between the probe itself and the analyte. This kind of strategies are similar to the previously described STSs, although for STSs the Raman reporter is unchanged in the presence of the analyte.
The interaction between the probe and the analyte could lead to three possible situations. i) The formation of molecules displaying a new absorption band closer to the excitation wavelength, thus a creation of resonant molecules. ii) A change in the distance between the probe and the substrate, leading to a creation of a turn-on signal when the distance is reduced by the presence of the analyte or a creation of a turn-off signal in the opposite case. In particular, the reduction of the distance occurs when the analyte creates a surfacephilic functional group upon reaction with the probe, otherwise it creates a surfacephobic one. iii) Chemical or conformational changes induced by the analyte in the bound between the probe and the surface.

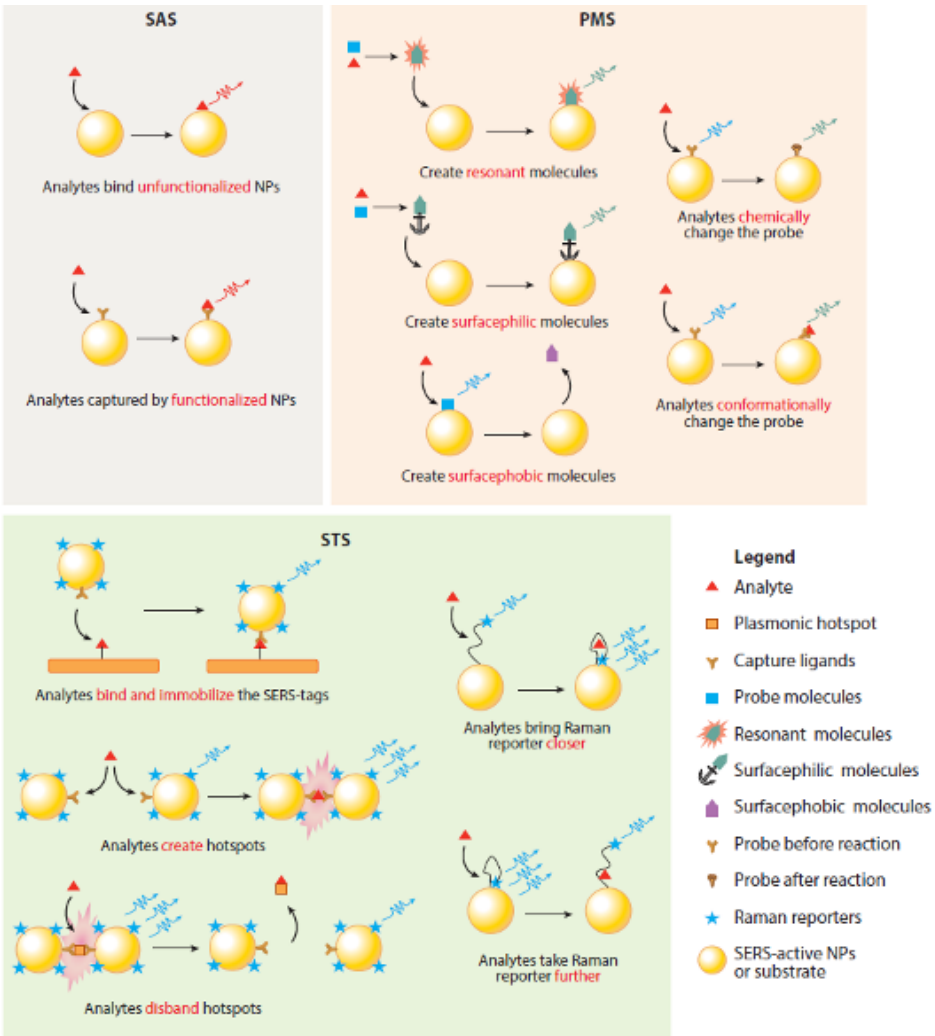

Figure 2.11: Schematization of the classification of SERS-active sensors according to the signal origin [57].

Chapter 3

SERS from metallic substrates

The research on SERS effect from metallic substrates has been widely carried on since its discovery pursuing advanced substrates characterized by ever higher enhancement and high homogeneity. This, in turn, has offered the possibility to better understand the basic principles of the SERS effect itself.
Indeed, what is almost clarified by the theory, it is still not simple to achieve from the experimental point of view. This leads us to deal with the study of the SERS effect by the preparation of metallic substrates through which some of the theoretical aspects can be studied and discussed, as for instance the dependence of the enhancement on the distance between the vibrating unit and the metallic surface, but also the possibility to achieve stability, reproducibility and also reusability of the substrate itself. These research activities have been carried out in collaboration with the chemical group of Prof. Taglietti at the InLab laboratory of the Chemical department of University of Pavia, where the enhancing structures have been prepared and partially characterized.

One could argue that different research works have already provided remarkable results on highly performant SERS substrates displaying these characteristics through the nanometric control of the surface morphologies and/or analyte positioning on the surface; however, in these cases the employed synthetic routes foresee sophisticate techniques like molecular beam epitaxy, lithography and so on.
Our aim is instead to prepare substrates, characterised by moderate enhancement factor, that could display reproducibility, stability and reusability through "fast" and economic synthesis methods and, in turn, to study the SERS effect in the most "simple" way in view of potential industrial applications.
For this purpose, we have prepared recyclable active glass chips in which the localized surface plasmon resonance contribution is given by gold nanostars (GNS) grafted on properly functionalized glasses through electrostatic interactions. The GNS with their branches and tips generally provide huge field concentration areas, i.e. *hot spots* and so they are considered as excellent SERS active nanoparticles. Indeed, the approach of exploiting an homogeneous dis-

tribution of nano-objects, characterised by a huge number of tips and edges, on a bulk flat surface has been explored by recent researches through different synthetic routes, in order to obtain solid SERS substrate performing high enhancement factor (EF) [58–60].
The way we have chosen, namely the surface assembly of GNS by electrostatic interaction, is a promising and also really economic way. However, this approach displays the main drawback of mechanical and chemical instability of the nano-objects monolayer covering due to the weak electrostatic bonding. Indeed, the simple handling could provoke the detachment of the GNS, but such instability could be also induced by competitive interactions due to dissolved substances in case of liquid analyte. Moreover, one has to take account of chemical reactivity with the contaminants, like for instance substances that display high affinity with noble metal surface that, in turn, could undermine the properties of the substrates themselves.
According to [61, 62], we have studied the SERS response of GNS monolayer covered by a thin layer of silica in order to achieve chemical stability and protection of the metallic nanostructures from the surrounding.
Moreover, the silica coating, acting as a spacer between the metallic surface and the analyte, has allowed us to follow the enhancement yield at variance of the spacer thickness.
Using this approach we demonstrate that a complete stabilization can be achieved, as well as protection and chemical isolation of nano-objects from the solution, inertness towards mechanical removal and chemical reactivity, conserving a good EF. Moreover, by simply washing with water, these surfaces can be reused, thus acting as a prototype of a low cost, homogeneous, reproducible, robust and reusable SERS substrate.

The satisfying results obtained on these silica-coated samples, lead us to deal with the preparation of robust and stable GNS functionalized chips through the same simple and low cost approach that could be employed for a specific biomedical application, namely the realisation of smart antibacterial surfaces to be employed in the pan-drug resistance bacteria emergency [63].
One of the most used approach to realise antibacterial surfaces is given by the use of silver nanoparticles (Ag NPs) grafted on bulk surfaces: in this case the antibacterial activity is based on the release of Ag^+ cations which display intrinsic antimicrobial features with a wide range of action and limited possibilities of the generation of resistant strains [64–67]. Alternatively, different kinds of biocides can be used, by loading, embedding or grafting them to almost every kind of surface. However, the general issue of biocidal releasing surfaces which is always present, is that these surfaces tend to lose their efficiency as the antibacterial substances are released. When the quantity of active molecules released becomes lower than the minimum inhibitory concentration (MIC), coatings will lose their antibacterial properties [68].
Anyway, a completely different approach could be exploited by using noble

metal nanoparticles, namely the hyperthermia generated by photo-thermal effects strictly related to their localized surface plasmon resonance (LSPR) absorption [69]. As for instance, Au anisotropic nano-objects like GNS, marked by two or more LSPRs, could produce hyperthermia in their surroundings as a result of thermal relaxation after laser irradiation and this generated overheating could be exploited to efficiently kill bacteria. This approach is especially fruitful when the LSPRs fall in the near-IR *biological window*, i.e. between 750 and 950 nm, where biological fluids and tissues are semi-transparent. Thus, a possible application for this strategy could be the treatment of infections through subcutaneous devices coated with this type of nanomaterials. At this regard, the chemical group with which we collaborate, started to investigate this strategy using self assembled monolayers (SAM) of GNS grafted on bulk glass surfaces [70] or silver nanoplates [71, 72] and also by exploiting the silica-coated procedure, previously described, adding a further layer made of Ag NPs: as already described, the silica coating was used to increase the stability of the GNS layers, avoiding contact with biomolecules and, in turn, the contamination of the active metal layer, while the combination of the photo-switchable activity of GNS with the sustained biocidal release of silver ions allowed to realize surfaces on which both planktonic and surface attached bacteria could be efficiently killed [73].

However, another possible strategy to achieve these goals is to combine antimicrobial functions with surfaces having anti-adhesive properties [68]; indeed, it is clear that strongly hydrophilic surfaces could almost completely avoid the adhesion of proteins and bacteria by forming a hydration layer [74] and, at the same time, super-hydrophobicity of surfaces was widely described as a tool that can be exploited for the same task [75]. The adhesion of bacteria is a very important issue, indeed they are able to attach to various surfaces and to multiply forming dense aggregates with a thickness ranging from few nanometers to many centimetres; thus, the capability to avoid their initial adhesion may represent a true advantage in avoiding bacteria colonization and biofilm formation.

On this matter, the feasibility of devices that could join the anti-adhesive functions with photo-thermal antibacterial action using the previously described simple and efficient self assembled monolayers (SAM) approach has been investigated. In particular, the photo-thermal activity of GNS grafted on bulk glass surfaces and the anti-adhesive properties given by thiols coating have been exploited; indeed, the passivation with selected thiols imparts strongly hydrophilic and hydrophobic features to the substrate surfaces and it also improves surface stability. This further thiol functionalization has been achieved without loosing in efficiency of the photo-thermally generated hyperthermia, essential to kill bacteria.

In this work, SERS spectroscopy has been used as an analytical technique. Indeed, we have exploited its high sensitivity detection in order to verify the uniformity of the thiol coating and also to determine the best concentration

of thiol solution in order to obtain a monolayer of covering. Moreover, SERS inspection has given the possibility to test and verify the stability of the functionalization after photo-thermal treatment.

The experimental details concerning the research works presented in this Chapter as well as of those illustrated in the following Chapters are briefly reported in Appendix (D).

3.1 Silica-coated GNS grafted SERS-active substrates

3.1.1 Samples

As already introduced, SERS bulk glass substrates have been prepared by a proper functionalization with a GNS monolayer covering; moreover, they have been stabilized with a further thin silica layer grown on the GNS monolayer. The logical sketch of the procedure used to obtain the substrates is reported in Figure (3.1).
The microscopy cover glass slides, properly cleaned and washed, have been used as base support. They have been coated whit a SAM of an amine bearing alcoxysilane, in this case aminopropiltrimethoxysilane (APTES), that provides the presence of positively charged ammonium groups on the glass surface. After the silanization with APTES, the substrates have been immersed in a colloidal solution of GNS which are negatively charged; thus, the electrostatic interaction between the APTES layer and the GNS provides the formation of a uniform monolayer of Au nanostars that acts as SERS-active substrate. Subsequently, these samples have been immersed in a (3-mercaptopropyl)trimetoxysilane (MPTS) ethanol solution and, after been properly washed and dried, they have been dipped in a sodium silicate solution in order to induce the silica deposition. Indeed, the thiol function of MPTS binds the gold surface, leaving the $Si(OCH_3)_3$ moieties pointing outside and exposed to the solution; thus, these groups guide the reaction with sodium metasilicate to form a thin layer of SiO_2 on the nanoparticles layer. In particular, it has been demonstrated [76–78] that this procedure leads to the formation of a silica layer with a rate of about 1 nm per hour of immersion; thus, in order to obtain different thicknesses, two different immersion times have been used, namely one hour to obtain 1 nm of silica covering and four hours, producing a thicker layer of about 4 nm. Hence forward, the prepared samples are named as follows: ZERO for the sample without silica coating, ONE and FOUR for the samples covered by a silica thickness of 1 and 4 nm, respectively.
The complete preparation procedure is described in detailed in Appendix (A.1.2).
The formation of the silica covering has been immediately proved by undergoing the ONE and FOUR samples to an ultrasound treatment of 5 min and no

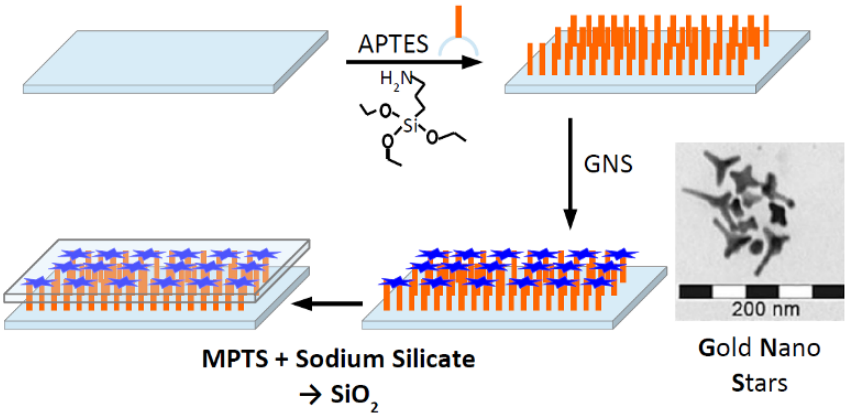

Figure 3.1: Schematization of the synthesis route followed to produce silica-protected GNS layer. TEM image of the starting GNS colloidal solution is also reported.

change in colour or appearance has been observed; moreover, even the scratching with a hard tip does not produce any degradation in the appearance of the coated glass, demonstrating that GNS layer is now effectively protected from detachment and mechanical degradation.
The in time stability has been easily verified by looking at the colouring of the samples after four months of storing in air from the preparation; indeed, as shown in Figure (3.2), the silica-coated sample (ONE type) still displays the correct blue colour which is given by the GNS monolayer, while the uncoated sample, the ZERO one, has a completely different colour which gives the information that the GNS have been degraded. This observation is supported by the SEM micrographs reported in Figure (3.3): while the shape of the nanostars is unchanged for the ONE sample, the degradation of the GNS monolayer for the ZERO sample is confirmed by the fact that only rounded objects could be observed on the surface after four months of storing in air.
The success of the overall substrate preparation has been proved by transmis-

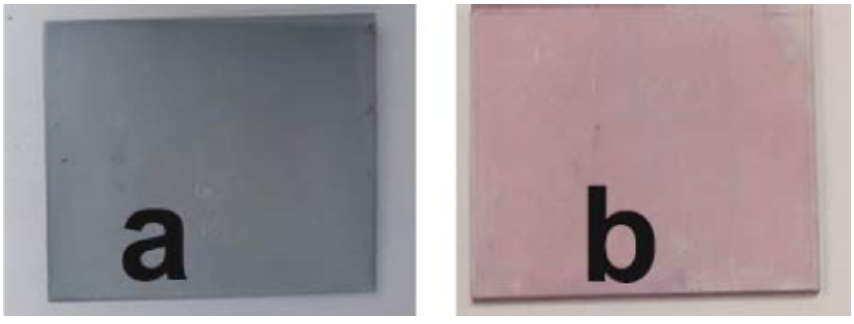

Figure 3.2: ONE (a) and ZERO (b) sample images taken after four months of storing in air.

sion electron microscope (TEM), scanning electron microscope (SEM), UV-Vis absorption and contact angle measures.
The absorbance of typical gold nanostars is reported in Figure (3.4). UV-Vis absorption measures have allowed to select the samples with the correct ab-

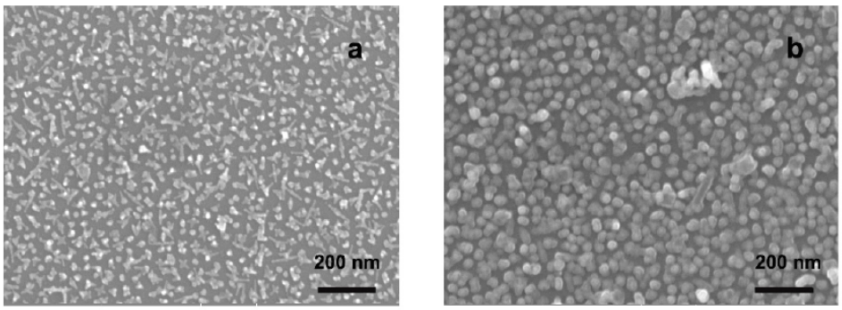

Figure 3.3: SEM micrographs of the ONE (a) and ZERO (b) samples taken after four months of storing in air.

sorption properties, in general a LSPR maximum of the long band peaked at about 800 nm, namely in the range of the "biological window".

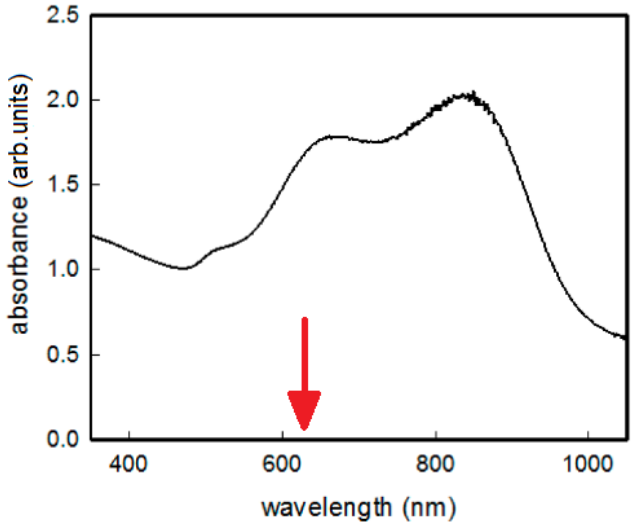

Figure 3.4: A UV-Vis-NIR spectrum of a standard GNS colloidal suspension. The arrow marks the wavelength at which SERS effect has been excited.

3.1.2 SERS results

SERS measurements have allowed us to verify the effect of the silica coating on the chemical inertness of the substrates as well as to evaluate the SERS response of the substrates in terms of homogeneity intra and inter samples and to test the reusability of the functionalized chips. Moreover, we have been able to study the variability of the SERS intensity at variance of the distance between the analyte and the metallic surface through the variation of the silica thickness. This final aspect is not only important from the point of view of the SERS effect itself, but also from the applicative point of view, indeed it is mandatory to understand how the EF scale with the distance from the metallic

surface in presence of a spacer that is used to stabilize the SERS-active medium in view of potential practical applications.

3.1.2.1 Stability, reproducibility and reusability

Stability. In order to verify the substrates inertness imparted by the silica layer, the adopted strategy has consisted in contaminating the samples with an analyte, namely 7-mercapto-4-methylcoumarine (MMC), characterized by a strong interfering signal and which is difficult to remove from the SERS active chips. We have precisely chosen MMC as a standard contaminant because it is characterized by an intense Raman signal, indeed it is a well-known Raman reporter, and also because it displays high affinity with the gold nanostars surfaces through the formation of stable Au-S bonds, thus it can be not only physisorbed, but also chemisorbed on the metal surface. In particular, we have immersed both the ZERO and ONE type samples in an ethanol (EtOH) solution of MMC with different molar concentration, namely 10^{-5}M for ZERO samples and 10^{-3}M for the ONE samples. After 15 min of immersion in the MMC ethanol solution, the SERS substrates have been washed three times through 5 min of immersion in fresh EtOH, in order to remove all the traces of the solution containing MMC and thus, to eliminate all the MMC molecules which have been not bound to sample surfaces. Subsequently, the samples have been gently dried under nitrogen flux and then the SERS spectra have been collected. The results are shown in Figure (3.5), together with the recorded SERS signal of MMC in GNS colloidal solution (black line). As it is possible to observe the SERS spectrum recorded on the ZERO sample, even after the washing cycles and although the contaminant solution is slightly concentrated, displays the characteristic features of the MMC molecule asserting that the substrate is definitively contaminated; while, the SERS spectrum of the ONE sample, for which we have used a more concentrated MMC solution, is completely flat, demonstrating that the silica coating, in addition to mechanical inertness, imparts to the nanostructured substrates a satisfying chemical stability avoiding interferences as well as chemical degradation.

Reproducibility. The homogeneity of the SERS response has been tested by recording the SERS signal of 10^{-5}M solution of another well-known Raman reporter, i.e. Rohdamine 6G (R6G), in four different points of the same sample and comparing the signals obtained from the same type sample, but coming from different preparation batches.
The measure procedure has consisted in the deposition of a 20 μl drop of 10^{-5}M R6G solution on the top of the SERS-active substrate and spreading it by covering the functionalized glass with a blank and clean glass slide of the same dimension in order to obtain an almost homogeneous film of R6G solution between the two glass slides. The so-assembled sample has been then used quickly for Raman analysis.
The main Raman modes of R6G are peaked at around 614, 766, 1178, 1306,

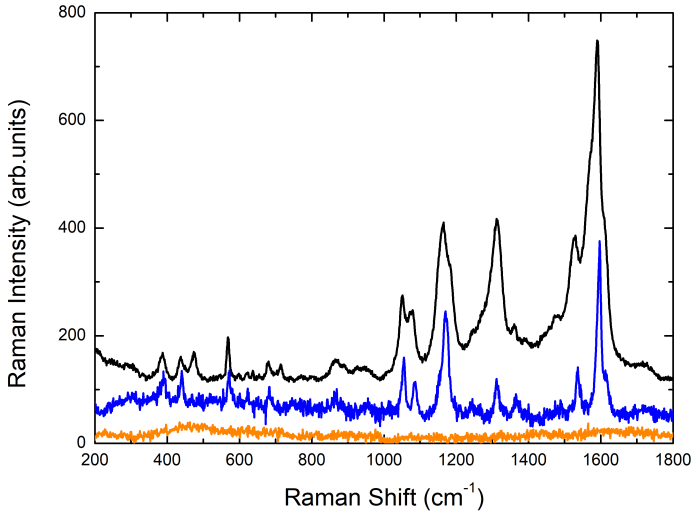

Figure 3.5: SERS spectra from the inertness testing: ZERO sample after immersion in 10^{-5}M MMC ethanol solution and subsequent three cycles washing (blue line) and ONE sample after immersion in 10^{-3}M MMC ethanol solution and subsequent three cycles washing (orange line). These results are shown in comparison with the SERS spectrum of 10^{-3}M MMC in colloidal GNS solution (black line).

1361, 1509, and 1647 cm^{-1}, corresponding to the C-H, C-O-C, and C=C vibrations of aromatic rings [79,80]. As it is possible to observe from Figure (3.6a), these main features are well recognizable in the SERS spectra taken from the ZERO sample in different four points. These reported spectra display almost the same intensity without appreciable changes at variance of the position in the substrate, demonstrating that GNS coating is homogeneous over the whole sample surface. Moreover, the homogeneity and, in turn, the reproducibility of the SERS response is also verified among ZERO samples coming from different preparation batches by the resulting spectra reported in Figure (3.7a). The coating with silica leads to a slightly reduction of the SERS spectrum yield in case of 1 nm thickness (Figure (3.6b)) and a more pronounced intensity reduction for the thicker silica coating (Figure (3.6c)); however the covering does not quench the signal, indeed the main R6G characteristic features are clearly recognizable with some changes in the lineshapes for the C-H bending modes in the range 1000-1200 cm^{-1} and 1400-1600 cm^{-1}, while the features proper of the xanthene stretching modes seem to be unchanged both in shape and relative intensity ratio.
The homogeneity of the GNS and silica covering has been also demonstrated; indeed, the recorded spectra, in different sample points, are all reproducible both for ONE and FOUR type samples (Figure 3.6 (b) and (c)). Also the inter-sample homogeneity has been tested and the results for the FOUR sample are shown in Figure (3.7b). In general, for all the investigated samples the homogeneity in the response has been demonstrated with variation in the intensity

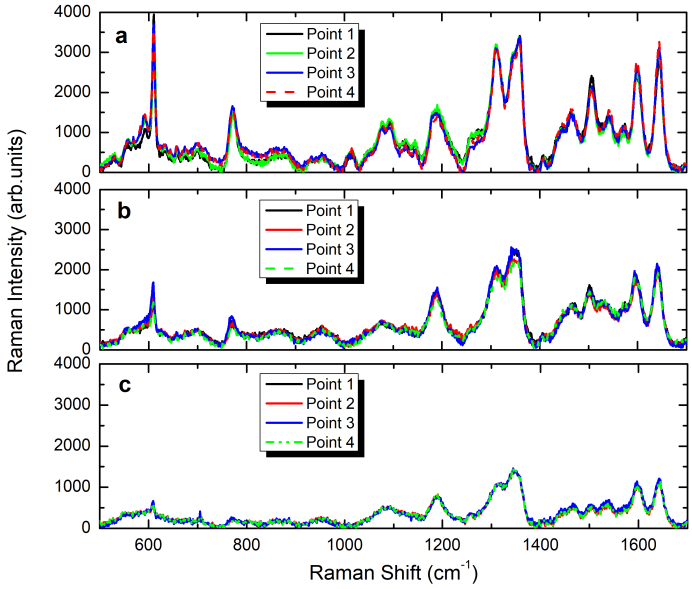

Figure 3.6: Intra-sample reproducibility of SERS spectra of 10^{-5}M solution of R6G for (a) ZERO, (b) ONE and (c) FOUR samples.

yield which is less than 10%, the common limit to assess the reproducibility of the SERS substrate [81]. Indeed, this can be appreciated in Figures (C.1) reported in Appendix (C), where a quantification of the intensity variability has been reported through the D parameter for the three investigated samples, using the spectra reported in Figure (3.6). In particular, this parameter has been calculated for seven R6G modes, namely 614, 766, 1178, 1306, 1361, 1600 and 1647 cm^{-1}, by using the following formula:

$$D = \frac{H_{m,i} - H_i}{H_{m,i}} \tag{3.1}$$

where $H_{m,i}$ is the intensity of each peak (H_i) obtained by averaging the four spectra collected on each sample.

Reusability The research on recyclable SERS-active substrates is very active because substrates that can regenerate their activity after every cycle of measurements are highly desired. In our case, the reusability of the as-prepared SERS-active chips derives directly from the mechanical and chemical inertness previously described; thus, since reusability should be a key feature for all SERS substrates, we have tested it in a very simple way.
A freshly prepared ONE silica-coated sample has been used to measure the SERS spectra of 20 μl drop of a 10^{-4}M solution of R6G using the "sandwich" like configuration described in the previous paragraph. After the measure, the blank glass used as a cover has been removed, and the SERS active substrate has been simply washed under a flow of bi-distilled water and then treated in

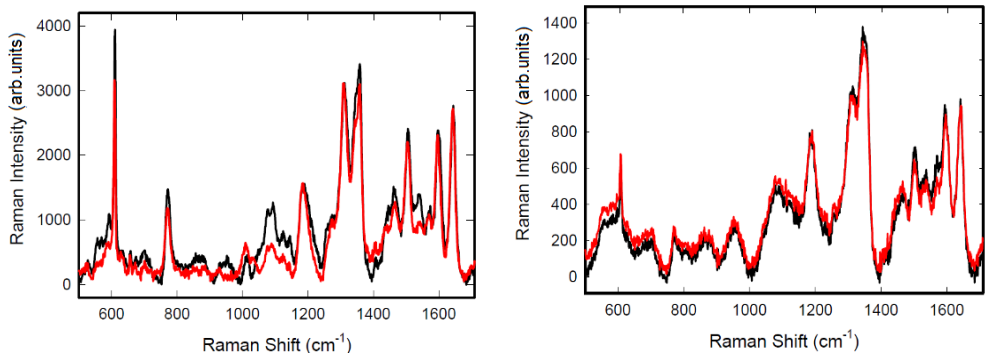

Figure 3.7: SERS spectra of a 10^{-5}M solution of R6G from two different points of: (a) two ZERO samples and (b) two FOUR samples coming from different preparation batches [82].

bi-distilled water with 1 minute of ultrasounds. Subsequently, a SERS spectra of a 20 μl water drop has been taken. After this, the sample has been dried with a clean tissue, and then it has been reused with another aliquot of 10^{-4}M solution of R6G and a second SERS spectra has been taken. The results are reported in Figure (3.8). The first measured spectrum of R6G (red one) displays the characteristic features of the tested Raman reporter, but the spectrum of water (black one), recorded after the washing procedure, is characterised by a lineshape where the R6G spectra fingerprint is absent; the very weak features above 800 cm^{-1} are due to the substrate contribution, as reported in Figure (C.2) in Appendix (C). This observation states again the chemical and mechanical inertness of our silica-coated substrate. Finally, the last recorded spectrum of R6G (blue one), taken after the cleaning procedure, is clearly almost identical to the first one, giving the proof of reusability of our samples.
The described procedure can be repeated several times without any change in behaviour. In literature very interesting papers report on reusability of SERS substrates, but using complex and quite expensive fabrication technologies [83, 84] or more complicated cleaning procedures, requiring optical [85] or chemical processing [86]: in our case both the fabrication and the cleaning procedures are simple and cheaper.

3.1.2.2 SERS response vs silica thickness

The performed silica covering with variable thicknesses has allowed us to evaluate the dependence of the SERS response at variance of the distance between the vibrating units and the metallic surface in presence of a spacer and in comparison with the response of the uncoated ZERO samples, using the same probed solution and an identical scattering geometry.
In particular, the measurements have been carried out in the same "sandwich" like configuration previously described; as regard the molar concentration of the probed solution, we have chosen to start with a 10^{-4}M R6G one because,

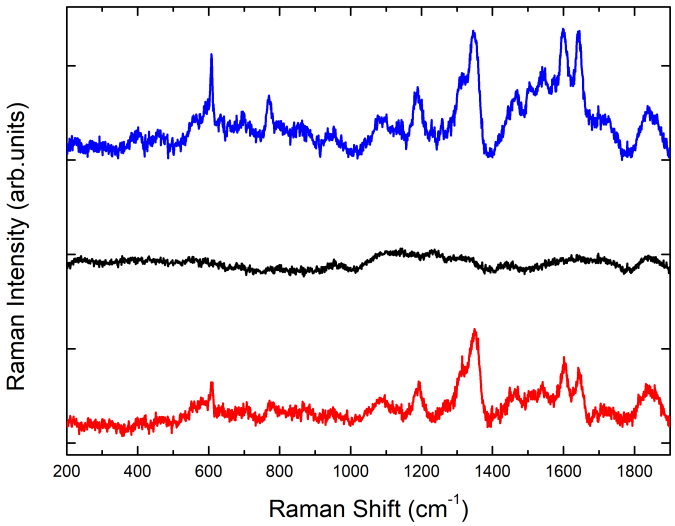

Figure 3.8: Reusability of silica-coated Raman substrates: SERS spectra of R6G 10^{-4}M on new ONE type substrate (red line); spectra of water on the same substrate after washing and sonication (black line); SERS spectra of R6G 10^{-4}M on the same recycled substrate (blue line).

as it has been already observed, the signal intensity decreases significantly with increasing the silica thickness, thus we need to have a molar concentration that guarantees to detect a clear signal which could be easily processed, for all the three investigated samples. However, we have also tested the SERS response of the substrates with a more diluted solution of R6G, namely 10^{-5}M.
The resulting R6G spectra for the ZERO, ONE and FOUR samples are plotted in Figures (3.9a) and (3.10) for the 10^{-4}M and 10^{-5}M solutions, respectively. In order to evaluate the effect of silica thickness on SERS EFs, we have calculated the SERS yield of three specific Raman modes peaked at 614 cm^{-1}, 770 cm^{-1} and 1641 cm^{-1} by performing a best fitting procedure using one or more lorentzian curves as fitting functions; the resulting integrated intensities are plotted for the 10^{-4}M solution in Figure (3.9b) and in the inset of Figure (3.10) for the 10^{-5}M one as a function of the expected thickness of the silica layers, expressed in nm, in the three cases. These thickness values have been considered as the minimum distances from the metal nano-objects at which the vibrational units of the molecule experience the SERS enhancement effect. The line interpolating the reported integrated intensities represents the output of the best fitting procedure using the following function, according to [87]:

$$G_{em}(\nu_s) \sim \left(\frac{r}{r+d}\right)^{10} \tag{3.2}$$

where $G_{em}(\nu_s)$ is the electromagnetic EF of a Raman mode at a given frequency ν_s, r is the radius of the spherical NP and d the distance where a

specific monolayer experiences the confined EM field [88].

The experimental behaviour is well reproduced by a weighted linear combi-

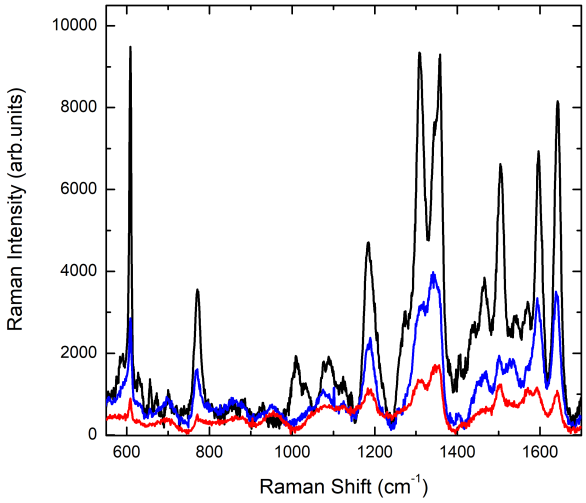

(a)

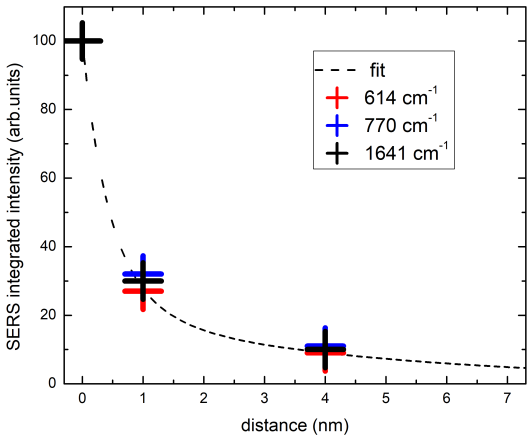

(b)

Figure 3.9: (a) SERS spectra of 10^{-4}M R6G solution recorded on the different sample types: ZERO (black line), ONE (blue line) and FOUR (red line). (b) Dependence of the normalized SERS yield as a function of the silica thickness for the three R6G Raman modes: 614 cm^{-1} (red symbol), 770 cm^{-1} (blue symbol) and 1641 cm^{-1} (black symbol). The dashed line represents the output of the best fitting procedure performed on the 614 cm^{-1} mode, according to Eq. (3.3).

nation of two terms with two values of r, namely

$$G_{em}(\nu_s) = w_1 \left(\frac{r_1}{r_1 + d} \right)^{10} + w_2 \left(\frac{r_2}{r_2 + d} \right)^{10} \tag{3.3}$$

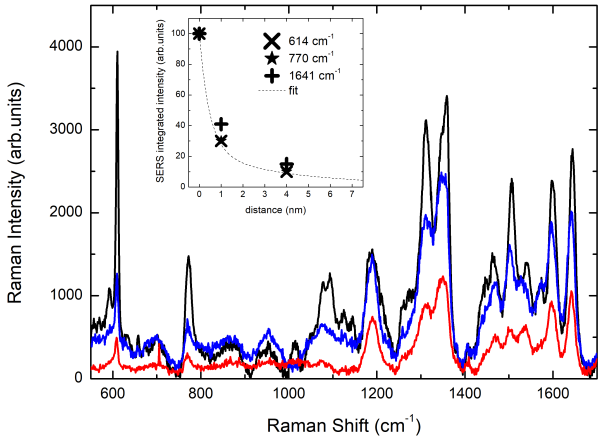

Figure 3.10: SERS spectra of 10^{-5}M R6G solution recorded on the different sample types: ZERO (black line), ONE (blue line) and FOUR (red line). Inset: Dependence of the normalized SERS yield as a function of the silica thickness for the three R6G Raman modes: 614 cm^{-1} ($\times$ symbol), 770 cm^{-1} (star symbol) and 1641 cm^{-1} (cross symbol). The dashed line represents the output of the best fitting procedure performed on the 614 cm^{-1} mode, according to Eq. (3.3) [82].

the first value, r_1, is close to 4 nm while the second one, r_2, is markedly larger, namely ≈ 43 nm. In particular, for the smaller radius term, a weight w_1 which is 4 times greater than w_2 has been used. This best fitting procedure has been used for SERS data from both 10^{-4}M and 10^{-5}M solutions and performed for the 614 cm^{-1} mode.
The value for the smaller radius well agrees with the average curvature of the tips as derived by TEM images. In Figure (3.11), a representative TEM image of a standard GNS colloidal solution is reported: as one can notice, the seed-growth procedure (see Appendix (A.1.1)), followed to synthesize these Au nano-objects, leads to an heterogeneous population mostly dominated by asymmetric branched nanostars, but in which also some spherical objects as well as regular monocrystalline nanostars are present. This heterogeneity reflects in the absorption spectrum (Figure (3.4)). Indeed, the absorption spectrum is characterized by three bands: the dominant LSPR whose maximum can range in the 750-1100 nm interval, is associated to the asymmetric pentatwinned branched objects which are the main component of the suspension, i.e about $40\% - 50\%$ of the total number of nano-objects; the second band, located in the 620–670 nm range, is related to more regular, monocrystalline symmetric 4-branched nanostars which are about $30\% - 40\%$ of total number of objects; the less intense LSPR one closed to 520 nm can be attributed both to the resonance of the spherical cores of nanostars and branched objects or to the presence of spheroidal objects with negligibly developed branches.
As regards the higher value r_2, it could be justified considering it as the mean radius of a sphere containing the whole GNS. Anyway, the greater weight for

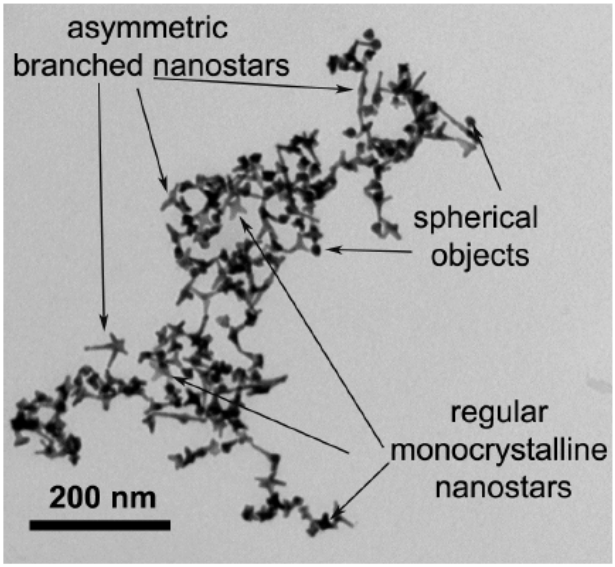

Figure 3.11: A representative TEM image of a standard preparation of GNS colloidal solution [89].

the smaller radius contribution highlights a more efficient SERS enhancement mechanism as expected for numerous sharp tips [90]. The second contribution has been introduced to account for a long-lasting component in SERS enhancement which is not satisfactorily reproduced by considering only a single function (Eq. (3.2)) with a value of r equal to the average curvature of the tips. An active role in sustaining SERS enhancement beyond the rapid decrease that follows from Eq. (3.2), can be played by the presence of silica coating. Indeed some authors [91] observed a persistence of EF at distances even grater than 30 nm and, tentatively, they justified it in terms of collective surface plasmon polaritons spatial spread or penetration depth into the dielectric which are just favoured by the presence of silica as dielectric medium.
Anyway, the observed behaviour points out that only a very thin part of the laser focus volume gives sizeable SERS signal; thus, molecular layers at distances greater than 10 nm from the nano-objects are expected to be SERS silent. Moreover, from the good best fitting results we can make another interesting consideration: indeed, since we have used a pure EM contribution to perform the data interpolation, this gives the evidence that the chemical contribution to the enhancement seems to be negligible even for ZERO samples. Finally, from these results we have derived a total average EF factor equal to $\sim 9 \times 10^5$ for the ZERO samples which is in good agreement with average EF values reported in Le Ru et al [56]. The methodology followed to evaluate the EF is reported in the next section.

3.1.2.3 Estimation of the enhancement factor

The good quality of a SERS substrate firstly derives from the value of the enhancement factor. However, as already introduced in Chapter 2, the estimation of such value is anything but easy.
Thus, in this paragraph I will illustrate at first the procedure we have followed to estimate the enhancement factor and subsequently some critical issues that in our opinion derive from the monitoring of the SERS EF on dried drops, a current common procedure presented in literature.

The SERS enhancement factor has been estimated by using the general equation (2.26) introduced in Chapter 2 according to Le Ru et al. [56], that we recall here:

$$SSEF = \frac{I_{SERS}/N_{SERS}}{I_{RS}/N_{RS}} \tag{3.4}$$

where I_{RS} and I_{SERS} are the intensities of Raman and SERS peak of the same vibrational mode, while N_{RS} and N_{SERS} are the numbers of R6G molecules participating at the Raman and SERS phenomena, respectively. Although this formula is so general that could lead to incorrect estimation of the EF, as already described in the previous Chapter and introduced by Le Ru et al. [56], provided that a detailed and honest description of how the measures have been carried on, namely describing the scattering geometry and reporting the measures parameters, also this expression (Eq.(3.4)) allows to obtain a realistic estimation of the average enhancement factor. Thus, in the following the procedure that we have used is described in detailed.

Since the comparison between Raman and SERS signals is usually difficult, the first requirement is to be able to carefully control the experimental conditions, thus, for this reason, we have used the same scattering geometry, performing in both cases a "sandwich"-like configuration.
The SERS measures have been carried out by depositing a 20 μl drop of 10^{-4}M R6G solution onto a ZERO substrate, while for Raman measures a drop of the same amount, but of a more concentrated R6G solution (10^{-3}M) has been deposited onto a blank glass slide. In both cases the drop has been spread using a blank glass slide, recovering the "sandwich" configuration and thus allowing us to control the total volume of the drops.
However, this approach imposes constrains in the choice of R6G concentrations used to estimate EF. Indeed, we have chosen 10^{-3}M for Raman experiments because this is the minimum value to obtain a sizeable signal in normal Raman experiments; on the other hand, we have not used the same concentration in SERS to avoid contribution in SERS scattering from normal Raman process and we have selected precisely 10^{-4}M to experience SERS in a similar concentration range, avoiding SERS effects, sometimes unstable, from local hot spots, since we are interested in the average and stable SERS response.
In view of the described geometry, the expression from the enhancement factor

that we have operatively used is then given by:

$$SSEF = \frac{I_{SERS}}{I_{RS}} \frac{c_{RS} H_{RS}}{c_{SERS} H_{SERS}} \tag{3.5}$$

where we have put $N_{SERS} = c_{SERS} H_{SERS}$ and $N_{RS} = c_{RS} H_{RS}$.
In particular we have estimated the number of molecules contributing to the recorded signals as the product between the molar concentration of the drop and the scattering volume $V_{scat} = H_{scatt} \times A_{scatt}$; since the geometry of the experiment is the same for both SERS and Raman measures, the area of the scattering volume, covered by the laser spot, is the same and it does not enter in Eq. (3.5). Thus, the term (N_{RS}/N_{SERS}) is strongly affected by the differences in the height of scattering volumes, other than the factor 10 in concentration ratio.
As regards normal Raman measures, all the volume between the two microscopy cover glass slides is detected by the beam waist of the laser, as depicted in the left side of Figure (3.12). Through previous analyses, performed on a drop of 10^{-3}M Rhodamine solution diluted in water, we have estimated H_{RS} to be about 18 μm.
On the other hand, we have just demonstrated that in the present case the SERS signal decreases with distance according to Eq. (3.2) that means it practically disappears at distances longer than 10 nm (Figure (3.12), right side).
More precisely, the ratio between the two heights should be 18000 nm/10 nm = 1.8×10^3. In turn, considering the ratio in concentration, we have obtained for (N_{RS}/N_{SERS}) a value of 1.8×10^4.
From the best-fitting procedure performed on the peak at 614 cm^{-1} using a

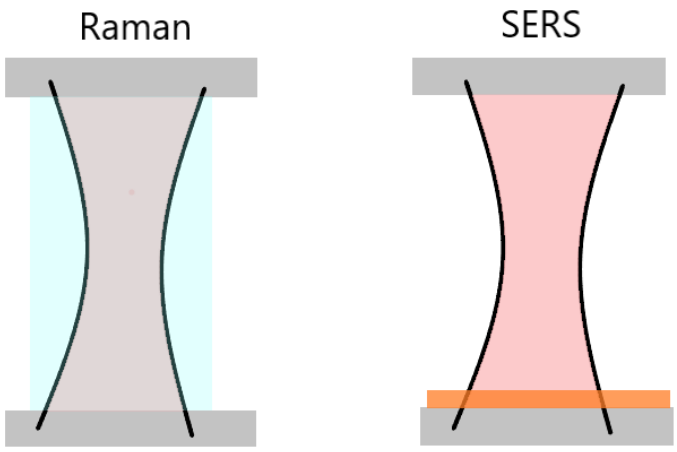

Figure 3.12: Scattering volume in case of Raman measures, highlighted in light blue (left side), and in case of SERS measures, highlighted in orange (right side).

single Lorentian function (Figure (3.13)) for both the SERS response of the

ZERO sample and the normal Raman response, we have obtained a value of the ratio (I_{SERS}/I_{RS}) equal to ~ 50. Thus, combining all the obtained results we have found out a total EF factor equal to $\sim 9 \times 10^5$ for the ZERO samples. We underline that this value is in good agreement with the ones reported in [56].

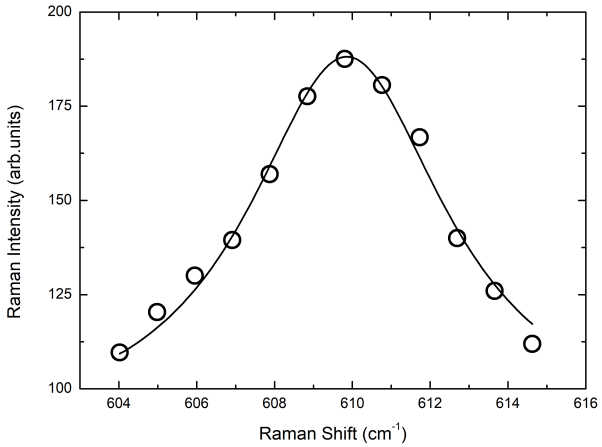

Figure 3.13: Example of the best-fitting procedure performed with a single Lorentzian curve (solid line) on the normal Raman peak (open circle) at 614 cm^{-1} of Rhodamine 6G, collected in the "sandwich" configuration for a drop of 10^{-3}M R6G solution spread onto a blank glass slide.

In literature, much higher EF values can be found. In this regard, it nevertheless necessary to make some considerations, as recalled at the beginning of this paragraph.
At first, if one is unaware in doing SERS or SERRS (Surface Enhanced Resonant Raman Spectroscopy), the correct EF estimation is implicitly affected. Indeed, if the radiation conditions are resonant to the analyte or to the metal/analyte complex, one could gain really high EF values. Thus, before estimating it, it is mandatory to verify this property.
Once this is done, the second aspect to be faced is the way in which the SERS measure is performed. Indeed, as previously introduced, if we consider recent results in literature, it is easy to find research works in which the study of the SERS response, in particular, from solid planar substrates, is carried out on dried drops of the investigated analyte solution, as reported for example in [48, 92, 93].
A simple question has come to us many times: is it possible that the SERS signal of dried droplet molecules could hide a not negligible contribution from the normal Raman effect of the analyte?
Thus, we have performed a simple, but clarifying experiment. We have deposited a 20 μl drop of 10^{-6}M R6G solution both on a blank glass slide and

on a ZERO substrate and let it dry. We have precisely chosen a molar concentration equal to 10^{-6} since with this concentration, the normal Raman signal of R6G is not detectable in liquid solution.
In Figure (3.14), the Raman yield profile of dried R6G molecules is reported as a function of the laser position for both the blank glass slide and SERS-active substrate. In particular, the reported data are the integrated intensities of the 614 cm^{-1} mode, obtained from the best fitting procedure performed by using a single Lorentzian function. For the dried drop on the blank glass slide, since as a consequence of the coffee ring effect, the R6G molecules have been deposited in the outer ring of the drop, we have recorded 20 spectra on a single linear scan performed at the turn of the ring. On the other hand, the functionalization of the SERS substrate leads to a different rearrangement of the dried molecules, namely the coffee ring effect is annulled and the molecules cover almost the entire area of the dried drop. Thus, we have performed three linear scans, in the edge, in the centre and in the middle of the dried drop; during each single scan 20 spectra have been collected.

As it is possible to observe, comparable values of R6G integrated intensities can be seen between Raman and SERS response.
This simple experiment has convinced us, at first, of the solidity of our wet approach, put in place with the previously described "sandwich"-like configuration, since it allows us to safely exclude possible Raman contribution to our SERS spectra; secondly, that when a dried approach is employed in the evaluation of the SERS response of a substrate, also the evaluation of the normal Raman contribution should be done in order to evaluate a proper estimation of the enhancement factor.
Thus, a clear description on how the experiment has been performed and if the resonant SERS effect as well as normal Raman one in dried approach could affect the performed measures, should be given.

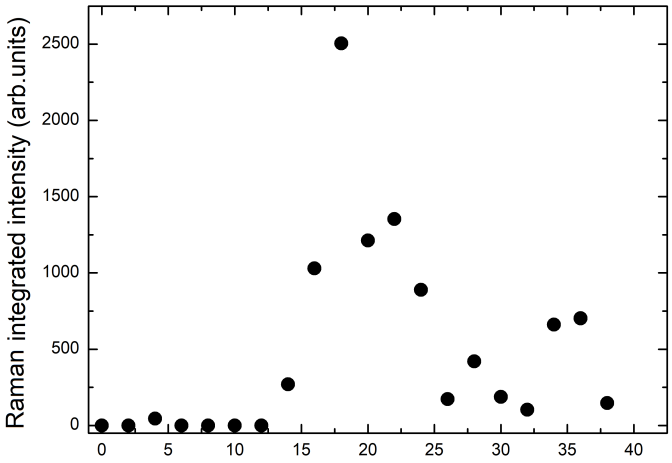

(a)

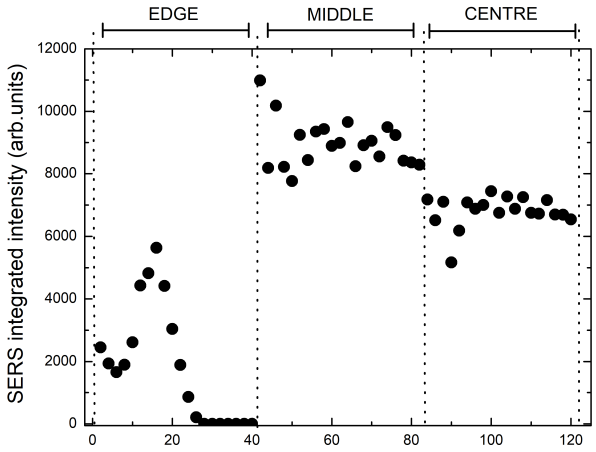

(b)

Figure 3.14: Profiles of the integrated intensities obtained by a best-fitting procedure performed with a single Lorentzian curve on the 614 cm^{-1} R6G mode, of dried drops deposited on (a) a blank glass slide and (b) ZERO sample.

3.2 SERS active-chips for biomedical purposes

3.2.1 Samples

The procedure followed to prepare these samples is similar to the one used to prepare the silica-coated functionalized glasses, namely the self-assembled monolayer approach.
As already described, microscopy cover glass slides, used as base support, have been properly cleaned and washed. Subsequently, they have been coated with a SAM of APTES. Inducing a variation of pH through acid values (5.5), the amino groups of APTES-terminated bulk glass samples have been protonated, thus their immersion in the GNS suspension yielded the self assembly of a GNS monolayer on glass samples, due to electrostatic interactions between the positively charged ammonium and negatively charged GNS. The formation of the GNS SAM has given the characteristic blue colour to the glass slides.
After that, the as-prepared samples have been functionalized with different thiols coating by simply immersing them in a thiol solution of different molar concentrations, namely from 10^{-3}M and 10^{-7}M. The time of immersion has not affected the features of the coated monolayer. The selected thiols are 4-Mercaptophenylboronic acid (4-MPBA), 4-Mercaptobenzoic acid (4-MBA), 7-mercapto-4-methylcoumarine (MMC) and 1-dodecanthiol (12C-SH). Finally, after washing and properly drying, the samples has been ready to be stored and characterised. The detailed description of the preparation procedure is reported in Appendix (A.1.3), while a schematization of such procedure is reported in Figure (3.15). Also in this case the success of the preparation has

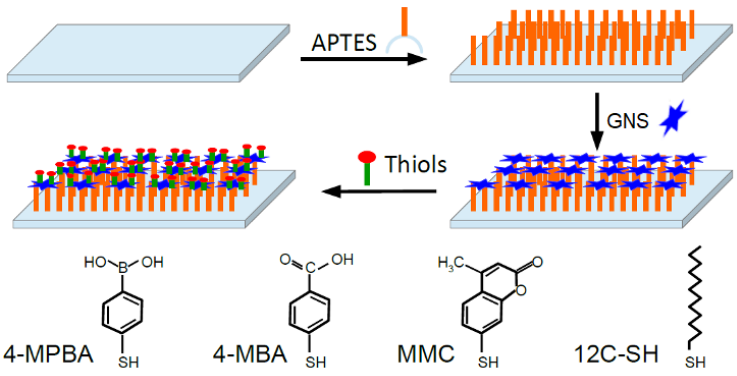

Figure 3.15: Schematisation of thiol-coated GNS substrates procedure together with the molecular representation of the used thiols.

been verified through SEM, TEM, UV-Vis absorption and contact angle measures. Moreover, photo-thermal measurements have been carried out in order to verify the hyperthermia activity of these substrates; while, in order to prove the antibacterial activity due to the photo-thermal effect, thermal microbicidal tests have been performed on Gram+ and Gram- planktonic bacteria specimens, namely *Staphylococcus aureus* ATCC 6538 (Gram+) and *Escherichia*

coli ATCC 10356 (Gram-). To the sake of completeness, these results are presented in a dedicated Section (see (3.2.3)).

3.2.2 SERS results

We have characterised through SERS technique only the samples functionalized with 4-MBA, MMC and 4-MPBA thiols since 12C-SH has not displayed Raman features to be easily exploited with SERS.
The SERS inspection has allowed us, at first, to determine the best molar concentration of thiol solution in order to obtain a monolayer of covering. Indeed, we have recorded SERS spectra in different points of the samples which have been functionalized with different thiol concentration, as described in the previous section.
As an explanatory case, Figure (3.16) reports the SERS spectra collected form different samples prepared starting from different molar concentrations of MMC solution, in particular ranging from 10^{-7} to 10^{-3}.

It is possible to notice that in case of 10^{-7}M concentration, two different

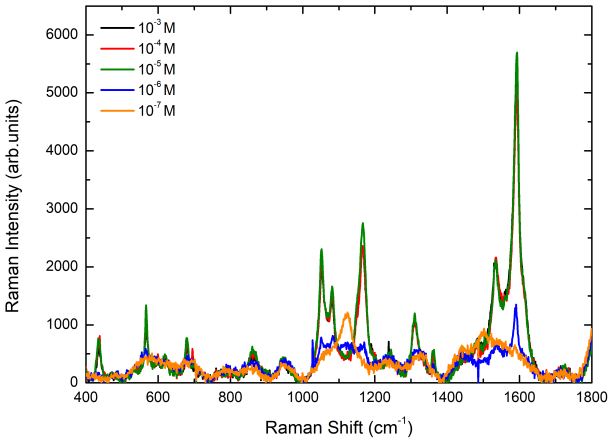

Figure 3.16: SERS spectra of GNS layers coated with MMC taken on different samples prepared starting from coating solution with different concentrations: 10^{-7}, 10^{-6}, 10^{-5} (green line), 10^{-4} (blue line) and 10^{-3} (red line).

peaks centred at about 1100 and 1500 cm^{-1} are clearly visible: these modes are characteristic of the GNS monolayer without further thiol functionalization (see Figure (C.3) in Appendix (C)). The presence of this modes indicates an inhomogeneous thiol covering of the SERS-active layer.
The variability of the SERS yield as a function of the molar concentration is better highlighted in Figure (3.17) where the integrated intensity of the peak centred at about 1600 cm^{-1} resulting from a best fitting procedure, using a single Lorentzian curve, is reported as a function of MMC solution concentration. As it is possible to observe the integrated intensity of this mode increases

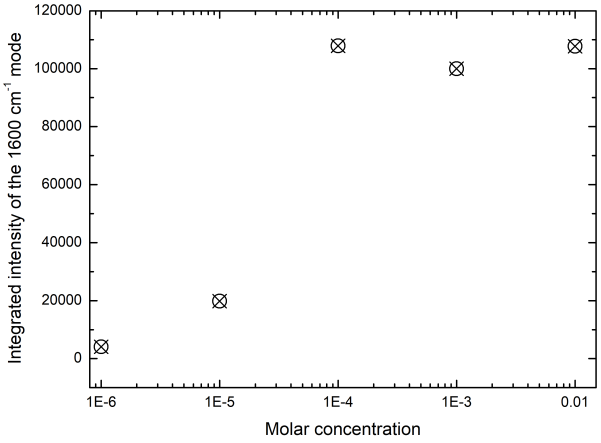

Figure 3.17: SERS integrated intensity of the peak centred at about 1600 cm^{-1} for the MMC thiol at variance of molar concentration of thiol solution used to functionalize the substrates surface.

till the corresponding concentration value of 10^{-5}M and then, for higher concentrations, it remains almost constant; thus, this missed change in the SERS yield points out that the conditions used for a standard coating procedure, namely 40 ml of 10^{-5}M solutions of thiols, ensure the formation of a monolayer of thiols fully covering the available surface of GNS and that the increase of the thiol concentration does not produce any corresponding increase of thiol binding.
We have observed a same behaviour for the other investigated thiols. Thus, we have reported the SERS spectra proper of samples functionalized with 4-MPBA (Figure (3.18a)) and 4-MBA (Figure (3.18b)) starting from two different thiols concentrations, namely 10^{-3} and 10^{-5}.

After having stated 10^{-5}M as the best concentration of thiols solution, we have characterised the samples in terms of homogeneity of the thiol coating. In particular, we have collected SERS spectra in different points of the same sample and also on samples coming from different preparation batches. The collected SERS spectra for the 4-MBA thiol coating are reported in Figure (3.19), as an example; the homogeneity in the response for the other samples, namely the ones functionalized with MMC and 4-MPBA, are reported in Appendix (C) (Figures (C.4) and (C.5)). In all the reported cases, we can appreciate slight differences in the SERS yield which are less than 10%, i.e. the marker of highly reproducible SERS substrates [81]. In particular, this applies to the signals in the region between 1000 and 1800 cm^{-1} which are due to the stretching modes inside the benzene ring for 4-MBA [94] and 4-MPBA [95] and also to the in plain C=C ones in the lactone ring in case of MMC [96].

Finally, SERS measures have allowed us to test the stability of the thiol

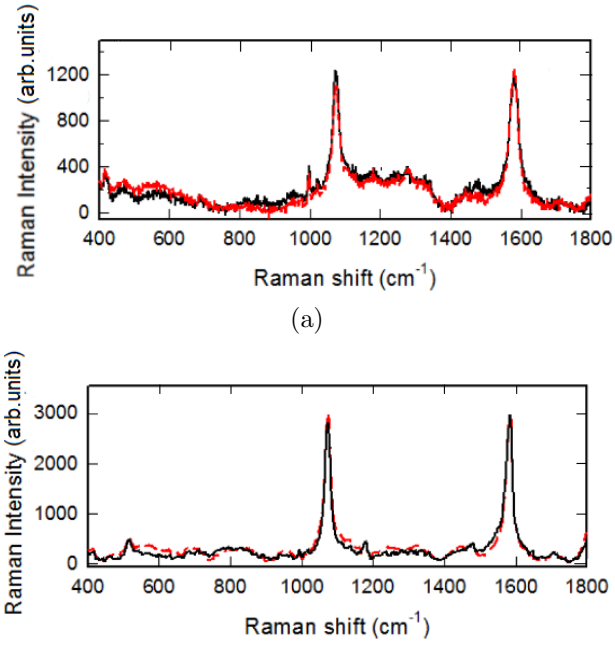

Figure 3.18: SERS spectra of GNS layers coated with (a) 4-MPBA and (b) 4-MBA taken on two different samples prepared using coating solution with different concentrations: 10^{-5} (black line) and 10^{-3} (red dashed line) [89].

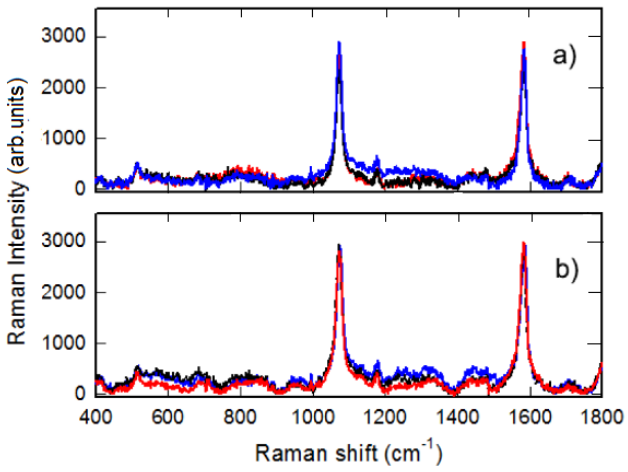

Figure 3.19: SERS spectra of GNS layers coated with 4-MBA taken on (a) three samples coming from different preparation batches and on (b) three points of the same sample [89].

coating after 808 nm laser irradiation during the photo-thermal treatment. In particular, we have recorded SERS spectra after one cycle and three cycles of 30 min of irradiation using the higher irradiance value (0.264 W/cm^2), and comparing them with the spectra taken before irradiation. This has been repeated three times for the samples coated with 4-MBA and 4-MPBA. As it is

possible to observe in Figures (3.20a and 3.20b), no changes in SERS patterns and intensities can be perceivable. These results are also validate from measurements on LSPR features of the samples and their contact angles values (see Appendix (D)). All these findings suggest that laser irradiation and the consequent hyperthermia have not produced any change in layers features.

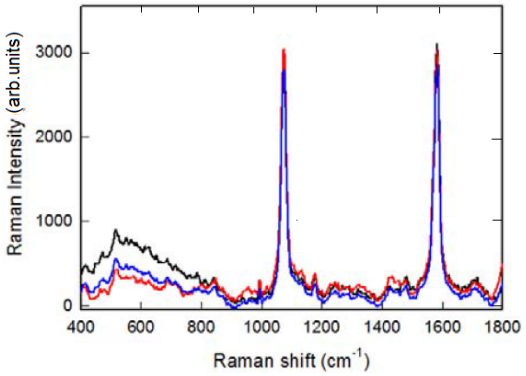

(a)

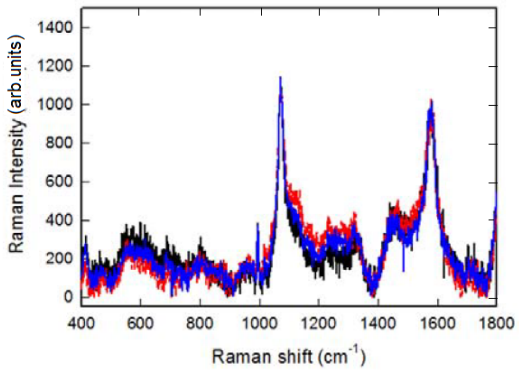

(b)

Figure 3.20: SERS spectra of GNS layers coated with (a) 4-MBA and (b) 4-MPBA taken on the same samples before (red line), after one cycle (black line) and after three cycles (blue line) of 30 min of irradiation at 808 nm with irradiance 0.264 W/cm^2 [89].

3.2.3 Photo-thermal and antibacterial activity

Since the principle aim of this research work is to demonstrate the feasibility to produce systems that display anti-adhesive functions with photo-termal antibacterial activity, it is important to report results at this regard, although my contribution concerns only the SERS investigation.
As regard the photo-thermal properties of the GNS used in this work, they have been already studied on their colloidal suspensions or when grafted on a SAM obtained with MPTS or APTES on glass [70, 73, 97]. Here the photo-thermal behavior has been tested for the described samples, coming from the same preparation sets described and characterized so far, for the coatings with 4-MBA, 4-MPBA and 12C-SH, which are the thiols giving the most interesting wettability values (i.e. the most hydrophilic and hydrophobic: the samples coated with MMC, having an intermediate contact angle value, have not been investigated at this point). In particular, the photo-thermal measures have been carried on by irradiating the slides with a continuous laser sources at 808 nm, using increasing power ranging from 39 to 207 mW (laser spot area = 0.785 cm^2, irradiances 0.049–0.264W/cm^2). The temperature reached on the samples has been measured as a function of irradiation time using a thermocamera. The same steep ascending-plateau profiles have been observed for all samples at every irradiance, as reported in Figure (3.21a). It is interesting to notice from Figure (3.21b), reporting the relation between applied power and ΔT obtained on changing the thiol coating, that the slopes of the lines interpolating the experimental data are almost the same for all samples. Thus, this means that the 808 nm laser irradiation of the GNS monolayers gives the same efficient photo-thermal conversion independently from the type of the thiol coating, as expected from the observation that thiol coatings have produced only negligible variations in the position and intensities of LSPR absorptions, which are the only source of the photo-thermal efficiency. As previously described, the stability of the thiol coating after photo-thermal treatment has been proved through SERS measures.
In order to test the effects of the photo-thermal induced hyperthermia of our substrates, the antibacterial activity has been investigated on *Staphylococcus aureus* and *Escherichia coli* as representative Gram + and Gram - "planktonic" bacterial specimens (namely, fluctuating and not yet organized in biofilm), respectively.
The microorganisms have been grown overnight in Tryptone Soya Broth at 37 °C. Washed cells have been resuspended in Dulbecco's phosphate-buffered saline (PBS) and optical density (OD) has been adjusted to 0.2 at 650 nm wavelength which corresponds approximately to 1×10^8 colony forming units (CFU)/ml. In order to perform photo-thermal measurements, one functionalized slide has been cut in four sections of about 10 mm $\times$ 10 mm in order to be almost completely irradiated by the laser and a volume of 0.02 ml of bacterial suspension has been deposited on two sections. For each pair of functionalized glasses, one has been irradiated for 30 min whereas the other has not been ir-

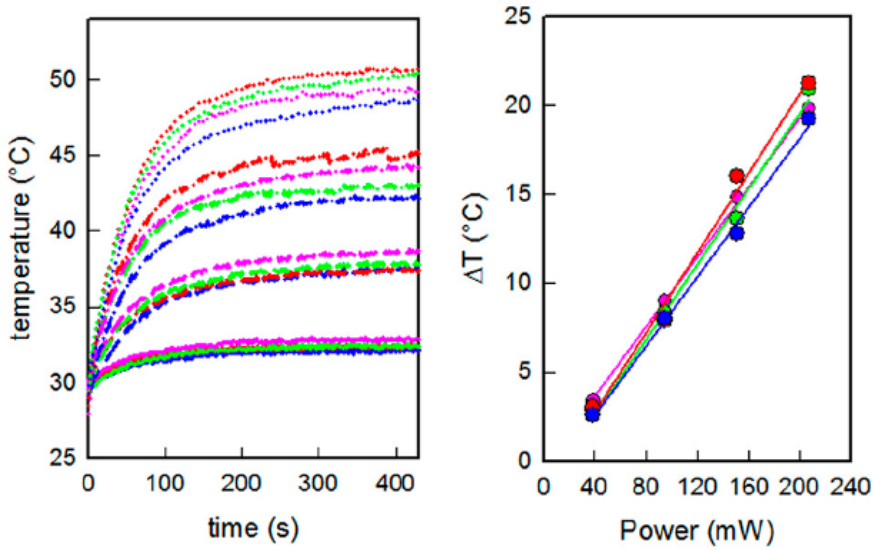

(a) (b)

Figure 3.21: (a) Temperature versus time thermograms recorded for different samples under laser irradiation at 808 nm with different power samples: 39 mW (solid lines), 95 mW (long dashed lines), 151 mW (dash-dot-dash lines) and 207 mW (dotted lines); (b) maximum temperature reached by each sample as a function of the laser power.
Uncoated GNS layers (blue lines/symbols), 4-MBA coated GNS layers (red lines/symbols), 4-MPBA coated GNS layers (green lines/symbols) and 12C-SH coated GNS layers (pink lines/symbols) [89].

radiated. After this time, the glass section covered with bacterial suspensions has been suspended in 1 ml of sterile water, gently shaken and then it has been suitable diluted in three different tubes: 1:100, 1:10000 and 1:100000. From each tube, 1 ml of suspension has been taken and then cultured on Tryptone Soya Agar to count viable cells.
The parameter that can assert the success of the antibacterial activity is the decimal-log reduction rate, i.e., the "thermal microbicidal effect" (ME_T) which has been calculated with the following formula:

$$ME_T = \log N_C - \log N_T \tag{3.6}$$

where N_C is the number of CFU/ml developed after the contact with a not irradiated functionalized glass sample, taken as a control, while N_T is the number of CFU/ml found in a sample kept in identical conditions but after exposure to laser irradiation.
The so calculated ME_T values have to be ascribed, for certain, only to the hyperthermia given by the photo-thermal effect, because any other influence from the features of the substrate surfaces in the absence of irradiation has been considered in the control count.
Moreover, a comparative "microbicidal effect" (ME) in the absence of irradiation has been performed comparing the effect of all functionalized samples with the effect obtained with a "blank" glass slide, using an identical procedure and

the same contact time. The obtained results have shown very low values (well below 1) in all cases which means lower antibacterial activity.
Finally, it is important to underline that the only effect of laser irradiation, namely in the absence of plasmonic objects, has no influence in killing bacteria, as already described [70–73].
The obtained ME_T values for uncoated GNS as well as for samples coated with a monolayer of 4-MBA, 4-MPBA and 12C-SH, are reported in Table (3.1). These results clearly demonstrate that a strong microbicidal effect has been obtained in all the samples for both the two bacteria specimens. Indeed, in all cases the ME_T is higher than 4 which corresponds to the elimination of at least 99.99% of bacteria and, in particular, in the case of *E. coli*, no more bacteria has been found after laser irradiation.
It is possible to conclude that the laser treatment has been able to eliminate almost completely the two investigated strains of planktonic bacteria cells after 30 min of irradiation at 0.264 W/cm^2, namely an irradiance value which is well below the safe limit for the exposure of skin [98], and at a wavelength that can be used in-vivo. Although, the behaviour of these surfaces in complex physiological environments as well as their effect on healthy cells needs further investigation, the stability in physiological media and safety towards healthy cells have been already assessed in previous papers for colloidal GNS coated with thiols like 7-Mercapto-4-methylcoumarin and PEG-thiols [99, 100].
A final consideration has to be done. Indeed, one can notice that the uncoated GNS layers, namely the samples which have been not treated with the thiols, are already extremely active in killing planktonic bacteria with their photo-thermal features. However, their practical use has been almost totally hindered by their instability, while, on the other side, the coating with thiols impart stability without altering photo-thermal efficiency in bacteria killing, as it has also been proved through the SERS inspection.

Sample	*Staphylococcus aureus*	*Escherichia coli*
Uncoated GNS	> 5	> 5
4-MBA	4.5(0.5)	> 5
4-MPBA	4.5(0.5)	> 5
12C-SH	> 5	> 5

Table 3.1: Thermal microbicidal effects measured for GNS layer coating with different thiols. The reported values are the average of at least three experiments. The uncertainties are given in parenthesis.

Chapter 4

Zinc ferrite nanoparticles: A Raman study

Zinc ferrite is a very popular and intriguing material which has been deeply investigated in its nanometric form for its interesting physical and chemical properties. Indeed, $ZnFe_2O_4$ (ZFO), as in general the whole class of nanostructured spinel ferrites (MFe_2O_4), exhibits a peculiar mixing of high-quality functional properties and so it is widely used in different applicative fields [101–104].
In particular, ZFO displays a high chemical stability and intriguing magnetic, thermal, electrical and mechanical properties that joint to its earth abundance, easy synthesis way as well as non-toxicity of the Zn ions, make it suitable to be used in information storage [105], ferrofluids [106], catalysis [107, 108], and also biomedical applications, as for instance, in either diagnosis or therapy, as magnetic resonance imaging (MRI) contrast agents and for radiofrequency magnetic hyperthermia (MH) [109, 110]. More recently, these nanostructured systems have been recognized suitable in engineering theranostic systems in which both therapeutics and diagnostics are integrated in the same nanostructure in order to simultaneously exploit detection and treatment of diseases [111].
These functional properties could be controlled by tuning composition, size, as well as synthesis methods; thus it is mandatory to well understand their crystal chemistry and structure at variance of these parameters.

The spinel ferrite systems, depending on the coordination of cationic sites, can occur in three different spinel types, namely direct, inverse and disordered, generally represented by the following formula $(Me_{1-x}Fe_x)^{2+}\,[Me_xFe_{2-x}]^{3+}\,O_4$ where the round and square brackets denote sites of tetrahedral (A) and octahedral [B] coordination, respectively, while x represents the inversion degree, defined as the fraction of (A) sites occupied by Fe^{3+} ions. Thus, a spinel ferrite system contains two Fe^{3+} cations and a single divalent one. A completely inverse spinel structure occurs when the trivalent cations are equally distributed on tetrahedral and octahedral sites, while the divalent cations occupy the re-

maining half of the octahedral positions.
An important aspect of spinel systems is that they admit an extremely large variety of total solid solutions; indeed, the choices of the divalent cation are different, the mostly used ones are Zn^{2+}, Ni^{2+}, Mn^{2+}, Ba^{2+}, Cu^{2+} and also partial substitutions of divalent or trivalent ions are possible, preserving the spinel crystal structure.
In case of zinc ferrite, the bulk form is characterised by a normal spinel structure AB_2O_4 where the oxygen atoms are arranged in a close-packed face-centred cubic units network, while the divalent Zn cations (A) occupy tetrahedral sites and trivalent Fe cations (B) the octahedral ones. The spinel unit cell contains 8 molecules, so it is composed by 8 Zn^{+2}, 16 Fe^{+3} cations and 32 anions oxide O^{-2}, for a total of 56 atoms [101–104]. A schematic illustration of the direct spinel structure is reported in Figure (4.1).

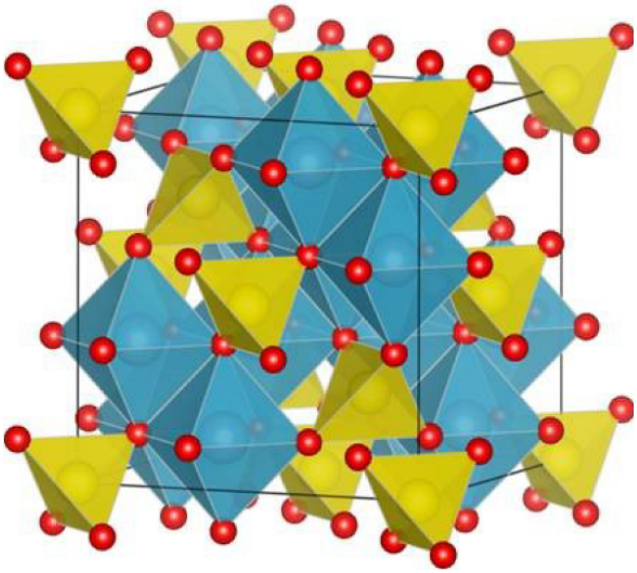

Figure 4.1: Scheme of ZFO direct spinel structure: Zn^{2+} and Fe^{3+} cations are located at the centre of the tetrahedral (ochre solid) and octahedral (cyan solid) sites, respectively, while the red circles represent the oxygen anions [112].

The nature, type, amount and distribution of cations strongly affect the functional properties of bulk ferrite systems and, in particular, their magnetic behaviour. In order to give an idea of how the cationic contribution affects the magnetic properties, let us consider a deeply studied system, namely, the mixed Zn-Ni ferrites ($Zn_{1-x}Ni_xFe_2O_4$, with $0 \leq x \leq 1$) whose ending compositions are zinc ferrite, $ZnFe_2O_4$ (for x = 0), a direct spinel, and nickel ferrite, $NiFe_2O_4$ (for x = 1) which is, in turn, an inverse one. In bulk regime, the direct zinc ferrite spinel is characterized by a paramagnetic behaviour with an antiferromagnetic ordering which occurs at a Néel temperature of about 10 K, while the nickel ferrite is ferrimagnetic with a Curie point at about T = 860 K [113].

The origin of this different behaviour lies in the different leading magnetic interactions in the two spinel structures. Indeed, three kinds of magnetic interactions are possible between the metallic ions, mediated by O^{2-} ions through superexchange mechanisms: the A-O-A and B-O-B interactions, occurring within each sublattice and the A-O-B one among the tetrahedral (A) and octahedral (B) ions (Figure (4.2)) [113]. The more efficient interactions are the A-O-B

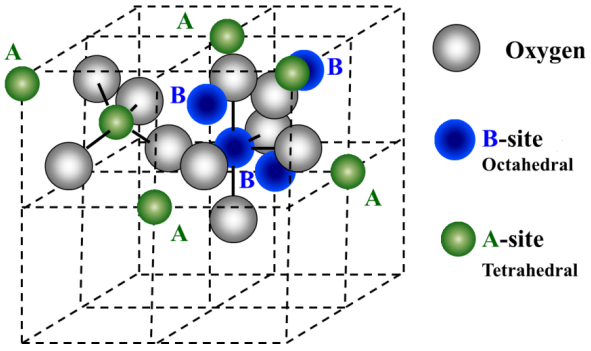

Figure 4.2: Picture of the A and B sites in the ZFO spinel structure [114].

ones, because of their axial symmetry, while the B-O-B interactions, being characterized by a 90° angle, are weaker. As a result, both spins on B sites are antiparallel to the A spins. Thus, the magnetic response of spinel is determined by the cationic distribution among the two sublattices. In particular, for an inverse spinel, like $NiFe_2O_4$, B sites are occupied by both the divalent and trivalent cations, in this case Ni^{2+} and Fe^{3+} ions, and the remnant Fe^{3+} is placed on the A site; thus, the magnetic moment of Fe^{3+} on A site cancels with the one of Fe^{3+} on B site, and the resulting magnetic moment is the spin value for nickel Ni^{2+} (2.3 Bohr magnetons). This is a strong interaction with a resulting high-temperature Curie transition. On the contrary, as regard the direct zinc ferrite spinel, iron ions occupy the B sites and zinc ones are located on the A sites. Since Zn^{2+} is a $3d^{10}$ ion, it has no magnetic moment, and the only leading magnetic interaction is the B-O-B one which is very weak since, as already described, the bond angle of Fe^{3+}-O-Fe^{3+} is 90°. This is the reason of the ZFO paramagnetic behaviour with a transition to an antiferromagnetic ordering only at the Néel temperature of about 10 K; this low Néel temperature clearly illustrates the weakness of this superexchange interaction, as compared with the leading A-O-B one in case of nickel ferrite [113].

The magnetic behaviour of bulk spinel ferrites markedly changes moving to the nanometer scale. Indeed, as regard nanostructured zinc ferrite, the reduction of the particle dimensions to the nanoscale regime induces a partial cation inversion between the two sites and in turn ZFO displays a mixed spinel structured in which Zn^{2+} and Fe^{3+} ions are distributed over the two sites. The cation inversion, with the consequent presence of Fe^{3+} ions on both the two sites, strengthens the A-O-B interaction and, in turn, nanostructured ZFO

could display a superparamagnetic (SPM) behaviour also at room temperature.
In general, systems which are ferro- and ferrimagnetic in bulk, express a SPM behaviour when the grain size is reduced to 50 nm or less. In SPM phase, the thermal energy is greater than the magnetic anisotropy energy, therefore random fluctuations of the magnetization are allowed. Thus, above the so-called blocking temperature (T_B), the magnetization of a SPM material is zero in the absence of an external applied field, while it rapidly increases as soon as an external field is applied. This results in a closed sigmoidal shape of the M-H curve without appreciable hysteresis. The T_B value can be experimentally derived in an easy way, since it generally corresponds to the "merging point" of the zero-field cooled (ZFC) and field-cooled (FC) magnetization curves [113]. However, one has to notice that the reduction in size and the increased surface/volume ratio not only cause the appearance of a room temperature SPM behaviour, but they can also induce other magnetic phenomena like, the generation of randomly oriented uncompensated surface spins, canted spins, and magnetically dead layer at the surface [115].
Anyway, superparamagnetism is, among all, the most discussed and studied magnetic phenomenon in nanostructured spinel ferrites, because it is especially important in applications such as drug delivery or MRI, where the nanoparticles exhibit no magnetic properties upon removal of the external field and thus they do not attract each other, eliminating the major driving force of aggregation. Moreover, superparamagnetic nanoparticles allow better control over the application of their magnetic properties because they provide a strong response to an external magnetic field.
It is thus clear that for biomedical applications, a careful control of the functional parameters, namely saturation magnetization (M_s), coercivity (H_c), and blocking temperature (T_B), is essential. This control can be achieved by tuning the material properties in terms of size, shape, composition (substitutions, doping, cation distribution in the crystal structure), and shell-core design, with possible different chemical and physical structures of internal-core and surface-shell parts of the nanoparticle [116]. Thus, the synthesis methods, used to prepare the spinel ferrite nanoparticles, play an important role in the control of the functional parameters. A large variety of synthesis methods has been reported, including, as for instance, conventional ceramic solid state synthesis, high-energy ball milling, microwave-assisted combustion, sol-gel, hydrothermal, co-precipitation, ultrasonic cavitation, and thermal plasma, with the peculiar aim to tune electric, catalytic, and magnetic properties.
This large number of methods used to prepare zinc ferrites nanoparticles leads to a corresponding variety in terms of properties of the synthesized materials; moreover, the above-mentioned strict correlation between functional parameters and morphology, gran size, doping, cation distribution as well as nanoparticle architecture opens a scenario that is not trivial. Thus, it is mandatory to verify and control magnetic, structural and chemical properties as well as

homogeneity of nanoparticles. At this regard, it is very important to monitor the presence of unwanted extrinsic phases, such as iron oxides ones, which are possible source of extrinsic contribution to the functional properties of zinc ferrites. In addition, different factors such as nucleation, growth, aggregation, and adsorption of impurities can affect the morphology of prepared particles [117]. For these reasons, the zinc spinel ferrites are generally investigated within a multi-technique approach. In particular, the magnetic response is usually probed by SQUID magnetometer or Vibrating Sample Magnetometry, through which it is possible to derive Saturation magnetization (M_s), Coercivity (H_c), and Blocking temperature (T_B). Together with the evaluation of the magnetic response, the source of such magnetic behaviour is also investigated through ^{57}Fe Mossbauer, XANES, XPS, and EPR investigations. The morphology of the nanoparticles is usually controlled by TEM and SEM techniques and the latter one also allows to investigate the chemical compositions of the samples through EDX analyses. The quality of the correct crystalline structure is generally probed by XRD analyses and micro-Raman measurements that also allow to estimate the inversion degree.

Raman spectroscopy (RS) has been widely used to characterize zinc ferrites and, of course, the general class of iron oxide spinels, from the routine identification of materials [118] to very accurate investigations concerning basic phenomena. Indeed, the RS probe is sensitive to cationic distribution [119], allowing, in turn, to extract (semi)-quantitative information like the inversion degree of the spinel. Furthermore, RS inspection gives the possibility to monitor the stability of the compound, evaluating possible phase and structural transitions that could be induced by light exposure or thermal treatment [120]. The sensitivity of this technique allows also to evaluate the presence of unwanted spurious phases like impurities or extrinsic iron oxide phases as haematite or maghemite [121]. Indeed, a general issue for ZFO nanoparticles is to reveal the presence of iron oxides phases that can infer an effective, but extrinsic magnetic behaviour, causing problems in terms of stability and aggregation if used for example in biomedical applications. Furthermore, it is possible to assess the effect induced by the nanometric scaling that affects the Raman lines features in terms of peak energies shifts, widths and shape changing [122]. Lastly, we have considered zinc ferrites as an effective element to realize SERS substrates according to [123]. In particular, we would like to investigate the possible enhancement mechanisms occurring in pure ZFO NPs substrates as well as in combined ZFO and Ag NPs systems.

For the above-mention interesting overlapping between characteristics of RS and properties of nanosized zinc ferrites, we have decided to investigate this systems. These research activities have been carried on in collaboration with the chemical group of Prof. Bini at the Chemical department, Chemical-Physical unit, of University of Pavia, where the samples have been synthesized

and characterized by means of XRPD and SEM measures.
In particular, in [112], we started to study pure and doped zinc ferrites nanoparticles prepared by using the microwave-assisted combustion method. The doping was performed by substituting different cations on both A and B sites, namely the doped sample were $Zn_{1-x}Ca_xFe_2O_4$ (x = 0.05 and 0.25), $ZnFe_{1.9}Gd_{0.1}O_4$, $Zn_{0.95}Sr_{0.05}Fe_2O_4$, and $ZnFe_{1.9}Al_{0.1}O_4$. Subsequently, in [124] we focused our attention on the Ca and Gd doped samples since the Ca substitution is particularly interesting due to the low toxicity of the substituent, while Gd ions are commonly used as contrast agents for MRI. The obtained results are presented and discussed in view of a new study performed on pure and Mg (on Zn site) and/or Ga (on Fe site) substituted ferrites synthesized by a different preparation route, namely co-precipitation. The investigated samples are named as follows: ZFO for pure sample, MZFO for $Zn_{0.9}Mg_{0.1}Fe_2O_4$, ZGFO for $ZnFe_{1.8}Ga_{0.2}O_4$ and MZGFO for $Zn_{0.9}Mg_{0.1}Fe_{1.8}Ga_{0.2}O_4$
The aim of this research study is to exploit the high sensitivity and the fast time scale investigation offered by RS in order to deeply understand the structural and chemical properties of these compounds. In particular, we have tested the structural homogeneity intra-sample and their thermal stability under laser irradiation. We have evaluated the Raman response of our samples to different laser sources, namely 266 nm, 533 nm and 633 nm. Moreover, we have get information about the cationic disorder by semi-quantitative analyses of the ZFO Raman peaks. Finally, in order to demonstrate the effectiveness of the Raman technique in the study of zinc ferrite, the obtained results are discussed and validated taking into account the information obtained from complementary analysis, like X-ray powder diffraction (XRPD), EPR spectroscopy and SQUID measurements to evaluate the magnetic response.

4.1 Learning about $ZnFe_2O_4$ nanoparticles from Raman response

As already introduced, $ZnFe_2O_4$ has a cubic spinel structure belonging to the Fd3m (O_h^7) space group in which the unit cell contains 8 molecules for a total of 56 atoms, but the smallest Bravais cell contains 2 formula units for a total of 14 atoms. Although the factor group analysis predicts five Raman active modes, namely $A_{1g} + E_g + 3F_{2g}$, the Raman spectrum is generally dominated by three most intense peaks, namely A_{1g}, $F_{2g}(2)$ and $F_{2g}(3)$, while the other two low frequency modes, E_g and $F_{2g}(1)$, could be sometimes detected. In Figure (4.3) the room temperature Raman spectrum of pure ZFO, synthesized by our group, is reported as an example. As it is possible to observed, the A_{1g} mode that falls between 600-800 cm^{-1}, is the most intense one; according to literature, it is associated to the symmetric breathing mode of the tetrahedron AO_4 unit in which the cation is at the centre of a cube, surrounded by four oxygen atoms in the non adjacent corners and the vibration involves

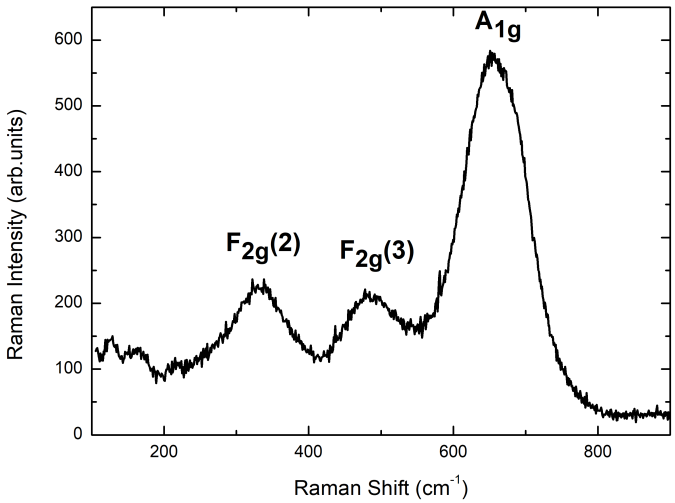

Figure 4.3: Room temperature Raman spectrum of pure zinc ferrite nanoparticles synthesized by co-precipitation route.

the four oxygen atoms that moves away from the tetrahedral cation along the bonds direction while the cation is at rest [125]. As regards the lower energy modes, a clearly stated assignation is still missing. In [126], all these Raman modes are attributed to vibrations of the octahedron units (BO_6), consisting in a cation surrounded by six oxygen atoms at the vertices of the octahedron itself. In particular, the E_g and $F_{2g}(3)$ modes correspond to the symmetric and asymmetric bending of oxygen atoms in the metal-oxygen bond, while the $F_{2g}(2)$ mode is due to asymmetric stretching vibrations also at the octahedral site [127]. However, different attributions could be found in literature. Indeed, the $F_{2g}(3)$ mode is attributed to the asymmetric bending motion of the oxygen atoms with respect to the tetrahedral cation or, otherwise, to the antisymmetric breathing of the AO_4 unit [128], while the E_g one to the symmetric bending [128, 129]. The $F_{2g}(2)$ should be due to the opposite motion of cation and anion along one lattice direction [129]. Lastly, there is more accordance on the assignation of the lowest energy mode, $F_{2g}(1)$, which is due to the translational motion of the whole AO_4 unit within the spinel structure.
In our previous work [112], we have highlighted the controversial landscape of Raman modes assignment in ZFO by reporting a brief overview on Raman results from nanosized pure and doped zinc ferrites obtained by different methods. Moreover, this summary points out the absence of a clear correlation between grain size and peak positions. In general, for both pure and doped nanoparticles zinc ferrites, it is not trivial to derive general rules for Raman modes behaviour, because several parameters, namely synthesis, grain size, composition, and chemical purity, can give rise to competing effects that reflect in opposite effects on Raman features.

However, the general effects of the grain size reduction are the asymmetric broadening of the Raman bands and a decreasing in the Raman yield [130] and, of course, it is the primary source of inversion which strongly affects the Raman modes as a consequence of the presence of different cations involved in the same vibrational unit [131]; this entails the broadening of the Raman features and it is common to recognize different contributions for each Raman mode [132]. This behaviour is the so-called two-mode behaviour and it is particular pronounced for the A_{1g} mode which is the result of the overlapping of two different modes: the vibration of the ZnO_4 tetrahedral unit that produces a signal at about 650 cm^{-1} and the vibration of the FeO_4 one whose related signal is generally located at about 690 cm^{-1}.
In case of doped samples, the Raman lineshape is not only affected by the inversion on A and B sites but also by the substitution of divalent or trivalent cations. In turn, the Raman signal could be the result of the overlapping of three contributions due to vibrations inside ZnO_4, FeO_4, caused by inversion, and MeO_4, as a result of substitution. As regard low frequency modes, the two mode behaviour is sometimes less detectable and, in some cases, a one-mode behaviour could not be excluded [133]. It is thus clear that Raman investigation on ZFO NPs enables the characterization of the samples structure in terms of inversion and/or cationic substitutions which are parameters that affect the magnetic response. Indeed, one can derive the inversion degree by using the empirical formula

$$x_{Fe}(A) = \left[1 - \frac{I_{Zn}}{I_{Zn} + I_{Fe}}\right] \tag{4.1}$$

where I_{Zn} and I_{Fe} are the integrated intensities of the Lorentzian functions used to perform a best fitting procedure on the A_{1g} mode. Moreover, the lorenzian intensities can be multiplied by corresponding force constants, although it is not generally simple to derive a reliable value [102, 132].

The RS capability to extract information about the cationic disorder of the spinel structure leads to an important issue in the study of ZFO NPs, namely the importance to reveal the presence of iron oxides, like haematite and maghemite, in synthesized samples [5]. Indeed, the presence of these iron oxides can infer, as already described, an effective but extrinsic magnetic behaviour, but it can also lead to an improper estimation of the inversion degree. Notwithstanding, Mossbauer and neutron diffraction measures can give important information on the spin ordering as well as on the nature of the magnetic response, also Raman spectroscopy can play an important role at this regard. Indeed, each iron oxide phase is characterized by its own Raman fingerprint. Haematite (α-Fe_2O_3) belongs to the rhombohedral system while maghemite (γ-Fe_2O_3) displays a cubic inverted spinel structure. This structural difference reflects on the Raman spectra. The simulation of the spectra of ZFO, hematite, and maghemite are reported in Figure (4.4). In particular, these simulated spectra have been carried out by using OriginPro 8.1 software. As

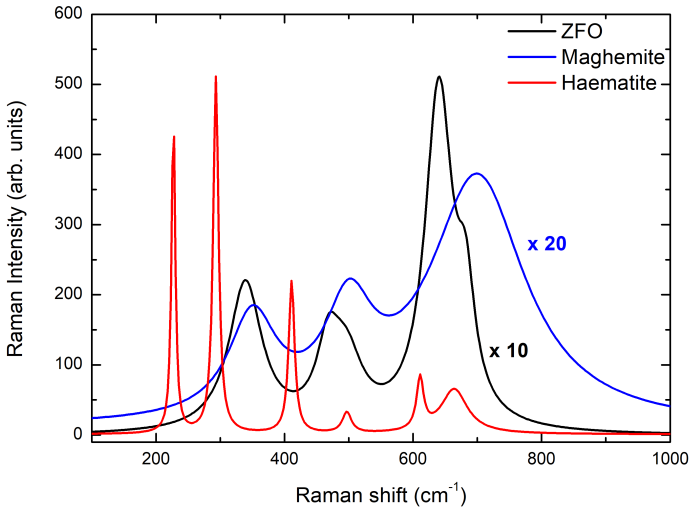

Figure 4.4: Simulated Raman specta of ZFO, haematite and maghemite.

it is possible to observe, the Raman spectra of ZFO and maghemite are obviously quite similar because they are both characterized by a cubic spinel structure; however, the total Raman yield is greater for ZFO. The main appreciable difference is the position of A_{1g} peak: for ZFO, the ZnO_4 vibrations are dominant and the peak is centred at around 650 cm^{-1}, while, for maghemite the energy peak is usually observed around or just above 700 cm^{-1}, because of the only presence of iron in the tetrahedral unit. On the other hand, haematite is characterised by a markedly different Raman spectrum with the main peaks located at lower energies and a Raman yield which is approximately about 10 and 20 times greater that the one of spinel ferrites; this means that a small amount of haematite can give evident signatures in the Raman spectrum.
However, quantifying this small amount is generally not trivial because it is often reported that in ZFO nanometric grains, surface shell of haematite or maghemite can be formed [134, 135]; in this case, it is important to evaluate the effective thickness sampled during Raman measurements.
A more difficult task is, instead, to reveal the presence of few amounts of maghemite. A possible way to do this consists in performing detailed best-fitting analyses that could give evidence of the presence of maghemite [136]; this procedure is generally performed on the A_{1g} data for which the presence of maghemite should give rise to a third component generally peaked at about 700 cm^{-1}. However, the variability in the peak energies which affects both pure and doped ZFO, together with the weak weight of maghemite contribution in Raman signal can not ensure a reliable attribution simply based on Raman data. Another possible strategy is to monitor the stability of maghemite to laser irradiation. Indeed, it is well-known that maghemite is an intermediate metastable phase in the oxidation route of iron ions while haematite is the ter-

minal and stable one [137]. Within this approach, the presence of maghemite in ZFO can be indirectly evaluated by the growth of haematite Raman signals under laser irradiation [138]. However, also in this case, it is not so simply to definitively assert that the insurance of haematite is linked to the presence of low amount of maghemite because a possible source could be also the presence of a highly defective Zn deficient external layer [112]. Indeed, as a function of the grain dimension, an inhomogeneity in the cationic distribution and oxidation state could occur along the radial dimension of the nanoparticles thereby forming an external shell rich in oxygen vacancies and characterized by a highly defectiveness. In turn, this inhomogeneous cationic distribution and stoichiometry could promote the occurrence of the hematite phase even in the absence of pre-existing maghemite clusters, but from a highly disordered shell of the zinc ferrite NPs.

4.1.1 Results

In Figure (4.5), the comparison between the room temperature Raman spectra of pure and doped zinc ferrite samples is reported in the range between 100 - 800 cm^{-1}. It is possible to notice that the first order Raman signatures typical

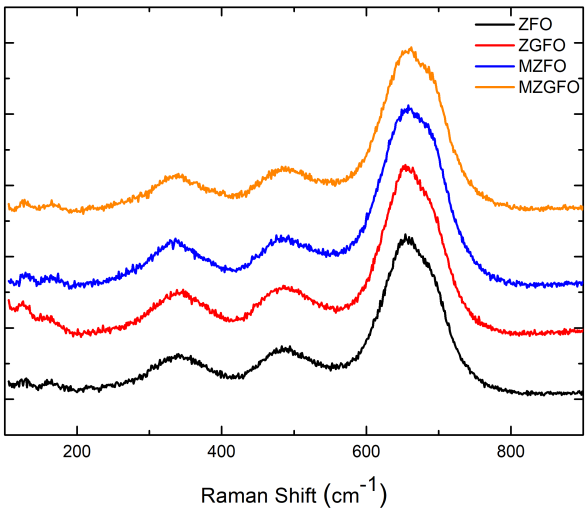

Figure 4.5: Comparison between the room temperature Raman spectra of the investigated samples: ZFO, ZGFO, MZFO and MZGFO.

of a zinc ferrite structure are clearly visible for all the investigate samples. In particular, the essential invariance of the Raman features among the samples is a proof of a good stability of the spinel structure and it is consistent with the fact that shifting in the peak position or peak broadening occurs upon variation in the synthesis preparation, heterogeneity in the nanoparticle size and doping. Indeed, our samples have been prepared by one single route, namely

the co-precipitation method that guarantees an homogeneous grain size dimension which is about 5 nm. In this case, the doping does not markedly affect the Raman bands, pointing out that the substitution of low amount of dopants has not altered the spinel cubic structure.

We have tested the phase homogeneity intra-sample by collecting 15 spectra on a single linear scan of about 30 μm. The results are shown in Figure (4.6) for pure ZFO and doped ZGFO samples. The results for the other samples can be found in Appendix (C). For all the investigated samples, the reported Raman spectra assert the homogeneity of the spinel zinc ferrite phase along all the tested surface. The variability in the intensity yield can be attributed to slight changes in the focus of the laser beam; indeed, these measure have been collected by an automatically mapping that has not given the possibility to precisely adjust the focus for each single measure. As it is possible to observe

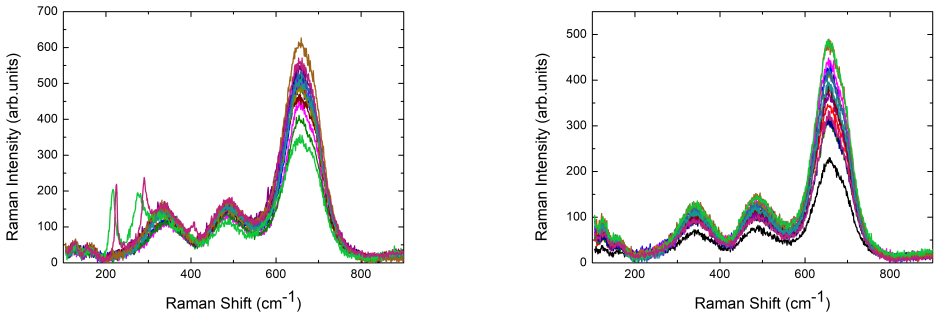

(a) (b)

Figure 4.6: Room temperature Raman spectra collected by a mapping acquisition in different region of (a) ZFO and (b) ZGFO samples.

for ZFO sample (Figure (4.6a)), two of the collected spectra are characterized by the distinctive features of the haematite peaks at low frequency. However, the appearance of the haematite features seems not to be due to the presence of clusters of this iron oxide phase, but instead to an instability of the spinel structure under laser irradiation. This inference is based on the following evidences: i) the XRPD results have clearly stated the purity of the samples (see Section (4.2.1)), although we know that this technique has a low sensitivity; ii) the different spectra collected in different region of the sample have not given evidence of haematite presence; iii) the two Raman signals, displaying the haematite features, have been recorded at the end of the mapping procedure and, thus, after long exposure to laser radiation.
In view of this result and in order to verify the phase stability under laser irradiation of the other samples, we have performed thermal cycles in different points by progressively increasing the incident laser power density from 5×10^4 to 5×10^5 W/cm^2 and, subsequently, decreasing it through the use of neutral filters. In Figure (4.7), the response to this thermal stress is reported for the

ZFO sample, as an explanatory case; in particular, the spectra recorded with a 5×10^4 W/cm^2 incident power density, before and after the thermal cycle, are shown. In Appendix (C), Figures (C.7) - (C.9) report the Raman spectra collected before and after the thermal cycles for the other samples. As it is possible to observe, all the samples display different response in two different investigated areas: stability under thermal treatment as well as a partial phase transition with the growth of new peaks proper of the haematite phase. These changes in Raman spectra due to laser induced effect are intrinsically difficult to control depending on different parameters like thermal conductivity of the irradiated region. It is thus extremely important to evaluate the local temperature at which this effect takes place; this can be done by simultaneously comparing Stokes and anti-Stokes features, at the moment not available in our set-up. Future investigations will be performed just for this scope.

For the sake of completeness in Figure (4.8), the overall Raman response of

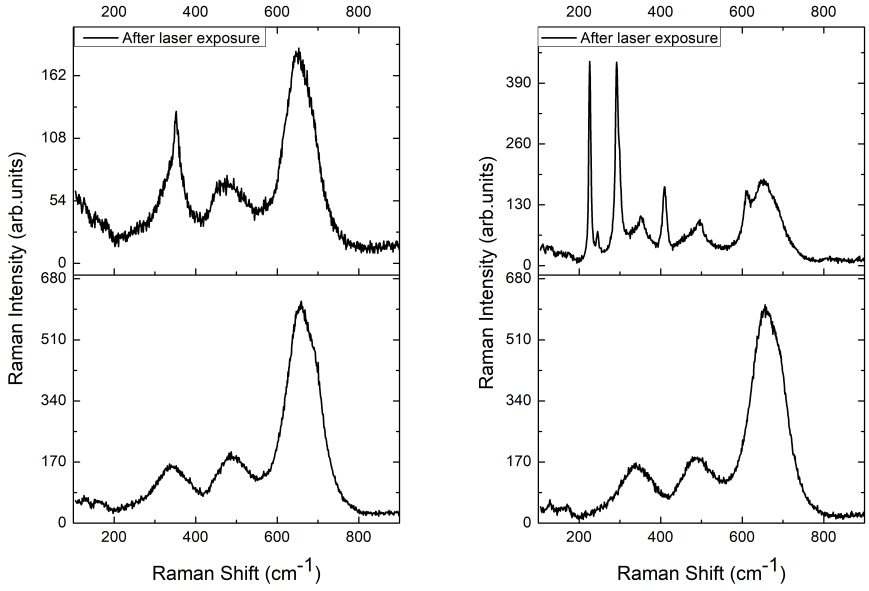

Figure 4.7: Raman response to the thermal strain of ZFO sample. The reported room temperature Raman spectra have been collected at the beginning and at the end of the thermal cycle with a 5×10^4 W/cm^2 incident power density, in two different regions of the sample displaying both thermal stability (a) and a partial transition to haematite phase (b).

the ZFO sample is reported at variance of the incident power density in presence and absence of the appearance of haematite features. As shown in the above-mentioned Figures, in case of thermal instability, four new peaks centred at 225, 299, 412 and 613 cm^{-1}, progressively rise by increasing the laser power. These bands are characteristic of the haematite phase; thus, we are looking at a partial phase transition to haematite which is irreversible since these peaks do not disappear in the descending phase of the cycle, with a resulting final spectrum characterized by the features of both haematite and

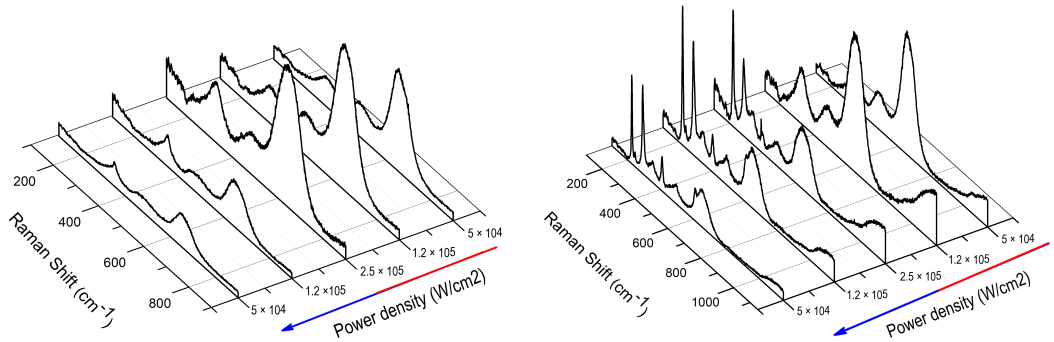

(a) (b)

Figure 4.8: Room temperature Raman spectra of the entire thermal cycle for the ZFO sample in two different regions of the sample displaying both thermal stability (a) and a partial transition to haematite phase (b).

zinc ferrite spinel. This phase transition to haematite is markedly noticeable for ZFO, MZGFO and MZFO, while for ZGFO sample a small signature of the haematite phase seems to arise at the end of the thermal cycle, but still recognizable.

On the basis of the results, reported so far, two possible sources responsible for this phase transition could be assumed:
i) the presence of maghemite clusters;
ii) the presence of a highly defective external shell in the ZFO nanoparticles surface.

Some information about phase/composition gradient at variance with penetration depth of the probe, has been obtained by performing Raman measurements with other two different excitation wavelengths, namely 532 nm and 266 nm. The UV Raman measurements have been carried out with a benchtop Raman set-up at the IUVS line at the Elettra synchrotron in Trieste, while the Raman measures with the 532 nm laser source have been recorded with a Horiba LabRAM HR Evolution, located at the Experimental Mineralogy Lab at the Earth and Environmental Science Department of University of Pavia.
In Figure (4.9), the comparison between the Raman spectra of the pure sample collected with 266, 532, 633 nm light is reported in the range between 100 and 800 cm^{-1}, where the first order Raman signal of zinc ferrite NPs can be observed.
Despite the difference in the intensity yield due to the different power density values used to perform the measures, and to the different scattering volumes, it is possible to observe the principle A_{1g} mode in each of the reported spectra. However, some differences can be noticed between the 633 nm Raman spectra and the other two spectra. In particular, as regard the spectrum collected with 532 nm wavelength, the ratio of the relative intensities proper of the $F_{2g}(2)$ and A_{1g} modes is markedly different; indeed the two modes have almost the

same Raman yield, while the $F_{2g}(3)$ peak is very weak, almost not noticeable. As regard the UV Raman spectrum, even if it displays a high signal to noise

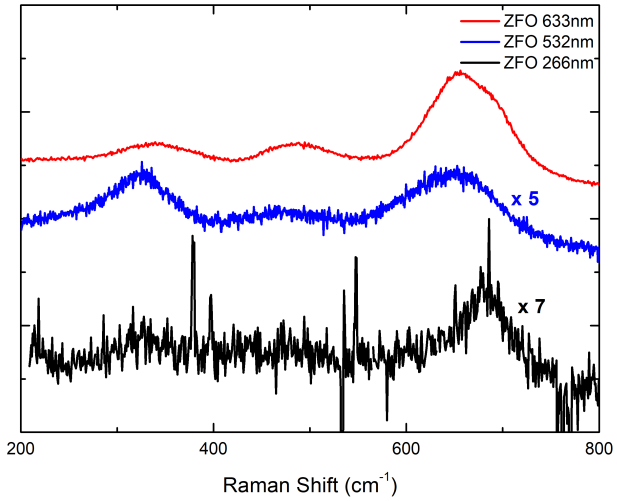

Figure 4.9: Comparison between the room temperature Raman spectra of ZFO sample, collected with three different laser excitation sources, namely 633 nm, 532 nm and 266 nm.

ratio and the low frequency modes are hardly noticeable, a visible difference in the shape of the A_{1g} mode can be observed. In particular, the component due to the vibration of the FeO_4 tetrahedral unit at about 680 cm^{-1}, is much more pronounced with respect to the same component in the other two spectra for which it consists of a small shoulder of the predominant peak pertinent to the ZnO_4 unit vibration centred at about 640 cm^{-1}. This observation is supported by the results obtained from the best-fitting procedure that we have performed on the A_{1g} mode. Indeed, for the Raman spectra collected with 532 and 633 nm, this mode is given by the overlap of two Lorentzian curves, which has been used to take into account the two-mode behaviour, as reported in Figures (4.10a) and (4.10b), respectively; on the contrary, for the Raman spectrum collected with 266 nm laser source, the best-fitting procedure has been performed by using a single Lorentzian curve peaked at 677 $\pm$ 2 cm^{-1} (Figure (4.10c)). The fact that this peak is centred well below 700 cm^{-1}, namely where the maghemite mode should occur, could support the hypothesis of a different cationic distribution from the stoichiometry ($Zn_xFe_{2-x}O_4$) in the external shell of the ZFO nanoparticles, characterized by a deficiency in Zn cations. Indeed, by diminishing the wavelength of the incident laser source, from the analyses of the A_{1g} peak, one can notice a progressively increase of the component pertinent to the Fe-O vibration in the tetrahedral unit and a corresponding lowering of the ZnO_4 component till its complete disappearance in the UV Raman spectrum (Figure (4.11)). This is consistent with the fact that with the more energetic incident source (4.66 eV) we are sensitive to

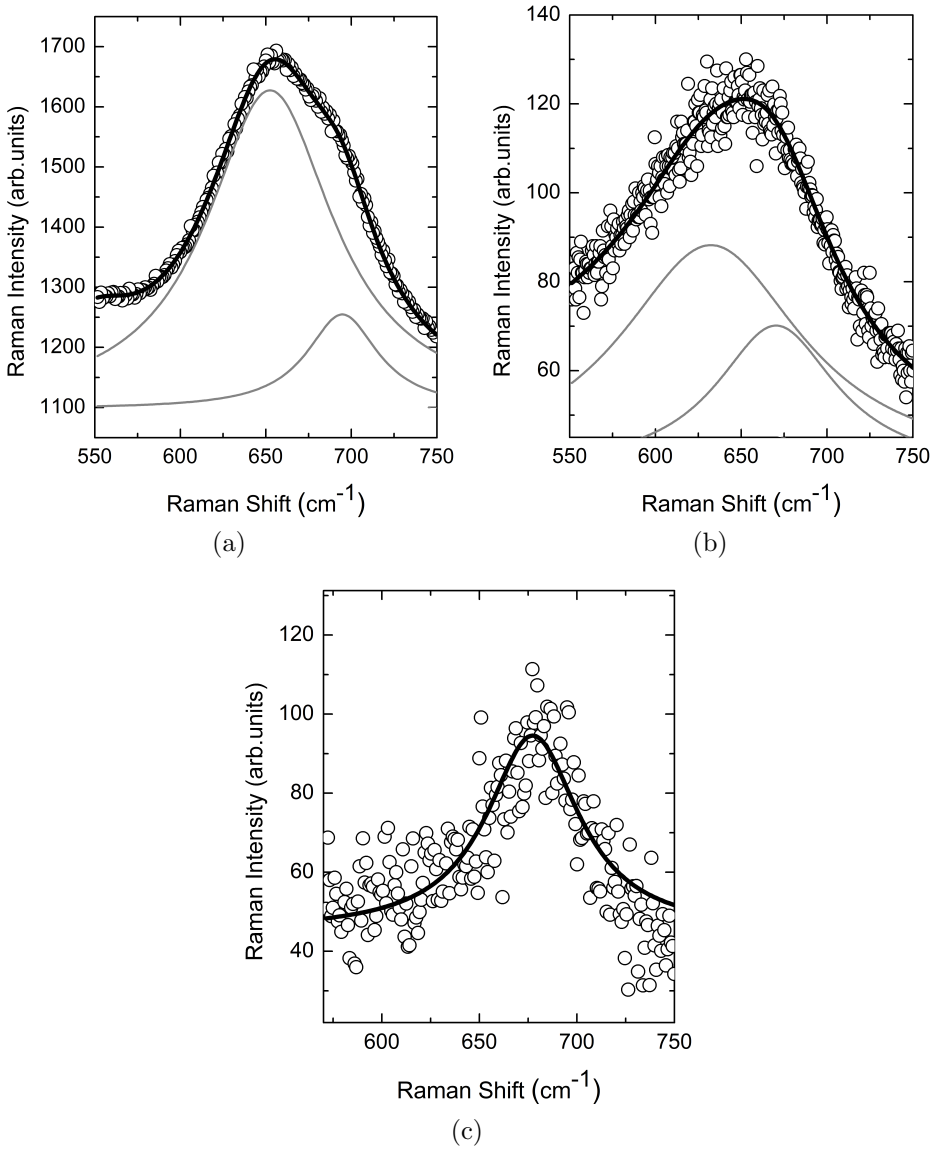

Figure 4.10: Raman data and curves from best-fitting procedure run for the A_{1g} mode of ZFO sample investigated with (a) 633 nm, (b) 532 nm and (c) 266 nm laser sources.

the external shell of the NPs. In particular, we have roughly estimated the penetration depth, generally defined as $\propto 1/\alpha$, from the absorption spectrum and Tauc plot (Figure (4.12)) reported in [139]; the authors have calculated the reported data for ZFO NPs synthesized by co-precipitation route with an average particle size of 11 nm, namely similar to our samples in synthesis route and closer to our nanoparticles dimension. In particular, we have found out that for 633 nm wavelength the penetration depth is about 4 nm, while for 532 nm it is about 3 nm and, finally, for 266 nm about 1.5 nm. Thus, we can ensure that with the 266 nm we are exploring a very thin outer thickness of the ZFO NPs.

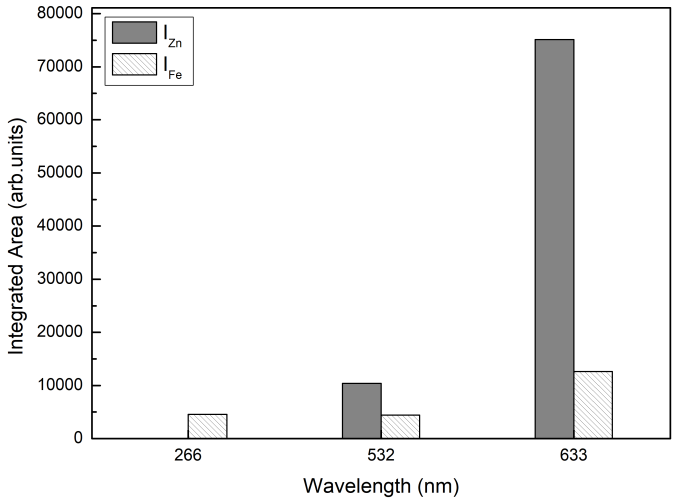

Figure 4.11: Integrated intensity values of the two Lorentzian curves obtained from the best fitting procedure which has been performed on the A_{1g} mode as a function of the incident laser wavelength.

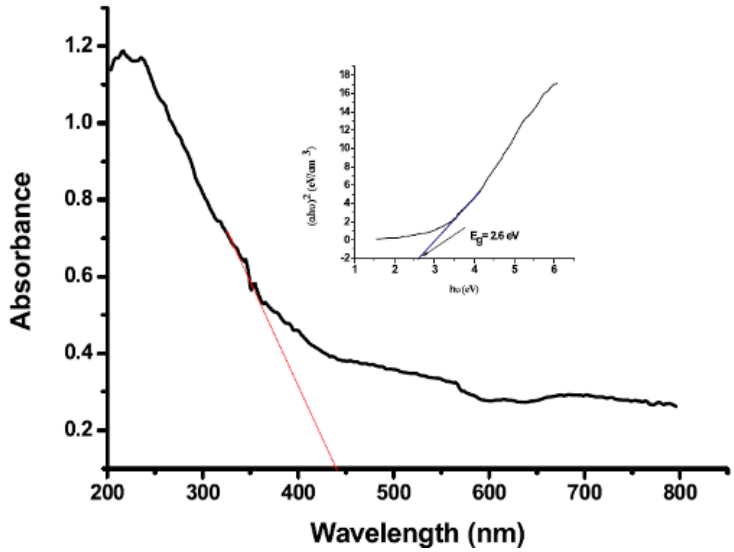

Figure 4.12: UV-vis absorption spectrum and Tauc plot (inset) of zinc ferrite nanoparticles taken from [139].

As previously described, RS probe allows also to characterize the cationic distribution between the two sublattices which is forced at the nanoregime. In particular, the pronounced two-mode behaviour of the A_{1g} mode, allows to evaluate the inversion degree of the spinel structure.
At first, we have normalized the intensity of each spectrum collected in the linear scan to the one of the A_{1g} peak and an average spectrum has been derived for each sample. Subsequently, we have analysed the A_{1g} mode in the

range between 570 and 750 cm^{-1} by performing a best-fitting procedure using to overlapping Lorentzian functions to take into account the two cationic vibration units in the tetrahedral site and one Gaussian function, centred out of the investigated range, i.e. at about 530 cm^{-1}. The Gaussian curve has been used to account for the asymmetric broadening towards low wavenumbers side of the peak; generally, this effect occurs as a consequence of the phonon confinement induced by the nanometer dimension of the particles, as well as the static disorder of cations, induced by the inversion, and of anions, due to oxygen vacancies [140, 141].
As it is possible to observe from Figure (4.13), where the best fitting procedure performed on the spectrum of the ZFO sample is illustrated, the peak is well reproduced by the sum of the three fitting functions. In particular, the first

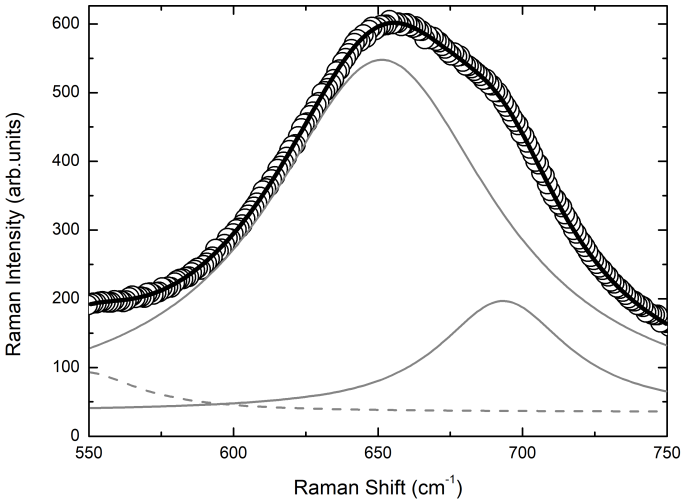

Figure 4.13: Best fitting procedure performed on the A_{1g} mode for the ZFO sample. The solid gray curves are the Lorentzian functions while the dashed one is the Gaussian one that has not been considered in the calculus of the inversion degree.

Lorentzian function, centred at 652 cm^{-1}, gives the main contribution, while the second one, centred at 695 cm^{-1}, results in a shoulder at higher energy. These energy values are in good agreement with the ones proper of the ZnO_4 and FeO_4 units vibrations reported in literature [112].
The inversion degree has been calculated by considering only the integrated intensities of the two Lorentzian functions and, in turn, by applying the formula given in Eq. (4.1). The obtained value demonstrate a slight inversion of the pure spinel: $x(Fe)_A = 0.15$.
Through this best fitting procedure it is possible to evaluate also the inversion degree of the other doped samples and the overall results are reported in Figure (4.14).
However, as we have already introduced, since in case of doped samples the

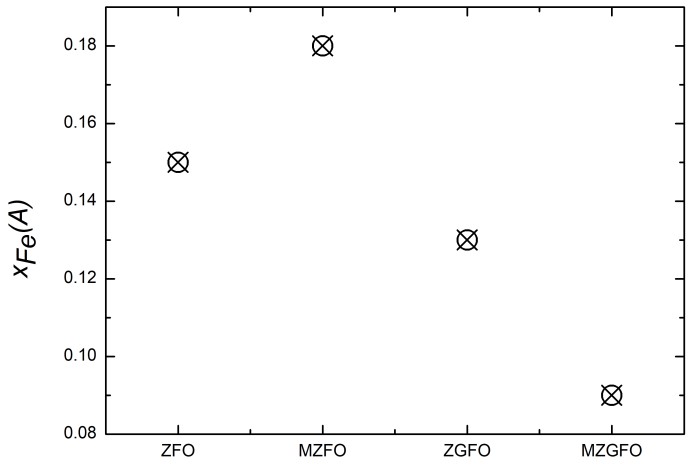

Figure 4.14: Inversion degree values estimated from the average spectrum by performing the best fitting procedure using one Gaussian and two Lorentzian curves for each sample.

Raman lineshape should be also affected by the substitution of divalent and trivalent cations, the use of only two Lorentzian functions in the fit is not properly correct and in turn to take account of the additional vibrating unit involving the doping cation, we should introduce a further Lorentzian function. This additional step in the best fitting procedure is not trivial, especially in case of a double doped sample like our MZGFO one. Indeed, in this case we have in principle to add two further Lorentzian functions to account for the Mg-O and Ga-O vibrating units. It is thus clear that a best fitting procedure with one Gaussian, to account for the reduced particle dimensions as well as static disorder, and four Lorentzian curves could display some drawbacks. Indeed, at first with this number of fitting functions, it is in principle possible to fit almost every kind of data, moreover, trying to set properly constrains is not simple. Just to better highlight this difficulty, let's consider the ending compositions of the spinel when the Mg ions substitute all the Zn cations, namely magnesioferrite $MgFe_2O_4$, as well as when the Ga ions replace all the Fe ones, namely $ZnGa_2O_4$. In literature, the mode associated to the Mg-O vibration unit in the tetrahedral site for magnesioferrite should occur at about 660 cm^{-1} [118], while in $ZnGa_2O_4$ the mode proper of the Ga-O units vibration seems to be Raman silent and only low mode could be observed at about 700 cm^{-1} upon slight inversion of the spinel structure [142, 143].
In view of this complicated scenario, we propose a more simplified approach for the evaluation of the inversion degree of our doped samples. In particular, we have evaluated the inversion degree by using the same Eq. (4.1), but instead of using the integrated intensity we have used the heights I_1 and I_2 of the Raman spectrum where the two A_{1g} mode components fall, as illustrated in Figure

(4.15a). Since the absolute value of the inversion degree obtained with this procedure is not consistent, we have also evaluated the inversion degree of the pure sample with this simplified procedure in order to normalized the obtained value with the one estimated through the rigorous best fitting procedure. The normalization factor has been used to rescale to the proper absolute values the inversion degree of all the doped samples. The obtained results together with the ones obtained from the best fitting procedure are reported in Figure (4.15b).

From the reported data, it is possible to assert that, despite the low degree

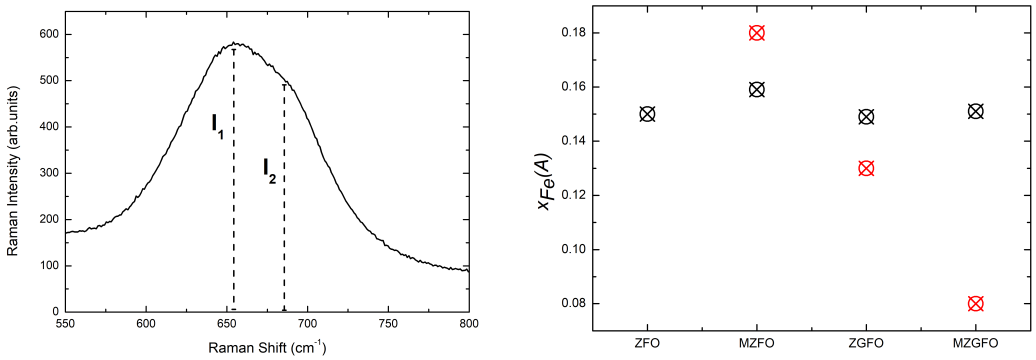

(a) (b)

Figure 4.15: Peak intensities I_1 and I_2, highlighted in the spectrum of pure ZFO (a), which have been used in Eq. (4.1) to evaluate with a simpler procedure the inversion degree of the investigated samples. (b) Inversion degree values of the investigated samples calculated with the more simplified approach and properly rescaled (black data) and the ones calculated with the integrated intensities extracted from the more rigorous approach of best fitting procedure (red data).

of inversion, the doping seems to affect the inversion; in particular, the ZGFO sample results slightly less inverted, while the doping performed with the Mg ions induces more inversion in the structure if compared to the behaviour of the undoped sample. This fact could be consistent with the inverted spinel structure proper of the magnesioferrite. The MZGFO sample has instead an in between behaviour. In particular, from the comparison shown in Figure (4.15b), it is possible to notice that from the best fitting procedure approach the double-doped sample turns out to be the less inverted of all; this observation well underline the improper application of the two-mode behaviour when at lest two substitutions are put in place. On the contrary when a single doping cation is present both the two method are almost well consistent at least in the trend of inversion, namely the Mg-doped sample is the more inverted while the ZGFO one is less inverted.

The trend of the calculated inversion degree with the more simplified approach well matches the values of T_B derived from magnetic measures (see Section (4.2.2)) and T_{EPR} derived from EPR measures (see Section (4.2.3)). Indeed, higher the inversion is, higher the T_B (and T_{EPR}) value is: this is consistent with the fact that the cationic disorder within the two sublattices strengthens

the magnetic interactions and, in turn, the transition to an order blocked state occurs at higher temperatures. Thus, the magnetic data validate the reasoning we have used to estimate the inversion degree of the spinel.
Moreover, this correlation between the inversion degree and the blocking temperature has been also observed in the previously investigated samples, namely zinc ferrites characterized by Ca or Sr substitutions on the A site and Al or Gd on the B one. The results reported in [112] shows this correlation expect for the Sr doped sample which also presented a $Sr(NO_3)_2$ impurity phase.
We have also calculated the inversion degree for the Raman spectra collected during thermal cycles, using the previously described procedure performed on the A_{1g} mode. Obviously, we have derived the inversion parameter of the spinel ferrite structure only for those spectra that have not displayed the transition to haematite. Figure (4.16) shows, as an explanatory case, the inversion degree values obtained for the MZFO sample. One can notice a kind of reversibility in the cationic disorder induced by the laser heating; however, the starting and final spectra of the sample are not characterized by the same inversion value which could be again consistent with the presence of a highly defective external shell that under laser heating could partial oxidize. Anyway, this kind of analyses has allowed us to safely assert that the incident power laser, used to performed the measures, namely $5 \times 10^4\ W/cm^2$, has not affected our characterization measures.

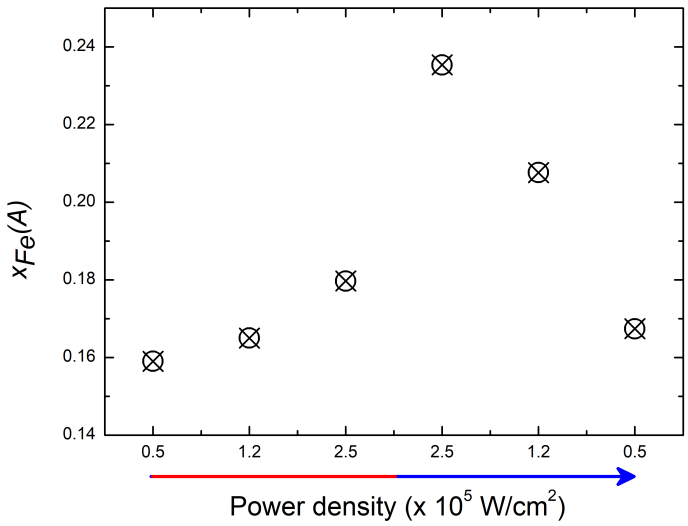

Figure 4.16: Inversion degree values estimated for each spectra of the thermal cycle performed on the MZFO sample.

4.2 Complementary techniques

4.2.1 X-ray powder diffraction

XRPD inspection has been used to evaluate the purity of the samples, to estimate the nanoparticle dimensions and to evaluate the possible inversion of the spinel structure. Indeed, during the refinements, the background coefficients, scale factor, zero (or displacement) error, lattice parameters, crystallite sizes, isotropic thermal factors and atomic positions have been allowed to vary, as well as the site occupancies, to verify the possible inversion degree of the spinel. A proper constraint has been used to limit the dopant amount to stoichiometric value and to allow the inversion of cations on the tetrahedral and octahedral sites.
In Figure (4.17), the XRPD patterns of pure and doped samples are shown. The peaks well agree with the $ZnFe_2O_4$ cubic spinel structure (JCPDS card N. 89e7412, franklinite mineral). The absence of unexpected bands confirms that traces of unreacted reagents or phase impurities are not present in the investigated samples; this also allows to infer that the performed doping has been effective. The structural and profile refinements has been performed for

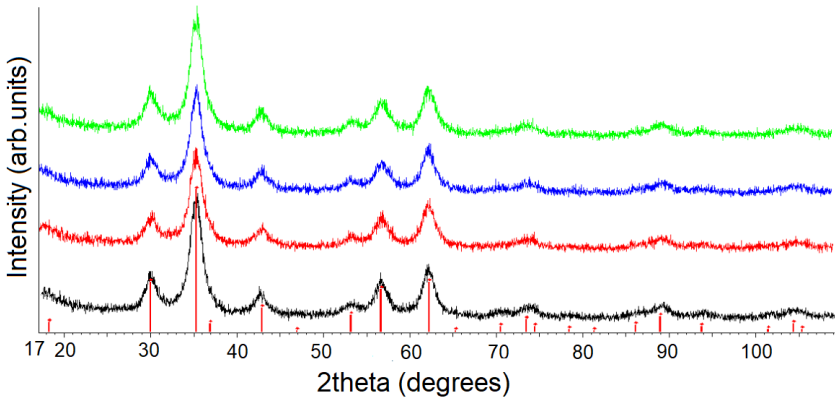

Figure 4.17: XRPD patterns of ZFO (black), ZGFO (red), MZFO (blue) and MZGFO (green) samples. The red bars proper of the expected angular peak positions for a spinel phase (Card N. 89-7412) are also reported.

all the collected patterns on the basis of the Rietveld method by using the known cubic spinel model. The main results of the refinement is reported in Table (4.1), together with the discrepancy factors R_{wp} and the goodness of fit S, whose values suggest a good quality of the refinements.
As it is possible to observe from the crystallite size values reported in Table (4.1), all the samples are characterized by nanoparticle sizes of about 5, ideal for the desired superparamagnetic effect. Indeed, the co-precipitation method, thanks to the confinement effect of the organic component and to the low temperature of thermal treatment, is able to produce materials with the required

Sample	a (Å)	Oxygen Coordinate	Cry. size (nm)	R_{wp}/S
ZFO	8.4354(25)	0.3746(11)	5.9(1)	10.64/1.02
ZGFO	8.4362(30)	0.3774(11)	5.4(1)	10.89/1.04
MZFO	8.4358(30)	0.3764(10)	5.5(1)	10.55/1.01
MZGFO	8.4300(29)	0.3776(10)	5.5(1)	10.76/1.07

Table 4.1: Lattice parameters, crystallite sizes, oxygen coordinates, and the discrepancy factors Rwp and S obtained from Rietveld structural refinements.

dimensions, also with a high purity level.
In Figure (4.18), as an example, the comparison between the experimental (blue) and calculated (red) patterns of ZFO are reported. As one can notice, the difference curve (grey) is almost flat, suggesting a good quality of the refinements, as also demonstrated by the agreement indices (Table (4.1)).
The structural refinement has also allowed to evaluate the inversion degree. However, the results indicates that all the samples are not characterized by an inverted spinel structure, in contrast with the slight inversion detected by the Raman inspection. This discrepancy can be due to the different penetration depths of the two probes leading to the detection of different structural features, especially when clustered nanometric particles are involved. Indeed, XRPD sampling involves the bulk of the sample while Raman measurements probe mainly the surfaces, i.e., as already described, the most defective and disordered sample zones and thus it is not surprising that for undoped and low-level doped samples higher inversion degree are derived from Raman analysis.

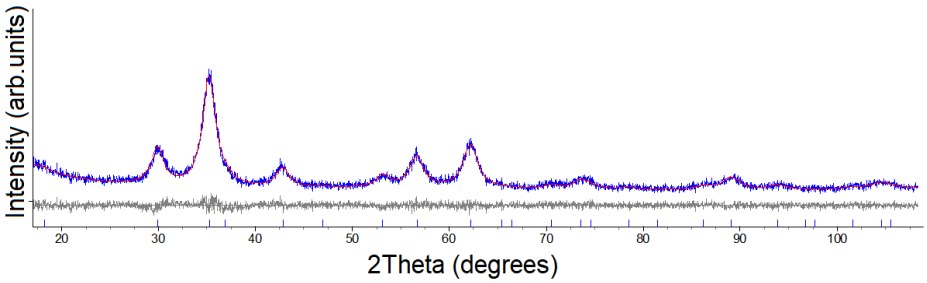

Figure 4.18: Rietveld structural refinements of ZFO pattern: comparison between the experimental pattern (blue) and the calculated one (red). The difference curve (grey) and the bars at the expected peak positions of the spinel phase are also reported.

4.2.2 Magnetic response

In Figure (4.19), the reported hysteresis cycles recorded at room temperature for pure and doped zinc ferrite samples provide a basic proof of room temperature superparamagnetism. Indeed, the main common features ascribable to

a superparamagnetic behaviour could be found: negligible values of coercive field and remanence magnetization with a no full saturation even at the highest applied magnetic fields, typical for nanoparticles of this kind of materials. As regard the shape of the RT hysteresis loops, the ones proper of ZFO and MZFO are almost superimposable showing the characteristic S-type shape of a superparamagnetic behaviour, on the other hand, the ZFGO one has a more linear trend, characteristic of a paramagnetic state, while the MZGFO sample has an in-between behaviour with respect to the other samples. However, the

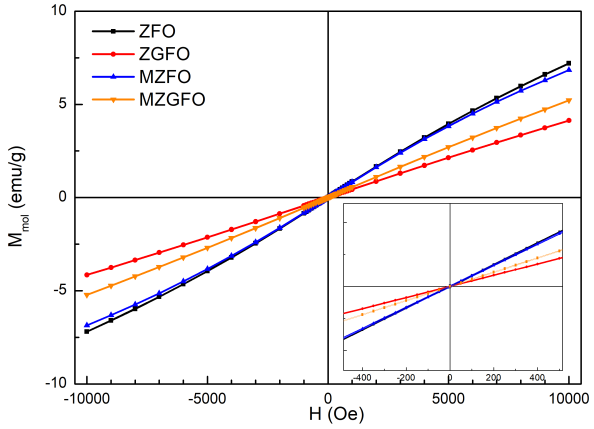

Figure 4.19: Hysteresis loops recorded at 300K for the investigated samples. Inset: the near zero-field behaviour.

hysteresis cycles recorded at 10 K reported in Figure (4.20), show for all the investigated samples a more pronounced S-like shape; small values of coercive field could be observed because the measures have been carried out below T_B, i.e. the temperature at which the transition between superparamagnetic and blocked state occurs.
In light of the obtained experimental evidences, we could state that the less marked S-type shape of the ZGFO hysteresis loop at room temperature could be ascribed to the effect of the performed doping: in particular, the Ga ions have been substituted to the Fe ones, consequently the sample has less magnetic iron centres, so the magnetic interactions could be interrupted by the presence of the dopant. This evidence also suggests that the Ga substitution tends to prevent the structural disorder of the spinel which is consistent with the lower inversion degree value estimated with Raman inspection. Moreover, the consequent interruption of the magnetic interactions is also corroborated by a weaker value of the coercive field of this sample, observable in the hysteresis loop recorded at 10 K (Figure (4.20) - inset). The effect of the Ga doping also reflects in a lower value of the saturation magnetization, M_S, with respect to the ones of ZFO and MZFO samples. However, also the MZFO sample displays a M_S value which is smaller than the one of pure sample, although it

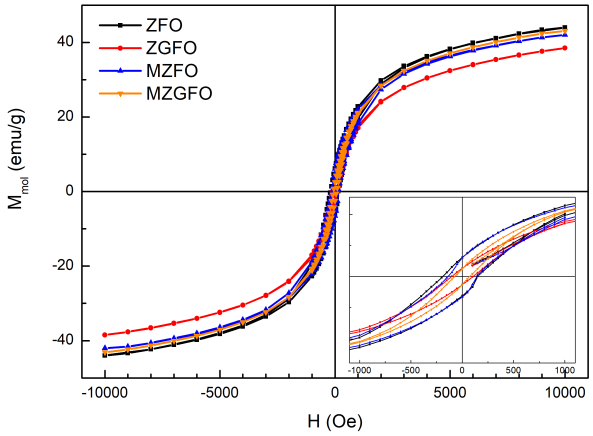

Figure 4.20: Hysteresis loops recorded at 10K for the investigated samples. Inset: the near zero-field behaviour.

is only a small discrepancy and still grater with respect to ZGFO sample. One should expect that more inversion corresponds to a higher magnetic moment, but probably in this case the inversion strengthens the antiferromagnetic interactions with a consequent slightly reduction of the magnetic yield. In general, the estimated M_S values recorded for the investigated samples are about 4 and 7 emu/g at an applied field of 1 T, which are in good agreement with the ones reported in literature for samples with comparable grain size and synthesized by co-precipitation route or others synthesis methods [144, 145].
The temperature dependence of the magnetization (Figure (4.21)) allows us to validate even more the relationship between magnetic properties and the degree of inversion of the spinel structure. As already described, we have found

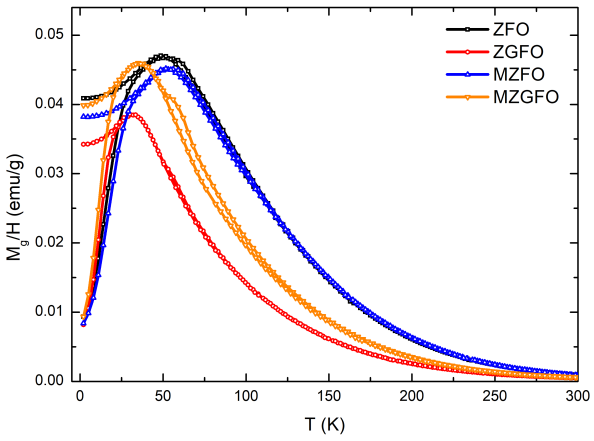

Figure 4.21: ZFC and FC M vs T curves at 100 Oe for pure and doped samples.

out a good relation between the T_B value, derived by the ZFC peak position, and the inversion degree, estimated with the Raman investigation. Indeed, higher inversion corresponds to a higher T_B value.

4.2.3 Electron paramagnetic resonance

In nanostructured zinc ferrite, as already described, two types of paramagnetic ions, namely Fe^{2+} and Fe^{3+}, are present. Since these two ions occupy two different sites (A and B, respectively), their contributions to the EPR signal are quite different. Indeed, although both Fe^{2+} and Fe^{3+} ions are paramagnetic, the EPR spectra of zinc ferrites are only due to Fe^{3+} ions because Fe^{2+} ones are characterized by a very short spin–lattice relaxation time and, in turn, their EPR signal can be observed only at temperature closed to liquid Helium temperature [146].
The room temperature derivative EPR signals, normalized to the unit mass, of pure and doped samples, are reported in Figure (4.22). The reported spectra

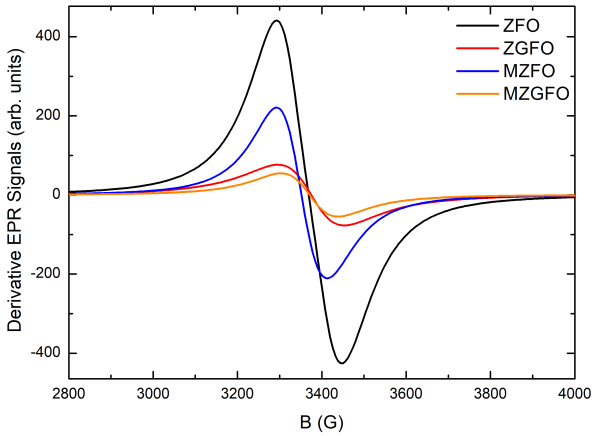

Figure 4.22: Comparison between room temperature derivative EPR signals of pure and doped samples.

are characterized by a single broadened signal with a resonant field $H_r \sim 3370$ G, correspondent to a spectroscopic splitting factor, g, of 2.003, typical of Fe^{3+} ions in nanostructured zinc ferrite; only the MZFO sample is characterized by a shifted signal corresponding to $g \sim 2.01$. The observed room temperature behaviour of the MZFO sample could be ascribed to the presence of a magnetically ordered extrinsic phase or to a SPM behaviour occurring at higher temperatures.
Thus, we have investigated all the samples by varying the temperature. This has allowed us to extract significant information about the magnetic behaviour of our samples.
In Figure (4.23), it is reported, as an example, the signal of the pure sample as a function of temperature. The spectra of the other samples are reported in Appendix (C).
As it is possible to observe, all the investigated sample are characterized by the same single broadened signal, observed at room temperature, without appreciable changing in the shape of the signal itself by varying the temperature.

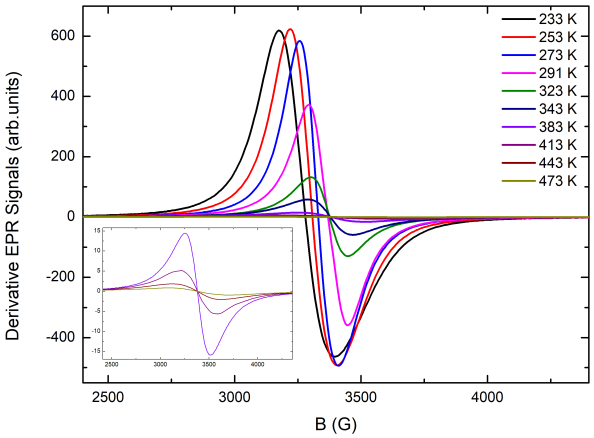

Figure 4.23: Derivative EPR signals of ZFO sample recorded by varying the temperature in the range 233-473 K. Inset: Derivative EPR signals recorded at T > 383 K.

This could be a first indication of the lack of extrinsic phases in the samples, at least within the limit of detection. In particular, the symmetry of the resonance signal can be evaluated on the basis of the *R parameter*, defined as $R = I^-/I^+$, namely the ratio between the intensity of the negative part of the signal and the one of the positive part. As an explanatory case, the trend of the *R parameter* for the ZFO sample is reported in Figure (4.24). The reported

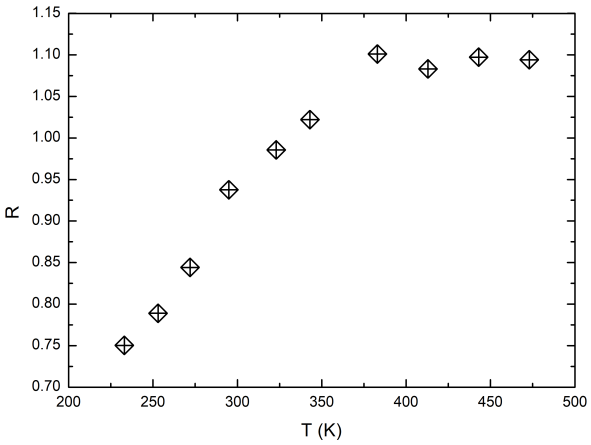

Figure 4.24: Trend of the *R parameter* for the ZFO sample.

values are well consistent with the ones of a pure zinc ferrite system; in particular, as temperature increases, the *R parameter* tends to unit as expected when ferrite progresses to a paramagnetic phase [147].

The behaviour of the g-factor as a function of the temperature, points out

two different regimes delimited by the transition temperature that we have called T_{EPR}. In particular, one can notice that above T_{EPR} the g values are almost closed to 2, typical of the zinc ferrite in the paramagnetic phase, while for $T < T_{EPR}$ it increases till a maximum value of 2.09 for the MZFO sample. This behaviour seems to point out the presence of homogenous magnetic phases characterized by weak interactions that leads to a microscopic superparamagnetic behaviour, as pointed out by the analyses on the magnetic response, previously described.

Also the trend of the signal line width, ΔH_{pp}, is consistent with a transition

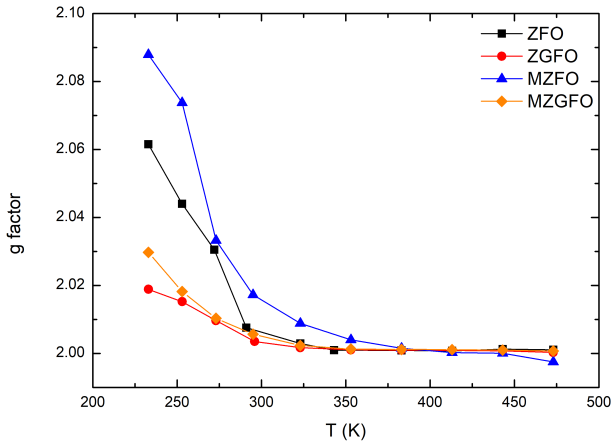

Figure 4.25: Trend of the g-factor as a function of temperature for all the investigated samples.

from a paramagnetic to an ordered magnetic phase or a superparamagnetic one, as in our case, by decreasing the temperature in the investigated temperature range, as reported in Figure (4.26).

From the trend of the ΔH_{pp} vs temperature, it is possible to clearly observe the transition from a paramagnetic state to a superparamagnetic one for each sample. In particular, the T_{EPR} values are well consistent with the one of T_B extracted form the magnetic measurements, previously described: a greater value of T_{EPR} for the MZFO sample with respect to the pure one, a smaller value for the ZGFO sample, while an intermediate value for the double-doped sample.

This evidences seem to confirm a possible SPM behaviour still at room temperature for the MZFO sample.

Another proof supporting the thesis of a SPM behaviour for all the investigated sample, it has been given by the estimation of the paramagnetic centres from the integrated area of the signals compared to the one proper of a standard (Pitch).

Indeed, the number of paramagnetic centres which has been estimated assuming that Fe^{3+} ions with a 5/2 spin contribute to the recorded EPR signal,

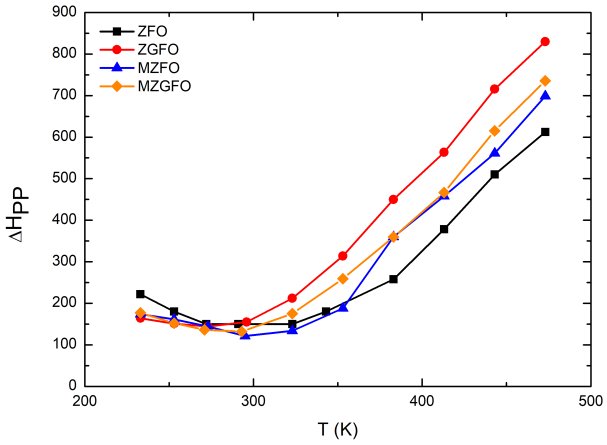

Figure 4.26: ΔH_{pp} vs temperature for all the investigated samples.

turns out to be 1.2 $\times 10^{24}$ for ZFO and MZFO samples, and 1.08 $\times 10^{24}$ for ZGFO and MZGFO ones. The estimated values are greater than the expected one in all the investigated samples. This supports the hypothesis of a SPM behaviours and also it is consistent with the observed magnetic behaviour.

The obtained results seems to indicate the presence of the only zinc ferrite spinel phase in a SPM phase also at room temperature, although the presence of an extrinsic iron oxide phase under the detection limit could not be surely excluded, in particular in case of the Mg doped sample.
However, the pure and doped zinc ferrite samples, subject of our previous works [112, 124], have been also investigated through EPR spectroscopy and, in some cases, the potential of the EPR probe has allowed us to safely attribute the extrinsic nature of the SPM behaviour for samples that have displayed the growth of haematite characteristic features in the Raman spectra collected under thermal cycles and, at the same time, for which the XRPD investigation has excluded the presence of spurious phases. One interesting sample is the one doped with 5% of Calcium.
The choice to reported this explanatory case is aimed to highlight that when an extrinsic iron oxide phase is present in an amount higher than the detection EPR limit, but lower than the XRPD one, the EPR probe allows to safely assert the extrinsic nature of the observed SPM behaviour.
For the Ca doped sample, XRPD patterns have clearly demonstrated its purity phase and the Raman investigation has revealed the phase instability under laser irradiation with the growth of haematite peaks. As already described, two possible source of this behaviour can be identified: i) the presence of traces of maghemite; ii) a high defectiveness of the external shell in zinc ferrite NPs. The EPR inspection has allowed us to unravel the real source.
Indeed, for this sample, the derivative EPR signal, for T $>$ 320 K, clearly

shows the presence of two contributions displaying a different behaviour by varying the temperature: as the temperature increases, the intensity of the component due to the spinel ferrite phase progressively decreases, while the contribution of the magnetic order phase at higher g prevails. From Figure (4.27), it is possible to appreciate that the experimental signals recorded at 363 and 383 K are well reproduced by the sum of the ferrite component at $g = 2$ and the one at $g > 2$ due to the magnetic ordered phase. In particular, while the intensity of the $g > 2$ component remains unchanged, the intensity of the component proper of the spinel ferrite reduces by increasing the temperature as it is expected for a pure paramagnetic phase.

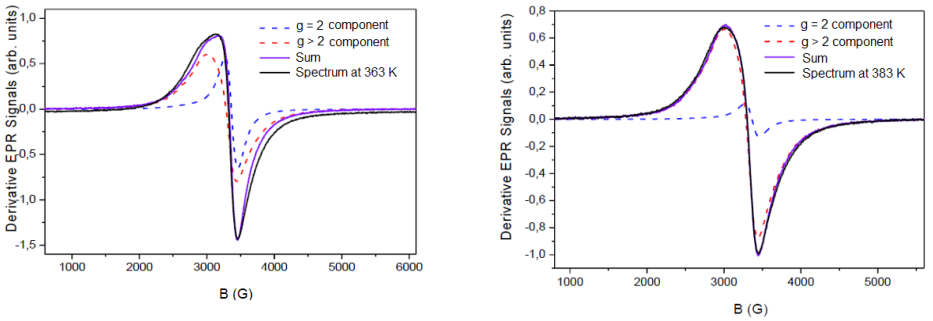

(a) (b)

Figure 4.27: Comparison between the experimental signals recorded at (a) 363 and (b) 383 K and the simulated ones for the Ca doped zinc ferrite sample.

Chapter 5

Other Raman activities in material science: hits and troubles

During my PhD course I have expanded and refined my experimental expertise in Raman spectroscopy also dealing with topics not strictly related to the focus of my activities but in any case well placed in the functional material frame.
In addition, concerning the main focus of my activity, we are moving forward and we have tried to synthesize and characterize SERS substrates based on zinc ferrite nanoparticles. Anyway the maturity of this new step is not enough and we have only some preliminary results. Thus, this chapter allows to: i) indicate the direction we are moving on, ii) highlight the versatility of Raman spectroscopy on studying different materials in the field of material science, iii) underline its ability to extract important structural information that deeply affects the functional properties of the investigated systems.
In this frame it naturally emerges the reality of a research activity; indeed, the successful results that one presents, are only the final stage of a long and deep investigation often full of troubles to be resolved. In this regard, behind the published data, there are often attempts and strategies put in place to overcome what is wrong. Sometimes, this type of work does not appear in the publication, but it is one of the most stimulating aspects of a research activity.

In all the reported case studies, Raman spectroscopy has been used within a multi-technique approach, but since the aim is to highlight the hits and troubles of the Raman investigation, I will precisely present the RS results of the performed analyses. Anyway, in order to corroborate their validity, in some cases, they will be discussed in terms of the results obtained with the other techniques.

5.1 Open projects

5.1.1 Hybrid substrate: $ZnFe_2O_4$/MPTS/Ag nanoparticles

The deep studies conducted on both SERS metallic substrates (Chapter 3) and zinc ferrite nanoparticles (Chapter 4) are also aimed to developed hybrid substrates. In particular, we would like to engineer hybrid substrates made up of zinc ferrite nanoparticles (NPs) properly decorated with metallic NPs with two possible applications: i) as SERS-active substrates exploiting the enhancement mechanisms from both metallic and ferrite nanostructures, ii) as coupled-nanostructured devices for biomedical purposes.
As regard the second possible application, the aim is to exploit the superparamagnetic properties of ZFO NPs, as for instance for hyperthermia treatments on cancer cells, and at the same time the sensitivity of SERS through the enhancement mechanisms carried out by means of the metallic NPs. A further development could be also the addition of therapeutic molecules, generating, in this way, complex theranostic systems.

The first attempt has been aimed to realize the simplest combined structure in view of the possible biomedical application, previously described. In particular, we have prepared zinc ferrite nanoparticles, starting from a standard nanosized powder (Sigma-Aldrich), embedded in an external 3-Mercaptopropyltrimethoxysilane (MPTS). The S-H terminal bonds of MTPS allow the Ag nanospheres to attach to this core-shell structure. A schematization of the synthesis process is reported in Figure (5.1).
We are still studying the correct proportions between ZFO and Ag NPs as

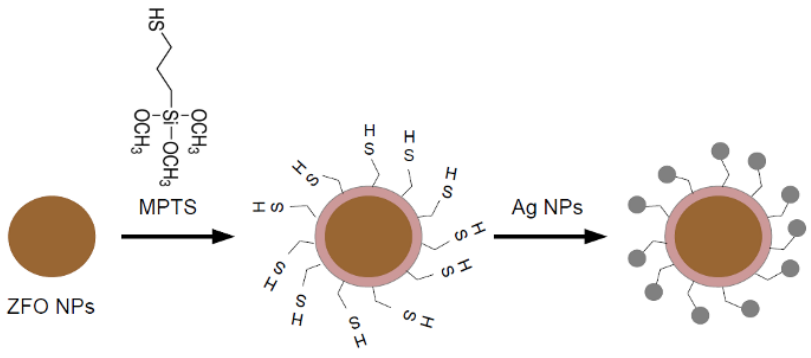

Figure 5.1: Schematization of the hybrid $ZnFe_2O_4$/MPTS/Ag nanoparticles.

well as refining each single step of the synthesis route in order to achieve performant colloidal suspensions and, in turn, high enhancement factors. However, first tentative steps forward have been done and preliminary results have been achieved.
We have prepared a colloidal suspension of $ZnFe_2O_4$/MPTS/Ag NPs with a ratio 1:1 of ZFO and Ag NPs. We have tested this sample with the well-known

Rhodamine 6G (R6G) with a 10^{-5}M concentration. In Figure (5.2), the raw SERS data are reported. As it is possible to notice in the inset of the Figure the characteristic R6G peak centred at about 614 cm^{-1} is recognizable, despite its low intensity.

In order to understand if the ZFO structures is preserved after the synthe-

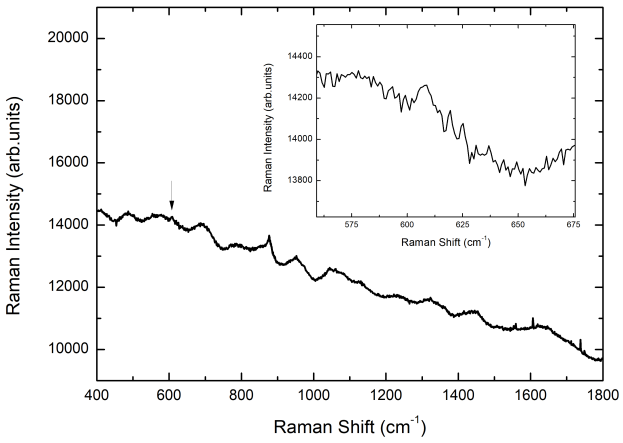

Figure 5.2: Raw SERS data collected from the 1:1 $ZnFe_2O_4$/MPTS/Ag NPs sample. Inset: the 614 cm^{-1} peak of R6G is highlighted.

sis process, we have taken a 20 μl drop of the colloidal suspension and let it dry on a microscope glass. Thus, we have investigated the outer region of the dried drop where, as a consequence of the coffee-ring effect, the ZFO NPs are concentrated. The collected Raman spectrum is reported in Figure (5.3) together with the Raman spectra of the starting Sigma-Aldrich zinc ferrite powder and the UV Raman spectrum of a pure ZFO sample, synthesised by our group through co-precipitation route (see Chapter 4). As it is possible to observe the characteristic Raman band of the ZFO NPs in the range 600-700 cm^{-1} is clearly visible in the spectrum of the dried drop, although it is weaker and broadened with respect to the one of the starting ZFO powder. Moreover, the contribution of the 600-700 cm^{-1} band peaked at higher energy, that, as already described, is ascribed to the Fe-O vibration in the tetrahedral unit, is more pronounced in the spectrum of the dried drop.
These observations prove the presence of the ZFO NPs in our hybrid devices and they could suggest that the ZFO NPs seem to display a more disorder structure with a possible Zn deficiency in the outer shell.

The outcome of this first preparation has also been verified through UV-Vis absorption and Z potential measures. In particular, in Figure (5.4), the absorption spectrum of our sample is reported in comparison with the one of pure ZFO NPs and the colloid of Ag nanospheres. In the absorption spectrum of our sample, displaying the same features of the ZFO one, a slight shoulder

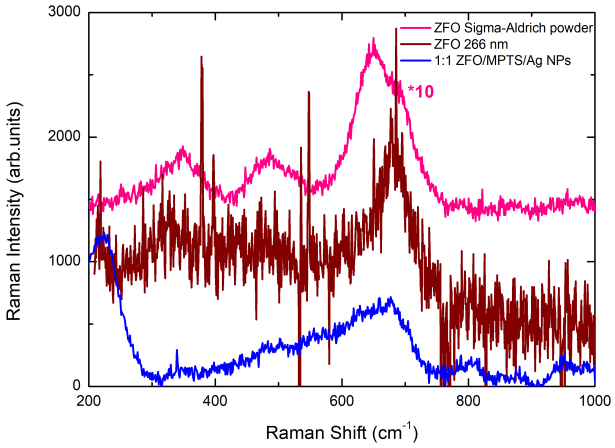

Figure 5.3: Room temperature Raman spectra of powder Sigma-Aldrich zinc ferrite nanoparticles (pink), pure ZFO NPs samples, synthesised through co-precipitation route and recorded with 266 nm laser source, (brown) and a dried drop of 1:1 $ZnFe_2O_4$/MPTS/Ag NPs sample.

at about 400 nm, namely in the region where the Ag NPs absorption peak falls, is clearly visible, providing the evidence of the presence of both ZFO and Ag nanoparticles. Finally, an indirect proof of the formation of the coupled

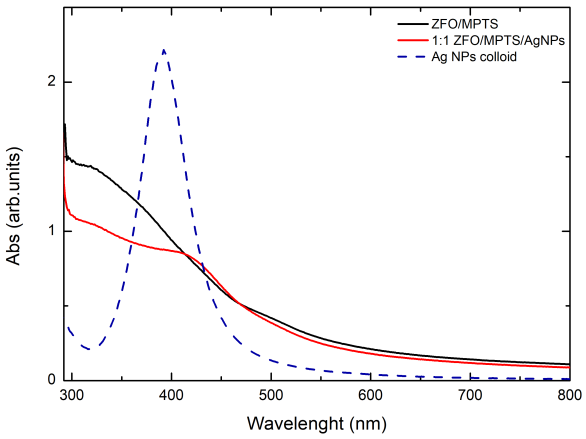

Figure 5.4: UV-Vis absorption spectrum of the 1:1 $ZnFe_2O_4$/MPTS/Ag NPs sample. For comparison, also the absorption spectra of zinc ferrite nanoparticles and Ag nanosphere colloid are reported.

ZFO and Ag nanostructures has been giving by Z potential measures. Indeed, the Z potential of the only zinc ferrite nanoparticles is positive (20 mV), while the MPTS covering have led to an opposite negative potential (-20 mV) and finally the addition of the Ag nanospheres have slightly changed the absolute

value of the potential which remains still negative (-17 mV).

After these first steps, we will try to improve the chemical matching between Ag and ZFO nanoparticles, in particular using home made zinc ferrite ones with different grain sizes and prepared by varying the synthesis methods. Moreover, as already introduced in the beginning of this section, we will evaluate proper functionalizations in order to develop theransotic systems.

5.1.2 ZnO and CeO_2 nanoparticles bonded with cancer cells

An other ongoing research project concerning the study of oxide-base systems, deals with the investigation of ZnO and CeO_2 nanoparticles bonded with cancer cells. This research activity has been developed thanks to the collaboration with the research group headed by Prof. Anselmi Tamburini of the Chemistry department of University of Pavia, very active in the field of complex oxide materials and their applications, and with Prof. Sommi of the Molecular Medicine department which provides the biomaterials and performed the incubation procedure for oxides fixing.
Indeed, different studies have been performed on the beneficial uses of this kind of nanostructured oxide based systems in treating human diseases. As regards CeO_2 nanoparticles, they are deeply investigated for their promising properties in several diseases involving, in particular, free radicals or oxidative stress. As for instance, these oxide nanoparticles reduce inflammation caused by reactive oxygen species and reactive nitrogen species [148] and they display selective anticancer activity [149]. CeO_2 nanoparticles seem also to be effective in the treatment of Alzheimer's disease [150]. For these reasons, also studies of the modification of the CeO_2 nanoparticles occurring upon their internalization in human cells, have been carried on [151].
ZnO nanoparticles have received great attention for their biomedical application. Indeed, different studies have been performed on ZnO NPs and their ability to induce toxicity in a cell-specific manner and, in turn, if they could be used against pathogenic cells [152]. However, the toxicity of ZnO NPs has to be considered in function of the type of investigated cell. As for instance, published studies have revealed that these nanoparticles are toxic to T cells, namely type of lymphocyte that plays a central role in the immune response, but also to neuroblastoma one [153]. Moreover, a research work has pointed out that nanophase ZnO actually improves normal osteoblast function, so indicating nontoxicity [154]. Within this framework, the research activity on the possible use of ZnO NPs for cancer treatment is still open and very active.

As regard our research activity, the crucial aim is to understand how these oxides nanoparticles bind the cell membrane and which is their behaviour in a biological environment. In particular, through the Raman inspection we would like to reveal the presence of the vibrational fingerprint of ZnO and CeO_2 nanoparticles and to evaluate their structural order/disorder upon binding to HeLa epithelial cancer cells.
In both cases, the detection of the Raman spectra of nanostructured oxides has been not trivial and till now, the collected spectra are still of difficult interpretation. We have investigated cell samples incubated with ZnO or CeO_2 NPs with different incubation time, but this parameter seems to not affect the Raman investigation.
Figure (5.5) summarizes the first results obtained on HeLa cells decorated with CeO_2 nanoparticles. In particular, we have reported the reference spectra of

CeO_2 NPs (a-b), collected from two different samples and treated with polyacrylic acid before being incubated with HeLa cells, and the Raman spectrum of the polyacrylic acid (c) for comparison. The (d) and (e) Raman spectra have been collected during a mapping acquisition in a region of the sample incubated for 24 h and grown on a Petri glass, while the (f) one is proper of the same sample, but after being centrifuged and dried, obtaining what we have called pellet.

CeO_2 crystallizes in the fluorite-type cubic structure, exhibiting only one Ra-

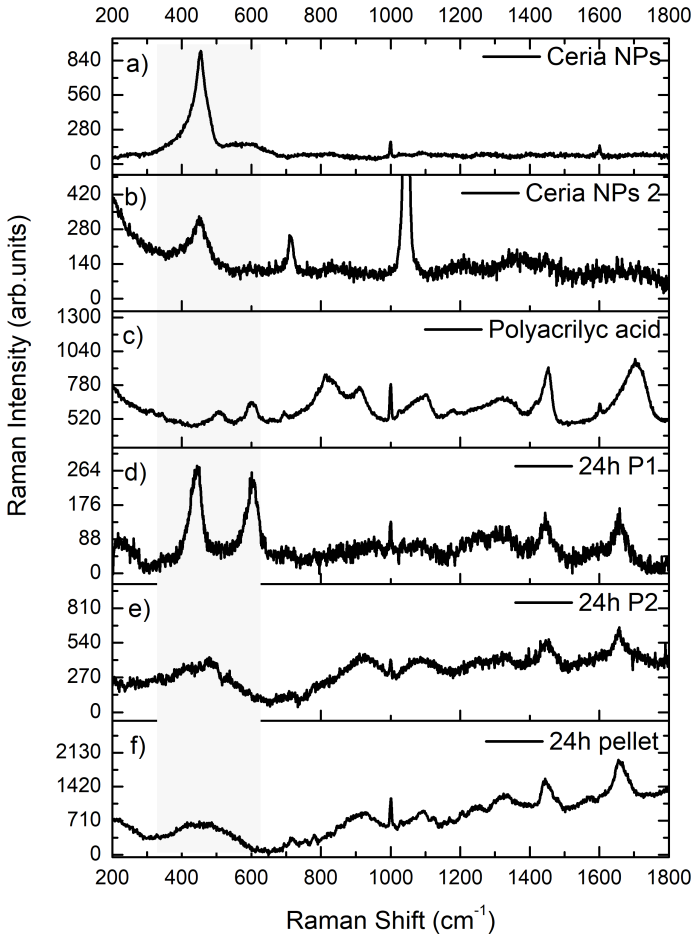

Figure 5.5: Room temperature Raman spectra of (a - b) Ceria nanoparticles treated with polyacrylic acid, (c) polyacrylic acid, (d) and (e) the HeLa cells samples incubated with CeO_2 NPs for 24h and (f) the pellet of the same sample.

man active fundamental mode at 464 cm^{-1}. This peak, a triply degenerate F_{2g} mode, corresponds to the symmetric breathing mode of six oxygen atoms around the central cerium ion [155]. Other three peaks could be observed at about 260, 600, and 1170 cm^{-1}: the peaks at 260 and 1170 cm^{-1} are attributed to second-order transverse acoustic and longitudinal optical modes,

respectively, while the mode at 600 cm^{-1} to a defect-induced mode which is generally easily observable with UV Raman measures because of resonant Raman effects, since ceria strongly absorbs in the UV region [156].
In general, as the particles size decreases, the Raman feature at 464 cm^{-1} tends to asymmetrically broaden and shifts to lower energies [157].
As it is possible to observe from Figure (5.5), the Raman spectra of our ceria NPs samples clearly exhibits the characteristic mode at 464 cm^{-1}, although it is quite enlarged, a possible indication of a disorder structure.
The three room temperature Raman spectra collected from the Hela cell samples incubated with CeO_2 NPs display the same Raman features at around 1400 and 1700 cm^{-1}, typical signatures of lipids and proteins in cellular material [158] and a sharp peak at 1000 cm^{-1}, proper of the polyacrylic acid (see spectrum (c)). However, the considered spectra show a different behaviour in the region between 400 and 600 cm^{-1}, where the Raman activity of ceria nanoparticles should fall. In particular, the (d) spectrum shows two intense and sharp features at about 460 and 600 cm^{-1} that could be assigned to crystallized CeO_2 NPs, while the (e) and (f) ones display a broaden and weak Raman band. This band is difficult to be assign to Raman features proper of ceria, although the incubation with cancer cells could have led to an extremely disorder nanoparticles structure.

Also in the case of Raman investigation on ZnO nanoparticles bonded to HeLa cells, the obtained results are difficult to be properly understood and further researches are needed. In particular, all the investigated samples display a Raman activity similar to the one reported in Figure (5.6).
The characteristic features, proper of the cellular material, are still recog-

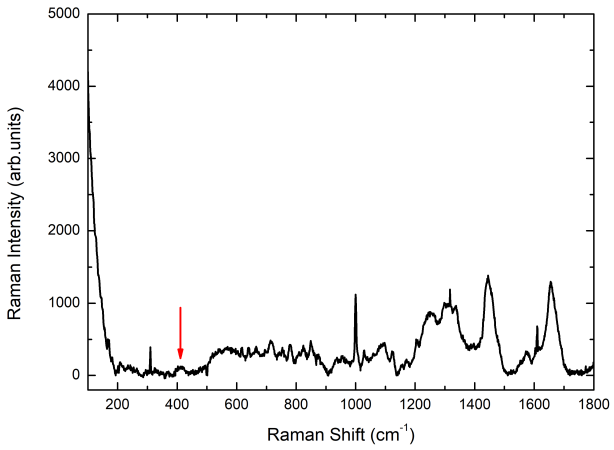

Figure 5.6: Representative room temperature Raman spectrum of HeLa cells incubated with ZnO nanoparticles.

nizable at about 1400 and 1700 cm^{-1} as well as the peak at 1000 cm^{-1} of

the polyacrylic acid with which the ZnO NPs have been treated before being incubated with the HeLa cells.
In general, the Raman spectrum of ZnO is mainly dominated by an intense E_2 optical phonon band at 438 cm^{-1} [159]. As it is possible to observe in our spectrum a very weak peak is present in the region of interest, although this mode is shifted of about 20 cm^{-1} towards lower energies with respect to the position of the E_2 mode proper of ZnO. Thus, further investigation to understand these observation are needed.

5.2 A successful use of Raman spectroscopy

5.2.1 How to assess the quality of synthesized black phosphorus

The interest in studying elemental phosphorus is due to the fact that, in recent years, this compound has emerged as one of the most interesting anode materials in rechargeable energy store devices. Indeed, phosphorus is characterized by intriguing properties like the high gravimetric and volumetric energy density, low cost and large availability [160–162].
At ambient condition, the most common forms of elemental phosphorus are white phosphorous (WP), red phosphorous (RP) and black phosphorous (BP). However, WP cannot be used for applicative purposes since it is chemically unstable and highly reactive because of the bond-strained P_4 molecular units. As regards red phosphorous, it can reversibly combine with alkaline cations, but it displays properties not suitable for its application in batteries, namely poor electronic conductivity ($\sim 10^{-14}$ S cm^{-1}), instability toward the electrolyte and a huge volume change ($\sim 400\%$) during cation insertion/deinsertion.
Thus, the only form suitable for electrochemical applications is BP which exists in four different crystal phases, i.e. triclinic, orthorhombic, rhombohedral and cubic; however, the orthorhombic-layered structure is the most stable one at ambient condition.
Although its good electronic conductivity (~ 1 S cm^{-1}) as well as its 2D nature, the performances obtained till now when it is used as anode material are not yet satisfying, in particular as regard the cyclability [163–165]. Thus, the research on BP is still very active.
BP can be synthesized from WP or RP following different procedures as for instance, high pressure synthesis, mineralized assisted synthesis, annealing at high temperatures with melting/evaporation steps and recrystallization from Bi, Au/Sn or Hg. However, these methodologies are time and energy consuming and also quite expensive. A more convenient approach consists in the mechanochemical synthesis route which is conducted through high-energy ball milling (HEBM) on commercial RP. This synthesis method is simple and versatile, since different experimental parameters can be tuned, like balls materials, rotation speed, treatment duration as well as jar dimension and filling factor. In turn, different combinations have been performed [166–168], but without a detailed characterization of the resulting product.
Our work falls within this framework. In particular, it has been carried out in collaboration with the research group of Prof. Quartarone of the Chemical department, Physical-Chemical unit, of University of Pavia, whose research activity is mostly focused in the field of solid state batteries.
What we have performed is a detailed study of the RP to BP conversion process achieved through HEBM route. In particular, our aim has consisted in finding the easy and best way to identify the HEBM products and in correlating the synthesis experimental parameters with the product phases.

Indeed, the synthesized BP samples have been obtained by varying three parameters of the ball milling procedure, namely the milling time, t, the rotation angular speed, ω_p and the weight ratio between balls and powder, i.e. ξ or "BtPw ratio".
The BP samples have been named with the corresponding experimental parameters values used to synthesized the samples themselves, e.g. ω_p-t-ξ. In particular, the three parameters have been allowed to vary from 250 to 500 r.p.m. for ω_p, from 15 to 3240 min for t and from 10:1 to 110:1 for the BtPw ratio. The synthesis procedure is described in Appendix (A.3).

Raman spectroscopy has been used to characterize the different phosphorus allotropes at variance of different chemical ad physical parameters [169–171] and, in particular, to evaluate the phase transition from RP to BP [172, 173]. Thus, we have successfully employed the RS probe in our research work. In particular, RS has allowed us to verify the presence of unreacted RP in BP samples and also to quantify the amount of amorphous and crystalline BP phases. Moreover, Raman results well correlate with the results obtained by NMR and XRD measurements performed by the chemical group that has synthesized the investigated samples.

Results. For each sample, 15 spectra have been collected on a single linear scan of about 30 μm, and an average spectrum has been derived.
In Figure (5.7) the comparison between the room temperature Raman spectra of the RP and the processed ball milled 500-120-30 sample is reported. As

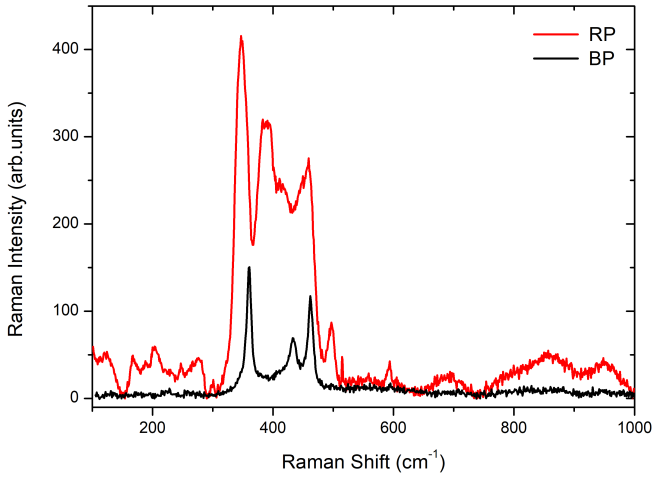

Figure 5.7: Room temperature Raman spectra of red phosphorous and 500-120-30 sample, as an example of black phosphorous Raman spectrum.

it is possible to observe, the main Raman signatures of RP appear in the region between 300 and 600 cm^{-1}, while a weaker activity is present below 300 cm^{-1}. In particular, the range from 300 to 600 cm^{-1} is characterized by

broadened and multicomponent features centred at about 347, 390, and 456 cm^{-1}. On the contrary, the Raman spectrum of the processed sample displays narrower features peaked at 354, 433, and 462 cm^{-1}. The collected Raman spectra of both RP and BP samples are well consistent with the ones reported in literature [174, 175]. However, the assignment of RP Raman active modes is really controversial, because different arrangements have been proposed to model its structure. On the contrary, the assignment of BP Raman modes is almost clearly defined; indeed, the three observed peaks are ascribed to the A_{1g}, B_{2g} and A_{2g} modes of the orthorhombic BP phase [175, 176].
By simply looking at the spectra reported in Figure (5.7), two main spectral differences can be clearly observed by passing from the RP sample to the processed BP one: indeed, the peak positioned just below 360 cm^{-1}, namely the A_{1g} mode for BP, is narrower and characterized by a marked redshift of about $\sim$ 10 cm^{-1} and also the Raman band centred at about 390 cm^{-1} disappears.
This information has allowed us to compare all the Raman spectra collected from the complete set of synthesized samples. In order to give an illustration of the general trend of the appearance of Raman modes as a function of the ball milling parameters, Figure (5.8) reports the room temperature Raman spectra in the range 320 - 480 cm^{-1} recorded at two different values of a determined ball milling parameter, while the other two HEBM ones are kept fixed. To highlight the degree of conversion from RP to BP, the RP spectra is also reported for comparison. Thus, the reported data confirm the possibility to use the Raman probe to monitor the RP to BP conversion since the appearance of a peak centred at around 390 cm^{-1} together with the broadening and blue-shift of the band at about 350 cm^{-1} clearly stated the presence of RP; on the other hand, the narrowing of the A_{1g} mode is a marker for the presence of a significant quantity of crystalline BP. However, also in this case, even if a marked peak is not observable at 390 cm^{-1}, a flat, unresolved Raman feature is present and its average intensity varies as a function of the HEBM procedure. The described spectra features can be used to semi-quantitatively extract information about the samples composition.
In particular, our strategy of data analysis is reported in Figure (5.9): I_1 is the intensity of the Lorentzian curve used to fit the Raman peak at 360 cm^{-1}, I_2 is the intensity of the flat contribution observable at around 390 cm^{-1}, while I_3 is the intensity of the structured peak centred at 390 cm^{-1} which emerges from the flat region. The intensity I_1 and I_3 are operative parameters ascribable for certain to BP and RP, respectively; while, as regards the intensity I_2, the broadened contribution to the Raman signal in this region can be ascribed to a disordered BP phase as well as to residues of an amorphous RP phase, because also the RP Raman signal displays this unstructured flat signal. Thus, the overall intensity at 390 cm^{-1} is given by $I_2 + I_3$.
Following this argument, we have derived, by using the following formula, the empirical parameter β which expresses the amount of ordered BP phase in the

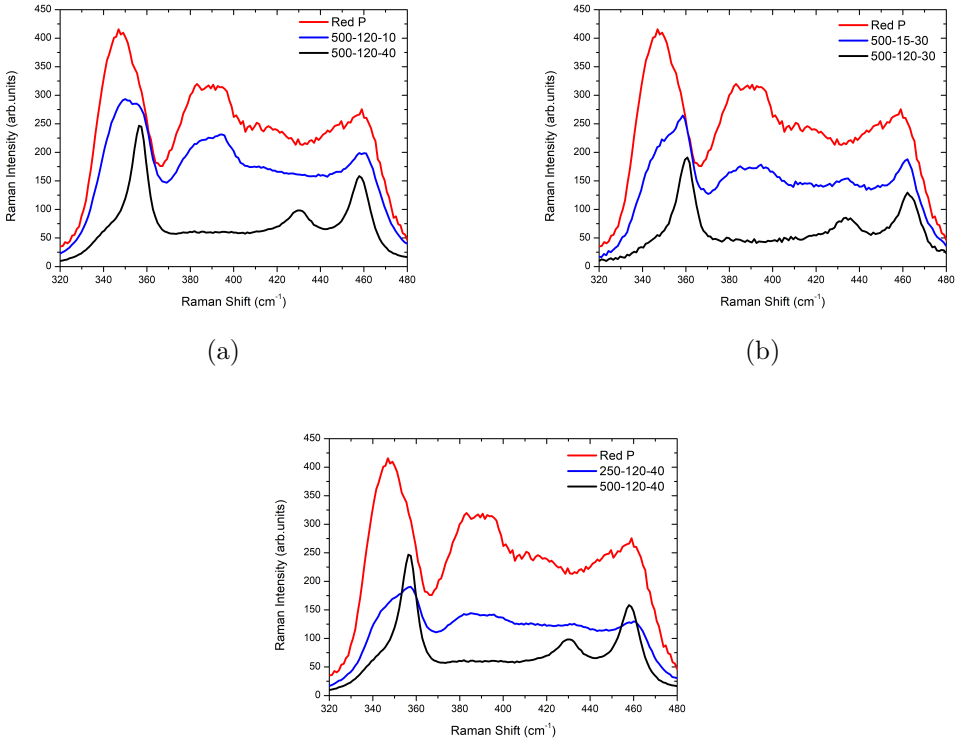

(a) (b)

(c)

Figure 5.8: A portrait of the general trend of Raman spectra as a function of the three HEBM synthesis parameters. Namely, the Raman spectra are proper of selected samples obtained at a fixed values of a) milling time and rotation speed, b) BtPw ratio and rotation speed, c) BtPw ratio and milling time.

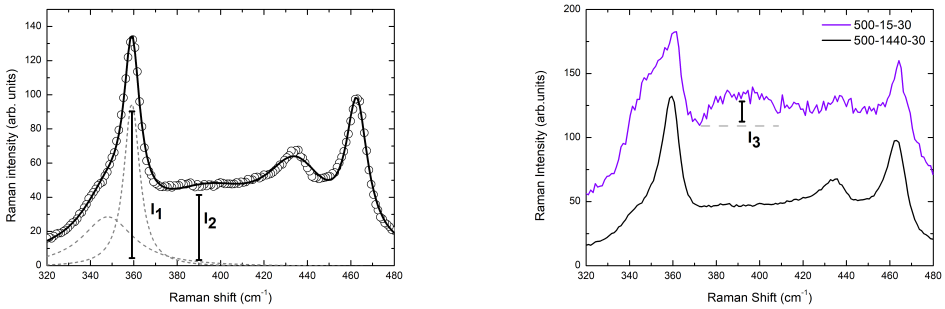

(a) (b)

Figure 5.9: (a) The result of the best-fitting procedure (the black solid line) for the Raman spectrum of the 500-1440-30 sample. The dashed lines represent the two Lorentzian components used to reproduce the Raman yield below 370 cm^{-1}. (b) Room temperature Raman spectra of the 500-1440-30 and 500-15-30 samples in the region of 320-480 cm^{-1}. In the figures, the vertical lines indicate the three intensity values used to derive the β parameter.

investigated samples for the given ball milling recipe:

$$\beta = \frac{I_1}{I_1 + I_2 + I_3} \tag{5.1}$$

In particular, high values of this parameter correspond to a high amount of BP.
To derive the β parameter, we have used the intensity of peaks instead of the integrated intensity, namely, the parameter generally used for the analyses of Raman features. However, we convinced ourselves that, in this case, a more simplified approach can be admissible because of the overlapping of the components proper of both RP and BP and also because the line widths as well as peak energies could depend on grains size and orientation [175, 177].
In Figure (5.10), we have reported the variability of β as a function of the laser spot position on the sample. As it is possible to observe, large variations of this parameter occur in samples with a lower BP amount.
In order to compare the semi-quantitative information extracted through the Raman probe with the one obtained from XRD and NMR investigations, we have derived an average β parameter over the 15 values reported in Figure (5.10) for each sample.
Figure (5.11) shows the comparison of our β values with the estimations of

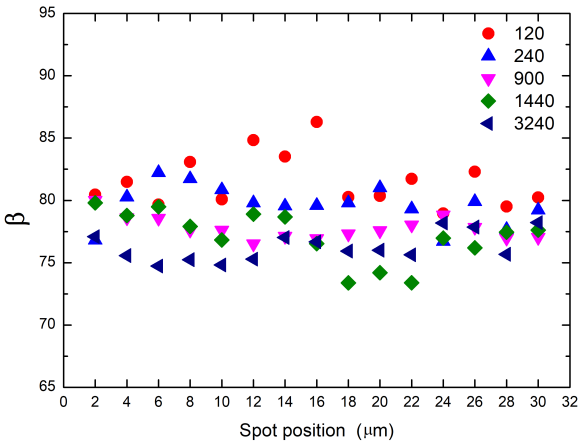

Figure 5.10: The variability of the β parameter as a function of the laser spot position on the sample. The reported values are proper of the series of samples obtained with a BtPw ratio of 30:1, rotation speed of 500 rpm and for different milling times.

the BP amount carried out by means of XRD and NMR, as a function of the ball milling parameters. As one can notice, a good agreement is matched in the trend of the BP presence, although the Raman-based estimations report slightly higher values of crystalline BP amount. This fact could be explained in terms of the different penetration depths of the optical probe with respect to the others; since, with the Raman probe, we are more sensible to an external shell of the HEBM grains whose average dimension is about 10 μm. Indeed, it is reasonable that the RP to BP conversion upon energy transfer occurs from the outside to the inner part of the grains, thus the Raman investigation can be used to assess information from the grains surface, while the NMR probes

all the grain volume, in particular for non-metallic sample like the ons herein investigated. In turn, it seems not surprising that when NMR measures give lower BP values, Raman, as well as XRD, gives about the 100% conversion rate.

The performed study focused on three experimental parameters, namely,

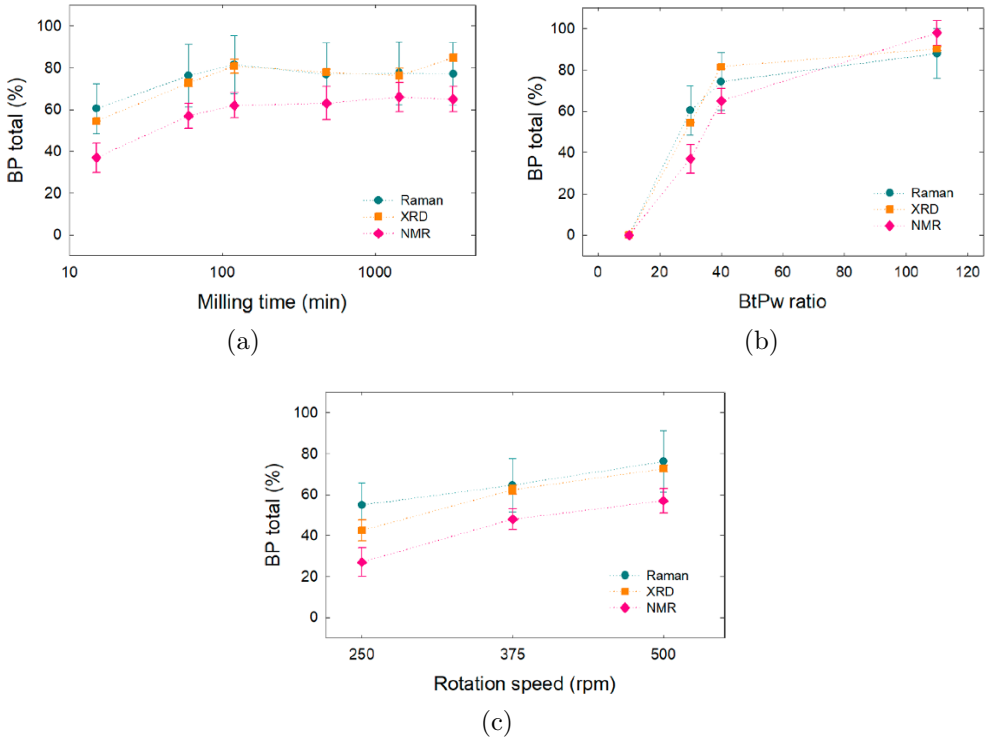

Figure 5.11: Amount of total BP determined by means of Raman (circle), XRD (square), and NMR (diamond) as a function of a) the milling time for a series of samples with a fixed rotation speed (500 rpm) and BtPw ratio (30:1); b) the BtPw ratio for a series of samples with a fixed milling time (15 min) and rotation speed (500 rpm); c) the rotation speed for a series of samples with a fixed milling time (60 min) and BtPw ratio (30:1) [178].

angular speed rotation, milling time and weight ratio between the milling balls and the material, has demonstrated that the first two experimental parameters seem to play just a minor influence on the efficiency of the RP to BP conversion process. Moreover, too long milling time may result in an increase of the disordered BP fraction. On the other hand, the BtPw ratio plays a primary role in the conversion. Indeed, a 100% conversion is achieved by using short milling times, a 500 r.p.m. rotation speed and 110:1 BtPw ratio.

5.2.2 Structural characterization of pure and doped $FeNb_{11}O_{29}$

$FeNb_{11}O_{29}$ (FNO) is one of the complex oxide compounds for which intriguing electrochemical and magnetic applications can be expected. Although the first study on this material dates back to 1976, only in recent years the interest in studying this compound as a possible anode material for lithium batteries has emerged [179].
FNO is isostructural with its parent compound $Nb_{12}O_{29}$; in particular, the insertion of iron is considered like doping because of the small number of cationic sites (less than 10%) involved in the iron substitution. As $Nb_{12}O_{29}$, also FNO presents ReO_3-type octahedral-blocks sharing edges and corners that can form both monoclinic and orthorhombic phases [180].
The substitution of iron in $Nb_{12}O_{29}$ can lead to interesting properties in terms of conductivity, namely, an important feature for its application in Li-ion batteries. Indeed, the redox couples Fe^{2+}/Fe^{3+}, Nb^{4+}/Nb^{5+} and Nb^{3+}/Nb^{4+} allow the transfer of up to 23 electrons per formula unit, leading to theoretical value of the capacity of 400 mA h g^{-1}, namely, even higher than the one of graphite [179]. The high working potential as well as the octahedral units in the open ReO_3-type structure can further improve the performances favouring the Li^+ diffusion. However, the experimental works performed on FNO, evidenced less satisfactory Li^+ diffusion coefficient as well as a poor electronic conductivity, in particular due to the oxidation states of Fe and Nb, i.e. 3+ and 5+ respectively. To overcame these limitations different strategies have been proposed, among which the doping with transitional elements working in the same potential window of Nb and Fe [181–183]. Till now only few papers have been published at this regards; moreover, also few studies report on the structural and physico-chemical properties of the two stable FNO polymorphs. Thus, we have investigated monoclinic and orthorhombic pure and Mn/V doped FNO (20% of Fe substitution) which have been synthesized by solid state method (see Appendix (A.4) for the synthesis details), in order to evaluate the influence of polymorphism and doping on structural, spectroscopic and magnetic properties of iron niobate [180]. In particular, for doped monoclinic samples, we have observed that the treatments in air have not allowed to obtain pure phases; thus, we have performed a detailed study on the the V-doped FNO sample which has been synthesized both in air and inert atmosphere, in order to improve the reaction yield and to stabilize cations with different oxidation states [184].
These studies have been realized in the frame of the tight and fruitful collaboration with Prof. Bini and co-workers, with which other important activities of my PhD have been developed.
We have approached the investigation of the $FeNb_{11}O_{29}$ samples with a multitechnique investigation. Indeed, XRPD measures have been used to determine the success of the performed doping as well as the main structural parameters of the phases through Rietveld structural refinement, SEM measurements have allowed to characterize the morphological aspects of the compounds, EPR

spectroscopy has been used to investigated the electronic population, SQUID magnetometry has been used to investigated the magnetic response and, finally, the Raman probe has allowed to monitor structural and vibrational properties. In the following, we illustrate the results obtained through the Raman investigation, while we refer to our works [180,184] to a detailed description of the results obtained with the other techniques.

Results. The spectra have been collected by using integration times of 10 s and mediated over 5 runs.
The room temperature spectra of monoclinic (M) and orthorhombic (O) pure FNO samples are reported in Figure (5.12). As it is possible to observe, the spectra are very similar to each other with the main difference in the total yield which is three times greater for the FNO-M sample. The observable Raman features are also quite similar to the ones characteristic of the so-called H-Nb_2O_5, namely the monoclinic phase of Nb_2O_5 which is usually obtained above 1000 °C, as the end-phase of the thermal route of the oxide [185]. The

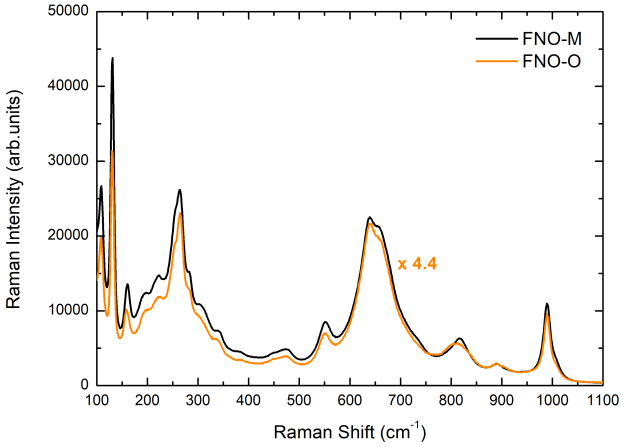

Figure 5.12: Room temperature Raman spectra of monoclinic and orthorhombic pure $FeNb_{11}O_{29}$.

two reported spectra (Figure (5.12)) clearly show three regions of intense Raman activity between 100 and 1000 cm^{-1}. Indeed, in the range 100-400 cm^{-1}, several lines can be observed with the main Raman peaks centred at 130 cm^{-1} and 260 cm^{-1}, while from 500 to 750 cm^{-1} an intense and broadened Raman feature, which is clearly the overlap of two bands, emerges and in the region above 950 cm^{-1} an other peak is clearly visible. Finally, less intense Raman features are also observable at about 470, 550, 820 and 885 cm^{-1}. Since, to the best of our knowledge, the Raman spectrum of FNO has never been reported before, the Raman behaviour of our samples can be discussed considering the Raman response of the parent compound, i.e. $Nb_{12}O_{29}$ and, more in general, the Raman response of different niobium oxides [185–188].

As it is possible to observe from Figure (5.12), the Raman yield of the orthorhombic sample is lower with respect to the monoclinic phase and this is consistent with the higher symmetry of the orthorhombic phase. On going from the monoclinic to the orthorhombic form, the rearrangement of the structure, causing long range and local changes, seems not to highly affect the Raman features in terms of bandshape, peak energy and linewidths, even if some weaker effects that will be discussed below, occur.
The Raman spectra of the monoclinic and orthorhombic doped samples are shown in Figure (5.13) and for comparison, also the spectra of pure samples are reported. The main features of the Raman spectra are still recognizable re-

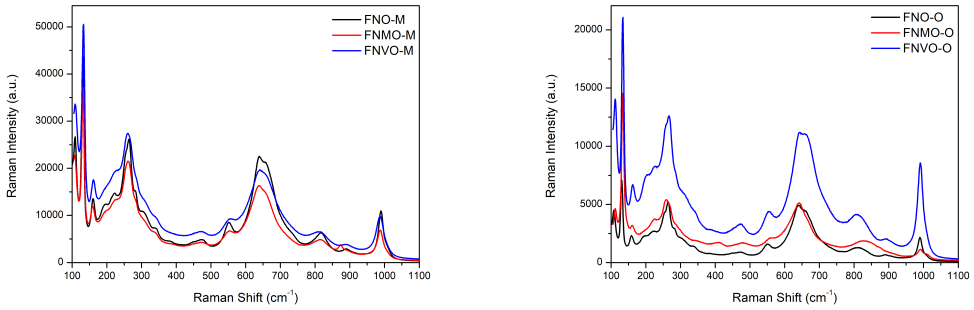

(a) (b)

Figure 5.13: Room temperature Raman spectra of pure and doped (a) monoclinic and (b) orthorhombic FNO samples.

gardless of the dopant. This is consistent with the fact that only 1 cation over 60 is replaced in the present doping. However, minor effects can be observed by looking at the Raman activity above 600 cm^{-1}. Indeed, for the undoped samples, the Raman band in the region 600-700 cm^{-1} is clearly the results of the overlapping of two components, peaked at about 640 and 670 cm^{-1}, while this behaviour is clearly reduced for the Mn-doped samples (FNMO), in particular for the orthorhombic one. On the contrary, the V-doped samples (FNVO) display a comparable intensity of the two components.
The doping with Mn ions also affects the weaker Raman features between 800 and 900 cm^{-1}; indeed, the mode centred at 885 cm^{-1} in FNO-M is shifted at 870 cm^{-1} and narrowed in FNMO-M. This mode could be due to the very intense A_{1g} stretching mode of the impurity phase $MnNb_2O_6$ [189]. Indeed, as previously introduced, the XRPD investigation has pointed out the presence of spurious phases in the monoclinic doped samples: in particular, 0.7 % of $MnNb_2O_6$ in FNMO-M and 19.5 % of Nb_2O_5 in FNVO-M.
As regard the orthorhombic phase, the Mn doping leads to an apparent conjunction of the two modes in one signal peaked at $\sim$ 840 cm^{-1}. Ultimately, also some differences can be noticed in the high energy Raman feature at 990 cm^{-1}. For the monoclinic form, the intensity of this peak is decreased for FNMO-M and increased for FNVO-M, when compared with the Raman intensity at 650

cm^{-1}. This effect is even more pronounced for orthorhombic samples: indeed, for FNVO-O, the intensity of this mode is comparable to that of the 650 cm^{-1} band, while, for FNMO-O, it is markedly decreased and split in two components.
We have also tested the thermal stability of the samples under laser heating, in order to exclude possible thermal effects induced by the laser irradiation. This has been performed by exposing the samples to the highest laser power density (5×10^5 W/cm^2) for a prolonged time. Just to give an example, we have reported the data collected before and after this thermal stress for the FNO-M sample in Figure (5.14). In particular, the intensities have been normalized in order to have the same intensity for the band in the range 600-700 cm^{-1}. In the inset the subtraction between the two spectra is reported. As it is possible to notice, the Raman spectra are completely superimposable. Since

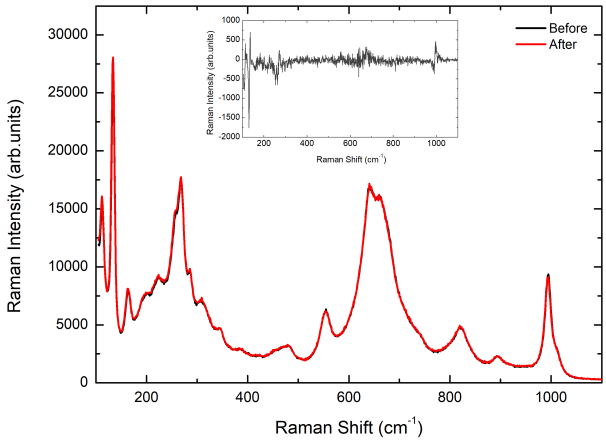

Figure 5.14: Raman spectra of FNO-M sample collected before and after the thermal cycle. Inset: Subtraction between the two reported spectra.

this behaviour is characteristic of all the other samples, we can assert that the Raman response of our samples is stable without thermal induced phase transformations. The obtained results give the indirect proof of the absence of sample regions containing Fe^{2+} ions, because, otherwise even a moderate laser heating in air should have been induced marked changes in the Raman features following the iron oxidation path [190].
The obtained Raman results can be qualitatively explained on the basis of the fundamental vibrational units in niobates; the main one is the NbO_6 octahedron, with different extents of distortion due to corner- or edge-shared NbO_6 polyhedra [188]. For the FNO compound, there are also FeO_6 (1 over 12 cations) and MnO_6/VO_6 octahedra (1 over 60) with the same vibrational behaviour.
One possible strategy to correlate the Raman spectrum with simple vibrational units in metal oxide compounds, is the so-called diatomic approximation [191],

according to which each distinct metal–oxygen bond is assumed to be completely separated from the crystalline lattice. This means that neighbouring metal–oxygen bonds in the lattice are vibrationally isolated. It has to be clear that this is a rough approximation that can not be applied to every Raman signal; in particular, in case of symmetry related Raman bands due to internal or external modes involving groups of three or more atoms, this approach can not be used.
According to [191], this is valid for longer Nb-O bonds. Indeed, the Raman spectrum of FNO below 400 cm^{-1} should be due to a mixing of bending, deformation and internal modes and thus the diatomic approximation is not valid. However, this Raman region does not show remarkable differences by varying crystal phase and/or doping.
On the contrary, the Raman activity between 600 and 750 cm^{-1} is generally correlated to the symmetrical stretching modes of metal–oxygen vibration units. These symmetry-related Raman modes should be sensitive to the local environment and so they should be affected by the monoclinic or orthorhombic form. Moreover, on the basis of the diatomic approximation, the stretching of Nb-O bonds in this region, should be characterized by a bond distance in the range 2-1.85 Å [191]. Thus, since shortening the bond distance results in higher peak energies, it is possible to assign the Raman features above 800 cm^{-1} to stretching vibrations characterized by reduced bond distances. In particular, the higher mode at 990 cm^{-1} is related to Nb-O shorter bonds as for edgeshared octahedra. Conversely, the weaker Raman bands, observable in the range 820-890 cm^{-1}, should be related to longer Nb-O bonds as for cornershared octahedra and highly distorted octahedral units, respectively [192].
Based on these results, we have analysed the most intense Raman signal at about 650 cm^{-1}, clearly composed of two modes, and the Raman signal at 990 cm^{-1}, which is narrower and more symmetric, except for FNMO-O. In particular, we have performed a best fitting procedure, using the sum of two Lorenztian curves for the mode between 600-700 cm^{-1} and a single Lorentzian function for the 990 cm^{-1} mode, expect for the pure samples, for which the peak at 990 cm^{-1} is characterized by a small shoulder at higher wavenumbers, probably ascribable to the presence of a distribution of even shorter Nb-O bonds; thus, in this last case, we have used two Lorentzian curves to perform the fit and, for the subsequent analyses, we have considered only the integrated intensity of the component at lower wavenumbers. In Figure (5.15), the performed best-fitting procedure is reported for the FNVO-O sample which has been shown as an example. Before starting the data analyses, all the spectra have been normalized in order to obtain the same value of the peak at 640 cm^{-1}.

The integrated intensities that we have derived from the fitting procedure, have been used to calculate two different parameters: S, which is the ratio between the low energy component, centred at 640 cm^{-1}, of the Raman feature in the range 600-750 cm^{-1} divided by the whole integrated intensity of this

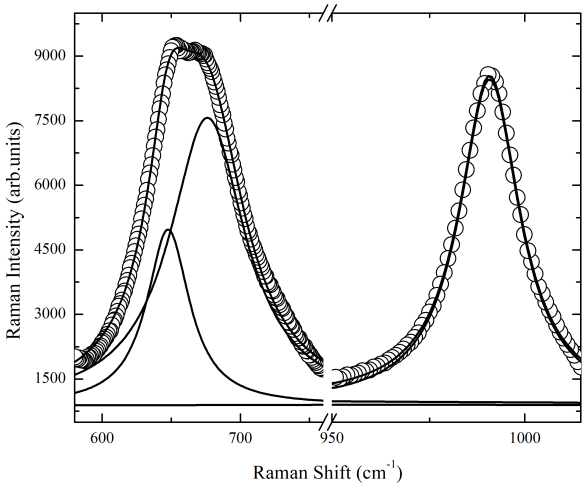

Figure 5.15: Example of the best fitting procedure performed on the Raman data proper of the FNVO-O sample in two different regions: 580-760 cm^{-1} and 950-1030 cm^{-1}.

mode and B, which is the ratio between the integrated intensity of the band at 990 cm^{-1} and the Raman integrated intensities used for the first parameter. The obtained results are reported in Figure (5.16).

The S parameter gives a measure of the symmetry degree of the Raman whole

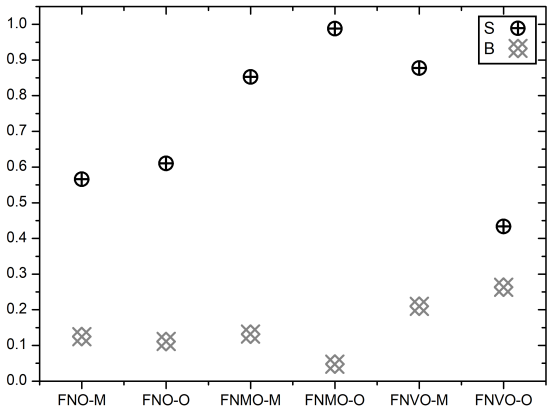

Figure 5.16: S (circle) and B (diamond) parameters.

signal due to the stretching modes inside NbO_6 octahedra and so it should be sensitive to the symmetries of the monoclinic and orthorhombic structures. Except for the FNVO-O sample, the symmetry degree is greater for orthorhombic samples, as expected. By comparing the S values for the V-doped samples, one has to taken account of the not negligible presence of Nb_2O_5 spurious phase in the monoclinic one; indeed, in the same energy region, the spectrum of

Nb_2O_5, used as starting material, is characterized by the overlapping of four clearly resolved Raman bands with an increased activity in the lower energy part [193], thus altering the estimation of S. The effect of Mn doping seems to be the reduction of distortions of the monoclinic structure. This could also be related to the presence of oxygen vacancies. The B parameter, instead, represents the relative abundance of shorter Nb-O bonds. In particular, we have observed that the estimated values are in good agreement with the ones reported in [187] for layered oxide compounds as a function of the number of blocks and the niobium amount in the unit formula. Moreover, one can notice that the B values display an opposite behaviour with respect to the S parameter, meaning that more symmetric Raman shape from the stretching modes inside NbO_6 units reflects in a lower presence of shorter Nb-O bonds.

As previously illustrated, the performed doping has not been completely successful for the monoclinic samples that present some percentages of unreactive agents. Thus, we have selected the V-doped monoclinic sample, which presents the Nb_2O_5 impurities, and we have synthesised it again through solid state route in different reaction atmospheres, namely air and inert atmosphere trough Argon flux. Subsequently, the sample synthesized in Argon flux has been treated again, in the same conditions, but in air. In the following, the samples will be named on the basis of the thermal treatment they have undergone, namely, A, for the synthesis in air, F, for the sample synthesized in Argon flux and R, for the sample synthesized in Argon flux and then treated again in air.
The room temperature Raman spectra for A, F and R samples are reported in Figure (5.17) in comparison with the undoped one. As it is possible to observe,

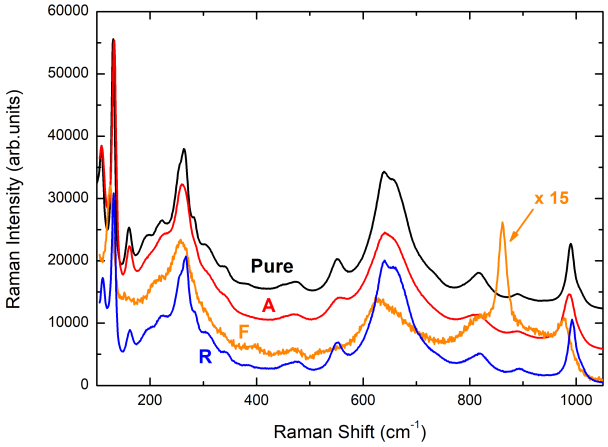

Figure 5.17: Room temperature Raman spectra of A, F and R samples together with the pure one, reported for comparison.

from the comparison with the pure sample, the characteristic features of FNO

that we have already described are present in both the A and R spectra. As regards the F sample, the whole Raman yield is markedly reduced and its Raman spectrum is characterized by very broad features clearly reminiscent of the Raman signal recorded from A sample. In general, a strong decrease in Raman activity is observed when the investigated compound displays a high degree of disorder. In our case, the main source of disorder is surely represented by the introduction of a large number of oxygen vacancies in the niobate structure, which in turn disturbs the long range ordering. Moreover, besides the broadening of the signal, a narrow peak is clearly observable at around 835 cm^{-1}. This is likely ascribable to the Raman mode of the impurity phase $FeNb_2O_6$, an example of metaldisordered tri-rutile structure [194]. On the contrary, the Raman spectrum of the R sample, is completely similar to the A one. This is a confirmation of the reversibility of the redox process. In particular, this has been also verified by a micrometer scale measurement of the Raman signal recorded in different areas of the sample, by progressively increasing the incident laser power density (from 5 $\times 10^4$ to 5×10^5 W/cm^2) and, thus, by gradually heating the sample through the use of neutral filters with different optical density. Indeed, by looking at the spectra reported in Figure (5.18), the Raman signal steadily changes as the laser power density increases: as the signal at around 835 cm^{-1}, proper of the impurity phase $FeNb_2O_6$, markedly reduces till its complete disappearance when the maximum power density is reached, the Raman features characteristic of the monoclinic FNO species are restored. This restoration is stable; indeed, the spectrum collected after the laser irradiation is different from the one collected at the beginning of the thermal cycle but perfectly equivalent to the one of the A sample.
Also for the A and R samples, we have estimated the S and B parameters, using the integrated intensities derived from the best-fitting procedure previously described, from the Raman spectra collected in different region of the sample. In this case, this two parameters allow to monitor the structural stability of the samples. In particular, in Figure (5.19) we report the variability of these parameters ($\delta S/S_m$, $\delta B/B_m$) with respect to their average values for A, R and pure samples. The trend in the variability of S parameter is quite similar for A and R samples as well as pure one, with values that are below 1.5%. This is a marker of a good stability of the crystal structure along the cristallites. On the contrary, the B parameters is more scattered in A sample, with a deviation from the average value often closer to 20%. This behaviour should be a consequence of an inhomogeneous distribution of shorter bonds, but more likely could be related to the presence of a large amount of unreacted Nb_2O_5 inside the sample, whose presence has been reviled by XRPD inspection. For the R sample, the deviation from the mean value is markedly reduced, which is consistent with the absence of impurity phases in the sample. Thus, this sampling indicates a good phase stability.

The reported results clearly point out that the choice of a proper atmosphere can drive the reaction path towards different phases. In particular, the

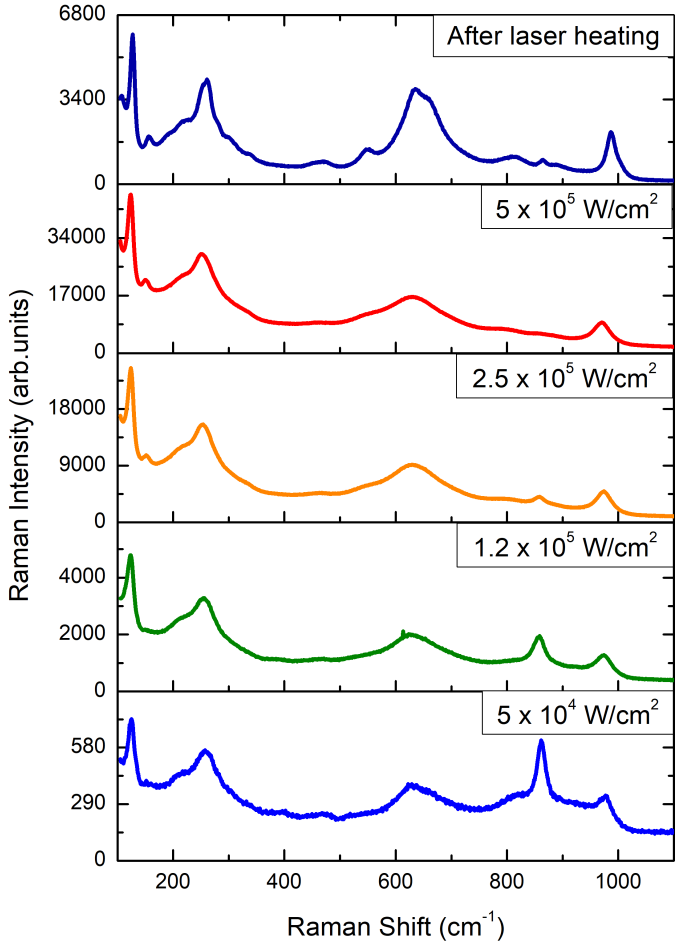

Figure 5.18: Raman spectra of the thermal cycle performed on the sample synthesized in Argon flux at variance of the incident power laser.

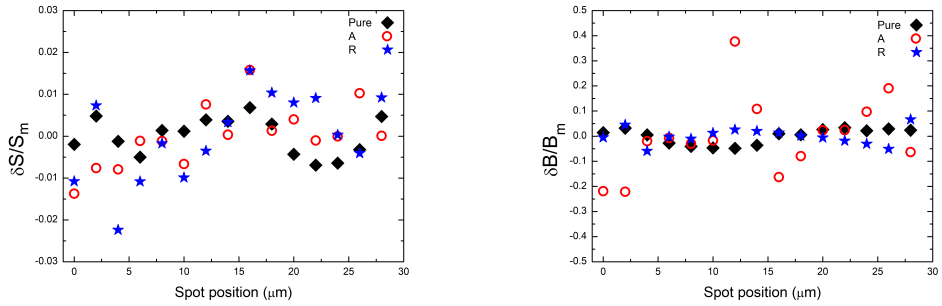

(a) (b)

Figure 5.19: Linear profile of (a) $\delta S/S_m$ and (b) $\delta B/B_m$ as a function of the spot positions for Pure, A and R samples.

intermediate step of thermal treatment in inert atmosphere seems to be an interesting synthetic way when difficulties are present in obtaining pure samples with determined oxidation states.

5.2.3 Micro-Raman investigation on dental screws for dental implants

Within this research work, we have used Raman spectroscopy to quantitatively evaluate the formation of a crystalline TiO_2 layer at the surface of dental screw-type implants made of Ti-6Al-4V (TA), also known as grade 5 titanium, and commercially pure titanium (CPT), also known as grade 4 titanium, that have undergone different manufacturing treatments. This research activity has been carried out in collaboration with the group of the department of Clinical Surgical, Diagnostic and Pediatric Sciences, University of Pavia, headed by Prof. Rizzo and Prof. Rodriguez y Baena, thanks to the efforts of Dr. Lupi.

Since its introduction in the late 1960s, titanium is still the most used material in the manufacture of endo-osseous implants [195]. The suitable physical, chemical and bio-compatibility features are due to its stable native oxide layer (TiO_2), which forms immediately when exposed to oxygen in a very low thickness (< 10 nm) [196–200]. In normal environmental conditions TiO_2 occurs in amorphous form, while crystalline forms, namely rutile, anatase and brookite, can be obtained after high temperature heating ($\geq 550°C$) or anodizing treatments [201–206]. Indeed, through the application of an appropriate heat treatment, amorphous TiO_2 transforms to the anatase, because of its lower surface free energy compared to rutile; then the anatase phase completely transforms into the rutile phase at 680°C [207]. To obtain rutile at low temperatures, precipitation of crystalline TiO_2 and hydrothermal methods are needed [208]. The biological effects of these implant surfaces have been thoroughly investigated [209].

Raman spectroscopy can be fruitfully employed to recognize the formation of crystalline or amorphous TiO_2 and, in particular, to discern between its three crystalline forms [207, 210]. TiO_2 anatase phase has a tetragonal structure with two chemical formula per unit cell, belonging to the space group $D_{4h}^{19}(I4_1/amd)$. Its Ramam spectrum is characterized by six active modes: one A_{1g} mode peaked at 519 cm^{-1}, two B_{1g} modes at 399 and 519 cm^{-1} and three E_g modes at 144, 197 and 639 cm^{-1}. Among these Raman features, the most intense one is the Eg mode, peaked at 144 cm^{-1}, whose linewidth is generally correlated to the average grain size or crystalline disorder. The rutile structure is tetragonal with two TiO_2 units per cell, belonging to the space group $D_{4h}^{14}(P4_2/mnm)$. The rutile form has four Raman active modes centred at 143 cm^{-1} (B_{1g}), 447 cm^{-1} (E_g), 612 cm^{-1} (A_{1g}), 826 cm^{-1} (B_{2g}) [210–212] and a broad band peaked at about 230 cm^{-1}, due to multiple phonon scattering processes [213]. As regards the brookite structure, it is characterised by a rich Raman spectrum with a larger number of Raman active modes, due to its lower symmetry and larger unit cell. The reference Raman spectra for the three crystalline forms of TiO_2 are reported in Figure (5.20).

In recent work [215, 216], the Raman probe has been used to investigate TiO_2

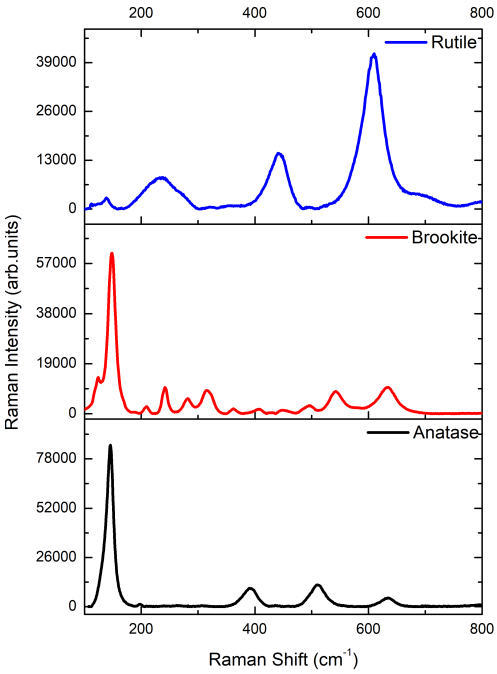

Figure 5.20: Raman spectra of the three crystalline phases of TiO_2, namely anatase, brookite and rutile, taken from the RRUFF database [214].

phases formation at the surface of commercially available titanium dental implants, subjected to various surface treatments. It has been suggested that the rapid formation of the oxide layer during manufacturing leads to an amorphous TiO_2 layer on implant surfaces [216, 217]. However, information on the formation of TiO_2 phases during manufacturing stages is extremely limited. Thus, we have analysed the Raman response of screw-form implants made of Ti-6Al-4V alloy as well as commercially pure titanium (CPT) at each stage of surface treatment. The samples, screw-type implants measuring 5.5 mm in diameter and 14 mm in length, have been produced by FMD Medical Devices (Rome, Italy).
All the samples have undergone a basic common procedure, like the one used for commercial Ti dental implants, which consists of: i) machining (milling) of the initial rod in the presence of a lubricant; ii) ultrasonication bath with solvents, and iii) packaging in glass tubes under laminar flow hood and dry heat sterilization at 170 °C for 3 h. The investigated samples differ from each other on the basis of the different surface treatments used in order to promote the formation of a thin crystalline TiO_2 layer. In particular, these surface treatments consist of: Al_2O_3 sandblasting with particles characterized by an average size of 180–200 μm; etching with a HNO_3 (64.5%) and HF (0.5%) solution for 15 s; direct current anodization at 60 V for 15 s; low-pressure plasma (LPP) treatment with Ar gas for a period of 20 min at 0.35 mbar with an

Atto Plasma Cleaner with integrated PC control. The investigated samples, correlated to the bulk starting titanium alloy and to the surface treatments that they have undergone, are listed in Table (5.1).

Code	Bulk material	Surface treatment
TA1	Ti-6Al-4V alloy	Machining
CP1	CP titanium	Machining
TA2	Ti-6Al-4V alloy	Machining + Al_2O_3 blasting
TA3	Ti-6Al-4V alloy	Machining + Al_2O_3 blasting + HNO_3/HF etching
CP3	CP titanium	Machining + Al_2O_3 blasting + HNO_3/HF etching
TA4	Ti-6Al-4V alloy	Machining + Al_2O_3 blasting + HNO_3/HF etching + anodization
TA4p	Ti-6Al-4V alloy	Machining + Al_2O_3 blasting + HNO_3/HF etching + anodization + cold plasma
CP4	CP titanium	Machining + Al_2O_3 blasting + HNO_3/HF etching + anodization

Table 5.1: List of the investigated samples correlated to the bulk starting material and the particular surface treatments that they have undergone.

Results. In Figure (5.21) the Raman spectra of the samples reported in Table (5.1) are reported in the energy range between 100-800 cm^{-1}, i.e. the region where the Raman modes of titanium dioxide should be active. Since the spectra of the TA1 and TA2 samples are completely equal to the CP1 one, we have omitted to report them. At this regard, Raman modes from different sample region or different samples have been considered equal when the peaks are centred at the same wavenumber within an interval of $\pm$ 1 cm^{-1} and the high difference in the relative intensities is less than 20%.
The reported spectra have been collected in different points of the samples both in the top and in the middle of the screw.
As it is possible to notice, the TA screw-type implants display Raman signals characterized by a very low yield and a weak, but detectable signal centred at around 143 cm^{-1}. The presence of this mode can be considered a direct proof of the formation of TiO_2 amorphous phase [216] which is characterized by a much less intense Raman signal than the one of anatase or rutile phases, but presenting a clear evidence which recalls the Raman signal the E_g mode of anatase structure.
The further surface process of TA screws, namely anodization (TA4) as well as plasma treatment (TA4p) induces a very small increase in the A_{1g} mode Raman yield [218].

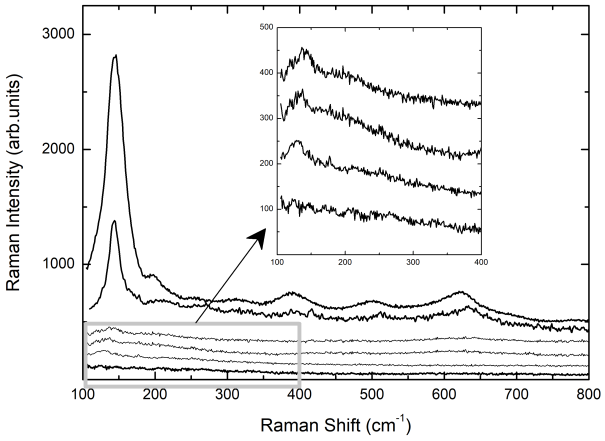

Figure 5.21: Raman spectra obtained from TA and CP implants. From the bottom: CP1/TA1 (post machining), TA3 (post Al_2O_3 blasting and HNO_3/HF etching); TA4 (post Al_2O_3 blasting, HNO_3/HF etching and anodization); TA4p (post Al_2O_3 blasting, HNO_3/HF etching and anodization and plasma treatment); CP3 (post Al_2O_3 blasting and HNO_3/HF etching); CP4 (Al_2O_3 blasting, HNO_3/HF etching and anodization). In the inset the low energy region for the TA samples is reported in order to highlight the Raman signal at around 145 cm^{-1}.

A different behaviour has instead been observed for CP dental implants. Indeed, the CP3 sample, namely the one that has undergone Al_2O_3 blasting and HNO_3/HF etching, is characterized by a Raman spectrum displaying a well defined and intense mode at 145 cm^{-1} and weaker but measurable additional Raman modes at around 400, 510 and 635 cm^{-1}. These modes represent the characteristic fingerprint of anatase TiO_2. Moreover, one can notice that in case of CP-based screws, the subsequent anodization treatment (CP4 sample) induces an increase in the whole Raman yield. This means a net increase of the crystalline order, which in any case is clearly already present in CP3 sample, namely the sample not yet anodized. Thus, it possible to conclude that the crystalline order in processed CP-based screws is missing in processed TA-based implants.
At this regard, a direct proof of a crystalline TiO_2 layer formation in CP samples versus an amorphous TiO_2 layer formation in TA ones, is reported in Figure (5.22), where the Raman linewidth of the E_g mode at 145 cm^{-1} of the (a) TA4 and (b) CP3 Raman spectra, collected in 10 different points of the samples, is reported as a function of the spot laser position. In particular, the Raman linewidth values have been derived by performing best fitting procedures in the 100-200 cm^{-1} range using a single Lorentzian curve as the fitting function (Figure (5.24a)).
In particular, the first and the last data in both the two graphs correspond to the values obtained from anatase single crystal and anatase nano-structured powders, with an average grain size of about 10 nm [219, 220]. As it is possible

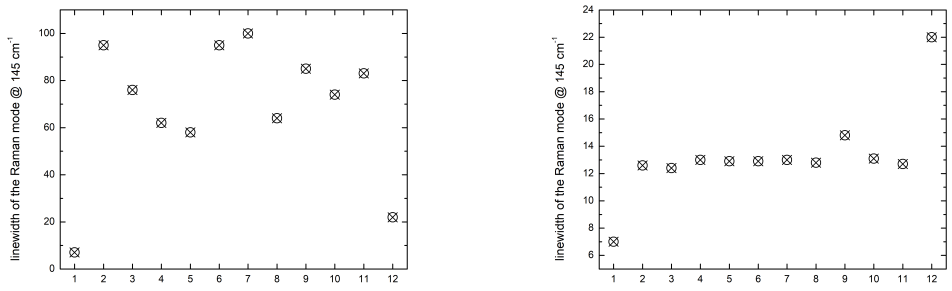

(a) (b)

Figure 5.22: Raman linewidth values of the E_g at 145 cm^{-1}, derived from the results of the best-fitting analyses performed on ten Raman spectra (point 2-point 11) for (a) TA4 and (b) CP3 samples. The first and the latter values in both the two graphs are the typical values obtained from a single crystal anatase crystal and nanosized (10 nm) powders, respectively.

to observe the values obtained from our TA4 sample are markedly scattered, ranging between 50 and 100 cm^{-1}, namely 8-14 times larger if compared to the ones obtained from single crystal (around 7 cm^{-1}) as well as from nanostructured crystals (around 20 cm^{-1}). This indicates that the titanium dioxide layer is characterized by a lacking crystal order both on the long-range and short-range scale. This is an indication of an amorphous surface layer, where in any case a weak presence of highly defective crystalline TiO_2 phase is observable. On the other hand, the reported values for CP3 sample fall within the first and the last data pointing put a good crystalline order of the TiO_2 superficial layer.
The inspection of the Raman response of all the investigated samples till 1800 cm^{-1} has highlighted the presence in different points of the surfaces of corundum Al_2O_3 phase as residual of the blasting treatment. In particular, Figure (5.23) reports the Raman signal of TA4 sample collected between 100 and 1800 cm^{-1}. The strong signal, peaked at 1390 cm^{-1} and characterized by a doublet structure, is the unmistakable fluorescence of the Cr^{3+} ion excited by the red light of HeNe laser. Indeed, as it is well known, chromium impurities are usually present in the corundum habit. Moreover, the correlation between Cr^{3+} luminescence and the presence of corundum is confirmed by the presence of the mode centred at 416 cm^{-1} which is characteristic of the Raman signal from the corundum system (see RRUFF database [214]).
One has to notice that the Cr^{3+} luminescence signal has a very high cross-section when chromium enters as substituent of Al ions in the octahedral coordination sites of the crystal lattice of corundum. Indeed it is well known that even Cr impurity amount of the order of few ppm can give photoluminescence signals quite stronger than those observed by us [221].

As a final analysis, we have tested the homogeneity of anatase TiO_2 layers in different screws by performing different Raman mapping, selecting sample areas not affected by the Cr^{3+} luminescence.

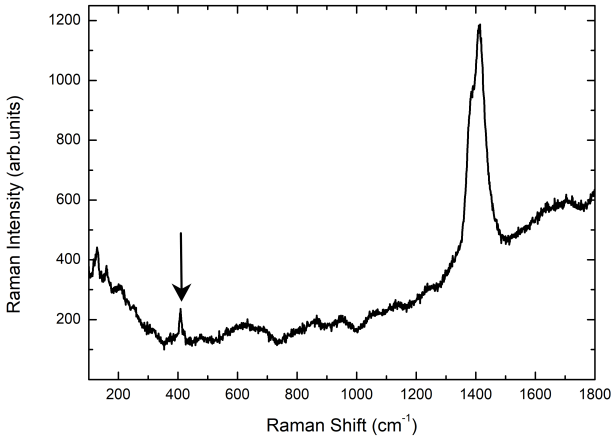

Figure 5.23: Raman spectrum of TA4 sample in the range 100-1800 cm^{-1}, characterized by the strong PL signal associated to Cr^{3+} impurities. The arrow indicates the Raman mode at 416 cm^{-1}, namely the marker of corundum structure.

The mapping has been obtained using as the intensity marker the integrated intensity of the anatase mode at 145 cm^{-1}, in particular two representative cases are reported in (Figure 5.24a) for CP3 and CP4 samples. The Raman mapping allows to give a pictorial representation of the occurrence and homogeneity of anatase TiO_2 phase, thus representing an indication of the thicknesses of anatase titania formed on the screws. In Figures (5.24b, 5.24c and 5.24d) the resulting Raman mapping for CP3, CP4 and TA4 are reported.

Important complementary information have been obtained by SEM measurements and correlated EDS analyses.
Figure (5.25) reports the micrographs proper of (a) TA1 and (b) CP4 samples collected with the Back Scattered Electrons (BSE) detector and (c) a representative Secondary Electrons (SE) micrograph of CP4 sample. For the machined surface TA implant (TA1), it is possible to appreciate a smooth and bright surface with the presence of grooves due to the turning and smoothing process of the surface. On the other hand the CP4 that has undergone all the surface processes (sandblasting, etching and anodization) is characterized by a strongly irregular surface, with indented and sharp grooves and ridges; moreover, dark areas within the bright matrix which are not observable in the only machined sample, are clearly visible. The EDS analyses have pointed out that these dark areas are corundum micrograins, present in the screw surface as residual products of the sandblasting process, since X-Ray fluorescence peaks from Al and O are largely prevalent, while the bright matrix is manly composed of titanium.
The EDS measures have allowed us to obtain complementary but quantitative information about elemental distribution among different samples. A detailed

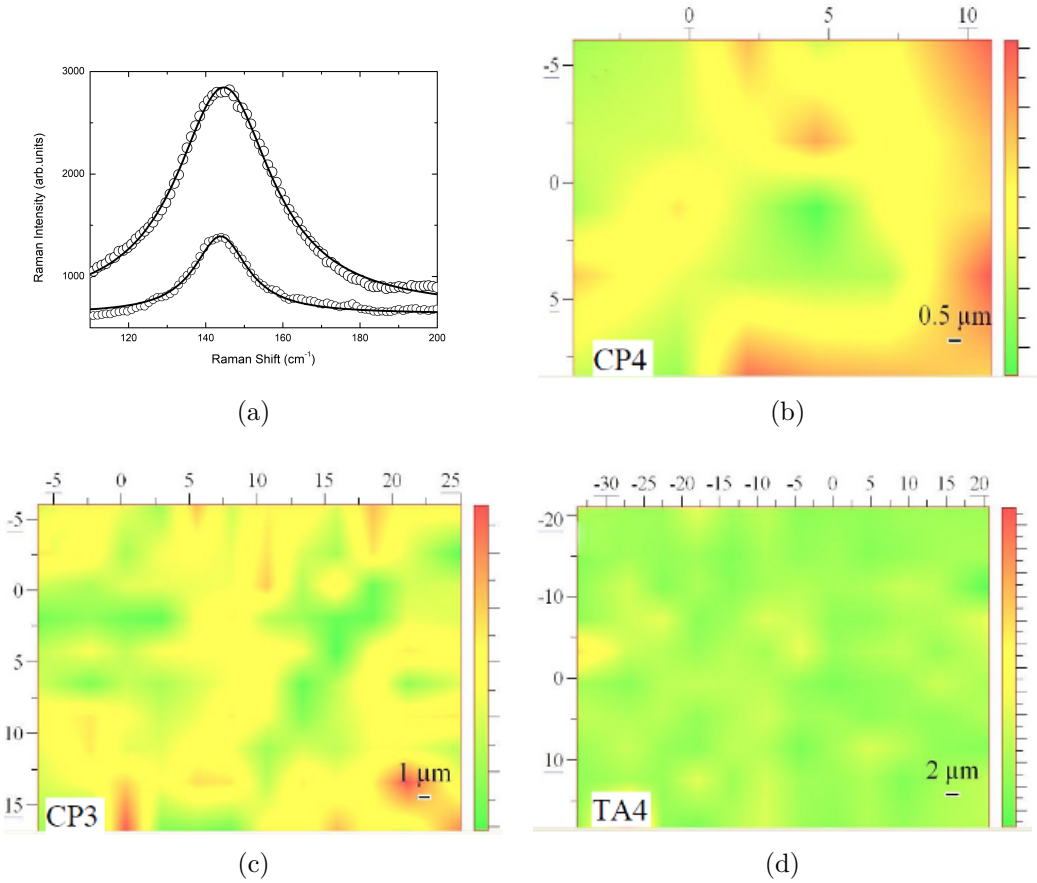

Figure 5.24: (a) Raman spectra in the region 100-200 cm^{-1} for CP3 and CP4 samples (open circle) and the best fitting Lorentzian curves (solid lines). The integrated intensities from best fitting procedures have been used to obtain: b) Raman mapping of a region of 15 × 15 μm^2 of CP4; c) Raman mapping of a region of 32 × 22 μm^2 of CP3; d) Raman mapping of a region of 55 × 40 μm^2 of TA4.

analysis has been made moving from the starting compositions of pristine materials, namely TA1 and CP1 samples, that we have used as standards for sake of comparison. We have considered for all the samples the ratio between oxygen and aluminium. Indeed this ratio reflects the amount of oxide formation not correlated to corundum residuals, but depending just from titania formation.
It is possible to appreciate an increase in the oxygen amount from the starting medium to the final precessed samples in both TA and CP series. However, the CP4 sample displays the highest O/Al ratio.
This increase could be associated to a corresponding increase in the thickness of the superficial TiO_2 layer as a result of the manufacturing process. It can be rule out that such an increase is due to the residual corundum phase because it has been verified that the oxygen percentage in a single corundum grain is almost the same for all the investigated samples.

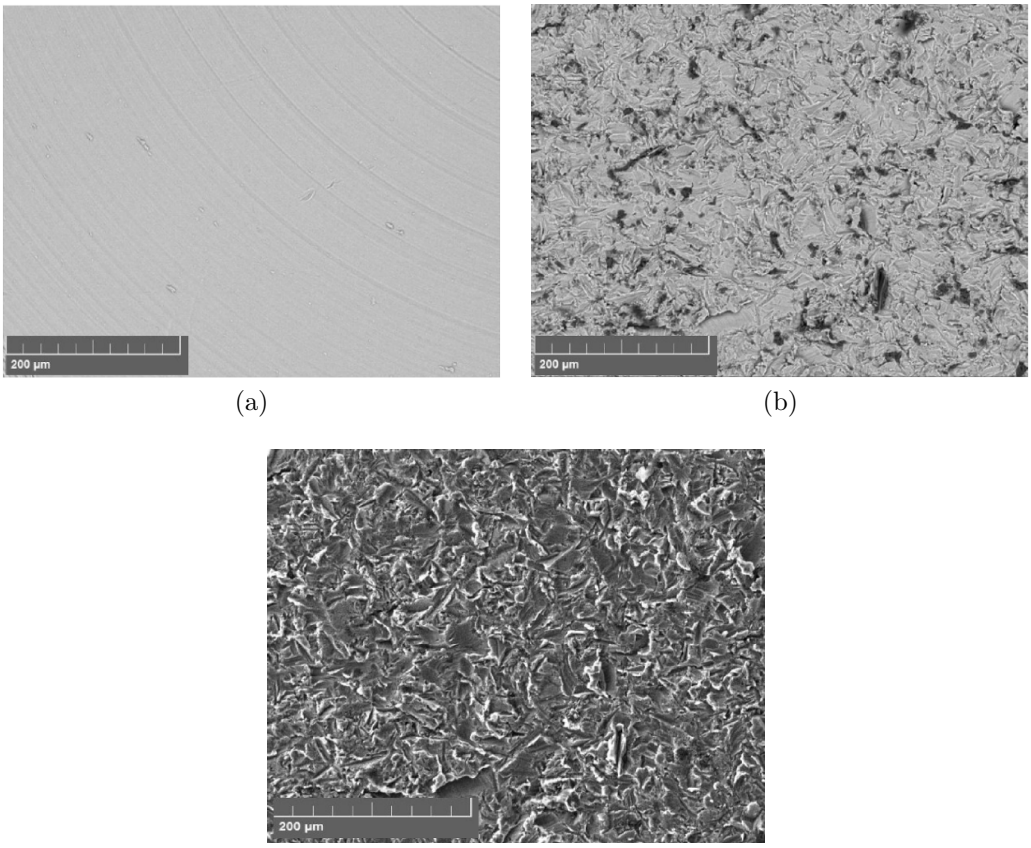

(a) (b)

(c)

Figure 5.25: SEM micrographs collected through the BSE detector for (a) TA1 and (b) CP4 samples and (c) the SE one for the only CP4 sample.

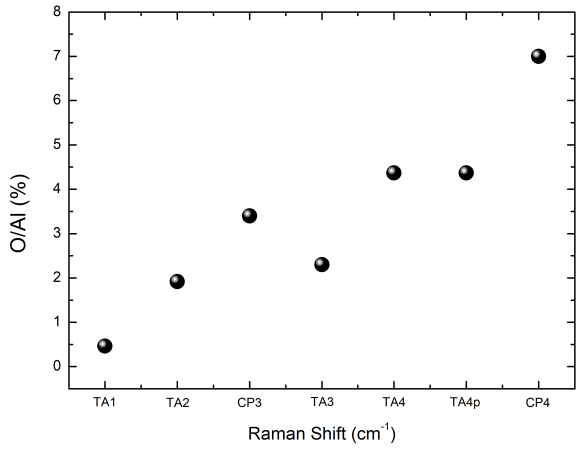

Figure 5.26: O/Al ratio in all the investigated samples. The data have been carried out by means of EDS probe.

Conclusions

At this point I should properly summarize the PhD research activity developed in these three years, but I suppose that the reader should be enough happy if I skip this point and, moving from the main results obtained, I will sketch the future steps in which I want to spend my efforts, highlighting the relative frame and the scientific goals.

The SERS study on metallic nanostructured substrates has demonstrated the feasibility of robust, reproducible and recyclable SERS chips properly functionalized with silica as well as thiols coatings for potential industrial applications, but in particular for biomedical ones, exploiting the photo-thermal activity of the metallic nano-objects. This study is framed in a collaboration with the research group of Prof. Taglietti at the Chemical department of University of Pavia. As illustrated in this thesis, within this collaboration we have obtained satisfactory results:

- we have demonstrated that the stabilization of the SERS-active layer, made up of gold nanostars, is effective and it thus not affected the enhancing properties of the metallic nanostructures;

- by varying the silica thickness, we have proved that the electromagnetic contribution to the enhancement persists till about 10 nm with a dependence on the distance from the SERS-active layer which is in accordance with the theoretical results presented in literature, while the chemical contribution is negligible;

- SERS spectroscopy, as a powerful analytical tool, has also allowed to determine the best thiol concentration in order to obtain a monolayer of covering;

- in all the investigated samples, we have also proved the homogeneity in the SERS response, thus validating the performed synthesis procedure.

These satisfactory results have been obtained on substrates which have been prepared with a fast and economic synthesis route, an aspect which is of great

importance in view of potential practical applications on large scale.

On the other side, the Raman characterization of pure and Ga and/or Mg doped nanostructured zinc ferrite spinels ($ZnFe_2O_4$) (ZFO) has produced intriguing results on their structural and crystalline properties. This study, carried out within a multi-technique approach, has been performed in collaboration with the chemical group of Prof. Bini at the Chemical department, Chemical Physical unit, of the University of Pavia.
This oxide system displays important magnetic properties that could be exploited in hyperthermia applications as well in theranostic systems. Indeed, at the nanoscale, ZFO could display a superparamagnetic behaviour in view of the rearrangement of the cationic distribution between the two sublattices, tetrahedral (A) and octahedral (B) ones, characterising the general structure of spinel oxides (AB_2O_4).
We have studied the magnetic response of these compounds through SQUID and EPR measures and we have correlated these results with the structural and vibrational properties investigated through the Raman inspection. In particular, the Raman probe has allowed us to evaluate the homogeneity of the samples at the micrometer scale and their stability under laser irradiation, evidencing the possible presence of extrinsic iron oxides phases that could affect their magnetic response. At this regard, we are likely to exclude the presence of extrinsic iron oxides in favour of a highly defective external shall of the nanoparticles. This hypothesis is corroborated by the measures performed by varying the incident laser wavelength and thus by varying the probed investigated volume. Moreover, we have been able to estimate the cationic distribution in terms of the amount of Fe^{3+} cations on the A site, i.e. the inversion degree of the spinel structure.
The obtained results both from SERS and Raman investigations have inspired to start a new research project aimed to design sensing devices made up of Ag nanospheres and zinc ferrite nanoparticles for biomedical applications. The task is to exploit the sensitivity of the SERS response of the nano-metallic systems and the superparamagnetic properties of nanostructured zinc ferrite. In this regard, we are only in the first stages of the research activity. In particular, we have prepared colloidal solutions of ZFO nanoparticles, stabilized with a MTPS layer and decorated with Ag nanospheres, obtaining evidence from Raman response about the formation of hybrid structure with signatures of the spinel phase and plasmonic scattering.

The versatility of the Raman spectroscopy as well as the experimental skills achieved during these three years research project have also lead me to deal with different thematics related to the field of material science.
In particular, we have fruitfully employed the Raman probe to investigate the properties of two different materials, namely black phosphorus and the complex oxide $FeNb_{11}O_{29}$, which are arising great interest for their peculiar properties

that make them suitable to be used as anode materials in solid state batteries. In these studies performed in collaboration with two different research groups of the Chemical department of University of Pavia, Raman spectroscopy has allowed us to extract important information on the structural order/disorder of the investigated samples and the obtained results have been validated by the information obtained by means of other probing techniques.
Furthermore, we have obtained very interesting results applying Raman probe in a highly applicative frame, i.e. to investigate the surface formation of a thin TiO_2 layer on dental screw-type implants. The anatase/rutile layer formation can improve the biocompatibility of the implants ensuring a durable and healthy implantation. The oxide formation has been monitored at variance with pristine materials (Ti-based alloy or commercially pure Titanium) and with machining and polishing and irradiation post-processes. In particular, we have been able to identify the formation of a crystalline titanium dioxide layer with an anatase form for samples made up of the more pure titanium starting alloy; in addition we have observed that the titania formation is insensitive to the plasma irradiation, contrarily to what reported in literature.

To conclude, I think that we have enough elements to support an affirmative answer posed in the title of the presence thesis. Indeed, Raman spectroscopy has allowed to deepen the knowledge on complex systems, but at the same time the complexity of the studied systems has allowed me to manage some intriguing basic aspects of the Raman effect that will be stressed in my future activity, as for instance the design and testing of new hybrid structures based on metallic nanoparticles and spinel oxides.

Perspectives

The research activity developed during my PhD has opened the way to different intriguing open projects that will characterize my following studies and that have been partially introduced in the final Chapter of this dissertation.

At first, I will continue the study on hybrid sensing devices made up of Ag and ZFO nanoparticles, trying to identify the best synthesis procedure with the support of the research group of the InLab laboratory, in order to achieve the best performant properties of these samples in terms of stability and enhancing capability.
The results that will be obtained, will be also exploited to further understand the physics at the basis of hybrid devices in order to design SERS-active substrates in which the enhanced effect will arise not only from the metallic part, but also from the oxide one. At this regard, our aim is to develop a deep theoretical study on zinc ferrite nanoparticles by performing proper simulations on their scattering properties; this will allow us to better design the geometry of the ZFO nanoparticles to achieve higher enhancement.

Against the background of the research on SERS effect, a large part of the future activity will be framed in the PRIN project SUNSET - SUpramolecular and Nanostructured Systems for the analysis of Emerging pollutants through optical Transduction. This project is focused on the development of sensor systems in order to efficiently analyse the class of the so-called emerging pollutants (EP) in the framework of water pollution. Indeed, the topic of water pollution is gaining more and more relevance, considering the importance of water for the life sustainability. Moreover, the huge amount of chemicals that can be found in the environment makes the problem even more stringent, because the group of materials affecting the water quality with potential environmental and toxicological risk is really enormous.
These contaminants include mainly chemicals that can be found in pharmaceuticals, personal care products, pesticides, industrial and household products, metals, surfactants, industrial additives and solvents. Their presence in water can cause chronic toxicity, endocrine disruption in humans and aquatic wildlife and the development of bacterial pathogen resistance [222].
These chemicals are currently detected by off-site analysis which requires collection, transportation, eventual pre-treating of the sample, and expensive instrumentations and specialist staff. Thus, the implementation of devices able to allow rapid *in situ* detection of target analytes would result in a dramatic impact in all the fields of environmental control with significant economic benefits.
The development of chemical sensors has been conceived to bypass restrictions related to classical analytical protocols and supports the use of conventional laboratory techniques for environmental control. Although the technology of chemical sensors already exists, its application on emerging pollutants detection is complicated by the large number of compounds that makes difficult the design of appropriate receptors.
Within this framework, the project aims to demonstrate the possible development of chemical sensors, targeting different model analytes chosen as representative of three different classes of EPs: antibiotics, non-steroidal anti-inflammatory drugs (NSAIDs) and plasticizers.
Our contribution will be focused on the exploitation of SERS sensitivity in the emerging pollutants detection through the use of SERS solid substrates exploiting the economic and cheap synthesis strategies illustrated in this thesis for SERS metallic substrates. In particular, the SERS-active layer will be coated with a layer of thiolated supramolecular hosts in order to exploit the specific recognition given by supramolecular interactions and the ability of SERS to give a specific fingerprint of a target molecule or a specific change of the SERS spectra of the host molecule upon guest recognition.
In practise, the experiments will be focused on identifying changes in SERS spectra of hosts as well as detecting SERS spectra from the guests upon identification of selected host/guest couples yielding the best selectivity performances.
For all SERS experiments Raman parameters like, peak energy, linewidths and integrated intensities, will be analysed as a function of excitation, concentra-

tion and preparation procedures, of course evaluating the enhancement factor. The final goal of this part of the project is to obtain SERS sensing chips which can be implemented on portable Raman apparatus for field analysis of emerging pollutants. These activities will be also useful to increase knowledge and perspectives in the water cycle and just for this I will contribute to the project Circular Economy for Wealth and Energy (CE4WE) 1139857 CALL HUB 2018 Ricerca e Innovazione granted by Regione Lombardia, headed by University of Pavia in which our research group is involved.

Another intriguing open project concerns the study of CeO_2 and ZnO nanoparticles bonded with HeLa epithelium cancer cells. We have only made first steps on this theme. The aim is to use Raman spectroscopy to identify the changes in the structural ordering of these oxides that occur as a consequence of their bonding with cancer cells. We foresee also to perform UV Raman measures in order to better evaluate also the cell response.

I would like to conclude by thanking some of the people which have allowed me to carry on my research activity. In particular, a first special thanks goes to Prof. Taglietti. Through its collaboration I have been able to perform all the intriguing studies on SERS effect and, moreover, he has given me the possibility to learn about the chemical aspects at the basis of our studies, also allowing me to participate to the synthesis preparation of the investigated samples.
Certainly, I have to express my gratitude to Prof. Bini and her group. We have collaborated not only in the study on zinc ferrite, but also we have faced different thematics in the field of material science.
I would like to thank also all the professors with whom I have collaborated in the different described projects, namely Prof. Anselmi Tamburini, Prof. Sommi, Prof. Quartarone and Dr. Lupi. A kind thank also to Dr. D'Amico which has assisted us during the UV Raman measures performed at the IUVS-line at the Elettra synchrotron in Trieste. The final acknowledgements go to Prof. Alvaro which has allowed me to get access to his laboratories in order to perform 532 nm Raman measures and also to Dr. Tredici which has allowed me to assist her in performing SEM/EDS measures at the Arvedi laboratories.

Appendix A

Sample preparation

A.1 SERS metallic substrates

A.1.1 GNS synthesis

GNSs have been prepared in water using a seed-growth method [97,99,223,224]. The seeds preparation is the first step in the synthesis of the GNS colloid. In particular, they have been prepared in a vial by adding 5.0 ml of LSB aqueous solution (0.2M) and 5.0 ml of $HAuCl_4$ aqueous solution (5×10^{-4} M). Subsequently, 600 μl of an ice-cooled solution of $NaBH_4$ in water (0.01M) have been added to the pale yellow solution of $AuCl_4$ which has been obtained in the previous step. The as prepared brown-orange solution has been gently hand-shaken for a couple of second; this solution is efficient for the growth procedure of GNS for 180 min from preparation if kept cold.
The second step is the preparation of the GNS growth solution: a mixture of 50 ml of LSB solution in water at the same concentration of the seed solution (0.2M), 1800 μl of $AgNO_3$ in water (0.004M), 50 ml of aqueous $HAuCl_4$ (0.001M) and 820 μl of an aqueous L-ascorbic acid solution (0.078M) has been prepared obtaining, after a few seconds of gentle mixing, a colourless solution. Subsequently, 120 μl of seed solution have been added to give a grey-blue colour liquid, the intensity of which rapidly increased. The solution has been allowed to react without agitation for 1 h. The colloidal suspensions have been stored in the preparation flask, maintained in the dark and used within 7 days from preparation.

A.1.2 Silica-coated GNS grafted substrate

At first, microscopy cover glass slides (21 $\times$ 26 mm) have been pretreated with piranha solutions (3:1 sulphuric acid 95% and hydrogen peroxide 30 wt%) for 30 min. Then the slides have been washed in water under sonication for 3 minutes, three times and dried in an oven for 1 h at 140°C.

Subsequently, the ZERO glass samples have been prepared, in general eight slides for each preparation have been obtained. Thus, the pretreated slides have been fully immersed in a solution of APTES ((3-aminopropyl)trimethoxysilane) 10% (v/v) in ethanol contained in a Hellendhal type glass staining jar, for 5 min at 60 °C. The silanized glasses have been washed three times with ethanol under sonication. After this step, the samples have been gently dried under N_2 flux. The slides have been then fully immersed in the GNS colloidal suspension for 14 h. After immersion, the slides have been washed three times in water without sonication and carefully dried in N_2 stream. Dried samples have been stored in the dark in a box with dryers.
The ONE and FOUR samples have been prepared starting from the eight dried ZERO samples by fully immersed them in a MPTS ethanol solution 5% (v/v) for 10min. After this step, the samples have been washed three times with fresh ethanol and dried by N_2 flux. For silica deposition, the slides have been then dipped for one or four hours in a 1.5 wt% sodium silicate solution (after dilution of a 27 wt% SiO_2 solution with water) kept at 90 °C. The strongly acidic cation exchanger Amberlite IR-120 has been used for the adjustment of the pH solution to 8.5–9. After the chosen immersion time, the silica-coated substrates have been washed three times in ethanol under sonication and dried in N_2 stream. All steps are performed in Hellendhal type glass staining jars.

A.1.3 Thiol-coated GNS substrates

As usual, all the glassware has been pre-treated before use: A wash in aqua regia for 30 min, then it has been washed and filled with bi-distilled water and ultrasonicated for 3 min before discarding the water. The bi-distilled water/ultrasound treatment has been repeated three times. Then the glassware has been dried in an oven for 1 h at 140 °C. Before APTES grafting, microscopy cover glass slides (21 mm × 26 mm) have been treated with a piranha solution (3:1 sulfuric acid 95% and hydrogen peroxide 30 wt.%) for 30 min. Then the slides have been washed in water under sonication for three minutes, three times. Then the glasses have been dried in an oven for 1 h at 140 °C.
For the functionalization with APTES, the pre-treated cover glass were fully immersed in a solution of APTES 10% (v/v) in ethanol and allowed to react for 5 min at 60 °C, using a Hellendhal type glass staining jar. Typically, eight slides have been coated in a single jar. The amino-modified glasses have been washed three times under sonication with ethanol. After this step, the samples have been gently dried under N_2 flux. Subsequently, APTES coated glass slides have been fully immersed in a GNS colloidal suspension for 14 h, using another Hellendhal type glass staining jar. After immersion, the slides have been washed three times in water without sonication and carefully dried in N_2 stream. Dried samples were stored in a desiccator in the dark.
The self assembled monolayer of thiols has been obtained by fully immersing the APTES-GNS coated glass slides in an ethanolic solution of the desired thiol, using a Hellendhal type glass staining jar, in a concentration range between

10^{-3} and 10^{-7} Mol/L. After 1 h of immersion, slides have been carefully washed three times with ethanol and carefully dried under nitrogen stream.

A.2 Zinc ferrite nanoparticles

$ZnFe_2O_4$ and Mg and/or Ga substituted samples have benn synthesized by and co-precipitation method. $Zn(NO_3)_2$ $6H_2O$ and $Fe(NO_3)_3$ $9H_2O$ with the eventual addition of the dopant nitrate ($Mg(NO_3)_2$ $6H_2O$ or $Ga(NO_3)_3$ $8H_2O$) have been dissolved in 50 ml of water, then heated at 80°C adjusting the pH value at about 10 with the addition of NaOH 2M. The obtained solutions have been maintained at 80°C for about 2h, cooled down to room temperature, then centrifuged (6000 rpm for 5 minutes) two times with water and ethanol. The obtained products have been dried overnight at 80°C in a muffle and finally treated at 300°C for 6 hours to decompose the organic component.

A.3 Red to Black phosphorus conversion

HEBM samples have been prepared starting from commercial RP (Sigma-Aldrich, > 97%) without any further purification. Batches in the mass range of 1.6-5 g have been treated. Proper amounts of powder have been weighed to match specific ξ values and put in a sealed bowl (both bowl and balls have been made of stainless steel). This operation has been performed in an Ar-filled glovebox (O_2 and H_2O < 1 ppm), in which the bowls have been sealed before being transferred to the ball milling equipment. After the HEBM treatment, the jar has been open in the glovebox, and the powder has been recovered. In order to maintain the optimal bowl filling of about 66%vol, the number of employed balls has been kept in the range of 13-50. Preliminary tests showed that this last parameter had a negligible effect on HEBM results.

A.4 $FeNb_{11}O_{29}$ samples

Undoped $FeNb_{11}O_{29}$ and $Fe_{0.8}M_{0.2}Nb_{11}O_{29}$ (M = Mn, V)-doped samples have been synthesized through a conventional solid-state route.
A specific amount of Fe_2O_3, Nb_2O_5 and Mn_2O_3 or V_2O_3 have been weighed and mixed by using a Fritsch ball milling apparatus (tungsten carbide jars, mixing at 600 rpm for 1 h with an intermediate rest). A portion of the milled mixture has been treated in an oven in air at 1100°C for 4 h (monoclinic polymorph), while the remaining powder has been heated at 1300°C for 4 h (orthorhombic phase).
The monoclinic Mn-doped polymorph has been prepared by starting from a Mn–Fe mixed oxide $Fe_{1.6}Mn_{0.4}O_3$ prepared by a co-precipitation method, because the use of the commercial Mn and Fe oxides has not led to a successful

doping. Moreover, to obtain the orthorhombic Mn-doped sample, the temperature has been increased to 1400°C, otherwise Mn impurity phases persisted.

Also the $Fe_{0.8}V_{0.2}Nb_{11}O_{29}$ doped samples synthesized in an inert atmosphere, have been prepared through a solid state synthesis.
Proper amount of Fe_2O_3, Nb_2O_5 and V_2O_3 have been weighted and mixed by using the same Fritsch ball milling apparatus. A portion of the milled mixture has been treated in oven at 1100°C for 4 h (monoclinic polymorph), and another portion has been put in the alumina boat in a sealed quartz tube through which Argon has been fluxed for an hour before and during the thermal treatment. Subsequently, the sample synthesized in Argon flux has been treated again, in the same conditions, but in air.

Appendix B

Molecules: structures and chemical/physical parameters

In this section, the chemical and physical parameters as well as the Raman characterization of the molecules which have been used in SERS experiments, are reported.

B.1 Rhodamine 6G (R6G)

Linear formula	$C_{28}H_{31}N_2O_3Cl$
Molecular weight	479.01

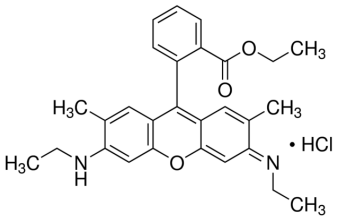

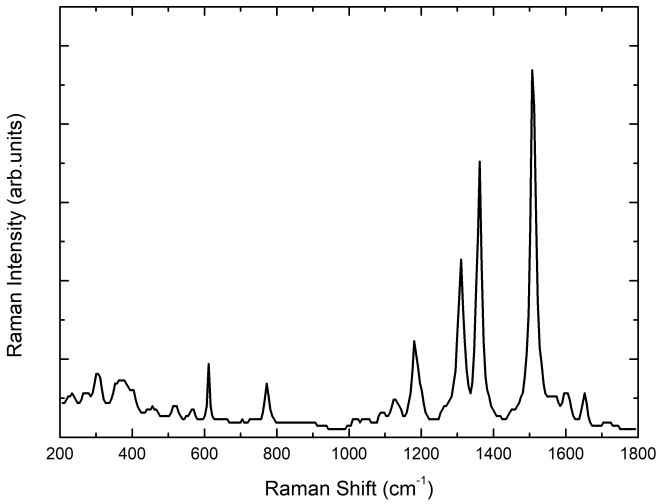

Figure B.1: Raman spectrum of Rhodamine 6G in ethanol solution, recorded with a 1064 nm laser source. Data are taken from [225].

Peak position (cm^{-1})	Assignment
613	Xanthene ring deformation
775	Out-of-plane C-H bend, in plane xanthene ring deformation
1184	In-plane xanthene ring deformation, C-H bending, N-H bending
1312	In-plane xanthene ring breathing, N-H bend, CH_2 wagging
1364	xanthene ring stretching, in-plane C-H bending
1512	xanthene ring stretching, C-H stretching, C-H bend, N-H bending
1577	xanthene ring stretching, in-plane N-H bending
1651	xanthene ring stretching, in-plane C-H bending

Table B.1: Assignments of the main Raman bands of R6G [80].

B.2 7-Mercapto-4-methylcoumarin (MMC)

Linear formula	$C_{10}H_8O_2S$
Molecular weight	192.23

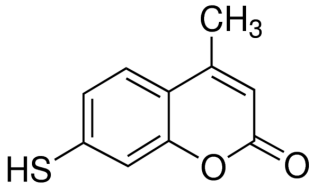

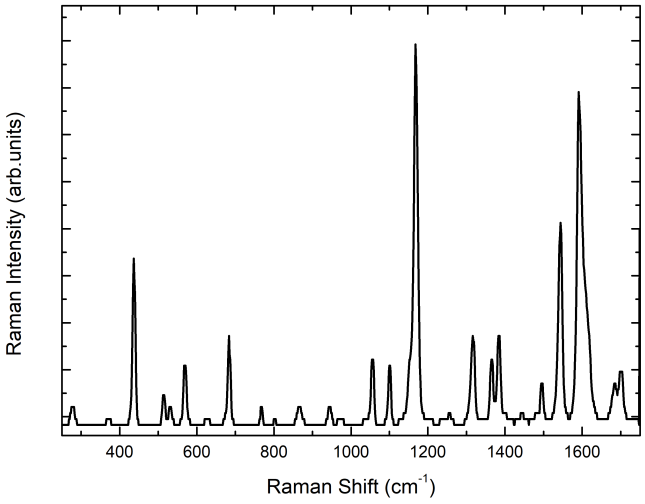

Figure B.2: Raman spectrum of solid 7-Mercapto-4-methylcoumarin, recorded with an excitation laser source at 780 nm. Data are taken from [226].

Peak position (cm^{-1})	Assignment
438	Skeletal vibration
570	Ring vibration
685	Skeletal vibration
1057	Characteristic ring vibration
1102	Characteristic ring vibration
1169	-C-O- stretching
1318	-C-O- stretching
1366	Conjugated -C=C- asymmetric stretching
1384	-C-H_3 deformation
1544	-C-C- stretching and -C-H_{ring} in-plane deformation
1593	Conjugated -C=C- symmetric stretching

Table B.2: Assignments of the main Raman bands of MMC [226].

B.3 4-Mercaptophenylboronic acid (4-MPBA)

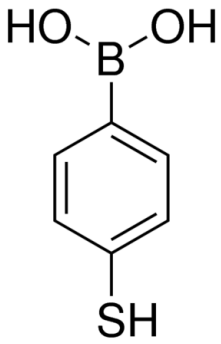

Linear formula	$HSC_6H_4B(OH)_2$
Molecular weight	153.99

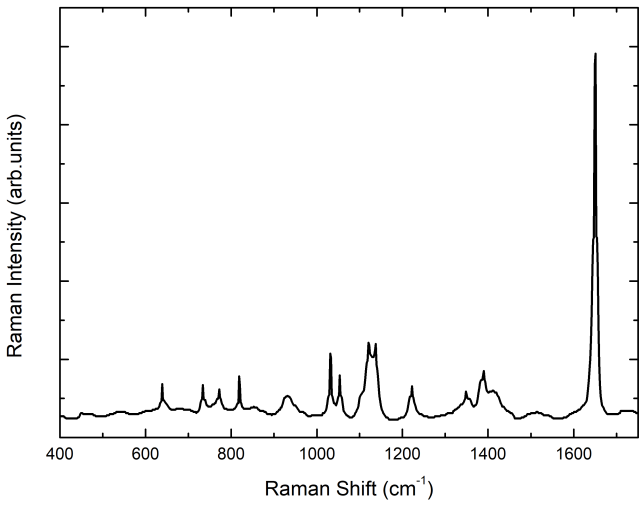

Figure B.3: Raman spectrum of solid 4-Mercaptophenylboronic acid, recorded with a 633 nm laser source. Data are taken from [227].

Peak position (cm^{-1})	Assignment
631	C-S stretching
721	C-C-C in-plane bending, C-S stretching
756	C-H out-of-plane bending
802	C-H out-of-plane bending
907	C-S-H in-plane bending
1005	C-C-C in-plane bending
1026	C-H in-plane bending
1091	C-C-C in-plane bending, C-S stretching
1105	C-H in-plane bending
1186	C-H in-plane bending, B-O-H in-plane bending
1310	B-O stretching
1346	B-O stretching
1369	B-O stretching
1594	C-C stretching

Table B.3: Assignments of the main Raman bands of 4-MPBA [227].

B.4 4-Mercaptobenzoic acid (4-MBA)

Linear formula	$HSC_6H_4CO_2H$
Molecular weight	153.99

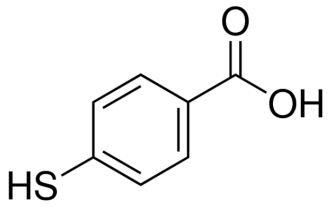

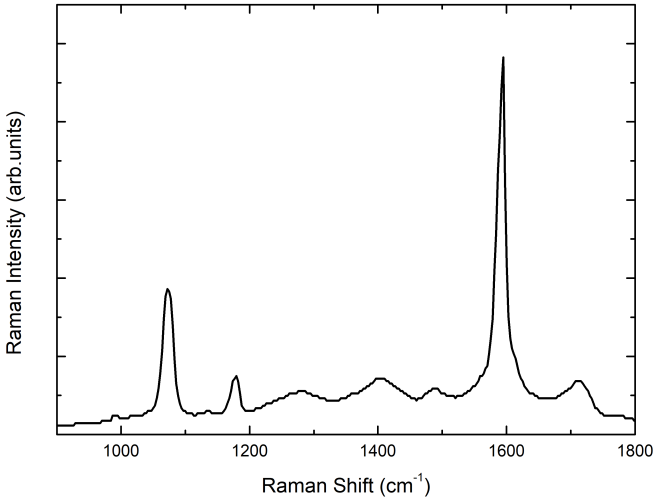

Figure B.4: Raman spectrum of solid 4-Mercaptobenzoic acid, recorded with a 532 nm laser source. Data are taken from [228].

Peak position (cm^{-1})	Assignment
1097	C-C stretching of the ring breathing mode
1180	C-H bending
1594	C-C stretching of the ring breathing mode

Table B.4: Assignments of the main Raman bands of 4-MBA [228].

Appendix C

Supporting Information

C.1 Chapter 5 - SERS from metallic substrates

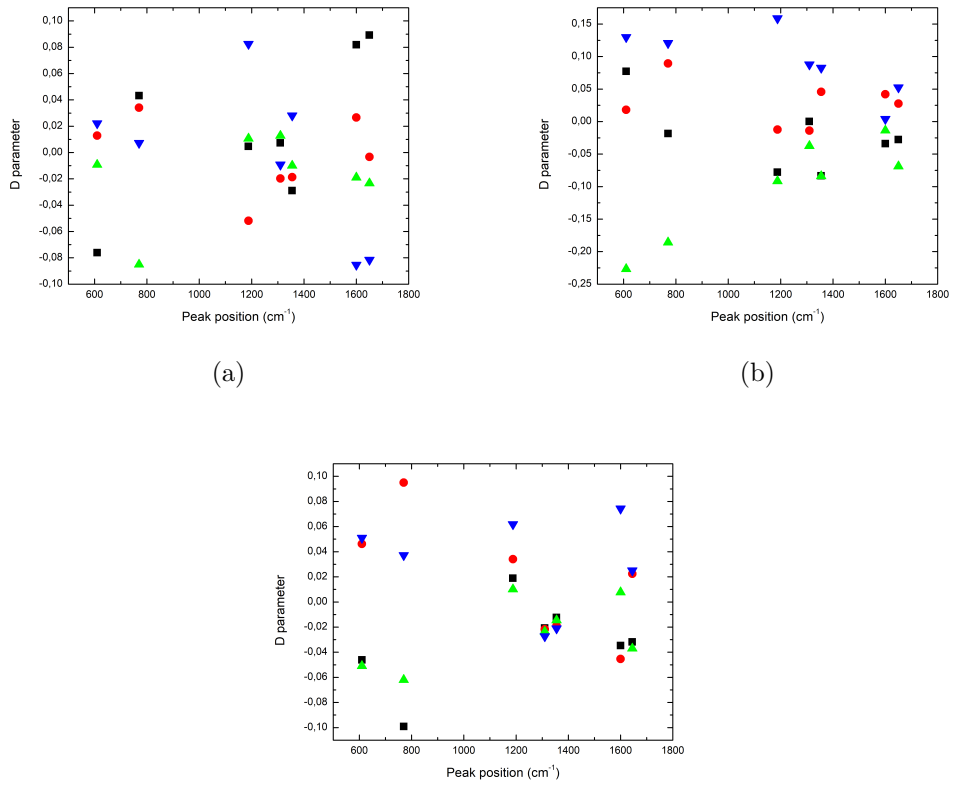

Figure C.1: D parameter calculated for seven R6G modes of the spectra collected on (a) ZERO, (b) ONE and (c) FOUR samples.

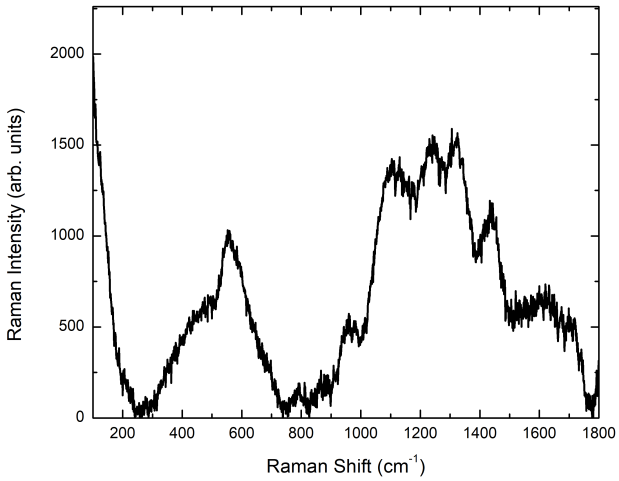

Figure C.2: Spectra of water collected on a clean ONE type substrate.

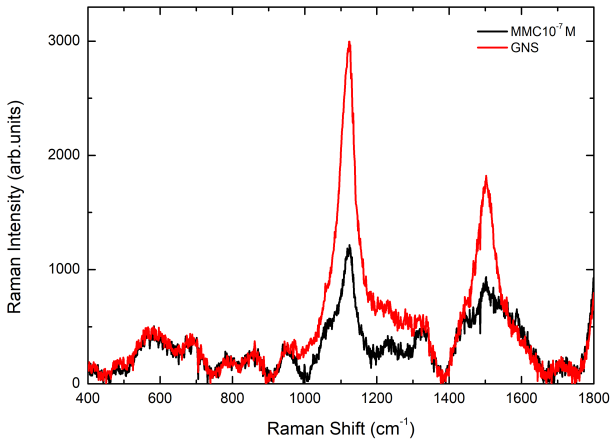

Figure C.3: Comparison between the SERS signals collected from the unfunctionalized (red spectrum) and functionalized with 10^{-7}M solution of MMC (black spectrum) GNS layer.

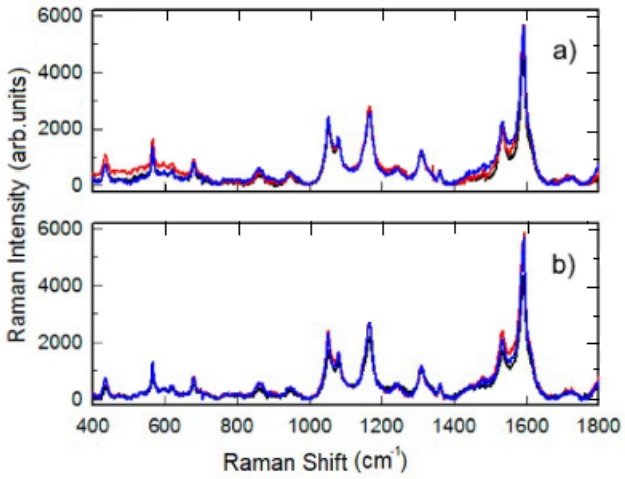

Figure C.4: SERS spectra of GNS layers coated with MMC taken on (a) three samples coming from different preparation batches and on (b) three points of the same sample [89].

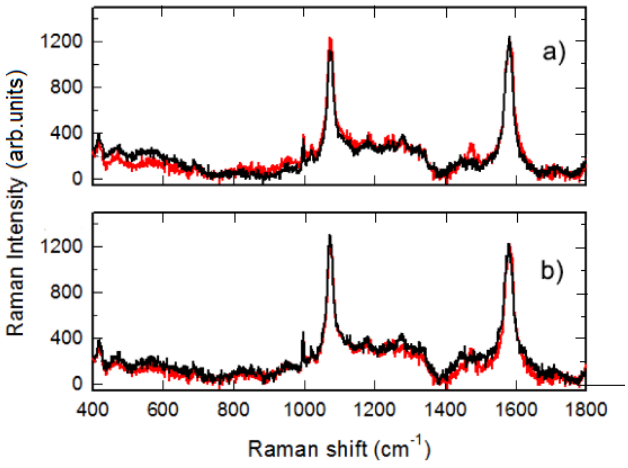

Figure C.5: SERS spectra of GNS layers coated with 4-MPBA taken on (a) two samples coming from different preparation batches and on (b) two points of the same sample [89].

C.2 Chapter 4 - Zinc ferrite nanoparticles: A Raman study

C.2.1 Raman results

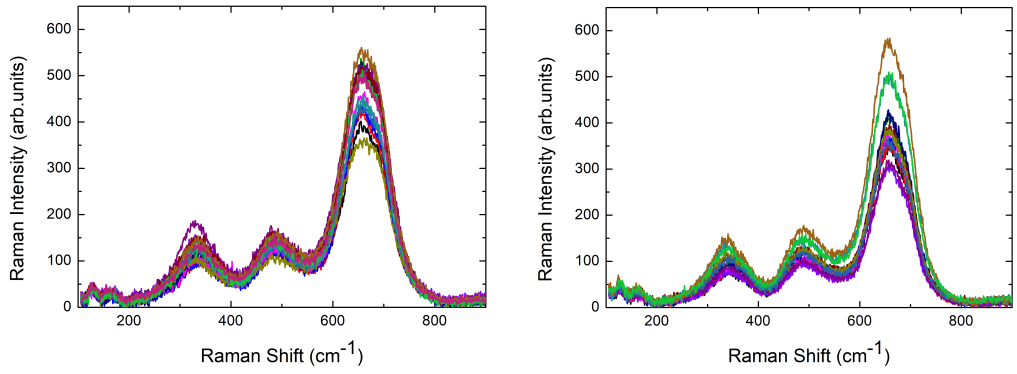

(a) (b)

Figure C.6: Room temperature Raman spectra collected by a mapping acquisition in different region of (a) MZFO and (b) MZGFO samples.

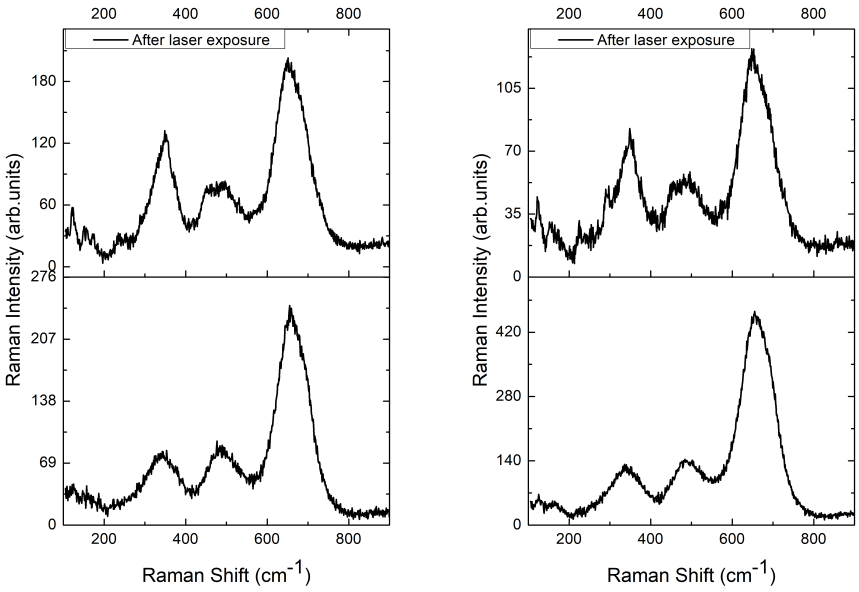

(a) (b)

Figure C.7: Raman response to the thermal stress of ZGFO sample. The reported room temperature Raman spectra have been collected at the beginning and at the end of the thermal cycle with a 5×10^4 W/cm^2 incident power density, in two different regions of the sample displaying both thermal stability (a) and a partial transition to haematite phase (b).

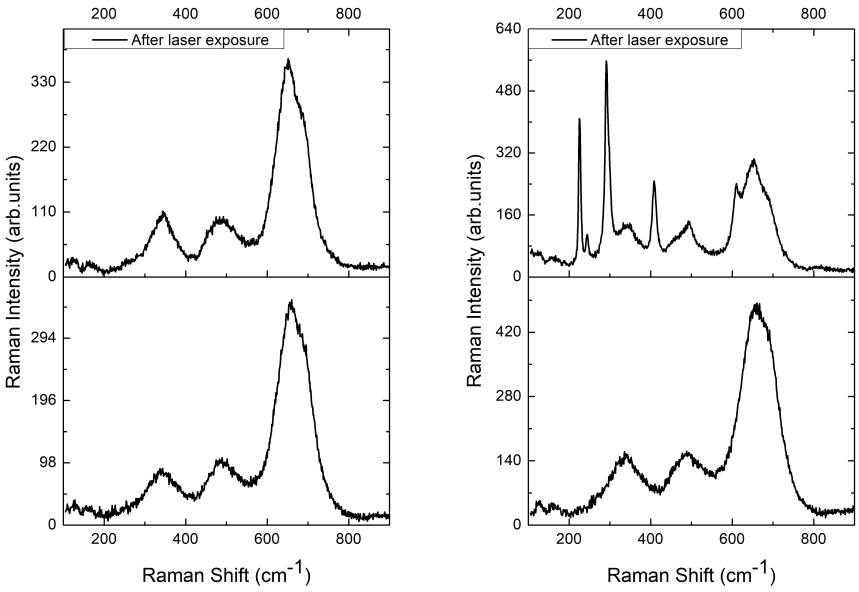

(a) (b)

Figure C.8: Raman response to the thermal stress of MZFO sample. The reported room temperature Raman spectra have been collected at the beginning and at the end of the thermal cycle with a 5×10^4 W/cm^2 incident power density, in two different regions of the sample displaying both thermal stability (a) and a partial transition to haematite phase (b).

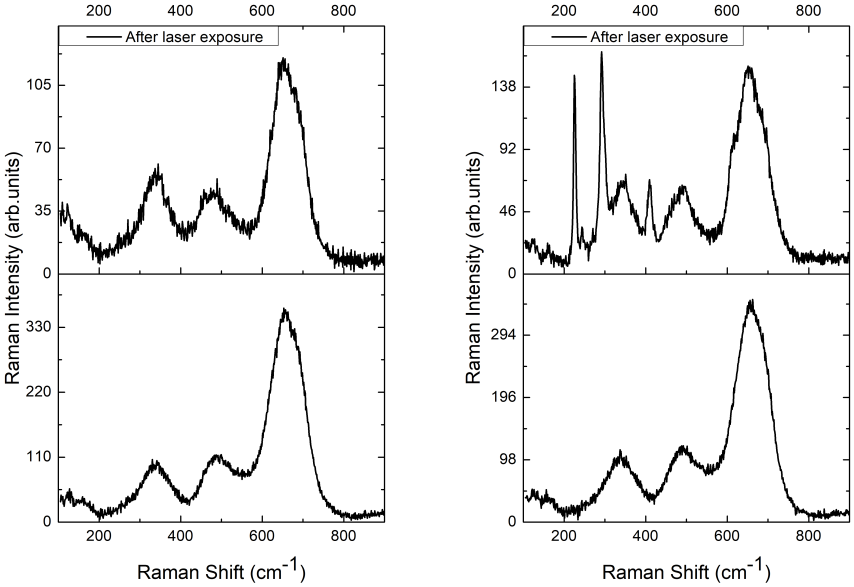

(a) (b)

Figure C.9: Raman response to the thermal stress of MZGFO sample. The reported room temperature Raman spectra have been collected at the beginning and at the end of the thermal cycle with a 5×10^4 W/cm^2 incident power density, in two different regions of the sample displaying both thermal stability (a) and a partial transition to haematite phase (b).

C.2.2 EPR results

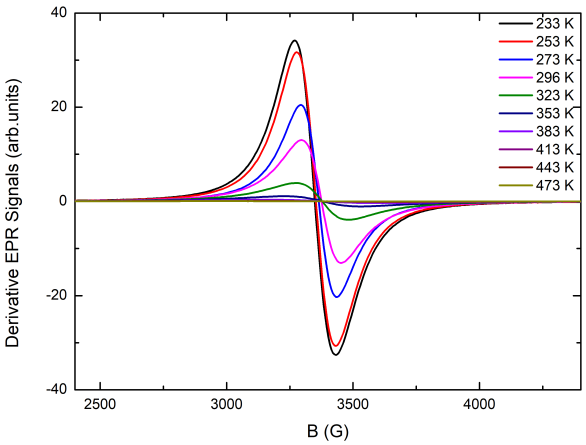

Figure C.10: Derivative EPR signals of ZGFO sample recorded by varying the temperature in the range 233-473 K.

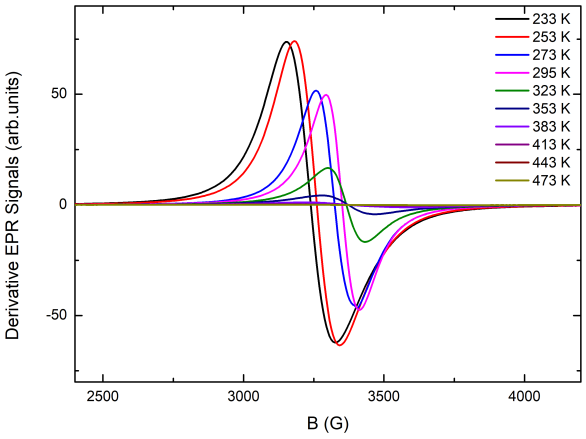

Figure C.11: Derivative EPR signals of MZFO sample recorded by varying the temperature in the range 233-473 K.

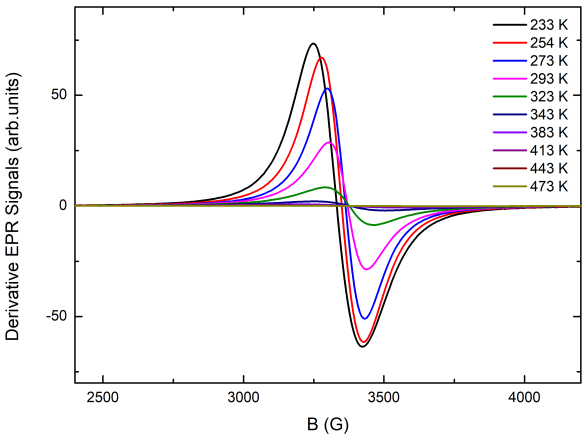

Figure C.12: Derivative EPR signals of MZGFO sample recorded by varying the temperature in the range 233-473 K.

Appendix D

List of experimental techniques

In the following, the experimental details of the research activities described in the thesis are presented. In particular, a more detailed description is given in the first part for the experimental set-up that I have directly used, while in the second part the experimental techniques used to characterize the investigated samples within the collaboration of other research groups are listed. Same representative cases, not discussed during the thesis, are also presented just to give a pictorial view of the results.

Micro-Raman measures have been performed at room temperature by using a Labram Dilor spectrometer equipped with an Olympus microscope HS BX40. The excitation radiation employed is the 632.8 nm light from He-Ne laser. The spectrometer is equipped with a motorized xy stage on which the investigated samples are positioned. The measures have been carried on in a backscattering configuration. The microscope set-up is equipped with four different objectives with 10x, 50x, 50x with a long working distance and 100x magnifications. The spectral resolution is about 1 cm^{-1}. Neutral filters with optical density equal to 2, 1, 0.6, 0.3 and 0 can be used to adapt the laser incident power, leading to power density values from $5\times10^3 W/cm^2$ to $5\times10^5 W/cm^2$. A cooled CCD camera is used as a detector.
The **UV Raman measurements** have been carried out with a benchtop Raman set-up at the IUVS line at the Elettra synchrotron in Trieste. A 266 nm light from a Nd:YAG laser has been used as excitation source. The samples have been mounted on an oscillating stage in order to avoid photo-damaging. The incident power laser has been set to 200 μW. A Czerny-Turner spectrometer equipped with a holographic dispersive element of 3600 lines/mm, coupled with a Peltier-cooled back-thinned CCD has been used to record the Raman signals. The calibration of the spectrometer was standardized using cyclohexane (Sigma-Aldrich).
Micro-Raman measures have been also performed with a Horiba LabRAM HR Evolution, located at the Experimental Mineralogy Lab at the Earth and

Environmental Science Department of University of Pavia. A 532 nm light from a Nd:YAG laser has been used as excitation source with a nominal power of 100 mW. The samples have been mounted on a motorized xyz stage. The microscope set-up is equipped with four different objectives with 5x, 20x, 50x with a long working distance and 100x magnifications. The spectral resolution is about 1 cm^{-1}. The apparatus is equipped with neutral filters with variable optical density that can be used to adjust the incident laser power. A Symphony CCD camera, cryogenically cooled (LN_2), is used as a detector.

EPR measurements have been carried out by using an X-band (about 9.3 GHz) Bruker spectrometer, in the range between 2000-5000 G. A continuous nitrogen flow cryostat, in the temperature range 200–500 K, has been used.

The **magnetic characterization** has been carried out by means of a SQUID magnetometer. A 100 Oe magnetic field has been applied to study the temperature dependence of the magnetization in the range 10-300 K, in zero-field cooling (ZFC) and field cooling (FC) regimes. Hysteresis loops have been collected at room temperature and at 10 K with magnetic field ranging between 0 and ± 10000 Oe.

Microstructural characterization on SERS metallic substrates has been performed by using a high-resolution **scanning electron microscope** (SEM, TESCAN Mira 3 XMU) operated at 25 kV and equipped with an energy dispersion spectroscopy (EDS) analysis unit (EDAX), located at the Arvedi laboratory, CISRiC, at the Earth and Environmental Sciences department of University of Pavia. Slides have been mounted onto Aluminum stubs using double sided carbon adhesive tape and then they have been made electrically conductive by coating in vacuum with a thin layer of Pt/Pd (3-5 nm). Observations have been made in backscattered electrons mode at 30 kV and with InBeam secondary electron detector for higher spatial resolution. As an explanatory case, the SEM image taken from the ZERO sample (i.e. without silica covering) is reported in Figure (D.1).

On the other hand, microstructural characterization on zinc ferrite samples

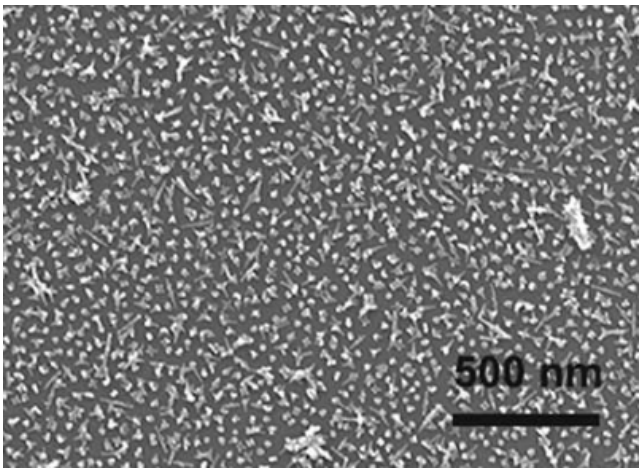

Figure D.1: SEM image of the uncoated ZERO sample [82].

has been done by means of a Zeiss EVO MA10 (Carl Zeiss, Oberkochen, Germany) scanning electron microscope coupled with an EDS detector (X-max 50 mm^2, Oxford Instruments) located at the chemical physical department of University of Pavia. In Figure (D.2), the SEM micrograph of the undoped zinc ferrite sample is reported.

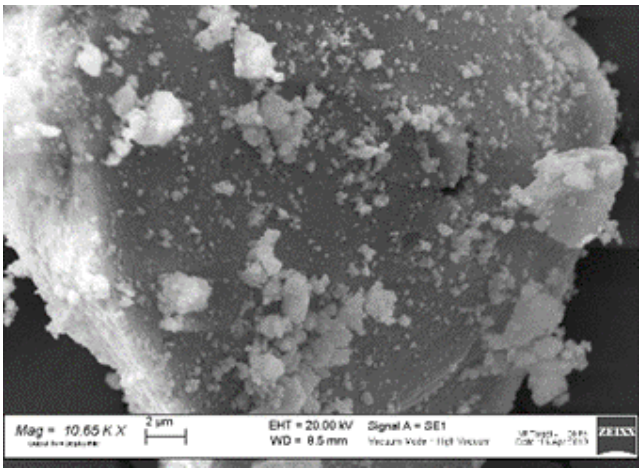

Figure D.2: SEM micrograph of the undoped zinc ferrite sample.

TEM measures have been used to characterize the GNS colloidal solution used in the synthesis process of SERS metallic substrates with a Jeol JEM-1200 EX II instrument. In particular, TEM images have been taken on 1:10 diluted GNSs solution, using a 10 μL sample dropped on copper grids (300 mesh) coated with a Parlodion membrane, in order to characterise their morphology, namely size and shape, before performing SAM onto the solid glass substrates.
XRPD measurements have been performed by using a Bruker D5005 diffractometer with CuKα radiation, graphite monochromator and scintillation detector. The patterns have been collected in air with a step size of 0.03° and counting time of 15s per step in the angular range 17-110°, by using a silicon sample holder with low background. Rietveld structural and profile refinement has been carried out by means of TOPAS 3.0 software on the basis of the known crystal structure model of the cubic spinel.
A Varian Cary 50 UV/Vis spectrophotometer has been used to perform **UV-Vis-NIR absorption measures** in air which allows a wavelength scan ranging from 300 to 1100 nm. The samples have been placed in a special holder enabling transmission measurements.
Static contact angle determinations have been made with a KSV CAM200 instrument with the water sessile drop method. The c.a. measures have been used to characterized the SERS metallic substrates, described in Chapter 3. This kind of measures allow to determine the success of the performed functionalization of the substrate surfaces. In the particular case of thiol-coated

GNS substrates, measurement of static contact angles have given further evidence of the success of thiol coating on the GNS grafted on glass as well as of substrates wettability at variance of the used thiol. In particular, the value of c.a. moved from the original value of about 50° to peculiar values of the functions brought on the used thiols, in particular from about 10° for 4-MPBA which allows to reach marked hydrophilicity, to intermediate values as in the case MMC, till the highest one, i.e. 120°, for 12C-SH that, thus, imparts high hydrophobicity to the substrate surface. The illustrates of such behaviour is reported in Figure (D.3).

Photothermal measurements: Thermograms have been collected using a Thermocam FLIR E40 and using a L808P200 Thorlabs as a laser source ($\lambda = 808$ nm) using a spot of 1 cm of diameter, using a power ranging between 39 and 207 mW.

Figure D.3: Example of contact angle images for: a) uncoated GNS monolayer, b) GNS monolayer coated with 4-MBA, c) GNS monolayer coated with 12C-SH [89].

List of publications

- G. Gazzola, M.C. Mozzati, B. Albini, P. Galinetto, and M. Bini. Tuning the superparamagnetic effect in $ZnFe_2O_4$ nanoparticles with Mg,Ga doping. *Submitted*

- M. Nuti, D. Spada, I. Quinzeni, S. Capelli, B. Albini, P. Galinetto, and M. Bini. From tunnel NMO to layered polymorphs oxides for sodium ion batteries. *SN Appl. Sci.*, 2:1839, 2020.

- S.M. Lupi, B. Albini, A. Rodriguez y Baena, G. Lanfrè, P. Galinetto. Anatase Forming Treatment without Surface Morphological Alteration of Dental Implant. *Materials. Materials*, 13:5280, 2020.

- A. Ruffo, M.C. Mozzati, B. Albini, P. Galinetto, and M. Bini. Role of non-magnetic dopants (Ca, Mg) in $GdFeO_3$ perovskite nanoparticles obtained by different synthetic methods: structural, morphology and magnetic properties. *J Mater Sci: Mater Electron*, 2020.

- S.M. Lupi, P. Galinetto, B. Albini, E. Di Ronza, S. Rizzo, R. Rodriguez y Baena. Micro-Raman Spectroscopy of Dental Implants Subjected to Different Surface Treatments. *Appl. Sci.*, 10:2417, 2020.

- D. Rovati, B. Albini, P. Galinetto, P. Grisoli, B. Bassi, P. Pallavicini, G. Dacarro, and A. Taglietti. High Stability Thiol-Coated Gold Nanostars Monolayers with Photo-Thermal Antibacterial Activity and Wettability Control. *Nanomaterials*, 9:1288, 2019.

- P. Galinetto, D. Spada, M.C. Mozzati, B. Albini, and M. Bini. Effects of reaction atmosphere on physico-chemical properties of V-doped $FeNb_{11}O_{29}$. *Optical Materials*, 92:373-378, 2019.

- C. Ferrara, E. Vigo, B. Albini, P. Galinetto, C. Milanese, C. Tealdi, E. Quartarone, S. Passerini, and P. Mustarelli. Efficiency and Quality Issues in the Production of Black Phosphorus by Mechanochemical Synthesis: A Multi-Technique Approach. *ACS Applied Energy Materials*, 2(4):2794-2802, 2019.

- B. Bassi, B. Albini, A. D'Agostino, G. Dacarro, P. Pallavicini, P. Galinetto, and A. Taglietti. Robust, reproducible, recyclable SERS substrates: monolayers of gold nanostars grafted on glass and coated with a thin silica layer. *Nanotechnology*, 30:025302, 2018.

- S. Bonomi, I. Tredici, B. Albini, P. Galinetto, A. Rizzo, A. Listorti, U. Anselmi Tamburini, and L. Malavasi. Ambient condition retention of band-gap tuning in $MAPbI_3$ induced by high pressure quenching. *Chem. Commun.*, 54(94):13212-13215, 2018.

- D. Spada, M.C. Mozzati, B. Albini, P. Galinetto, I. Quinzeni, D. Capsoni, and M. Bini. Deepening the share structure $FeNb_{11}O_{29}$: influence of polymorphism and doping on structural, spectroscopic and magnetic properties. *Dalton Transactions*, 47(44):15816-15826, 2018.

- P. Galinetto, B. Albini, M. Bini, and M.C. Mozzati. Raman spectroscopy in Zinc Ferrites Nanoparticles. In: Raman Spectroscopy. Editor: G.M. Do Nascimento. *IntechOpen*, 2018.

- M. Bini, C. Tondo, D. Capsoni, M.C. Mozzati, B. Albini, and P. Galinetto. Superparamagnetic $ZnFe_2O_4$ nanoparticle: the effect of Ca and Gd doping. *Materials Chemistry and Physics*, 204:72-82, 2018.

Bibliography

[1] M.S. Dresselhaus, G. Dresselhaus, R. Saito, and A. Jorio. Raman spectroscopy of carbon nanotubes. *Physics Reports*, 409:47–99, 2005.

[2] C. Raman and K. Krishnan. A New Type of Secondary Radiation. *Nature*, 121:501 – 502, 1928.

[3] RA802 Pharmaceutical Analyser. `https://www.renishaw.it/it/ra802-pharmaceutical-analyser--39680`.

[4] T. Vankeirsbilck, A. Vercauteren, W. Baeyens, G. Van der Weken, F. Verpoort, G. Vergote, and J. P. Remon. Applications of Raman spectroscopy in pharmaceutical analysis. *TrAC Trends in Analytical Chemistry*, 21:869 – 877, 2002.

[5] Petroleum & Petrochemical. `https://bwtek.com/industries/petroleum-petrochem`.

[6] J. Heuer and A. Luttge. Kinetics of pipeline steel corrosion studied by Raman spectroscopy-coupled vertical scanning interferometry. *npj Mater Degrad*, 2(40), 2018.

[7] Verifying Raw Materials by Spatially Offset Raman Spectroscopy. `https://www.cobaltlight.com`.

[8] P. Matousek, I.P. Clark, E. R. C. Draper, M. D. Morris, A. E. Goodship, N. Everall, M Towrie, W. F. Finney, and A. W. Parker. Subsurface Probing in Diffusely Scattering Media Using Spatially Offset Raman Spectroscopy. *Applied Spectroscopy*, 59(4):393 – 400, 2005.

[9] J.-U. Lee, S. Lee, Ji H. Ryoo, S. Kang, T. Y. Kim, P. Kim, C.-H. Park, J.-G. Park, and H. Cheong. Ising-Type Magnetic Ordering in Atomically Thin $FePS_3$. *Nano Letters*, 16(12):7433 – 7438, 2016.

[10] Xingzhi Wang et al. Raman spectroscopy of atomically thin two-dimensional magnetic iron phosphorus trisulfide ($FePS_3$) crystals. *2D Materials*, 3(3):031009, 2016.

[11] Amber McCreary, Jeffrey R. Simpson, Thuc T. Mai, Robert D. McMichael, Jason E. Douglas, Nicholas Butch, Cindi Dennis, Rolando Valdés Aguilar, and Angela R. Hight Walker. Quasi-two-dimensional magnon identification in antiferromagnetic $FePS_3$ via magneto-Raman spectroscopy. *Phys. Rev. B*, 101(6):064416, 2020.

[12] C. Ho, N. Jean, and C.A. et al. Hogan. Rapid identification of pathogenic bacteria using Raman spectroscopy and deep learning. *Nat Commun*, 10:4927, 2019.

[13] I. W. Schie and T. Huser. Methods and Applications of Raman Microspectroscopy to Single-Cell Analysis. *Applied Spectroscopy*, 67(8):813 – 828, 2013.

[14] D.R. Parachalil, J. McIntyre, and H.J Byrne. Potential of Raman spectroscopy for the analysis of plasma/serum in the liquid state: recent advances. *Anal Bioanal Chem*, 412(9):1993 – 2007, 2020.

[15] M. S. Bergholt, W. Zheng, K. Y. Ho, M. Teh, K. G. Yeoh, J. B. Yan So, A. Shabbir, and Z. Huang. Fiberoptic Confocal Raman Spectroscopy for Real-Time In Vivo Diagnosis of Dysplasia in Barrett's Esophagus. *Gastroenterology*, 146(1):27 – 32, 2014.

[16] B. B. Johnson and W. L. Peticolas. The Resonant Raman Effect. *Annual Review of Physical Chemistry*, 27(1):465–521, 1976.

[17] W. M. Tolles, J. W. Nibler, J. R. McDonald, and A. B. Harvey. A Review of the Theory and Application of Coherent Anti-Stokes Raman Spectroscopy (CARS). *Applied Spectroscopy*, 31(4):253–271, 1977.

[18] B. Pettinger, P. Schambach, C. J. Villagómez, and N. Scott. Tip-Enhanced Raman Spectroscopy: Near-Fields Acting on a Few Molecules. *Annual Review of Physical Chemistry*, 63(1):379–399, 2012.

[19] M. Fleischmann, P.J. Hendra, and A.J. McQuillan. Raman spectra of pyridine adsorbed at a silver electrode. *Chemical Physics Letters*, 26(2):163 – 166, 1974.

[20] D. L. Jeanmaire and R. P. Van Duyne. Surface raman spectroelectrochemistry. Part i. Heterocyclic, aromatic, and aliphatic amines adsorbed on the anodized silver electrode. *Journal of Electroanalytical Chemistry*, 84(1):1 – 20, 1977.

[21] M. G. Albrecht and J. A. Creighton. Anomalously intense Raman spectra of pyridine at a silver electrode. *Journal of the American Chemical Society*, 99(15):5215 –5217, 1977.

[22] M. Moskovits. Surface roughness and the enhanced intensity of Raman scattering by molecules adsorbed on metals. *The Journal of Chemical Physics*, 69(9):4159 – 4161, 1978.

[23] M. Moskovits. Surface-enhanced spectroscopy. *Rev. Mod. Phys.*, 57:783–826, 1985.

[24] A. Otto. Surface enhanced Raman scattering ($SERS$), what do we know? *Applications of Surface Science*, 6(3):309 – 355, 1980.

[25] A. Otto, I. Mrozek, H. Grabhorn, and W. Akemann. Surface-enhanced Raman scattering. *J. Phys.: Condens. Matter*, 4:1143, 1992.

[26] T.E. Furtak and S.H. Macomber. Voltage-induced shifting of charge-transfer excitations and their role in surface-enhanced Raman scattering. *Chemical Physics Letters*, 95(4):328 – 332, 1983.

[27] J. Billman and A. Otto. Charge transfer between adsorbed cyanide and silver probed by sers. *Surface Science*, 138(1):1–25, 1984.

[28] H. Yamada and Y. Yamamoto. Surface enhanced Raman scattering ($SERS$) of chemisorbed species on various kinds of metals and semiconductors. *Surface Science*, 134(1):71 – 90, 1983.

[29] S. Hayashi, R. Koh, Y. Ichiyama, and K. Yamamoto. Evidence for surface-enhanced Raman scattering on nonmetallic surfaces: Copper phthalocyanine molecules on GaP small particles. *Phys. Rev. Lett.*, 60(11):1085 – 1088, 1988.

[30] D. Maznichenko, K. Venkatakrishnan, and B. Tan. Stimulating Multiple SERS Mechanisms by a Nanofibrous Three-Dimensional Network Structure of Titanium Dioxide (TiO_2). *The Journal of Physical Chemistry C*, 117(1):578 – 583, 2013.

[31] W. Li, R. Zamani, P. Rivera Gil, B. Pelaz, M. Ibáñez, D. Cadavid, A. Shavel, R. A. Alvarez-Puebla, W. J. Parak, J. Arbiol, and A. Cabot. CuTe Nanocrystals: Shape and Size Control, Plasmonic Properties, and Use as SERS Probes and Photothermal Agents. *Journal of the American Chemical Society*, 135(19):7098 – 7101, 2013.

[32] I. Alessandri and J. R. Lombardi. Enhanced Raman Scattering with Dielectrics. *Chemical Reviews*, 116(24):14921 – 14981, 2016.

[33] J. R. Lombardi and R. L. Birke. A Unified Approach to Surface-Enhanced Raman Spectroscopy. *The Journal of Physical Chemistry C*, 112(14):5605 – 5617, 2008.

[34] John R. Lombardi and Ronald L. Birke. Theory of Surface-Enhanced Raman Scattering in Semiconductors. *The Journal of Physical Chemistry C*, 118(20):11120 – 11130, 2014.

[35] John R. Lombardi. The theory of surface-enhanced Raman scattering on semiconductor nanoparticles; toward the optimization of SERS sensors. *Faraday Discuss.*, 205:105 – 120, 2017.

[36] Peter F. Bernath. *Spectra of Atoms and Molecules*. Oxford University Press, Inc.

[37] Derek A. Long. *The Raman Effect: A Unified Treatment of the Theory of Raman Scattering by Molecules*. John Wiley & Sons, Ltd.

[38] M.D. Williams, D.S. Bradshaw, and D.L. Andrews. Raman scattering mediated by neighboring molecules. *The Journal of Chemical Physics*, 144(17):174304, 2016.

[39] R.P. Prasankumar and A.J. Taylor. *Optical Techniques for Solid-State Materials Characterization*. CRC Press.

[40] G. Gouadec and P. Colomban. Raman spectroscopy of nanomaterials: How spectra relate to disorder, particle size and mechanical properties. *Progress in Crystal Growth and Characterization of Materials*, 53(1):1–56, 2007.

[41] A.K. Arora, M. Rajalakshmi, T.R. Ravindran, and V. Sivasubramanian. Raman spectroscopy of optical phonon confinement in nanostructured materials. *Journal of Raman Spectroscopy*, 38(6):604–617, 2007.

[42] Haibin Tang, Chuhong Zhu, Guowen Meng, and Nianqiang Wu. Review—surface-enhanced raman scattering sensors for food safety and environmental monitoring. *Journal of The Electrochemical Society*, 165(8):B3098–B3118, 2018.

[43] S. Hayashi and T. Okamoto. Plasmonics: visit the past to know the future. *Journal of Physics D: Applied Physics*, 45(43):433001, 2012.

[44] .l L. Stiles, J. A. Dieringer, N. C. Shah, and R. P. Van Duyne. Surface-enhanced raman spectroscopy. *Annual Review of Analytical Chemistry*, 1(1):601–626, 2008.

[45] S.-Y. Ding, E.-M. You, Z.-Q. Tian, and M. Moskovits. Electromagnetic theories of surface-enhanced raman spectroscopy. *Chem. Soc. Rev.*, 46:4042–4076, 2017.

[46] B. J. Kennedy, S. Spaeth, M. Dickey, and K. T. Carron. Determination of the Distance Dependence and Experimental Effects for Modified

SERS Substrates Based on Self-Assembled Monolayers Formed Using Alkanethiols. *The Journal of Physical Chemistry B*, 103(18):3640–3646, 1999.

[47] G. Compagnini, C. Galati, and S. Pignataro. Distance dependence of surface enhanced Raman scattering probed by alkanethiol self-assembled monolayers. *Phys. Chem. Chem. Phys.*, 1(9):2351–2353, 199.

[48] V. Kukushkin, A. Van'kov, and I. Kukushkin. Long-range nature of surface-enhanced raman scattering. *JEPT Letters*, 98:64–69, 2013.

[49] U. Aslam, V.G. Rao, S Chavez, and et al. Catalytic conversion of solar to chemical energy on plasmonic metal nanostructures. *Nature Catalysis*, 1:656–665, 2018.

[50] M. Moskovits. Surface-enhanced raman spectroscopy: a brief retrospective. *Journal of Raman Spectroscopy*, 36(6-7):485–496, 2005.

[51] J. Grand, M.L. del la Chapelle, J.-L. Bijeon, P.-M. Adam, A. Vial, and P. Royer. Role of localized surface plasmons in surface-enhanced Raman scattering of shape-controlled metallic particles in regular arrays. *Phys. Rev. B*, 72(3):033407, 2005.

[52] P. G. Etchegoin and E.C. Le Ru. Basic Electromagnetic Theory of SERS. In S. Schlücker, editor, *Surface Enhanced Raman Spectroscopy: Analytical, Biophysical and Life Science Applications*, chapter 1, pages 1–37. John Wiley & Sons, Ltd, 2010.

[53] E. Le Ru and P. Etchegoin. *Principles of Surface Enhanced Raman Spectroscopic and related plasmonic effets*. Elsevier, 2008.

[54] M.I. Stockman. Electromagnetic Theory of SERS. In K. Kneipp, M. Moskovits, and H. Kneipp, editors, *Surface-Enhanced Raman Scattering: Physics and Applications*, chapter 3, pages 47–65. Springer, 2006.

[55] John R. Lombardi and Ronald L. Birke. A Unified View to Surface-Enhanced Raman Spectroscopy. *Accounts of Chemical Research*, 42(6):734–742, 2009.

[56] E. C. Le Ru, E. Blackie, M. Meyer, and P. G. Etchegoin. Surface Enhanced Raman Scattering Enhancement Factors : A Comprehensive Study. *The Journal of Physical Chemistry C*, 111(37):13794 – 13803, 2007.

[57] X. Gu, M.J. Trujillo, J.E. Olson, and J.P. Camden. SERS Sensors: Recent Developments and a Generalized Classification Scheme Based on the Signal Origin. *Annual Review of Analytical Chemistry*, 11(1):147–169, 2018.

[58] A. S. D. S. Indrasekara, S. Meyers, S. Shubeita, L. C. Feldman, T. Gustafsson, and L. Fabris. Gold nanostar substrates for SERS-based chemical sensing in the femtomolar regime. *Nanoscale*, 6(15):8891–8899, 2014.

[59] L. Pérez-Mayen, J. Oliva, A. Torres-Castro, and E. De la Rosa. SERS substrates fabricated with star-like gold nanoparticles for zeptomole detection of analytes. *Nanoscale*, 7(22):10249–10258, 2015.

[60] Q. Su, X. Ma, J. Dong, C. Jiang, and W. Qian. A Reproducible SERS Substrate Based on Electrostatically Assisted APTES-Functionalized Surface-Assembly of Gold Nanostars. *ACS Applied Materials & Interfaces*, 3(6):1873–1879, 2011.

[61] M. G. Cha, H.-M. Kim, Y.-L. Kang, M. Lee, H. Kang, J. Kim, X.-H. Pham, T. H. Kim, E. Hahm, Y.-S. Lee, D. H. Jeong, and B.-H. Jun. Thin silica shell coated Ag assembled nanostructures for expanding generality of SERS analytes. *PLOS ONE*, 12(6):1–13, 2017.

[62] I. Ruach-Nir, T. A. Bendikov, I. Doron-Mor, Z. Barkay, A. Vaskevich, and I. Rubinstein. Silica-Stabilized Gold Island Films for Transmission Localized Surface Plasmon Sensing. *Journal of the American Chemical Society*, 129(1):84–92, 2007.

[63] E. Brown and G. Wright. Antibacterial drug discovery in the resistance era. *Nature*, 529:336–343, 2016.

[64] S. Chernousova and M. Epple. Silver as Antibacterial Agent: Ion, Nanoparticle, and Metal. *Angewandte Chemie International Edition*, 52(6):1636–1653, 2013.

[65] P. Pallavicini, G. Dacarro, and A. Taglietti. Self-Assembled Monolayers of Silver Nanoparticles: From Intrinsic to Switchable Inorganic Antibacterial Surfaces. *European Journal of Inorganic Chemistry*, 2018(45):4846–4855, 2018.

[66] A. Taglietti, C. R. Arciola, A. D'Agostino, G. Dacarro, L. Montanaro, D. Campoccia, L. Cucca, M. Vercellino, A. Poggi, P. Pallavicini, and L. Visai. Antibiofilm activity of a monolayer of silver nanoparticles anchored to an amino-silanized glass surface. *Biomaterials*, 35(6):1779 – 1788, 2014.

[67] G. Dacarro, L. Cucca, P. Grisoli, P. Pallavicini, M. Patrini, and A. Taglietti. Monolayers of polyethilenimine on flat glass: a versatile platform for cations coordination and nanoparticles grafting in the preparation of antibacterial surfaces. *Dalton Trans.*, 41(8):2456–2463, 2012.

[68] X. Zhu and X. Jun Loh. Layer-by-layer assemblies for antibacterial applications. *Biomater. Sci.*, 3(12):1505–1518, 2015.

[69] D. J. de Aberasturi, A. B. Serrano-Montes, and L. M. Liz-Marzán. Modern Applications of Plasmonic Nanoparticles: From Energy to Health. *Advanced Optical Materials*, 3(5):602–617, 2015.

[70] P. Pallavicini, A. Donà, A. Taglietti, P. Minzioni, M. Patrini, G. Dacarro, G. Chirico, L. Sironi, N. Bloise, L. Visai, and L. Scarabelli. Self-assembled monolayers of gold nanostars: a convenient tool for near-IR photothermal biofilm eradication. *Chem. Commun.*, 50(16):1969–1971, 2014.

[71] A. D'Agostino, A. Taglietti, R. Desando, M. Bini, M. Patrini, G. Dacarro, L. Cucca, P. Pallavicini, and P. Grisoli. Bulk Surfaces Coated with Triangular Silver Nanoplates: Antibacterial Action Based on Silver Release and Photo-Thermal Effect. *Nanomaterials*, 7(1), 2017.

[72] A. D'Agostino, A. Taglietti, P. Grisoli, G. Dacarro, L. Cucca, M. Patrini, and P. Pallavicini. Seed mediated growth of silver nanoplates on glass: exploiting the bimodal antibacterial effect by near IR photo-thermal action and Ag^+ release. *RSC Adv.*, 6(74):70414–70423, 2016.

[73] P. Pallavicini, B. Bassi, G. Chirico, M. Collini, G. Dacarro, E. Fratini, P. Grisoli, M. Patrini, L. Sironi, A. Taglietti, and et al. Modular approach for bimodal antibacterial surfaces combining photo-switchable activity and sustained biocidal release. *Scientific Reports*, 7:5259, 2017.

[74] S. Chen, L. Li, C. Zhao, and J. Zheng. Surface hydration: Principles and applications toward low-fouling/nonfouling biomaterials. *Polymer*, 51(23):5283 – 5293, 2010.

[75] X. Zhang, L. Wang, and E. Levänen. Superhydrophobic surfaces for the reduction of bacterial adhesion. *RSC Adv.*, 3(30):12003–12020, 2013.

[76] Y. Chaikin, O. Kedem, J. Raz, A. Vaskevich, and I. Rubinstein. Stabilization of Metal Nanoparticle Films on Glass Surfaces Using Ultrathin Silica Coating. *Analytical Chemistry*, 85(21):10022–10027, 2013.

[77] I. Ruach-Nir, T. A. Bendikov, I. Doron-Mor, Z. Barkay, A. Vaskevich, and I. Rubinstein. Silica-Stabilized Gold Island Films for Transmission Localized Surface Plasmon Sensing. *Journal of the American Chemical Society*, 129(1):84–92, 2007.

[78] Q. Wu, C. Luo, H. Yu, G Kong, and J. Hu. Surface sol–gel growth of ultrathin SiO_2 films on roughened Au electrodes: Extending borrowed SERS to a SERS inactive material. *Chemical Physics Letters*, 608:35 – 39, 2014.

[79] T. Vosgröne and A. J. Meixner. Surface- and Resonance-Enhanced Micro-Raman Spectroscopy of Xanthene Dyes: From the Ensemble to Single Molecules. *ChemPhysChem*, 6(1):154–163, 2005.

[80] L. Jensen and G. C. Schatz. Resonance Raman Scattering of Rhodamine 6G as Calculated Using Time-Dependent Density Functional Theory. *The Journal of Physical Chemistry A*, 110(18):5973–5977, 2006.

[81] X. Liu, Y. Shao, Y. Tang, and K. F. Yao. Highly Uniform and Reproducible Surface Enhanced Raman Scattering on Air-stable Metallic Glassy Nanowire Array. *Sci Rep*, 4:5835, 2014.

[82] B. Bassi, B. Albini, A. D'Agostino, G. Dacarro, P. Pallavicini, P. Galinetto, and A. Taglietti. Robust, reproducible, recyclable SERS substrates: monolayers of gold nanostars grafted on glass and coated with a thin silica layer. *Nanotechnology*, 30(2):025302, 2019.

[83] X. Li, G. Chen, L. Yang, Z. Jin, and J. Liu. Multifunctional Au-Coated TiO_2 Nanotube Arrays as Recyclable SERS Substrates for Multifold Organic Pollutants Detection. *Advanced Functional Materials*, 20(17):2815–2824, 2010.

[84] J. Shi, T. You, Y. Gao, X. Liang, C. Li, and P. Yin. Large-scale preparation of flexible and reusable surface-enhanced Raman scattering platform based on electrospinning AgNPs/PCL nanofiber membrane. *RSC Adv.*, 7(75):47373–47379, 2017.

[85] Y.-C. Lai, H.-C. Ho, B.-W. Shih, F.-Y. Tsai, and C.-H. Hsueh. High performance and reusable SERS substrates using Ag/ZnO heterostructure on periodic silicon nanotube substrate. *Applied Surface Science*, 439:852 – 858, 2018.

[86] H. J. Yin, Z. Y. Chen, Y. M. Zhao, M. Lv, C. Shi, Z. Wu, X. Zhang, L. Liu, M. Wang, and H. Xu. Ag@au core–shell dendrites: a stable, reusable and sensitive surface enhanced Raman scattering substrate. *Sci Rep*, 5:14502, 2015.

[87] T. M. Cotton, R. A. Uphaus, and D. Mobius. Distance dependence of surface-enhanced raman enhancement in Langmuir-Blodgett dye multilayers. *The Journal of Physical Chemistry*, 90(23):6071–6073, 1986.

[88] M. F. Cardinal, E. Vander Ende, R. A. Hackler, M. O. McAnally, P. C. Stair, G. C. Schatz, and R. P Van Duyne. Expanding applications of SERS through versatile nanomaterials engineering. *Chem. Soc. Rev.*, 46(13):3886–3903, 2017.

[89] D. Rovati, B. Albini, P. Galinetto, P. Grisoli, B. Bassi, P. Pallavicini, G. Dacarro, and A. Taglietti. High Stability Thiol-Coated Gold Nanostars Monolayers with Photo-Thermal Antibacterial Activity and Wettability Control. *Nanomaterials*, 9(9):1288, 2019.

[90] A. Guerrero-Martínez, B. Barbosa, I. Pastoriza-Santos, and L. M. Liz-Marzán. Nanostars shine bright for you: Colloidal synthesis, properties and applications of branched metallic nanoparticles. *Current Opinion in Colloid & Interface Science*, 16(2):118 – 127, 2011.

[91] V.I. Kukushkin, A.B. Van'kov, and I.V. Kukushkin. Long-range manifestation of surface-enhanced Raman scattering. *JETP Lett*, 98:64–69, 2013.

[92] M. Pucetaite, M. Velicka, J. Pilipavicius, A. Beganskiene, J. Ceponkus, and V. Sablinskas. Uric acid detection by means of SERS spectroscopy on dried Ag colloidal drops. *Journal of Raman Spectroscopy*, 47(6):681–686, 2016.

[93] R. Chen, L. Zhang, X. Li, L. Ong, Y.G. Soe, N. Sinsua, S.L. Gras, R.F. Tabor, X. Wang, and W. Shen. Trace Analysis and Chemical Identification on Cellulose Nanofibers-Textured SERS Substrates Using the "Coffee Ring" Effect. *ACS Sensors*, 2(7):1060–1067, 2017.

[94] C. J. Orendorff, A. Gole, T. K. Sau, and C. J. Murphy. Surface-Enhanced Raman Spectroscopy of Self-Assembled Monolayers: Sandwich Architecture and Nanoparticle Shape Dependence. *Analytical Chemistry*, 77(10):3261–3266, 2005.

[95] Xia Zhou, Qian Zhao, Guangqiang Liu, and Weiping Cai. 4-Mercaptophenylboronic acid modified Au nanosheets-built hollow submicrocubes for active capture and ultrasensitive SERS-based detection of hexachlorocyclohexane pesticides. *Sensors and Actuators B: Chemical*, 293:63–70, 2019.

[96] A. Taglietti, Y.A. Diaz Fernandez, P. Galinetto, P. Grisoli, C. Milanese, and P. Pallavicini. Mixing thiols on the surface of silver nanoparticles: Preserving antibacterial properties while introducing SERS activity. *J. Nanopart. Res.*, 15:2047, 2013.

[97] A. Casu, E. Cabrini, A. Donà, A. Falqui, Y. Diaz-Fernandez, C. Milanese, A. Taglietti, and P. Pallavicini. Controlled Synthesis of Gold Nanostars by Using a Zwitterionic Surfactant. *Chemistry – A European Journal*, 18(30):9381–9390, 2012.

[98] Ansi. *American National Standard for Safe Use of Lasers*. Laser Institute of America: Orlando, FL, USA.

[99] B Bassi, A Taglietti, P. Galinetto, N. Marchesi, A. Pascale, E. Cabrini, P. Pallavicini, and G. Dacarro. Tunable coating of gold nanostars: Tailoring robust SERS labels for cell imaging. *Nanotechnology*, 27(26):265302, 2016.

[100] P. Pallavicini, E. Cabrini, G. Cavallaro, G. Chirico, M. Collini, L. D'Alfonso, G. Dacarro, A. Donà, N. Marchesi, C. Milanese, A. Pascale, L. Sironi, and A. Taglietti. Gold nanostars coated with neutral and charged polyethylene glycols: A comparative study of in-vitro biocompatibility and of their interaction with SH-SY5Y neuroblastoma cells. *Journal of Inorganic Biochemistry*, 151:123 – 131, 2015.

[101] M. Holtzer, A. Kmita, A. Pribulova, P. Futas, and A. Roczniak. Use of Specific Properties of Zinc Ferrite in Innovative Technologies. *Archives of Metallurgy and Materials*, 61(4):2141–2146, 2016.

[102] C. Suchomski, B. Breitung, R. Witte, M. Knapp, S. Bauer, T. Baumbach, C. Reitz, and T. Brezesinski. Microwave synthesis of high-quality and uniform 4 nm $ZnFe_2O_4$ nanocrystals for application in energy storage and nanomagnetics. *Beilstein Journal of Nanotechnology*, 7:1350–1360, 2016.

[103] S. Goutham, D. S. Kumar, K. K. Sadasivuni, J.-J. Cabibihan, and K. Venkateswara Rao. Nanostructure $ZnFe_2O_4$ with *Bacillus subtilis* for Detection of LPG at Low Temperature. *Journal of Electronic Materials*, 46:2334–2339, 2017.

[104] A. H. Mady, M. L. Baynosa, D. Tuma, and J.-J. Shim. Facile microwave-assisted green synthesis of Ag-$ZnFe_2O_4$@rGO nanocomposites for efficient removal of organic dyes under UV- and visible-light irradiation. *Applied Catalysis B: Environmental*, 203:416–427, 2017.

[105] R. Sharma, P. Thakur, P. Sharma, and V. Sharma. Ferrimagnetic Ni^{2+} doped Mg-Zn spinel ferrite nanoparticles for high density information storage. *Journal of Alloys and Compounds*, 704:7–17, 2017.

[106] Defi Yuliantika, Ahmad Taufiq, and Edy Giri Rahman Putra. Hierarchical structure and antibacterial activity of olive oil based $MZFe_2O_4$ ferrofluids. *Journal of Physics: Conference Series*, 1436:012145, 2020.

[107] F. Ajormal, F. Moradnia, S. Taghavi Fardood, and A. Ramazani. Zinc Ferrite Nanoparticles in Photo-Degradation of Dye: Mini-Review. *Journal of Chemical Reviews*, 2(2):90–102, 2020.

[108] R.M. Borade, S.B. Somvanshi, S.B. Kale, R.P. Pawar, and K.M. Jadhav. Spinel zinc ferrite nanoparticles: an active nanocatalyst for microwave irradiated solvent free synthesis of chalcones. *Materials Research Express*, 7(1):016116, 2020.

[109] S.B. Somvanshi, P.B. Kharat, M.V. Khedkar, and K.M. Jadhav. Hydrophobic to hydrophilic surface transformation of nano-scale zinc ferrite via oleic acid coating: Magnetic hyperthermia study towards biomedical applications. *Ceramics International*, 46(6):7642 – 7653, 2020.

[110] S.R. Patade, D.D. Andhare, S.B. Somvanshi, P.B. Kharat, S.D. More, and K.M. Jadhav. Preparation and characterisations of magnetic nanofluid of zinc ferrite for hyperthermia. *Nanomaterials and Energy*, 9(1):8–13, 2020.

[111] D. Yoo, J.-H. Lee, T.-H. Shin, and J. Cheon. Theranostic Magnetic Nanoparticles. *Accounts of Chemical Research*, 44(10):863–874, 2011.

[112] P Galinetto, B. Albini, M. Bini, and M.C. Mozzati. *Raman spectroscopy in Zinc Ferrites Nanoparticles*. IntechOpen, 2018.

[113] R. Díaz-Pardo and R. Valenzuela. Characterization of Magnetic Phases in Nanostructured Ferrites by Electron Spin Resonance. In Saad Osman Bashir, editor, *Advanced Electromagnetic Waves*, chapter 6. IntechOpen, Rijeka, 2015.

[114] C.-L. Chen and C.-L. Dong. Characterization of the Electronic Structure of Spinel Superconductor $LiTi_2O_4$ using Synchrotron X-ray Spectroscopy. In A. Gabovich, editor, *Superconductors*, chapter 2. IntechOpen, Rijeka, 2015.

[115] B. Issa, I.M. Obaidat, B.A. Albiss, and Y. Haik. Magnetic Nanoparticles: Surface Effects and Properties Related to Biomedicine Applications. *International Journal of Molecular Sciences*, 14(11):21266–21305, 2013.

[116] A.G. Kolhatkar, A.C. Jamison, D. Litvinov, R.C. Willson, and T.R. Lee. Tuning the Magnetic Properties of Nanoparticles. *International Journal of Molecular Sciences*, 14(8):15977–16009, 2013.

[117] A. Ali, H. Zafar, I ul Haq, A.R. Phull, J.S. Ali, and A. Hussain. Synthesis, characterization, applications, and challenges of iron oxide nanoparticles. *Nanotechnol Sci Appl*, 9:49–67, 2016.

[118] V. D'Ippolito, G.B. Andreozzi, D. Bersani, and P.P. Lottici. Raman fingerprint of chromate, aluminate and ferrite spinels. *Journal of Raman Spectroscopy*, 46(12):1255–1264, 2015.

[119] P. Chandramohan, M.P. Srinivasan, S. Velmurugan, and S.V. Narasimhan. Cation distribution and particle size effect on Raman spectrum of $CoFe_2O_4$. *Journal of Solid State Chemistry*, 184(1):89–96, 2011.

[120] J.P. Singh, R.C. Srivastava, H.M. Agrawal, and R. Kumar. Micro-Raman investigation of nanosized zinc ferrite: effect of crystallite size and fluence of irradiation. *Journal of Raman Spectroscopy*, 42(7):1510–1517, 2011.

[121] D.L.A. de Faria, S. Venâncio Silva, and M.T. de Oliveira. Raman microspectroscopy of some iron oxides and oxyhydroxides. *Journal of Raman Spectroscopy*, 28(11):873–878, 1997.

[122] D. Varshney, K. Verma, and A. Kumar. Structural and vibrational properties of $Zn_xMn_{1-x}Fe_2O_4$ (x=0.0, 0.25, 0.50, 0.75, 1.0) mixed ferrites. *Materials Chemistry and Physics*, 131(1):413–419, 2011.

[123] D. Song, R. Yang, C. Wang, R Xiao, and F. Long. Reusable nanosilver-coated magnetic particles for ultrasensitive SERS-based detection of malachite green in water samples. *Scientific Reports*, 6:22870, 2016.

[124] M. Bini, C. Tondo, D. Capsoni, M.C Mozzati, B. Albini, and P. Galinetto. Superparamagnetic $ZnFe_2O_4$ nanoparticle: the effect of Ca and Gd doping. *Materials Chemistry and Physics*, 204:72–82, 2018.

[125] Brian D. Hosterman. Raman Spectroscopy Study of Solid Solution Spinel Oxides. *UNLV Thesis, Dissertations, Professional Papers, and Capstones*, page 1087, 2011.

[126] Z. Wang, D. Schiferl, Y. Zhao, and H.St.C. O'Neill. High pressure Raman spectroscopy of spinel-type ferrite $ZnFe_2O_4$. *Journal of Physics and Chemistry of Solids*, 64:2517–2523, 2003.

[127] M. Virumbrales-del Olmo, A. Delgado-Cabello, A. Andrada-Chacón, J. Sánchez-Benítez, E. Urones-Garrote, V. Blanco-Gutiérrez, M. J. Torralvo, and R Sáez-Puche. Effect of composition and coating on the interparticle interactions and magnetic hardness of MFe_2O_4 (M = Fe, Co, Zn) nanoparticles. *Phys. Chem. Chem. Phys.*, 19(12):8363–8372, 2017.

[128] T. Yamanaka and M. Ishii. Raman scattering and lattice vibrations of Ni_2SiO_4 spinel at elevated temperature. *Phys. Chem. Minerals*, 13:156–160, 1986.

[129] J. Larry Verble. Temperature-dependent light-scattering studies of the Verwey transition and electronic disorder in magnetite. *Phys. Rev. B*, 9:5236–5248, 1974.

[130] A.K. Arora, M. Rajalakshmi, T.R. Ravindran, and V. Sivasubramanian. Raman spectroscopy of optical phonon confinement in nanostructured materials. *Journal of Raman Spectroscopy*, 38(6):604–617, 2007.

[131] Z.Z. Lazarević, Č. Jovalekić, V.N. Ivanovski, A. Rečnik, A. Milutinović, B. Cekić, and N.Z. Romčević. Characterization of partially inverse spinel $ZnFe_2O_4$ with high saturation magnetization synthesized via soft mechanochemically assisted route. *Journal of Physics and Chemistry of Solids*, 75(7):869–877, 2014.

[132] Z.Z. Lazarević, A.N. Milutinović, D.J. Čedomir, V.N. Ivanovski, N. Daneu, I. Mađarević, and N.Z. Romčević. Spectroscopy investigation of nanostructured nickel–zinc ferrite obtained by mechanochemical synthesis. *Materials Research Bulletin*, 63:239–247, 2015.

[133] L. Malavasi, P. Galinetto, M.C. Mozzati, C.B. Azzoni, and G. Flor. Raman spectroscopy of AMn_2O_4 (A = Mn, Mg and Zn) spinels. *Phys. Chem. Chem. Phys.*, 4:3876–3880, 2002.

[134] R.S. Yadav, I. Kuřitka, J. Vilcakova, P. Urbánek, M. Machovsky, M. Masař, and M. Holek. Structural, magnetic, optical, dielectric, electrical and modulus spectroscopic characteristics of $ZnFe_2O_4$ spinel ferrite nanoparticles synthesized via honey-mediated sol-gel combustion method. *Journal of Physics and Chemistry of Solids*, 110:87 – 99, 2017.

[135] J.A. Gomes, G.M. Azevedo, J. Depeyrot, J. Mestnik-Filho, F.L.O. Paula, F. A. Tourinho, and R. Perzynski. Structural, Chemical, and Magnetic Investigations of Core–Shell Zinc Ferrite Nanoparticles. *The Journal of Physical Chemistry C*, 116:24281–24291, 2012.

[136] Z. Ž. Lazarević, D. L. Sekulić, V. N. Ivanovski, and N. Ž. Romčević. A Structural and Magnetic Investigation of the Inversion Degree in Spinel $NiFe_2O_4$, $ZnFe_2O_4$ and $Ni_{0.5}Zn_{0.5}Fe_2O_4$ Ferrites Prepared by Soft Mechanochemical Synthesis. *International Journal of Materials and Metallurgical Engineering*, 9(8):1066–1070, 2015.

[137] I.V. Chernyshova, M.F. Hochella Jr, and A.S. Madden. Size-dependent structural transformations of hematite nanoparticles. 1. Phase transition. *Phys. Chem. Chem. Phys.*, 9:1736–1750, 2007.

[138] P. Galinetto, M.C. Mozzati, M.S. Grandi, M. Bini, D. Capsoni, S. Ferrari, and V. Massarotti. Phase stability and homogeneity in undoped and Mn-doped $LiFePO_4$ under laser heating. *Journal of Raman Spectroscopy*, 41:1276–1282, 2010.

[139] P.A. Vinosha, L.A. Mely, J.E. Jeronsia, S. Krishnan, and S.J. Das. Synthesis and properties of spinel $ZnFe_2O_4$ nanoparticles by facile co-precipitation route. *Optik*, 134:99–108, 2017.

[140] A.K. Arora, M. Rajalakshmi, T.R. Ravindran, and V. Sivasubramanian. Raman spectroscopy of optical phonon confinement in nanostructured materials. *Journal of Raman Spectroscopy*, 38(6):604–617, 2007.

[141] J.P. Singh, R.C. Srivastava, H.M. Agrawal, and R. Kumar. Micro-Raman investigation of nanosized zinc ferrite: effect of crystallite size and fluence of irradiation. *Journal of Raman Spectroscopy*, 42(7):1510–1517, 2011.

[142] X. Lu, Z. Du, B. Quan, W. Bian, H. Zhu, and Q. Zhang. Structural dependence of the microwave dielectric properties of Cr^{3+}-substituted $ZnGa_2O_4$ spinel ceramics: crystal distortion and vibration mode studies. *J. Mater. Chem. C*, 7(27):8261–8268, 2019.

[143] L. Li, F. Pan, P.A. Tanner, and K.-L. Wong. Tunable Dual Visible and Near-Infrared Persistent Luminescence in Doped Zinc Gallogermanate Nanoparticles for Simultaneous Photosensitization and Bioimaging. *ACS Applied Nano Materials*, 3(2):1961–1971, 2020.

[144] M. Milanović, E.G. Moshopoulou, D. Stamopoulos, E. Devlin, K.P. Giannakopoulos, A.G. Kontos, K. Eleftheriadis, M.I. Gini, and L.M. Nikolić. Structure and magnetic properties of $Zn_{1-x}In_xFe_2O_4$ and $ZnY_xFe_{2-x}O_4$ nanoparticles prepared by coprecipitation. *Ceramics International*, 39(3):3235–3242, 2013.

[145] M.K. Roy, B. Haldar, and H.C. Verma. Characteristic length scales of nanosize zinc ferrite. *Nanotechnology*, 17(1):232–237, 2005.

[146] J.P. Singh, R.C. Srivastava, H.M. Agrawal, R.P.S. Kushwaha, P. Chand, and R. Kumar. EPR STUDY OF NANOSTRUCTURED ZINC FERRITE. *International Journal of Nanoscience*, 07(01):21–27, 2008.

[147] R. Díaz-Pardo and R. Valenzuela. Characterization of Magnetic Phases in Nanostructured Ferrites by Electron Spin Resonance. In Saad Osman Bashir, editor, *Advanced Electromagnetic Waves*, chapter 6. IntechOpen, Rijeka, 2015.

[148] T. Xia, M. Kovochich, M. Liong, L. Mädler, B. Gilbert, H. Shi, J.I. Yeh, J.I. Zink, and A.E. Nel. Comparison of the mechanism of toxicity of zinc oxide and cerium oxide nanoparticles based on dissolution and oxidative stress properties. *ACS Nano*, 2(10):2121–2134, 2008.

[149] L. Alili, M. Sack, A.S. Karakoti, S. Teuber, K. Puschmann, S.M. Hirst, C.M. Reilly, K. Zanger, W. Stahl, S. Das, S. Seal, and P. Brenneisen. Combined cytotoxic and anti-invasive properties of redox-active nanoparticles in tumor–stroma interactions. *Biomaterials*, 32(11):2918–2929, 2011.

[150] H.J. Kwon, M.-Y. Cha, D. Kim, D.K. Kim, M. Soh, K. Shin, T. Hyeon, and I. Mook-Jung. Mitochondria-Targeting Ceria Nanoparticles as Antioxidants for Alzheimer's Disease. *ACS Nano*, 10(2):2860–2870, 2016.

[151] D. Ferraro, I.G. Tredici, P. Ghigna, H. Castillio-Michel, A. Falqui, C. Di Benedetto, G. Alberti, V. Ricci, U. Anselmi-Tamburini, and P. Sommi. Dependence of the Ce(iii)/Ce(iv) ratio on intracellular localization in ceria nanoparticles internalized by human cells. *Nanoscale*, 9(4):1527–1538, 2017.

[152] C. Hanley, J. Layne, A. Punnoose, K.M. Reddy, I. Coombs, A. Coombs, K. Feris, and D. Wingett. Preferential killing of cancer cells and activated human T cells using ZnO nanoparticles. *Nanotechnology*, 19(29):295103, 2008.

[153] S. Nair, A. Sasidharan, V.V. Divya Rani, D. Menon, S. Nair, K. Manzoor, and S. Raina. Role of size scale of ZnO nanoparticles and microparticles on toxicity toward bacteria and osteoblast cancer cells. *J Mater Sci: Mater Med*, 20:235, 2019.

[154] G. Colon, B.C. Ward, and T.J. Webster. Increased osteoblast and decreased Staphylococcus epidermidis functions on nanophase ZnO and TiO_2. *Journal of Biomedical Materials Research Part A*, 78A(3):595–604, 2006.

[155] W.H. Weber, K.C. Hass, and J.R. McBride. Raman study of CeO_2: Second-order scattering, lattice dynamics, and particle-size effects. *Phys. Rev. B*, 48(1):178–185, 1993.

[156] Z. Wu, M. Li, J. Howe, H.M. Meyer, and S.H. Overbury. Probing Defect Sites on $CeO_2$2 Nanocrystals with Well-Defined Surface Planes by Raman Spectroscopy and O_2 Adsorption. *Langmuir*, 26(21):16595–16606, 2010.

[157] J.E. Spanier, R.D. Robinson, F. Zhang, S.-W. Chan, and I.P. Herman. Size-dependent properties of CeO_{2-y} nanoparticles as studied by raman scattering. *Phys. Rev. B*, 64(24):245407, 2001.

[158] T.C. Bakker Schut, P.J. Caspers, G.J. Puppels, A. Nijssen, F. Heule, M.H.A. Neumann, and D.P. Hayes. Discriminating Basal Cell Carcinoma from its Surrounding Tissue by Raman Spectroscopy. *Journal of Investigative Dermatology*, 119(1):64–69, 2002.

[159] M. Rajalakshmi, A.K. Arora, B.S. Bendre, and S. Mahamuni. Optical phonon confinement in zinc oxide nanoparticles. *Journal of Applied Physics*, 87(5):2445–2448, 2000.

[160] G.-L. Xu, R. Amine, A. Abouimrane, H. Che, M. Dahbi, Z.-F. Ma, I. Saadoune, J. Alami, W. L. Mattis, F. Pan, Z. Chen, and K. Amine. Challenges in Developing Electrodes, Electrolytes, and Diagnostics Tools to Understand and Advance Sodium-Ion Batteries. *Advanced Energy Materials*, 8:1702403, 2018.

[161] X. Wu, W. Zhao, H. Wang, X. Qi, Z. Xing, Q. Zhuang, and Z. Ju. Enhanced capacity of chemically bonded phosphorus/carbon composite as an anode material for potassium-ion batteries. *Journal of Power Sources*, 378:460–467, 2018.

[162] J. Pang, A. Bachmatiuk, Y. Yin, B. Trzebicka, L. Zhao, L. Fu, R.G. Mendes, T. Gemming, Z. Liu, and M.H. Rummeli. Applications of Phosphorene and Black Phosphorus in Energy Conversion and Storage Devices. *Advanced Energy Materials*, 8(8):1702093, 2018.

[163] C.-M. Park and H.-J. Sohn. Black Phosphorus and its Composite for Lithium Rechargeable Batteries. *Advanced Materials*, 19(18):2465–2468, 2007.

[164] L. Wang, X. He, J. Li, W. Sun, J. Gao, J. Guo, and C. Jiang. Nano-Structured Phosphorus Composite as High-Capacity Anode Materials for Lithium Batteries. *Angewandte Chemie International Edition*, 51(36):9034–9037, 2012.

[165] M. Lao, Y. Zhang, W. Luo, Q. Yan, W. Sun, and S.X. Dou. Alloy-Based Anode Materials toward Advanced Sodium-Ion Batteries. *Advanced Materials*, 29(48):1700622, 2017.

[166] Y. Fu, Q. Wei, G. Zhang, and S. Sun. Advanced Phosphorus-Based Materials for Lithium/Sodium-Ion Batteries: Recent Developments and Future Perspectives. *Advanced Materials*, 29(48):1700622, 2017.

[167] J. Qian, X. Wu, Y. Cao, X. Ai, and H. Yang. High Capacity and Rate Capability of Amorphous Phosphorus for Sodium Ion Batteries. *Angewandte Chemie International Edition*, 52(17):4633–4636, 2013.

[168] I. Sultana, M.M. Rahman, T. Ramireddy, Y. Chen, and A.M. Glushenkov. High capacity potassium-ion battery anodes based on black phosphorus. *J. Mater. Chem. A*, 5(45):23506–23512, 2017.

[169] S. Huang and X. Ling. Black Phosphorus: Optical Characterization, Properties and Applications. *Small*, 13(38):1700823, 2017.

[170] G. Abellán, C. Neiss, V. Lloret, S. Wild, J.C. Chacón-Torres, K. Werbach, F. Fedi, H. Shiozawa, A. Görling, H. Peterlik, T. Pichler, F. Hauke, and A. Hirsch. Exploring the Formation of Black Phosphorus Intercalation Compounds with Alkali Metals. *Angewandte Chemie (International ed. in English)*, 56(48):15267—15273, 2017.

[171] M. Ceppatelli, S. Fanetti, R. Bini, M. Caporali, and M. Peruzzini. High pressure chemistry of red phosphorus by photo-activated simple molecules. *Journal of Physics: Conference Series*, 500(2):022008, 2014.

[172] E.N. Rissi, E. Soignard, K.A. McKiernan, C.J. Benmore, and J. Yarger. Pressure-induced crystallization of amorphous red phosphorus. *Solid State Communications*, 152:390–394, 2012.

[173] M. Shimizu, H. Usui, K. Yamane, T. Sakata, T. Nokami, T. Itoh, and H. Sakaguchi. Electrochemical Na-Insertion/Extraction Properties of Phosphorus Electrodes in Ionic Liquid Electrolytes. *Int. J. Electrochem. Sci.*, 10:10132–10144, 2015.

[174] B.V. Shanabrook and J.S. Lannin. Structural and vibrational properties of amorphous phosphorus. *Phys. Rev. B*, 24:4771–4780, 1981.

[175] H.B. Ribeiro, M.A. Pimenta, and C.J.S. de Matos. Raman spectroscopy in black phosphorus. *Journal of Raman Spectroscopy*, 49(1):76–90, 2018.

[176] Y. Akahama, M. Kobayashi, and H. Kawamura. Raman study of black phosphorus up to 13 GPa. *Solid State Communications*, 104(6):311–315, 1997.

[177] M. Snure, S. Vangala, and D. Walker. Probing phonon and electrical anisotropy in black phosphorus for device alignment. *Opt. Mater. Express*, 6(5):1751–1756, 2016.

[178] C. Ferrara, E. Vigo, B. Albini, P. Galinetto, C. Milanese, C. Tealdi, E. Quartarone, S. Passerini, and P. Mustarelli. Efficiency and Quality Issues in the Production of Black Phosphorus by Mechanochemical Synthesis: A Multi-Technique Approach. *ACS Applied Energy Materials*, 2(4):2794–2802, 2019.

[179] I. Pinus, M. Catti, R. Ruffo, M.M. Salamone, and C.M. Mari. Neutron Diffraction and Electrochemical Study of $FeNb_{11}O_{29}$/$Li_{11}FeNb_{11}O_{29}$ for Lithium Battery Anode Applications. *Chemistry of Materials*, 26(6):2203–2209, 2014.

[180] D. Spada, M.C. Mozzati, B. Albini, P. Galinetto, I. Quinzeni, D. Capsoni, and M. Bini. Deepening the shear structure $FeNb_{11}O_{29}$: influence of polymorphism and doping on structural, spectroscopic and magnetic properties. *Dalton Trans.*, 47(44):15816–15826, 2018.

[181] X. Lou, Z. Xu, Z. Luo, C. Lin, C. Yang, H. Zhao, P. Zheng, J. Li, N. Wang, Y. Chen, and H. Wu. Exploration of $Cr_{0.2}Fe_{0.8}Nb_{11}O_{29}$ as an advanced anode material for lithium-ion batteries of electric vehicles. *Electrochimica Acta*, 245:482–488, 2017.

[182] X. Lou, C. Lin, Q. Luo, J. Zhao, B. Wang, J. Li, Q. Shao, X. Guo, N. Wang, and Z. Guo. Crystal Structure Modification Enhanced $FeNb_{11}O_{29}$ Anodes for Lithium-Ion Batteries. *ChemElectroChem*, 4(12):3171–3180, 2017.

[183] D. Spada, I. Quinzeni, and M. Bini. Orthorhombic and monoclinic modifications of $FeNb_{11}O_{29}$, as promising anode materials for lithium batteries: Relationships between pseudocapacitive behaviour and structure. *Electrochimica Acta*, 296:938–944, 2019.

[184] P. Galinetto, D. Spada, M.C. Mozzati, B. Albini, and M. Bini. Effects of reaction atmosphere on physico-chemical properties of V-doped $FeNb_{11}O_{29}$. *Optical Materials*, 92:373–378, 2019.

[185] C. Nico, M.R.N. Soares, L.C. Costa, T. Monteiro, and M.P.F. Graça. Effects of Zr and Ga doping on the stoichiometry and properties of niobium oxides. *Ceramics International*, 42(1, Part B):1688–1697, 2016.

[186] T. McQueen, Q. Xu, E.N. Andersen, H.W. Zandbergen, and R.J. Cava. Structures of the reduced niobium oxides $Nb_{12}O_{29}$ and $Nb_{22}O_{54}$. *Journal of Solid State Chemistry*, 180(10):2864–2870, 2007.

[187] R. Brayner and F. Bozon-Verduraz. Niobium pentoxide prepared by soft chemical routes: morphology, structure, defects and quantum size effect. *Phys. Chem. Chem. Phys.*, 5(7):1457–1466, 2003.

[188] J.M. Jehng and I.E. Wachs. Structural chemistry and Raman spectra of niobium oxides. *Chemistry of Materials*, 3(1):100–107, 1991.

[189] F. Huang, Q. Zhou, L. Li, X. Huang, D. Xu, F. Li, and T. Cui. Structural Transition of $MnNb_2O_6$ under Quasi-Hydrostatic Pressure. *The Journal of Physical Chemistry C*, 118(33):19280–19286, 2014.

[190] P. Galinetto, M.C. Mozzati, M.S. Grandi, M. Bini, D. Capsoni, S. Ferrari, and V. Massarotti. Phase stability and homogeneity in undoped and Mn-doped $lifepo_4$ under laser heating. *Journal of Raman Spectroscopy*, 41(10):1276–1282, 2010.

[191] F.D. Hardcastle and I.E. Wachs. Determination of niobium-oxygen bond distances and bond orders by Raman spectroscopy. *Solid State Ionics*, 45(3):201–213, 1991.

[192] H.T. Kreissl, M.M.J. Li, Y.-K. Peng, K. Nakagawa, T.J.N. Hooper, J.V. Hanna, A. Shepherd, T.-S. Wu, Y.-L. Soo, and S.C. E. Tsang. Structural Studies of Bulk to Nanosize Niobium Oxides with Correlation to Their Acidity. *Journal of the American Chemical Society*, 139(36):12670–12680, 2017.

[193] M.P.F. Graça, A. Meireles, C. Nico, and M.A. Valente. Nb_2O_5 nanosize powders prepared by sol-gel - Structure, morphology and dielectric properties. *Journal of Alloys and Compounds*, 553:177–182, 2013.

[194] A. Aruga, E. Tokizaki, I. Nakai, and Y. Sugitani. Structure of iron diniobium hexaoxide, $FeNb_2O_6$: an example of metal-disordered trirutile structure. *Acta Crystallographica Section C*, 41(5):663–665, 1985.

[195] P.I. Brånemark, R. Adell, U. Breine, B.O. Hansson, J. Lindström, and A. Ohlsson. Intra-osseous anchorage of dental prostheses. I. Experimental studies. *Scand J Plast Reconstr Surg*, 3(2):81–100, 1969.

[196] D. Bollati, M. Morra, C. Cassinelli, S.M. Lupi, and R. Rodriguez Y Baena. In Vitro Cytokine Expression and In Vivo Healing and Inflammatory Response to a Collagen-Coated Synthetic Bone Filler. *Biomed Res Int*, 2016:6427681, 2016.

[197] D. Prithviraj, S. Deeksha, K. Regish, and N. Anoop. A systematic review of zirconia as an implant material. *Indian Journal of Dental Research*, 23(5):643–649, 2012.

[198] A.M. Roos-Jansåker, C. Lindahl, H. Renvert, and S. Renvert. Nine- to fourteen-year follow-up of implant treatment. Part I: implant loss and associations to various factors. *J Clin Periodontol*, 33(4):283–289, 2006.

[199] S. Rizzo, P. Zampetti, R. Rodriguez Y Baena, D. Svanosio, and S.M. Lupi. Retrospective analysis of 521 endosseous implants placed under antibiotic prophylaxis and review of literature. *Minerva Stomatol*, 59(3):75–88, 2010.

[200] S.M. Lupi, M. Cislaghi, S. Rizzo, and R. Rodriguez Y Baena. Rehabilitation with implant-retained removable dentures and its effects on perioral aesthetics: a prospective cohort study. *Clinical, cosmetic and investigational dentistry*, 8:105–110, 2016.

[201] S.M. Lupi, M. Granati, A. Butera, V. Collesano, and R. Rodriguez Y Baena. Air-abrasive debridement with glycine powder versus manual debridement and chlorhexidine administration for the maintenance of peri-implant health status: a six-month randomized clinical trial. *Int J Dent Hyg*, 15(4):287–294, 2017.

[202] R. Rodriguez y Baena, R. Pastorino, E. Gherlone, L. Perillo, S. Saturnino, and A. Lucchese. Histomorphometric evaluation of two different bone substitutes in sinus augmentation procedures: A randomized controlled trial in humans. *Int. J. Oral Maxillofac. Implant*, 32:188–194, 2016.

[203] S.M. Lupi, A. Rodriguez Y Baena, G. Cervino, C. Todaro, and S. Rizzo. Long-Term Effects of Acute Myeloid Leukemia Treatment on the Oral System in a Pediatric Patient. *Open Dent J*, 12:230–237, 2018.

[204] S.M. Lupi, A. Rodriguez Y Baena, C. Todaro, G. Ceccarelli, and R. Rodriguez y Baena. Maxillary Sinus Lift Using Autologous Periosteal Micrografts: A New Regenerative Approach and a Case Report of a 3-Year Follow-Up. *Case Rep Dent*, 2018:3023096, 2018.

[205] P. Ducheyne. Titanium and calcium phosphate ceramic dental implants, surfaces, coatings and interfaces. *J Oral Implantol*, 14(3):325–340, 1988.

[206] J. Lausmaa. Surface spectroscopic characterization of titanium implant materials. *Journal of Electron Spectroscopy and Related Phenomena*, 81(3):343–361, 1996.

[207] C.A. Chen, Y.S. Huang, W.H. Chung, D.S. Tsai, and K.K. Tiong. Raman spectroscopy study of the phase transformation on nanocrystalline titania films prepared via metal organic vapour deposition. *J. Mater. Sci. Mater. Electron.*, 20:303–306, 2009.

[208] H. Shin, H.S. Jung, K.S. Hong, and J.K. Lee. Crystal phase evolution of TiO_2 nanoparticles with reaction time in acidic solutions studied via freeze-drying method. *Journal of Solid State Chemistry*, 178(1):15–21, 2005.

[209] M.M. Hatamleh, X. Wu, A. Alnazzawi, J. Watson, and D. Watts. Surface characteristics and biocompatibility of cranioplasty titanium implants following different surface treatments. *Dent Mater*, 34(4):676–683, 2018.

[210] U. Balachandran and N.G. Eror. Raman spectra of titanium dioxide. *Journal of Solid State Chemistry*, 42(3):276–282, 1982.

[211] T. Ohsaka, F. Izumi, and Y. Fujiki. Raman spectrum of anatase, TiO_2. *Journal of Raman Spectroscopy*, 7(6):321–324, 1978.

[212] S.P.S. Porto, P.A. Fleury, and T.C. Damen. Raman spectra of TiO_2, MgF_2, ZnF_2, FeF_2, and MnF_2. *Phys. Rev.*, 154(2):522–526, 1967.

[213] H.L. Ma, J.Y. Yang, Y. Dai, Y.B. Zhang, B. Lu, and G.H. Ma. Raman study of phase transformation of TiO_2 rutile single crystal irradiated by infrared femtosecond laser. *Applied Surface Science*, 253(18):7497–7500, 2007.

[214] https://rruff.info/.

[215] C. Galli, S. Guizzardi, G. Passeri, D. Martini, A. Tinti, G. Mauro, and G.M. Macaluso. Comparison of Human Mandibular Osteoblasts Grown on Two Commercially Available Titanium Implant Surfaces. *Journal of Periodontology*, 76(3):364–372, 2005.

[216] M. Gaintantzopoulou, S. Zinelis, N. Silikas, and G. Eliades. Micro-Raman spectroscopic analysis of TiO_2 phases on the root surfaces of commercial dental implants. *Dental Materials*, 30(8):861–867, 2014.

[217] W. Xia, C. Lindahl, J. Lausmaa, and H. Engqvist. Biomimetic Hydroxyapatite Deposition on Titanium Oxide Surfaces for Biomedical Application. In Anne George, editor, *Advances in Biomimetics*, chapter 20. IntechOpen, 2011.

[218] S.M. Lupi, P. Galinetto, B. Albini, E. Di Ronza, S. Rizzo, and R. Rodriguez y Baena. Micro-Raman Spectroscopy of Dental Implants Subjected to Different Surface Treatments. *Applied Sciences*, 10(7):2417, 2020.

[219] W.F. Zhang, Y.L. He, Zhang. M.S., Z. Yin, and Q. Chen. Raman scattering study on anatase TiO_2 nanocrystals. *Journal of Physics D: Applied Physics*, 33(8):912–916, 2000.

[220] M. Salis, P.C. Ricci, and A. Anedda. Effective Linewidth in Raman Spectra of Titanium Dioxide Nanocrystals. *The Open Condensed Matter Physics Journal*, 2:15–18, 2009.

[221] B. Henderson and G.F. Imbusch. *Optical spectroscpy of inorganic solids.* Oxford: Clarendon Press.

[222] https://en.unesco.org/emergingpollutants.

[223] A. D'Agostino, A Taglietti, B Bassi, A. Donà, and P. Pallavicini. A naked eye aggregation assay for Pb^{2+} detection based on glutathione-coated gold nanostars. *J Nanopart Res*, 16:2683, 2014.

[224] B. Bassi, G. Dacarro, P. Galinetto, E. Giulotto, N. Marchesi, P. Pallavicini, A. Pascale, S. Perversi, and A. Taglietti. Tailored coating of gold nanostars: rational approach to prototype of theranostic device based on SERS and photothermal effects at ultralow irradiance. *Nanotechnology*, 29(23):235301, 2018.

[225] H. Watanabe, N. Hayazawa, Y. Inouye, and S. Kawata. DFT Vibrational Calculations of Rhodamine 6G Adsorbed on Silver: Analysis of Tip-Enhanced Raman Spectroscopy. *The Journal of Physical Chemistry B*, 109(11):5012–5020, 2005.

[226] E. Cara, L. Mandrile, F. Ferrarese Lupi, A.M. Giovanozzi, M. Dialameh, C. Portesi, K. Sparnacci, N. De Leo, A.M. Rossi, and L. Boarino. Influence of the long-range ordering of gold-coated Si nanowires on SERS. *Scientific Reports*, 8:11305, 2018.

[227] S. Li, Q. Zhou, W. Chu, W. Zhao, and J. Zheng. Surface-enhanced Raman scattering behaviour of 4-mercaptophenyl boronic acid on assembled silver nanoparticles. *Phys. Chem. Chem. Phys.*, 17(27):17638–17645, 2015.

[228] S. Zhu, C. Fan, J. Wang, J. He, and E. Liang. Surface-enhanced raman scattering of 4-mercaptobenzoic acid and hemoglobin adsorbed on self-assembled Ag monolayer films with different shapes. *Applied Physics A*, 117:1075–1083, 2014.